Title
Thermal Ion Orbit Loss in Diverted Tokamaks and its Role Approaching the L-H Transition

Author
Brzozowski, Robert William

Publication Date
2021

Peer reviewed|Thesis/dissertation

UNIVERSITY OF CALIFORNIA

Los Angeles

Thermal Ion Orbit Loss in Diverted Tokamaks and its Role Approaching the L-H Transition

A dissertation submitted in partial satisfaction

of the requirements for the degree

Doctor of Philosophy in Physics

by

Robert William Brzozowski III

2021

ABSTRACT OF THE DISSERTATION

Thermal Ion Orbit Loss in Diverted Tokamaks and its Role
Approaching the L-H Transition

by

Robert William Brzozowski III
Doctor of Philosophy in Physics
University of California, Los Angeles, 2021
Professor Frank S Jenko, Co-Chair
Professor Troy A. Carter, Co-Chair

The exact nature of the physics governing the L-H transition seen in tokamak magnetic confinement experiments has eluded fusion researchers for several decades. To date, a first principles model for the transition does not exist. The improved particle and energy confinement realized by the suppression of turbulence in the post-transition H-mode motivates an understanding of the transition and the empirically known conditions necessary for its initiation, generically an input power threshold with key sensitivities to the edge electron density, main ion mass and charge, plasma configuration, divertor conditions, ∇B drift direction, etc. Modern consensus that an increase in the $E \times B$ shear at the plasma edge is responsible for the turbulence suppression and formation of a transport barrier invigorates research into possible driving mechanisms. The loss of thermal ions from the imperfectly confining magnetic field of a tokamak manifests as a steady-state radial current in the edge and has long been suspected to play a role in the generation of the $E \times B$ shear and hence the L-H transition.

The body of this thesis presents the development of a model for the steady-state thermal

orbit loss based on the identification of the phase-space loss cone. The presented model boasts several improvements over other loss cone models found in the literature, largely rooted in the careful consideration of local pitch angle scattering on ions within and near the velocity-space boundaries of projections of the phase-space loss cone to observation points in configuration-space. The probability that ions within the loss cone will be lost on a first orbit is estimated by comparing the rates of collisionally scattering out of the loss cone to the periods of orbit loss. The steady-state is determined by the rates of collisional loss cone refueling modified by the statistical chance of first orbit loss. A competition arises between the sufficiently large temperatures necessary for appreciable parts of the distribution to interact with the loss cone and the reduced rate of collisional refueling of high energy ions.

The steady-state orbit loss current calculated by the model exhibits several features of the experimentally measured L-H transition power threshold not present in other models. The orbit loss current displays branching behaviors in the edge density, peaking at densities similar to those minimizing the required transition power on ASDEX Upgrade. Additionally, the loss current features the suspected strong ∇B drift direction asymmetry of the orbit loss. The unfavorable drift configuration requires about a factor of two greater input power to produce a similar orbit loss current seen in the favorable drift, again echoing a known behavior of the power threshold. Other explored features that suggest a promising connection between the thermal orbit losses and the transition are the main ion mass and the horizontal position of the X-point.

The orbit loss current has been implemented into the edge fluid transport code SOLPS. The first order plasma response to the current is studied over the high-density branch of the loss current. The leading order effect is an increase in the magnitude of the edge E_r well and the associated $E \times B$ shear. Over the explored parameter space, the input power necessary to reach some threshold E_r magnitude lessens on the order of $\sim$ 10–20% in the presence of the loss current. Thermal ion orbit loss appears capable of influencing the onset of the L-H transition.

The dissertation of Robert William Brzozowski III is approved.

Marco CM Velli

Christoph Niemann

Frank S Jenko, Committee Co-Chair

Troy A. Carter, Committee Co-Chair

University of California, Los Angeles

2021

To my family and friends:

your presence is indescribably important

Table of Contents

List of Figures

ACKNOWLEDGMENTS

I owe gratitude to numerous individuals, groups, and institutions that have each led to my development as a human being and scientist, presently culminating in the production of this dissertation. Whether it be emotional, intellectual, or financial support, I am appreciative to all that have provided for me over the years. This section is non-exhaustive, and if you are reading this, you should most likely be included.

It would be remiss not to first thank my immediate family: my mother, Joan, my father, Bob, and my sister, Samantha. My personality and self-esteem were shaped by their sharp wit and constant encouragement of my pursuits. I thank them for establishing an environment in which learning and doing the right thing were expected. In particular, I would like to thank my mom. Throughout my life, she has always been my strongest supporter and defender, roles which were immeasurably important during the last months of writing this thesis. It is my hope that they each know the value they hold in my life.

I would next like to generally thank the University of Michigan, Ann Arbor for providing a rich and challenging environment during my undergraduate studies. I will always value the friendships I made and times I had in Ann Arbor. Furthermore, my years in the Department of Physics taught me the joys of studying the physical world and gave me the tools to attempt to do so. I thank all the professors and educational staff that helped bolster the foundation upon which I approach all problems in life. In particular, I would like to thank Professor Fred Adams for guiding my introduction into theoretical physics research. An excellent educator and communicator, Professor Adams taught me the importance of understanding through explanation.

I similarly owe gratitude to the University of California, Los Angeles and the Department of Physics and Astronomy for fostering my growth as a researcher and an educator. I thank the professors, other PhD students, and administrative staff that each contributed to this environment. I express thanks to the members of my doctoral committee for their time and

expertise in providing feedback for this work. Furthermore, I believe that I also experienced a great deal of personal growth in California and would like to thank my friends for the experience.

Upon moving to Los Angeles for my graduate studies, I did not expect to spend nearly four years in Munich, Germany researching at the Max Planck Institute for Plasma Physics. I sincerely thank Professor Frank Jenko, my advisor, for inviting me to join him in his relocation. I additionally thank Frank for suggesting this project, offering continual support, and providing the resources necessary to pursue it. Among these resources are the many researchers at the institute. I would like to directly thank Dr. David Coster for serving as an additional mentor during the final years of this project. Dave provided emotional and intellectual support during this time, for which I am immensely appreciative. I would also like to thank Dr. Eleonora Viezzer and Pilar Cano Megías for their conversations and help in bridging the experimental–theory gap. I would next like to thank Dr. Roberto Bilato and Dr. Marco Cavedon for their conversations and contributions to our paper. My general thanks go to the other PhD students and more senior research staff that I interacted with during my time at the institute. In particular, I would like to thank the regular attendees to our weekly Friday tea hour; I enjoyed the company and conversations. I would like to specifically thank both Cole Stephens and Karl Stimmel for the support they provided in the months of writing this thesis. Finally, I would like to express gratitude to the friends I made in Germany outside of the institute. Living in Munich was a rewarding experience, and I am a better person for the time we have spent together.

This document was written during the COVID-19 pandemic, and I would like to thank the health care workers that helped to keep as many people as possible healthy during this time and the researchers that developed the necessary vaccines.

Chapter 3 includes reproduced elements from (Robert W. Brzozowski III, Frank Jenko, Roberto Bilato, Marco Cavedon, and the ASDEX Upgrade team, "A geometric model of ion orbit loss under the influence of a radial electric field" Physics of Plasmas **26**, 042511 (2019),

DOI: 10.1063/1.5075613), for which Frank Jenko was the PI, Roberto Bilato contributed to the development of the steady-state picture, Marco Cavedon oversaw the connections made to the experimental data, and the ASDEX Upgrade team provided the experimental data. Chapters 4–6 include yet to be published work that is in preparation for publication, for which Frank Jenko is the PI and David Coster contributed to the inclusion of the model into the SOLPS code, provided input on the simulations, and helped develop some details of the steady-state pitch angle scattering out of the loss cone in the steady-state model.

VITA

2010–2014 Honors B.S. in Physics, University of Michigan, Ann Arbor

2014–2016 M.S. in Physics, University of California, Los Angeles

2017–2020 Visiting Scientist, Max Planck Institute for Plasma Physics, Tokamak Theory Division, Garching, Germany

PUBLICATIONS

Robert W. Brzozowski III, Frank Jenko, Roberto Bilato, Marco Cavedon, and the ASDEX Upgrade team, "A geometric model of ion orbit loss under the influence of a radial electric field" Physics of Plasmas **26**, 042511 (2019).

Cole D. Stephens, Robert W. Brzozowski III, and Frank Jenko, "On the limitations of gyrokinetics: Magnetic moment conservation" Physics of Plasmas **24**, 102517 (2017).

Robert W. Brzozowski III, Frank Jenko, and David Coster, "Steady-state collisionally driven thermal ion orbit loss in diverted tokamaks approaching the L-H transition." In preparation.

Robert W. Brzozowski III, David Coster, and Frank Jenko, "Thermal ion orbit loss in SOLPS: Radial current balance and edge E_r response." In preparation.

Chapter 1

Introduction

1.1 Nuclear fusion as a source of power

Nuclear fusion, the combining of one or more atomic nuclei, is the most widely used source of energy on Earth, at least indirectly. Plants and other organisms absorb light emitted from the sun, converting the energy to a usable form through photosynthesis. The foundation of the food chain is set by these lifeforms, by which predatory species, including human beings, can survive. Following the first industrialization of human societies, new sources of energy have been increasingly demanded in increasing quantities.[1] It is well known that our first solutions to such demands, the fossil fuels, are limited in quantity and cause irreparable damage to our environment when implemented at scale. The combined challenges of climate change and scarcity have all too slowly encouraged investment in sustainable sources of energy; currently $\sim 80\%$ of energy demand in the United States is still supplied by fossil fuels.[2] Nonetheless, human beings have developed both new and more efficient technologies to control alternative forms of energy: solar, wind, water, geothermal, nuclear, etc.[3] Many of these solutions seek to either directly or indirectly harness the energy output of the sun.

Inspired by our distant relatives and food sources, the development of photo-voltaic technology allows for the generation of electricity from sunlight. Well placed turbines steal

energy from the fluid of their immersion, typically the atmosphere or water, whose cycles are driven by the solar heating of the Earth. Each of these energy sources is touched by the nuclear fusion reactions happening some 150 million kilometers away in the sun. *By accident*, the sun radiates $3.85 \cdot 10^{26}$ W of power by way of energy released via the nuclear fusion of light elements in its core. A mere fraction of this energy is incident on the Earth, on average about $1.75 \cdot 10^{17}$ W, with only a fraction reaching the surface. Human energy consumption is roughly four orders of magnitude less.[4] The magnitude of the sun's energy output is awe-inspiring; how can something so far away provide us so much power?

The answer lies in the relevant physics underlying the fusion process. The convenience of fossil fuels is dual in nature: they are capable of providing a sufficient amount of energy for most human activity, and this energy is relatively simple to harness. Fossil fuels release energy through combustion, a chemical reaction by which bonds between negatively charged electrons and positively charged atomic nuclei are broken and rearranged, leaving the nuclei themselves unchanged. The energy scale of combustion and other chemical reactions is that of the electromagnetic interaction. The shifted components only gain or lose energy on the scale of the binding interaction, typically in the electronvolt (eV) range for the electromagnetic interaction, thus setting a limit on the energy output of and the required energy for such reactions. Physical reactions governed by the strong nuclear force, with bonds typically in the MeV range, result in energy output typically about a million times greater than chemical reactions and consequently require larger input energies to catalyze.

Both nuclear fusion and nuclear fission, the splitting of atomic nuclei, are governed by the strong interaction. Individual fission reactions release about an order of magnitude more energy than fusion reactions, but fusion reactions release more energy per fuel mass; fusion and fission are energetically viable for low and high mass elements, respectively. Fission boasts one significant advantage over fusion as a power source: nuclear fission power plants are currently feasible and at work across the Earth. Fusion boasts many advantages over fission. Several high profile disasters surrounding nuclear fission reactors, for instance, the

events of Chernobyl (1986) or more recently in Fukushima Daiichi (2011) have understandably soured the public opinion of such facilities. In contrast, a nuclear fusion power plant does not run the risk of an uncontrolled nuclear meltdown. Furthermore, the byproducts of nuclear fusion are not radioactive for comparable lengths of time, avoiding the difficult problem of nuclear waste disposal.[5] Fusion reactions also have the benefit of requiring less exotic sources of fuel, contributing to the ease of monitoring the non-proliferation of nuclear weaponry. Although the problem of creating a nuclear fusion reactor is an open one, the advantages of safe and sustainable energy production on the scale of the strong force demand continued experimental and theoretical research in the field. The challenge at hand is to not only recreate conditions similar to those within the sun's core but to do so in a controlled fashion that can reliably and continuously convert energy to a usable form.

For any nuclei to fuse, they must overcome their mutual electromagnetic repulsion such that they can interact on the shorter length scale of the strong force. Collisions of the nuclei dictate these reactions such that the rates are often discussed in terms of cross-sections. A fusion reaction with a particularly large cross-section, due to quantum mechanical tunneling effects, is the fusion of hydrogen's two isotopes, deuterium and tritium:[6]

$$ {}_1\mathrm{D}^2 + {}_1\mathrm{T}^3 \rightarrow {}_2\mathrm{He}^4 + {}_0\mathrm{n}^1 + 17.6 \text{ MeV}. \tag{1.1} $$

The excess 17.6 MeV was originally held by the strong force carrying gluons, binding the nucleons together, and is carried away as kinetic energy by the α-particle and neutron products. The cross-section for the above reaction is maximized for particle energies around 100 keV, about 100 times hotter than the sun's core. Decreasing the deuteron energies by an order of magnitude results in a cross-sectional decrease of about three orders of magnitude,[6] emphasizing the importance of the fuel temperature. To capitalize on such reactions, they must be sufficiently numerous, demanding that the fuel be maintained at some ideal density for a given temperature. The extreme gravitational pull of the sun finds equilibrium in bal-

ancing the large outward pressure found in its core, effectively confining a large number of fusing nuclei. Without access to comparably large confining fields, it is necessary to achieve fusion while maintaining outward pressures that can be realistically balanced, encouraging the use of warmer and less dense fuels compared to the solar core.

The confinement problem extends beyond the particles, and the timescale of the system's energy confinement, τ_E, must be considered. This time scale is inversely proportional to the fuel temperature,[6] discouraging the use of arbitrarily large heating input, not to mention the looming concerns of operational cost and potential structural damage. In any case, continued heating of the fuel is necessary until the energy of the fusion reactions is able to sustain the conditions necessary for fusion, a state referred to as ignition, requiring a triple product of the fuel temperature, density, and the energy confinement time

$$nT\tau_E \geq 3 \cdot 10^{21} \text{ m}^{-3} \text{ keV s}. \tag{1.2}$$

This relationship is known as the Lawson criterion for the deuterium-tritium fusion reaction.[7] Other fuels require a quantitatively different criterion.

The constituent particles in such a state are unsurprisingly nearly all ionized, as the thermal energies are far above the typical energies of the electromagnetic interaction. The individual charged particles are sensitive to any electromagnetic fields, including those that arise from the collective motions of the charges, via the Lorentz force

$$\boldsymbol{F} = q\left(\boldsymbol{E} + \boldsymbol{v} \times \boldsymbol{B}\right).$$

The result is a complex system of N particles each coupled to the electromagnetic fields obeying Maxwell's equations

$$\nabla \cdot \boldsymbol{E} = \frac{\rho}{\epsilon_0}, \tag{1.3}$$

$$\nabla \cdot \boldsymbol{B} = 0, \tag{1.4}$$

$$\nabla \times \boldsymbol{E} = -\frac{\partial \boldsymbol{B}}{\partial t}, \tag{1.5}$$

$$\nabla \times \boldsymbol{B} = \mu_0 \left(\boldsymbol{J} + \epsilon_0 \frac{\partial \boldsymbol{E}}{\partial t} \right). \tag{1.6}$$

Thus, the physics governing the particle and collective behaviors is that of plasma physics. Often, the confining gravitational field of a stellar fusion plasma is replaced by complex magnetic field configurations, an approach aptly known as magnetic confinement fusion.

1.2 Properties of a plasma

According to Krall and Trivelpiece, "Plasma physics is the study of charged particles collected in sufficient number so that the long-range Coulomb force is a factor in determining the statistical properties, yet low enough in density so that the force due to a near-neighbor particle is much less than the long-range Coulomb force exerted by the many distant particles."[8] Within this statement is the definition of a plasma, which can be parameterized and understood following the introduction of the Debye length.

Any charged point particle affects the space around it by way of its electric field,

$$\boldsymbol{E} = \frac{1}{4\pi\epsilon_0} \frac{Ze}{r^2} \hat{r}, \tag{1.7}$$

with an electrostatic potential of the form

$$\Phi = \frac{1}{4\pi\epsilon_0} \frac{Ze}{r}. \tag{1.8}$$

Here, Ze is the charge of the particle, r is the distance away from the charge, and ϵ_0 is the well-known permittivity of free space. If this point particle exists within a collection of charged particles, those of similar charge will feel a repulsive force while oppositely charged particles will experience an attraction, each charge also projecting its own electric field. The drawn charges of opposite sign shield more distant charges from interactions with the point

particle in much the same way that the electric field of a dipole decays far faster than a monopole. The shielding is expressed by a characteristic length scale

$$\Phi = \frac{1}{4\pi\epsilon_0}\frac{Ze}{r}e^{-r/\lambda_D}, \tag{1.9}$$

where λ_D is the Debye length,

$$\lambda_D = \sqrt{\frac{\epsilon_0 T}{n_e e^2}}. \tag{1.10}$$

Here, e is the elementary charge, n_e is the electron density, and T is an assumed equilibrium temperature. The internal plasma energy is insufficient to maintain charge separations over distances longer than the Debye length, a property known as the quasi-neutrality condition. On length scales longer than the Debye length,

$$n_e = \sum_i Z_i n_i, \tag{1.11}$$

where n_i is the density of each ion species and Z_i is the charge state. In opposition to true charge neutrality, quasineutrality does not imply the nonexistence of a finite charge density,

$$\nabla \cdot \boldsymbol{E} = \frac{\rho}{\epsilon_0} \neq 0, \tag{1.12}$$

where $\boldsymbol{E}$ is the electric field and ρ is the charge density. In the steady-state, the charge density is taken to be time independent

$$\frac{\partial}{\partial t}\left(\nabla \cdot \boldsymbol{E}\right) = 0, \tag{1.13}$$

implying a dearth of current sources by connection with Ampere's law, Eq. (1.6),

$$\nabla \cdot \boldsymbol{J} = 0, \tag{1.14}$$

where $\boldsymbol{J}$ corresponds to the current density. Integrating Eq. (1.14) about some closed volume and applying the divergence theorem makes clear the consequence of equilibrium quasineutrality

$$\oiint (\boldsymbol{J} \cdot \hat{\boldsymbol{n}})\, dS = 0; \tag{1.15}$$

the net current flow across any closed surface must be zero. The currents that arise from the particle motions must create self closing loops to prevent any net current flow. Therefore, the net particle transport in a tokamak must be ambipolar. Any non-ambipolar transport mechanism must be compensated by another non-ambipolar type transport.

For a collection of charged particles to depend more on long range particle interactions than on collisions with its nearest neighbors, the number of particles within a Debye sphere, $\sim \lambda_D^3$, must be very large to supply the necessary shielding, leading to the definition of the plasma parameter,

$$\begin{aligned} g &= \frac{1}{n\lambda_D^3} \\ &= \sqrt{n}\left(\frac{e^2}{\epsilon_0 T}\right)^{3/2}. \end{aligned} \tag{1.16}$$

The plasma parameter is clearly inversely proportional to the number of particles within a Debye sphere, and $g \ll 1$ is called the plasma approximation. Perhaps contrary to intuition, low densities for a given temperature are required to maintain a large number of particles within a Debye sphere since the sphere's volume shrinks with increasing density.[8] The plasmas of interest for magnetically confined fusion typically satisfy the plasma approximation and are treated using the techniques of plasma physics, some of which are discussed in Chapter 2.

1.3 The tokamak and the L-H transition

In pursuance of achieving sustained energy-positive terrestrial nuclear fusion, a variety of devices have been developed which act to confine plasmas within magnetic field geometries. The work of this thesis is directly applicable to one such type, the tokamak, a well explored solution to the problem of magnetic confinement. Fusion plasmas exhibit such complex behaviors that are deeply connected to their confining field geometries that vast fields of academic study revolve around the particularities of each. The direct focus of this document on the tokamak configuration is rooted in several practicalities. First and foremost, the majority of the presented work was performed at the Max Planck Institute for Plasma Physics in Garching, Germany. The on-site experimental tokamak ASDEX Upgrade (AUG) has a strong influence on the research interests of the institute and its collaborators. Furthermore, this work seeks to investigate a proposed factor in the L-H transition, a fast time-scale phase change seen in tokamaks in response to increased heating power from a low confinement behavior to a regime of high confinement, first seen at AUG's predecessor ASDEX.[9] Finally, foundational techniques for the developed model rely on the toroidal symmetry of the tokamak's magnetic field, a hallmark of the device. For the remainder of the document, the discussion will focus on the field geometry of a tokamak, in particular that of a poloidally diverted tokamak.

The plasma in a tokamak is confined in the shape of a torus. The tokamak magnetic field primarily consists of a large toroidal component maintained by external superconducting coils. An additional poloidal magnetic field component is required to combat the planar drift motions of the charged particles out of the device, discussed in more detail in the upcoming chapter. A transformer is manipulated to change the magnetic flux through the tokamak itself, inducing a toroidal electric field in line with Faraday's law, Eq. (1.5). This electric field drives a toroidal plasma current, generating the required poloidal magnetic field. The changing magnetic flux sets an operational limit on the tokamak; the flux cannot increase indefinitely, and the device must run in a pulsed fashion. An alternative magnetic confinement

device that avoids this problem is the stellarator. Highly complex and precise field coils are designed to naturally create a twisting magnetic field structure that confines the majority of charged particles. The driven toroidal plasma current in the tokamak is often associated with disruption events where confinement is lost, a notable problem avoided by the stellarator design.[6,10] Although, the resulting magnetic field geometry of a stellarator is highly dependent on the toroidal coordinate, unlike the nearly toroidally symmetric, axisymmetric, field of a tokamak.

The tokamak plasma is kept separate from the material wall as both an act of confinement and to prevent the accumulation of radiating impurities within the plasma, a problem for the confinement of energy.[6] One method of bolstering this separation is the so-called divertor configuration. The magnetic field is altered to create a null point in the poloidal magnetic field and thus a saddle point in the magnetic flux. This X-point creates a surface of constant magnetic flux with the shape of a figure-eight. The confined plasma exists in one of these loops within the vacuum vessel while the other loop intersects with the vessel in the divertor region. The flux surfaces within the loop confining the plasma are closed while the surfaces outside are open to the wall or divertor, effectively distancing the confined plasma from the impurity releasing surfaces. The last closed flux surface (LCFS) is often referred to as the separatrix, and to be 'within the separatrix' is to be in the closed field line region.

The axisymmetric nature of the tokamak often allows for simple visualizations of phenomena projected onto a poloidal cross-section. Figure 1.1 shows the field geometry in the poloidal plane for AUG discharge 16151 used as an example case in the SOLPS transport code. SOLPS models the edge region of the confined plasma and the scrape of layer (SOL) beyond the separatrix. Consequently, the plots omit the inner core region. Subplot (a) shows the toroidal field structure, where the basic R^{-1} field strength dependence can be easily seen. Subplot (b) shows the poloidal magnetic flux where the surfaces of constant flux are visible. The separatrix is shown demarcating the closed flux surfaces from those open. Also shown is the vessel structure, including the divertor structure found at the bottom of

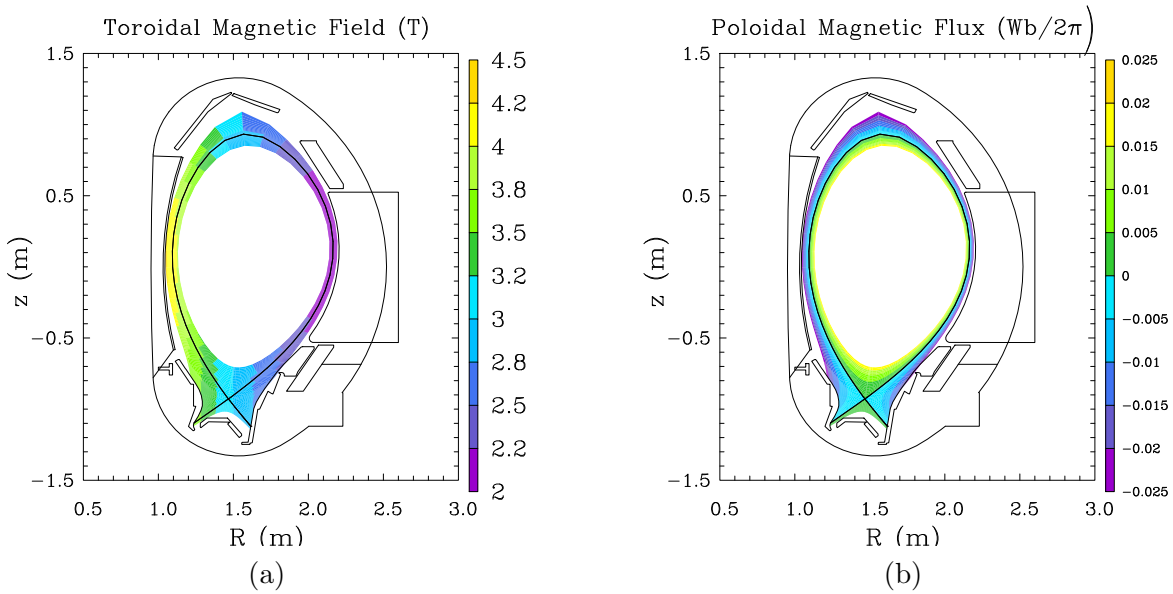

Figure 1.1: The field geometry for the baseline AUG discharge 16151. The poloidal field can be seen in Fig. 4.8.

the device. Rotation of the images about $R = 0$ over 2π in the toroidal angle reproduces the full tokamak geometry.

To leading order, the single particle motions of the charged particles follow helical orbits about the magnetic field lines, constraining the particles to a flux surface. If this were the complete picture, any particle within the separatrix would be confined for all time and the Lawson criterion would be trivially satisfied. The second order particle motions include the perpendicular drifts resulting from particle motion in the inhomogeneous magnetic field of a tokamak. Neoclassical theory considers the multitude of effects of the toroidal field geometry on the confined plasma, culminating in the neoclassical transport:[11] the outward diffusive radial motions of particles associated with interparticle Coulomb collisions in the tokamak field geometry. The diffusion coefficients calculated from such theories often fail to predict the high levels of radial particle and energy transport experimentally measured. The observed transport of energy and particles above the neoclassically predicted levels was originally labeled 'anomalous' in relation to its unpredicted nature. It is generally accepted that the anomalous transport describes the outward fluxes of particles and energy due to

the evolution of small scale fluctuations in the plasma linked to turbulence.[12,13]

A suppression in the anomalous transport is seen in response to some threshold input heating power by way of a phase transition of sorts into a regime of high confinement on a fast timescale.[9,14–21] This improved mode of operation is called the H-mode and the low confinement phase the L-mode. Although possible on limiter tokamak configurations, the power threshold is significantly lower for poloidally diverted tokamaks.[36,37] In the diverted configuration, the power threshold is minimized when the ion ∇B drift direction is toward the active X-point[15,16] and for some machine dependent edge density,[22,23] birthing low and high density branches for the power threshold. Additional known dependencies include the mass and charge of the main ion species[24–28] and the X-point and divertor conditions.[20,29]

Remarkably, the H-mode has improved energy confinement by about a factor of two,[15] and it is assumed that tokamak reactors of the future will operate in such a regime.[30] The anomalous transport reduction manifests as the formation of a transport barrier in the edge of the confined plasma, defined by the so-called pedestal region marked by steep gradients in the radial temperature and density profiles. Concurrently present in the pedestal region is a significantly deepened radial electric field well, which has long been suspected of playing a role in the turbulence suppresion.[15,64] Modern understanding of the turbulence suppression indicates that rather than the well depth it is the large gradients of the electric field and the related strongly sheared $E \times B$ flows that are instrumental,[31] although in many cases the two are inextricably linked.

The exact physics of the transition is still unknown. There is interest in exploring any mechanism related to the increase of the E_r magnitude and thus the stabilizing shear $E \times B$ flows in the edge. Bodies of evidence exist which suggest that the necesarry flows to enter the H-mode are driven by turbulence while others indicate that neoclassical orbit loss is responsible.[32] It appears likely that an interplay between the two sources holds the truth.

1.4 This thesis

The focus of this document is to investigate the neoclassical orbit losses thought to contribute to the shear $E \times B$ flows in the tokamak edge,[32,33] possibly playing a role in the L-H transition. The effect is neoclassical in the sense that it is a direct result of the toroidal field structure. The second order particle drift motions disproportionately move the heavier ions further from the flux surfaces of their lowest order motion, allowing for the generation of a plasma current from the confined orbits. The magnitudes of these orbital widths are proportional to the ions' energies. Thus, for sufficiently energetic particles, the orbits are able to intersect the first wall, essentially being removed from the system. Since the charge loss associated with these ions is inherently non-ambipolar, it must be closed by a current driven by another plasma phenomenon.

The X-point geometry of a diverted tokamak allows for topologically open orbits connected to the divertor for particles of arbitrarily low energy, see Chapter 3. The radial domain of the low energy losses is related to the orbital widths, again favoring the loss of ions, allowing for a non-ambipolar transport of ions out of the confined region on trajectories to the divertor. The loss of thermal ions is dominated by these trajectories.[33,34] The net transport and sourcing of ions onto such orbits within the confined region of the plasma corresponds to an excess outward flux of ions across the separatrix.[35] The ions carry an electric current that cannot close itself as the particles are lost to the divertor, again necessitating closure from another plasma phenomenon.

Several properties of the orbit losses make them noteworthy in regard to the L-H transition. For any configuration, the trigger to enter the H-mode is the application of a threshold heating power, with evidence indicating that the ion channel plays a more fundamental role.[23] The direct scaling of the average orbital width with the ion temperature suggests that the orbit losses are more prevalent for increasing input powers. The fact that the L-H transition power threshold is significantly higher for limiter configuration plasmas further supports the importance of the thermal orbit losses in the diverted configuration.[36,37] Furthermore, the

loss orbits are expected to produce greater losses in the favorable ∇B drift configuration due to the on-average shorter loss periods for ions originating in the confined region,[38,39] aligning with the experimentally observed reduction in the power threshold in this orientation. The orbit losses are additionally expected to scale directly with the ion mass and inversely with the charge, qualitatively agreeing with experimental observation.[40] The majority of thermal orbit losses pass nearby the X-point on their way to the divertor, suggesting that the physics of ions on these trajectories can help explain the additional sensitivities of the L-H transition on the X-point and divertor geometries.

The portion of phase-space describing orbits lost to the wall or divertor can be identified and is referred to as the loss cone. Often projected to a specific point in configuration-space, the resulting velocity-space loss cone contains all collisionless ion trajectories passing through an observation point that are removed from the plasma on a first orbit. If initially full, a loss cone containing collisionless orbits empties itself on the orbit timescale and further losses occur only if the cone is refilled by some mechanism. The ion orbit loss phenomenon is explicitly dependent on the distribution of particles within phase-space and is therefore a kinetic effect. Plasma descriptions that are insensitive to such details are incapable of resolving the orbit losses, and the effect is most naturally included in a fully kinetic model, where it has been reported to be of crucial importance.[32]

Nevertheless, there have been many efforts to understand ion orbit loss within a reduced context both analytically[41–44,64] and numerically.[33,34,45–47] The static loss cone structure is well diagnosed and has been reproduced in a variety of contexts: in circular and other analytic flux geometries,[41,43] in experimental flux geometries,[42,44] under the influence of a radial electric field,[42,44,45,47] for different plasma triangularities,[47,48] etc. Solutions to the static problem suggest under which conditions the orbit losses are most significant; however, steady-state solutions are necessary to probe the interaction between the plasma and the loss mechanism. Existing steady-state solutions, those concerning the refueling of the loss cone, typically assume purely collisionless loss orbits,[49,50] omitting a fundamental

sensitivity of the problem, or rely on a simplified collisional cutoff.[64] Such solutions also either use liberal definitions of orbit loss[49,64] or do not resolve the phenomenon over the entire confined region,[50,64] leaving additional room for improvement. Furthermore, the mechanisms responsible for refilling the loss cone serve as the driving force for the losses and have only tentatively been explored. An eventual complete characterization of each process will be necessary to perfectly resolve the steady-state ion orbit loss, a feat beyond the scope of this thesis.

The body of this thesis provides solutions to some of these open problems. The document is presented in a procedural fashion, with the content of each chapter paving the way for the next. The primary goals of the work are to develop a steady-state ion orbit loss model that accounts for sensitivities missing in the literature, largely through a detailed comparison of the collisional and loss timescales, and to implement the loss current into an established fluid model, SOLPS, to study the first order influence of the loss mechanism on confined L-mode plasmas nearing the L-H transition.

- Chapter 2 includes the necessary theoretical background to understand and contextualize the remainder of the work. The basic theories of tokamak plasmas and their modeling are discussed, as well as an introduction to the fluid transport code suite SOLPS.

- Chapter 3 reviews the orbit loss theory and presents a method for the relatively fast determination of the static loss cone structure in an experimental diverted geometry while maintaining key sensitivities to the radial electric field. Computational levity allows for the eventual inclusion of the orbit loss model into existing fluid codes without hindering their computational advantage over kinetic simulations. This chapter deviates from what is typically seen in the literature by placing focus on the projections of the phase-space loss cone to various positions in configuration-space.

- Chapter 4 considers the effects of pitch angle scattering on ions following orbits within

the loss cone, determining the rates of scattering onto confined orbits. Methods for estimating the loss orbit periods are presented, and the rates of scattering out of the loss cone are compared to the loss orbit periods. The loss cone projections are demarcated about a qualitative change in the nature of the orbit loss, resulting in collisionless and collisional portions of the loss cone.

- Chapter 5 works toward a steady-state solution for the orbit loss, handling the collisionless and collisional portions of the loss cone separately. The pitch angle scattering into and out of the loss cone structure is self-consistently compared, finding estimates for the orbit loss current. The dependencies of the loss current on the ion temperature, electron density, ∇B drift direction, ion mass, and X-point position are explored and qualitatively compared to the behaviors of the empirically known L-H transition power threshold.

- Chapter 6 illustrates the implementation of the orbit loss model into the fluid transport code SOLPS. The edge radial electric field is discussed both before and after the inclusion of the orbit loss current. The plasma response to the orbit losses is further considered over scans in the input power and core density.

- Chapter 7 gathers the conclusions and highlights the next steps for future work.

Chapter 2

Theoretical background

The field of tokamak research applies the basic theory of plasma physics to the engineering challenges of designing and operating a reactor type device, becoming both academic and pragmatic in nature.[6] The techniques of basic plasma physics[8,51] are generally applicable to the interacting charged particles in a strong magnetic field, and the phenomena often share similarities to those found in the natural astrophysical plasmas. Unlike the study of basic plasma physics or astrophysical plasmas, engineering practicalities constrain the considered plasma boundary conditions and parameters,[52,53] narrowing the focus of the applied theory.

This chapter discusses the theoretical techniques used to understand, predict, and control the behaviors of plasmas confined by the magnetic field of a tokamak. Each of these methods are deep and have been studied in great detail for decades, and the following cursory presentation cannot do the field justice. The focus here is to highlight the motivating ideas for investigating the orbit loss and the necessary tools for its consideration. A major component of contemporary plasma physics research focuses on the evolution of small scale turbulent fluctuations. Throughout this work, the thermal orbit losses in the diverted field geometry are considered while allowing for Coulomb collisions both into and out of the loss orbits. The exact interaction between the loss mechanism and the turbulent flows is an open question that will motivate future investigations,[32,34,35,49,54,55] although there is evidence

that suggests that the turbulence can enhance the losses.[34,49,55]

2.1 Equilibrium: field structure and single particle orbits

The equilibrium magnetic field structure of the tokamak is determined by external coils and a toroidal plasma current driven by induction. Although the equilibrium field is often taken to be constant in time, the loop voltage maintained by the induced field implies an evolution of the equilibrium field structure, ocurring on the long resistive skin time,[74,75] and can thus be considered constant for faster time scale processes. Finer control of the field and thus the plasma shape is made possible by secondary external coils. The field structure is designed to confine the ions and electrons against their internal self pressure, playing the role of the gravitational force present in stellar fusion plasmas. Recalling the Lorentz force,

$$\boldsymbol{F} = Ze\left(\boldsymbol{E} + \boldsymbol{v} \times \boldsymbol{B}\right), \tag{2.1}$$

one can see that motions of charged particles in a paired null electric field and homogeneous magnetic field are circular about the lines of magnetic field and unabated in the direction parallel to the magnetic field. In other words, the motion is helical about the field lines. For the creation of a magnetically confined nuclear fusion device, the choice of a constant magnetic field proves problematic as the motion parallel to the magnetic field will eventually lead all particles to the boundary of any finite device.

A natural solution to this problem is to bend the magnetic field into itself, resulting in the famous 'donut' shape of the tokamak. The external field coils generate a toroidal magnetic field that the orbits gyrate around to lowest order. Recall the magnetic field of a toroid with

N windings carrying current I easily obtained from Ampere's law,

$$\boldsymbol{B} = \frac{\mu_0 N I}{2\pi R}\hat{\phi}, \tag{2.2}$$

where μ_0 is the well-known permeability of free space. A natural consequence of the toroidal shaping is observed: the magnetic field is stronger at smaller major radii, $B \sim R^{-1}$. The inhomogeneity of the magnetic field gives rise to the perpendicular, with respect to the magnetic field direction, drifts associated with single particle motions in nonuniform magnetic fields: the so-called ∇B and curvature drifts,

$$\boldsymbol{v}_{\nabla B} = \frac{m v_\perp^2}{2ZeB}\frac{\boldsymbol{B}\times\nabla B}{B^2}, \tag{2.3}$$

$$\boldsymbol{v}_C = \frac{m v_\parallel^2}{Ze}\frac{\boldsymbol{B}\times(\boldsymbol{b}\nabla)\boldsymbol{b}}{B^2}. \tag{2.4}$$

Here, m is the particle mass, $\boldsymbol{b}$ is the unit vector for the local magnetic field, and the parallel and perpendicular directions are taken with respect to $\boldsymbol{b}$. For the inhomogeneous toroidal field of a tokamak, the drifts described by Eqs. (2.3) and (2.4) are nearly vertically directed and oppositely signed for ions and electrons, leading to a charge separation and a vertical restoring electric field, leading to yet another drift motion, the $E \times B$ drift,

$$\boldsymbol{v}_{\boldsymbol{E}\times\boldsymbol{B}} = \frac{\boldsymbol{E}\times\boldsymbol{B}}{B^2}. \tag{2.5}$$

In the presence of a purely toroidal field, we again encounter the problem that all of the particles would eventually reach the edge of the device due to this drift.

There are two famous solutions to this problem, manifesting as two different nuclear fusion devices: the tokamak and the stellarator. The former makes use of a driven toroidal electric current, the primary generator of a poloidally directed magnetic field component. The induction solution forces the tokamak to only operate under pulsed scenarios, limited

by the ability to apply an increasing magnetic flux. The poloidal component complicates the orbital motions, closing a majority of the trajectories even in the presence of the drifts. Alternatively, the stellarator implements coils of increased complexity that automatically generate a twisting magnetic field structure, both necessarily breaking the axisymmetry while providing the desired confinement properties and avoiding disruption type events. As discussed in Chapter 1, the work of this thesis is focused on the magnetic field geometry found in a tokamak. Furthermore, the methods employed make use of the tokamak's approximate axisymmetry, distancing direct applicability to stellarators. Axisymmetry is not guaranteed for a tokamak but will be assumed throughout the work.

The magnetic field lines of a tokamak lie within an infinite series of nested toroidal surfaces called flux surfaces.[56] The surfaces can be labeled by counting either the toroidal or poloidal flux of the magnetic field incident on some surface. When considering orbit losses, it is natural to work with the poloidal flux,

$$\psi_{\text{pol}} = \iint_S \boldsymbol{B} \cdot d\boldsymbol{S}, \tag{2.6}$$

since it directly appears in the canonical toroidal momentum, a conserved quantity for collisionless orbits in an axisymmetric field geometry. Here, S is a plane extending from the magnetic axis to the defined flux surface. The concentric magnetic flux surfaces are often used as a radial coordinate since many plasma parameters are leading order constant over a flux surface.[6] For example, the density, temperatures (therefore pressure), and the electric potential, are approximately flux functions, making this a convenient choice. This is alluded to in the lowest order pressure balance for the plasma, the magnetohydrodynamic (MHD) force balance,

$$\boldsymbol{j} \times \boldsymbol{B} = \nabla p, \tag{2.7}$$

where the magnetic force balances the plasma pressure, implying that the pressure gradient

is perpendicular to the field's direction. The MHD force balance is considered the basic condition for equilibrium. Using properties of the poloidal flux, Eq. (2.7) can be transformed into the Grad-Shafranov equation,[56,57]

$$R^2\nabla\cdot\left(\frac{1}{R^2}\nabla\psi_{\rm pol}\right) = -I\frac{dI}{d\psi_{\rm pol}} - R^2\mu_0\frac{dp}{d\psi_{\rm pol}}, \tag{2.8}$$

where $I = RB_\phi$. Eq. (2.8) can be solved to find the equilibrium magnetic field geometry. An alternative label for the radial coordinate that is employed throughout the text is a dimensionless radial coordinate,

$$\rho_{\rm pol} = \sqrt{\frac{\psi_{\rm pol} - \psi_{\rm axis}}{\psi_{\rm sep} - \psi_{\rm axis}}}, \tag{2.9}$$

where $\psi_{\rm sep}$ and $\psi_{\rm axis}$ are the poloidal flux values measured respectively at the separatrix and the magnetic axis.

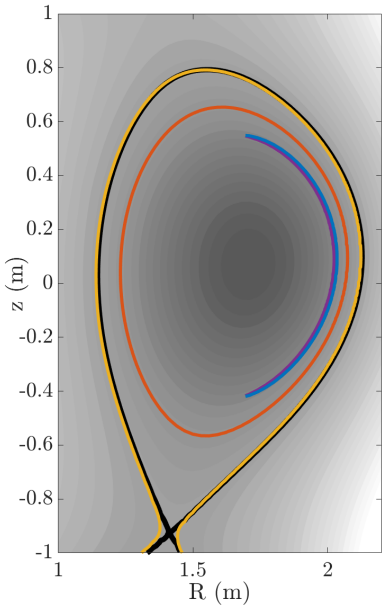

Figure 2.1: The equilibrium for ASDEX Upgrade discharge 31533 with three orbits overlayed: a trapped (banana) orbit in blue and purple, a passing orbit in orange, and a lost orbit in yellow. The separatrix is in black.

Figure 2.1 illustrates the equilibrium flux surfaces for ASDEX Upgrade shot 31533.

Two dimensional cross-sections of tokamaks are often appropriate, considering the ignorable toroidal coordinate with regard to the field structure. The shaded contours correspond to the nested surfaces of constant poloidal magnetic flux, with the thick black contour representing the boundary between the open and closed field line regions, the separatrix. The X-point found at the bottom of the closed field line region is a null point in the poloidal field and a saddle point in the poloidal flux. Recall the spatial inhomogeneity of the toroidal magnetic field: the left half of the plot is often referred to as the high field side (HFS) while the right half the low field side (LFS).

Also illustrated in Figure 2.1 are three sample orbital paths in the tokamak. Each orbit follows the helical combination of the toroidal and poloidal magnetic field components. Of the parallel motions, only the component about the poloidal field is apparent in the figure as the toroidal motions are lost in the projection. The second order drift motions are nearly entirely perceptible since they are perpendicular to the magnetic field vector, although the slow toroidal drift is similarly unseen. The orbit in blue and purple is trapped on the LFS of the plasma, experiencing magnetic mirror like bounce motions at positions of sufficiently great magnetic field. At each bounce location, the parallel velocity changes sign, signified by the different colors, and the leading order motion about the field line continues in the opposite direction. Such orbits are referred to as 'trapped', due to their behavior, or 'banana' orbits, due to their shape. In orange, the ion orbit has a sufficiently large parallel velocity that its magnitude is only reduced on the HFS of the tokamak and the orbit circulates around the device in a helical fashion. These orbits are called 'passing' or 'transit' orbits. The orbit in yellow starts within the separatrix at the LFS but is lost from the plasma near the X-point. It is this class of ion orbits that will be of interest throughout this work. Either a trapped or a passing orbit can be a lost orbit. Trapped orbits are able to be lost with lower energies, a direct result from their larger radial widths; however, trapped orbits can only be lost via the X-point if they are not too deeply trapped, if their bounce locations allow for interaction with the null point.

A description of a plasma is incomplete when only considering the motions of single particles. Plasmas are often defined by the collective behavior of the large number of charged particles with motions coupled by the electromagnetic fields. More comprehensive descriptions are required.

2.2 Kinetic and fluid modeling

Generically, the field of plasma physics involves the study of a large number of charged particles interacting with electromagnetic fields that are themselves sensitive to the motions of the charged particles. Winnowing the field down to the specifications of a tokamak sets a permissible range of magnetic field strengths and geometries and characteristics of the plasma, for example, the temperature and density. The focus shifts from purely understanding the plasma to also controlling it. Nonetheless, the same basic theory applies.

Consider the time development of a collection of charged particles that are justifiably conserved,[8]

$$\frac{dN_\alpha}{dt} = \frac{\partial N_\alpha}{\partial t} + \boldsymbol{v} \cdot \nabla N_\alpha + \frac{Ze}{m} (\boldsymbol{E} + \boldsymbol{v} \times \boldsymbol{B}) \cdot \nabla_{\boldsymbol{v}} N_\alpha = 0, \tag{2.10}$$

where $N_\alpha(\boldsymbol{x}, \boldsymbol{v}, t)$ specifies the location, $\boldsymbol{x}$, and velocity, $\boldsymbol{v}$, of a particle α at a given time t. The particles described by $N_\alpha(\boldsymbol{x}, \boldsymbol{v}, t)$ are appropriately coupled by the electric and magnetic fields via the Maxwell equations:

$$\nabla \cdot \boldsymbol{E} = \frac{1}{\epsilon_0} \sum_\alpha Z_\alpha e \int N_\alpha(\boldsymbol{x}, \boldsymbol{v}, t) d\boldsymbol{v}, \tag{2.11}$$

$$\nabla \cdot \boldsymbol{B} = 0, \tag{2.12}$$

$$\nabla \times \boldsymbol{E} = -\frac{\partial \boldsymbol{B}}{\partial t}, \tag{2.13}$$

$$\nabla \times \boldsymbol{B} = \mu_0 \sum_\alpha Z_\alpha e \int \boldsymbol{v} N_\alpha(\boldsymbol{x}, \boldsymbol{v}, t) d\boldsymbol{v} + \epsilon_0 \mu_0 \frac{\partial \boldsymbol{E}}{\partial t}. \tag{2.14}$$

Here, the charge densities and currents are supplied by the particles. The above description completely models the plasma up to including quantum mechanical or relativistic effects and is considered fully kinetic. The number of interacting particles within any system of interest is typically so great that anything beyond a statistical description is untenable. A reduction in the problem's complexity becomes necessary.

A statistical particle distribution function is introduced, a smooth six dimensional field spanning both physical- and velocity-space that describes the probability for a subset of the particles to exist in some physical location with some particular velocities,

$$f(\boldsymbol{x},\boldsymbol{v})d\boldsymbol{x}d\boldsymbol{v} = N \text{ in volume } d\boldsymbol{x}d\boldsymbol{v} \text{ centered about } \boldsymbol{x},\boldsymbol{v}. \tag{2.15}$$

Every particle must be described by some velocity, so integration over velocity-space returns the particle density,

$$n(\boldsymbol{x}) = \int f(\boldsymbol{x},\boldsymbol{v})d\boldsymbol{v}, \tag{2.16}$$

and each particle must have a position, so integration about both configuration- and velocity-space returns the total number of particles in the system,

$$N = \int n(\boldsymbol{x})d\boldsymbol{x} = \iint f(\boldsymbol{x},\boldsymbol{v})d\boldsymbol{x}d\boldsymbol{v}. \tag{2.17}$$

Such a statistical particle distribution function is naturally obtained by averaging Eq. (2.10) over the microstates that correspond to an equivalent macrostate,

$$\frac{\partial f_a}{\partial t} + \boldsymbol{v}\cdot\nabla f_a + \frac{Z_a e}{m}(\boldsymbol{E}+\boldsymbol{v}\times\boldsymbol{B})\cdot\nabla_{\boldsymbol{v}} f_a = C_a. \tag{2.18}$$

Note that the electromagnetic fields have also been averaged and represent the smooth macroscopic fields associated with the averaged plasma. The collision operator, the single

term on the right hand side of Eq. (2.18), is often complicated and contains all of the particle interactions that are lost by only considering the smooth macroscopic fields, the particle interactions within a Debye sphere. Recall from the introduction that the plasma does not tolerate charge separation on scales longer than the Debye length, Eq. (1.10), due to the natural shielding of positive charges by those negative and vice versa. In other words, on length scales longer than the Debye length, the plasma motions are described by the particle interactions with the large scale electromagnetic fields sustained by the collective plasma behavior or externally applied, and the interactions between individual particles are treated by the collision operator. In the above, the subscript 'a' signifies that the distribution function applies for only species 'a'; through this procedure, there is a distribution function for each species in the plasma. Eq (2.18) is the kinetic equation for a plasma species 'a', and solutions to and systematic reductions of this equation represent large fields of research.

Lower dimensionality models are often attractive for plasma analysis. A reduction in the description will always result in a loss of model fidelity, and one must be careful to ascertain what it is that is being lost. A common procedure is to take moments of the kinetic equation. Each moment is constructed by integrating the distribution function scaled by increasing integer powers of the velocity, starting from zero, over velocity-space. For example, the first three velocity-space moments can be taken as

$$n = \int f d\boldsymbol{v}, \tag{2.19}$$

$$\boldsymbol{\Gamma} = n\boldsymbol{V} = \int \boldsymbol{v} f d\boldsymbol{v}, \tag{2.20}$$

$$\boldsymbol{P} = m \int (\boldsymbol{v} - \boldsymbol{V})(\boldsymbol{v} - \boldsymbol{V}) f d\boldsymbol{v}. \tag{2.21}$$

Here $\boldsymbol{V}$ are the average fluid flows, $\boldsymbol{\Gamma}$ are the particle fluxes, and $\boldsymbol{P}$ is the pressure tensor. Note that the pressure tensor is often written as the sum of the scalar pressure, the diagonal

elements, and the viscous stress tensor,

$$\boldsymbol{P} = p\boldsymbol{\mathcal{I}} + \boldsymbol{\pi}. \tag{2.22}$$

Integrating Eq. (2.18) in the same way provides equations for each quantity, defining their evolution,

$$\frac{\partial n}{\partial t} + \nabla \cdot (n\boldsymbol{V}) = 0, \tag{2.23}$$

$$\frac{\partial}{\partial t}(mn\boldsymbol{V}) + \nabla \cdot (mn\boldsymbol{V}\boldsymbol{V}) = Zen(\boldsymbol{E} + \boldsymbol{V} \times \boldsymbol{B}) - \nabla p - \nabla \cdot \boldsymbol{\pi} + \boldsymbol{R}, \tag{2.24}$$

$$\frac{3}{2}\frac{\partial p}{\partial t} + \nabla \cdot (\frac{3}{2}p\boldsymbol{V} + \boldsymbol{q}) + p\nabla \cdot \boldsymbol{V} + \boldsymbol{\pi} : \nabla \boldsymbol{V} = Q. \tag{2.25}$$

Here, $\boldsymbol{R}$ is the force density given by the Coulomb collision operator, $\boldsymbol{q}$ is the heat flux, and Q is the heat exchange due to the Coulomb collisions. Such equations are referred to as fluid equations as opposed to those kinetic, because they model the macroscopic phenomena of a composite system of interacting elements and resemble the standard equations of fluid dynamics;[51] however, the fluids of plasma physics are coupled by the Maxwell equations. The advective term in Eq. (2.18), $\boldsymbol{v} \cdot \nabla f$, requires that the equation governing the n^{th} velocity-space moment depends on information concerning the next higher order moment.[58] The six dimensional kinetic problem is reduced to one in three dimensions described by an infinite number of coupled equations. To progress, an assumption is usually made concerning the relationship between two moments, an equation of state. The choice of such a closure relationship largely determines the modeling and must be carefully considered.

By construction, the fluid equations are insensitive to differences in the velocity-space distribution function that lead to the same macroscopic fluid moments. Consequently, fluid models are unable to resolve phenomena that result from such dynamics. When these effects are of interest but a fully kinetic description is too unwieldy, one can often used reduced descriptions that maintain non-trivial velocity-space coordinates.

The single particle motion of a charged particle in the presence of a magnetic field natu-

rally separates the cross field motions from those parallel. In the case of a large magnitude magnetic field, like the toroidal field of a tokamak, the gyroradius, the radius of orbit gyration, defines a small length scale, and the gyrofrequency, the rate of gyration, defines a fast time scale. When these scales are smaller than the turbulent plasma dynamics, drift kinetic theory[11] prescribes a method to average over the gyration, reducing the velocity-space dynamics to two dimensions, greatly reducing the computational cost compared to fully kinetic models. To date, the most successful reduced model which incorporates velocity-space sensitivities while remaining computationally feasible is the gyrokinetic model,[59–62] which allows for more significant variation in the electromagnetic fields across the gyrating orbit. Although significant, the reduction in computational expense achieved by the gyrokinetic model is dwarfed by the fluid models and their complete elimination of the velocity-space dimensions.

The work presented in this thesis involves the study of a kinetic phenomenon, the first orbit loss of ions inhabiting a region of phase-space, and its implementation within a fluid framework. There are several advantages to studying a kinetic effect in this way. The first and perhaps the most obvious is an issue of practicality, in that the fluid simulations are comparatively inexpensive. The second and perhaps more interesting advantage comes from the fact that the orbit loss is independently modeled and is not simply the consequence of a larger whole; it is possible to study various components of the model by artificially switching on and off various effects.

2.3 Equilibrium: force balance and the radial electric field

The characterization of the radial electric field, E_r, in the edge of a tokamak plasma appears necessary to fully diagnose the physics of the L-H transition and the associated sheared $E \times B$ flows thought responsible for the suppression of the edge turbulent transport.[21,46,63–68] Here,

the determination of the radial electric field within the plasma fluid theory framework is clarified by following two approaches: first a heuristic approach employed by Stroth *et al*[69] and then a more general two-fluid calculation similar to that of Callen *et al.*[75]

2.3.1 Heuristic approach

Consider a two-fluid description of a cylindrical plasma composed of electrons and singly charged ions and the friction exerted by the neutrals on each fluid in a direction perpendicular to the local magnetic field,

$$\boldsymbol{F}_{jn} = -n\nu_{jn}\boldsymbol{V}_{j\perp}. \tag{2.26}$$

F_{jn} is the associated force density, $\nu_{j,n}$ are the j-neutral collision frequencies, and $V_{j\perp}$ here are the flows perpendicular to the local magnetic field, with the subscript j serving as a species label.

To leading order, the fluid force balance, Eq. (2.24), reduces to

$$0 = nZ_j e\left(\boldsymbol{E} + \boldsymbol{V}_j \times \boldsymbol{B}\right) - \nabla p_j, \tag{2.27}$$

where the inertial, viscous, and frictional terms have been ordered out. Eq (2.27) shows that the leading order perpendicular velocity, $V_{j\perp}$, can be expressed by the diamagnetic and E×B drifts,

$$\begin{aligned} \boldsymbol{V}_{j\perp} &= \boldsymbol{V}_j^{\mathrm{dia}} + \boldsymbol{V}_j^{\mathrm{E\times B}} \\ &= -\frac{\nabla p_j \times \boldsymbol{B}}{Z_j e n B^2} - \frac{\boldsymbol{E}\times\boldsymbol{B}}{B^2}. \end{aligned} \tag{2.28}$$

If the pressure and electrostatic potential are assumed to be flux functions, then

$$V_{j\perp} = -\frac{p_j'}{Z_j e n B} - \frac{E_r}{B}. \tag{2.29}$$

Here, $p_j' = \frac{1}{h_y}\frac{\partial p_j}{\partial y}$, where y is the radial coordinate, see Section 2.3.2.1. The frictional force leads to a radial particle drift, described in the usual way,

$$V_{jy} = \frac{F_{j,n}}{Z_j e n B}. \tag{2.30}$$

To ensure ambipolarity, the ion and electron flows must be equal, and hence the frictional forces must sum to zero, providing an expression for the electric field that ensures ambipolarity,

$$\frac{E_r}{B} = -\frac{1 - \sqrt{\frac{m_e}{m_i}}\frac{p_e'}{p_i'}}{1 + \sqrt{\frac{m_e}{m_i}}}\frac{p_i'}{Z_i e n B} = \frac{1 - \sqrt{\frac{m_e}{m_i}}\frac{p_e'}{p_i'}}{1 + \sqrt{\frac{m_e}{m_i}}} V_i^{\mathrm{dia}}. \tag{2.31}$$

Here, the collision frequencies are assumed to differ only due to the particle mass differences, essentially an assumption that the ions and electrons are in thermal equilibrium.

The approach can be similarly extended for toroidal systems, including viscous damping effects of the form $F = -n\sqrt{m_j}\mu_j V_{jx}$ and eventually external forces, such as from neutral beam injectors. For brevity, the result is only quoted:[69]

$$\frac{E_r}{B} = \frac{\left(1 - \Delta_\mu \frac{p_e'}{p_i'}\right) V_i^{\mathrm{dia}} + (1 + \Delta_\mu)\epsilon q V_\parallel}{1 + \Delta_\mu} \pm \frac{|F_\perp^{\mathrm{NBI}}|}{n m_i^{1/2} \mu_i} \frac{1}{(1 + \Delta_\mu)\cos^2\alpha}. \tag{2.32}$$

Here, $\Delta_\mu = \sqrt{m_e/m_i}\mu_e/\mu_i$, where the μ_j are the poloidal viscosity coefficients, ϵ is the inverse aspect ratio, q is the safety factor, $V_\parallel$ is the flow parallel to the local magnetic field, $F_\perp^{\mathrm{NBI}}$ is the force density perpendicular to the local magnetic field imparted from the NBI, and α is the angle between the toroidal direction and the magnetic field.

It is worth noting that Eq. (2.32) can be further generalized to include other 'force'

terms that are associated with radial particle flows: ion orbit loss, the Stringer spin-up, or the Reynolds stress.[69] The inclusion of these additional terms does not alter the meaning of the leading order radial force balance; Eq. (2.32) and generalizations thereof are the leading order force balance with the additional ambipolarity considerations injected. The system is further specified by accounting for the various radial flows.

2.3.2 Fluid moment approach: Momentum balance

Here, a more general approach similar to that of Callen *et al*[75] is considered, beginning with the Boltzmann equation, including both sources and Coulomb collisions,

$$\frac{\partial f_j}{\partial t} + \boldsymbol{v} \cdot \nabla f_j + \boldsymbol{a} \cdot \nabla_{\boldsymbol{v}} f_j = C(f_j) + S(f_j). \tag{2.33}$$

The distribution function for each species is f_j, $C(f_j)$ is the Coulomb collision operator, and $S(f_j)$ are the kinetic source terms. Two species are assumed: the electrons and a singly charged ion species. Therefore, $n_e = n_i = n$, $Z_i = 1$, and $Z_e = -1$.

The first three velocity-space moments are taken, resulting in

$$\frac{\partial n}{\partial t} + \nabla \cdot (n\boldsymbol{V}_j) = S_{jn}, \tag{2.34}$$

$$\frac{\partial}{\partial t}(m_j n \boldsymbol{V}_j) + \nabla \cdot (m_j n \boldsymbol{V}_j \boldsymbol{V}_j) = Z_j e n(\boldsymbol{E} + \boldsymbol{V}_j \times \boldsymbol{B}) - \nabla p_j - \nabla \cdot \boldsymbol{\pi}_j + \boldsymbol{R}_j + \boldsymbol{S}_{jm}, \tag{2.35}$$

$$\frac{3}{2}\frac{\partial p_j}{\partial t} + \nabla \cdot (\frac{3}{2} p_j \boldsymbol{V}_j + \boldsymbol{q}_j) + p_j \nabla \cdot \boldsymbol{V}_j + \boldsymbol{\pi}_j : \nabla \boldsymbol{V}_j = Q_j + S_{jE}, \tag{2.36}$$

differing from Eqs. (2.23), (2.24), and (2.25) by the S_n, $\boldsymbol{S_m}$, and S_E, respectively the kinetic density, momentum, and energy sources.

2.3.2.1 Coordinate conventions

For the sake of consistent readability throughout this thesis, we introduce early the coordinate system conventions used in the B2.5 plasma solver component of SOLPS.[70,71]

The magnetic field is expressed by its equilibrium components,

$$\boldsymbol{B} = B_x \hat{\boldsymbol{x}} + B_z \hat{\boldsymbol{z}}, \tag{2.37}$$

where (x, y, z) are a curvilinear orthogonal coordinate system: x is the poloidal coordinate and varies along flux surfaces, y is the radial coordinate and varies perpendicular to flux surfaces, and z is the standard toroidal direction, often identified with ϕ. The x-coordinate is measured in the clock-wise direction when viewing the poloidal plane from above, the y-coordinate is positive when pointing radially outward, and the z-coordinate is directed out of the poloidal plane.

Being curvilinear, scale factors, elements of the metric tensor, are necessary to understand the transformational properties of the coordinate vectors,[72]

$$\boldsymbol{e}_i = h_{(i)} \hat{e}_{(i)} = g_{ij} \boldsymbol{e}^j, \tag{2.38}$$

with

$$h_{(i)} = \frac{1}{|\boldsymbol{e}^i|}, \tag{2.39}$$

and

$$g_{ij} = h_{(i)} h_{(j)} \delta_{ij}. \tag{2.40}$$

The final expression relies on the orthogonal nature of the coordinate system. The toroidal symmetry allows for the replacement of the toroidal scale factor by $h_z = 2\pi R$.

The B2.5 convention is to express components of vectors in terms of their projections on

the unit base vectors,[71] the $\hat{e}_i$,

$$A_{(i)} = \boldsymbol{A} \cdot \hat{e}_{(i)} = h_{(i)} A^i = \frac{1}{h_{(i)}} A_i. \tag{2.41}$$

For example, the components of the unit magnetic field vector would simply be written as

$$\begin{aligned} \hat{b} &= \frac{B_x}{B}\hat{x} + \frac{B_z}{B}\hat{z} \\ &= b_x \hat{x} + b_z \hat{z}. \end{aligned} \tag{2.42}$$

Note, we have dropped the parentheses in the subscripts. For the rest of the thesis, it will be understood that vector components are expressed in terms of their projections along the physical unit vectors as described above.

The electric field takes the form

$$\boldsymbol{E} = -\nabla\Phi + \boldsymbol{E}^A. \tag{2.43}$$

Here, Φ is the electric potential, and $\boldsymbol{E}^A$ is the inductive part of the electric field,

$$\boldsymbol{E}^A = -\frac{\partial \boldsymbol{A}}{\partial t}, \tag{2.44}$$

with $\boldsymbol{A}$ being the magnetic vector potential. The inductive electric field implies the evolution of the equilibrium magnetic field that maintains the constant loop voltage. The evolution of the equilibrium occurs on the long resistive skin time[74,75] and the field structure is often treated as fixed, as is the case in the SOLPS fluid transport code, and the following form is assumed beyond this chapter:

$$\boldsymbol{E} = -\nabla\Phi. \tag{2.45}$$

With the above in mind, it is fruitful to consider projections of a slightly modified mo-

mentum equation for ions,

$$m_i n \frac{\partial \boldsymbol{V}_i}{\partial t} = Z_i e n(\boldsymbol{E} + \boldsymbol{V}_i \times \boldsymbol{B}) - \nabla p_i - \nabla \cdot \boldsymbol{\pi}_i + \boldsymbol{R}_i + \boldsymbol{S}_{im} - m_i S_{in} \boldsymbol{V}_i \\ - m_i n \left(\boldsymbol{V}_i \cdot \nabla\right) \boldsymbol{V}_i, \tag{2.46}$$

along coordinate directions relevant to the magnetic field configuration.[73,75] Eq. (2.46) is obtained by expanding the inertial term and eliminating the time derivative in the density using the continuity equation.

2.3.2.2 Radial momentum balance

First consider the radial ($\boldsymbol{e}_y = h_y \hat{\boldsymbol{e}}_y$) projection of Eq. (2.46),

$$m_i h_y \frac{\partial (n V_{i,y})}{\partial t} = -Z_i e n \frac{\partial \Phi}{\partial y} - Z_i e n h_y V_{i,x} B_z + Z_i e n h_y V_{i,z} B_x - \frac{\partial p_i}{\partial y} - \boldsymbol{e}_y \cdot \nabla \cdot \boldsymbol{\pi}_i \\ + h_y R_{i,y} + h_y S^m_{i,y} - m_i h_y S^n_i V_{i,y} - m_i n \boldsymbol{e}_y \cdot \left(\left(\boldsymbol{V}_i \cdot \nabla\right) \boldsymbol{V}_i\right), \tag{2.47}$$

where the tensorial terms are left in their general form. The first four terms on the RHS describe the leading order balance between the perpendicular flows while the remaining terms are generally considered lower order in comparison,[75] resulting in

$$0 = -\frac{1}{h_y} \frac{\partial \Phi}{\partial y} - V_{i,x} B_z + V_{i,z} B_x - \frac{1}{Z_i e n} \frac{1}{h_y} \frac{\partial p_i}{\partial y}. \tag{2.48}$$

Equation (2.48) is applicable to any individual plasma species and is a powerful tool for experimentally measuring the radial electric field, as the rotations of impurity species are easier to measure than those of the main ions.[69,76]

Summing Eq. (2.48) with the similarly obtained electron equation provides the lowest order MHD force balance,

$$0 = \frac{1}{h_y} \frac{\partial P}{\partial y} + J_x B_z - J_z B_x. \tag{2.49}$$

Here, P is the combined electron and ion pressures, while $\boldsymbol{J} = nZ_i e\boldsymbol{V}_i - ne\boldsymbol{V}_e$ is the current density. The quantities found in Eq. (2.48) are not specified in this relationship, but the equality must hold true for the lowest order equilibration achieved on the fast MHD compressional Alfvén wave timescale.[75] Similarly, Eq. (2.49) stipulates that the total plasma pressure, current, and magnetic field evolve together over longer timescales.

2.3.2.3 Parallel momentum balance

Next the parallel, $\boldsymbol{B}$, projection of equation (2.46) is investigated,

$$m_i n B \frac{\partial V_{i,\parallel}}{\partial t} = Z_i e n \boldsymbol{B} \cdot \boldsymbol{E}_A - \frac{B_z}{h_x}\frac{\partial p_i}{\partial x} - \boldsymbol{B} \cdot \nabla \cdot \boldsymbol{\pi}_i + \boldsymbol{B} \cdot \boldsymbol{R}_i + \boldsymbol{B} \cdot \boldsymbol{S}_{im} - mS_n(\boldsymbol{B} \cdot \boldsymbol{V}_i) \\ -m_i n \boldsymbol{B}(\cdot(\boldsymbol{V}_i \cdot \nabla)\boldsymbol{V}_i). \tag{2.50}$$

The dominant terms found in the radial force balance are absent in the parallel balance, and it would no longer be prudent to order out the viscous forces. To continue, a closure scheme is typically chosen. Flux surface averaging the parallel momentum balance for the ions and summing the result with the similarly obtained electron equation under equilibrium conditions yields the plasma parallel force balance,

$$0 = -\langle \boldsymbol{B} \cdot \nabla \cdot \boldsymbol{\pi}_i \rangle + \langle \boldsymbol{B} \cdot \boldsymbol{S}_{im} \rangle + \langle \boldsymbol{B} \cdot \boldsymbol{S}_{em} \rangle - m_i \langle \boldsymbol{B} \cdot \boldsymbol{V}_i S_{in} \rangle - m_i \langle n \boldsymbol{B} \cdot \boldsymbol{V}_i \cdot \nabla \boldsymbol{V}_i \rangle. \tag{2.51}$$

The electron momentum terms typically are much smaller than the ion terms and were dropped from Eq. (2.51).

In the illustrative case that the sources and sinks for the parallel momentum and the equilibrium inertial terms are negligible, one recovers the neoclassical condition,

$$0 = \langle \boldsymbol{B} \cdot \nabla \cdot \boldsymbol{\pi}_i \rangle. \tag{2.52}$$

A general expression for Eq. (2.52) has been calculated in the neoclassical theory,[97]

$$\langle \boldsymbol{B} \cdot \nabla \cdot \boldsymbol{\pi}_i \rangle = -\nu_{\mathrm{mp}} n m_i \left(\frac{1}{h_y} \frac{B}{B_x} \left(\frac{\partial \Phi}{\partial y} + \frac{T_i}{Z_i e n} \frac{\partial n}{\partial y} + \frac{k}{Z_i e} \frac{\partial T_i}{\partial y} \right) - \langle B V_{\parallel} \rangle \right). \tag{2.53}$$

The prefactor k is the poloidal flow coefficient and is primarily dependent on the collisionality regime and ν_{mp} is the magnetic pumping frequency. Together, Eqs. (2.52) and (2.53) give the well-known expression for the neoclassical radial electric field,

$$E_r^{(\mathrm{NEO})} = \frac{T_i}{Z_i e} \left(\frac{1}{h_y} \frac{1}{n} \frac{\partial n}{\partial y} + k \frac{1}{h_y} \frac{1}{T_i} \frac{\partial T_i}{\partial y} \right) - \frac{B_x}{B} \langle B V_{\parallel} \rangle. \tag{2.54}$$

Again, Eq. (2.54) simply constitutes a necessary relationship between the elements of the radial force balance for the system to be in equilibrium when Eq. (2.52) holds true, but in any case, Eq. (2.48) still necessarily holds. The picture is completed by considering the radial particle fluxes; setting the flux surface average of the radial current due to non-ambipolar particle fluxes to zero determines the evolution of the toroidal flow, and thus of the radial electric field.

2.3.2.4 Toroidal ion momentum balance

Finally, consider the toroidal ($\boldsymbol{e}_z = h_z \hat{\boldsymbol{e}}_z = R \hat{\boldsymbol{e}}_z$) projection of Eq. (2.46),

$$\begin{aligned} m_i n R \frac{\partial V_{i,z}}{\partial t} = Z_i e n R E_{zA} - Z_i e n R B_x V_{i,y} - \boldsymbol{e}_z \cdot \nabla \cdot \boldsymbol{\pi}_i + R R_{iz} + R S_{iz}^m - m_i R V_{i,z} S_i^n \\ - m_i n (\boldsymbol{e}_z \cdot \boldsymbol{V}_i \cdot \nabla \boldsymbol{V}_i). \end{aligned} \tag{2.55}$$

Note that the second term on the RHS can be rewritten as

$$\begin{aligned} -Z_i e n R B_x V_{i,y} &= Z_i e n \boldsymbol{V}_i \cdot \nabla \psi_{\mathrm{pol}} \\ &= Z_i e \boldsymbol{\Gamma_i} \cdot \nabla \psi_{\mathrm{pol}}, \end{aligned} \tag{2.56}$$

the radial particle flux scaled by the ion charge.[73] The ambipolarity condition requires that there be no net radial charge flows. Summing Eq. (2.55) over the species and taking the flux surface average provides a relationship between the torque associated with the net radial particle flux and the toroidal projections of the remaining terms in the momentum balance. Setting that sum to zero provides a condition that determines the radial electric field necessary for quasineutrality,

$$\langle \boldsymbol{\Gamma_i} \cdot \nabla \psi_{\mathrm{pol}} \rangle - \langle \boldsymbol{\Gamma_e} \cdot \nabla \psi_{\mathrm{pol}} \rangle = 0, \tag{2.57}$$

thus allowing the determination of the toroidal rotation using the lower order force balances. Note that the inductive radial electric field does not enter the total toroidal force balance and does not play a direct role in determining the radial electric field.[77,78] The above is tantamount to enforcing the standard requirement for net ambipolar flows,

$$\nabla \cdot \boldsymbol{J} = 0. \tag{2.58}$$

The identification of the currents flowing in the plasma and the satisfaction of Eq. (2.58) determines the equilibrium radial electric field and toroidal rotation of the plasma.

The orbit loss model developed in this thesis considers the calculation of a single radial current in the plasma edge associated with the orbit lost ions. Implementation of the orbit loss current into the continuity equation necessitates the further consideration of the other relevant non-ambipolar transport processes in the plasma edge. The fluid transport code SOLPS is chosen to determine the background equilibrium plasma and the associated current balance. The response of the simulated plasma to the orbit loss current will be studied in Chapter 6. The SOLPS model solves a particular regime of equations, encapsulating the physics held within the first three fluid moment equations and the current continuity equation. The modeled equations are presented in the next section, with a focus on the terms most important for the inclusion of the orbit losses. See the Appendix for a short

discussion on the boundary conditions used in the simulations.

2.4 SOLPS (Scrape-Off Layer Plasma Simulation)

The SOLPS code package was born of the B2 multifluid code designed for modeling the transport of helium and impurities in the edge of a tokamak plasma.[79] In its present state, SOLPS comprises several distinct components, where the upgraded 2d multi-fluid plasma transport code, B2.5,[70] is of greatest relevance for this work. In 2005, the ITER organization merged several existing improvements to the SOLPS code, presenting a new code suite named SOLPS-ITER.[80] Release 3.0.6 of the SOLPS-ITER package[81] is used in this thesis and is coupled to an ion orbit loss subroutine developed as part of the work of this thesis.

B2.5 solves a modified set of the Braginkii equations, including the effects of drifts and fluid neutral particles. The 3D Monte Carlo neutral code EIRENE,[82] another component of the SOLPS package, allows for coupling with B2.5 to include the effects of kinetic neutrals, replacing the simpler fluid neutral model. Throughout this thesis, the fluid neutral model is used due to its lesser computational weight, a typical choice when investigating the leading order drift effects.[83] The neutral physics does not enter directly into the orbit loss calculations, only playing a more secondary role in the heat flux and ion-neutral friction current.

The DG and Carre codes,[71] also part of the SOLPS-ITER package, are used to respectively generate the tokamak geometry and computational grids used for the B2.5 and Eirene simulations, only each needing to be run once. Since the fluid neutral model is acceptable for the orbit loss studies, the orbit loss model is more specifically only coupled to the B2.5 plasma solver, only requiring standalone runs of B2.5. Below, we present the B2.5 equations with a focus on the terms most important for the orbit loss studies. The equations are not fundamentally reworked and the orbit losses are included as kinetic source terms. The leading order effects of the orbit loss are investigated. Existing extensions to the fluid equations

for a simpler orbit loss model should be explored to investigate the next order orbit loss effects of the presented model.[86–88]

2.4.1 B2.5 equations

The modification of the Braginskii equations solved in the B2.5 code are presented below for reference.[70,89] Refer to the SOLPS user manual[71] or the literature[70,84] for further information. The electron and ion energy equations are omitted from the discussion as they do not necessarily provide further context for the orbit loss studies and can be found in the literature.[70] Refer to Section 2.3.2.1 for the coordinate system conventions used in B2.5. Also, refer to Appendix A.3 to see the mapping of the computational cells to the real-space coordinates. SOLPS performs calculations on a two-dimensional grid, with indices labeling the radial and poloidal coordinates.

The average species velocity can be decomposed into components parallel and perpendicular to the local magnetic field,

$$\boldsymbol{V}_j = V_\parallel \boldsymbol{b} + \boldsymbol{V}_\perp, \tag{2.59}$$

where the perpendicular velocity is further decomposed into the y-direction, which is perpendicular to both the magnetic field and the flux surfaces, and the $\wedge$-direction, which is perpendicular to both the magnetic field and the y-axis,

$$\boldsymbol{V}_j = V_\parallel \boldsymbol{b} + \boldsymbol{V}_y + \boldsymbol{V}_\wedge, \tag{2.60}$$

such that

$$\hat{\wedge} = \frac{B_z}{B}\hat{x} - \frac{B_x}{B}\hat{z}. \tag{2.61}$$

The perpendicular velocity can be expressed as the sum of the drifts and the diffusive trans-

port velocities,[70,84]

$$\boldsymbol{V}_{\perp} = \boldsymbol{V}^{(E\times B)} + \boldsymbol{V}^{(in)} + \boldsymbol{V}^{(vis)} + \boldsymbol{V}^{(s)} + \boldsymbol{V}^{(\mathrm{dia})} + \boldsymbol{V}^{(D)} + \boldsymbol{V}^{(AN)}. \tag{2.62}$$

In order, the terms represent the $E \times B$ drift, the inertial drift, the viscosity drifts, the ion-neutral friction drift, the diamagnetic drift, the strictly ambipolar classical and thermodiffusive processes, and the anomalous transport.

We write down the standard projected forms of the $E \times B$ and diamagnetic velocities for the ions.

$$V_y^{(E\times B)} = \frac{b_z}{B}\frac{1}{h_x}\frac{\partial \Phi}{\partial x}, \qquad V_{\wedge}^{(E\times B)} = \frac{1}{B}\frac{1}{h_y}\frac{\partial \Phi}{\partial y}, \tag{2.63}$$

and

$$V_y^{(\mathrm{dia})} = \frac{b_z}{ZenB}\frac{1}{h_x}\frac{\partial nT_i}{\partial x}, \qquad V_{\wedge}^{(\mathrm{dia})} = -\frac{1}{ZenB}\frac{1}{h_y}\frac{\partial nT_i}{\partial y}. \tag{2.64}$$

The diffusive particle motions due to the neoclassical and anomalous particle transport take the following forms:

$$V_y^{(D)} = -\frac{D}{T_e + T_i}\frac{1}{h_y}\left(\frac{1}{n}\frac{\partial p}{\partial y} - \frac{3}{2}\frac{\partial T_e}{\partial y}\right), \quad V_{\wedge}^{(D)} = -\frac{D}{T_e + T_i}\frac{b_z}{h_x}\left(\frac{1}{n}\frac{\partial p}{\partial x} - \frac{3}{2}\frac{\partial T_e}{\partial x}\right), \tag{2.65}$$

and

$$V_y^{(AN)} = -D_{AN}^n \frac{1}{h_y n}\frac{\partial n}{\partial y} - D_{AN}^p \frac{1}{h_y n}\frac{\partial p_i}{\partial y}, \quad V_{\wedge}^{(AN)} = -D_{AN}^n \frac{b_z}{h_x n}\frac{\partial n}{\partial x} - D_{AN}^p \frac{b_z}{h_x n}\frac{\partial p_i}{\partial x}. \tag{2.66}$$

Here, D is the classical diffusion coefficient,

$$D = \frac{T_e + T_i}{eB}\frac{\nu_{ei}}{\omega_{ce}}. \tag{2.67}$$

In Eq. (2.67), ν_{ei} is the electron-ion collision frequency and ω_{ce} is the electron cyclotron frequency. The D_{AN} are the anomalous diffusion coefficients which approximate the unresolved turbulent transport; the classical diffusion can be neglected in favor of the more significant anomalous diffusion.[84] The remaining terms in Eq. (2.62) can be read off from the enumerated currents in Section 2.4.1.4 as $\boldsymbol{V}^{(j)} = \boldsymbol{j}^{(j)}/en$.

2.4.1.1 Ion continuity equation

Expanding Eq. (2.34) using Eq. (2.60) results in,

$$\frac{\partial n}{\partial t} + \frac{1}{\sqrt{g}}\frac{\partial}{\partial x}\left(\frac{\sqrt{g}}{h_x} n b_x V_{\parallel}\right) + \frac{1}{\sqrt{g}}\frac{\partial}{\partial x}\left(\frac{\sqrt{g}}{h_x} n b_z V_{\wedge}\right) + \frac{1}{\sqrt{g}}\frac{\partial}{\partial y}\left(\frac{\sqrt{g}}{h_y} n V_y\right) = S_n. \tag{2.68}$$

Numerical problems arise in calculations that rely on the small differences between large flows. To avoid this, when appropriate, the SOLPS derivation makes use of effective terms that provide the same result under the divergence operation.[70,84] The effective diamagnetic velocity is introduced,

$$\tilde{V}_{\wedge}^{(\mathrm{dia})} = \frac{T_i B_z}{Z e b_z}\frac{1}{h_y}\frac{\partial}{\partial y}\left(\frac{1}{B^2}\right), \tag{2.69}$$

$$\tilde{V}_{y}^{(\mathrm{dia})} = \frac{T_i B_z}{Z e}\frac{1}{h_x}\frac{\partial}{\partial x}\left(\frac{1}{B^2}\right). \tag{2.70}$$

These effective diamagnetic velocities represent the vertical guiding center drifts caused by the inhomogeneous magnetic field, and take on a form proportional to derivatives of the magnetic field, requiring accurate representation of the field geometry.[85] A comparison between the guiding center and fluid approximations indicates that the divergence of the diamagnetic flux is of the same order as the fluxes associated with the ∇B and curvature drifts.[89,90] The forms seen in Eqs. (2.69) and (2.70) have been quite successful for simulating L-mode plasmas, but need suitable replacement for the correct calculation of density profiles when modeling H-modes due to the interplay between the convective and diffusive terms in the numerics.[70] In the present version of the code, the 3.0.6 release, the effective diamagnetic

drifts are modeled by the following:

$$\tilde{V}_{\wedge}^{(\mathrm{dia})} = -\left(\frac{1}{B^2} - \frac{1}{\langle B^2 \rangle}\right) \frac{B_z}{Ze} \frac{1}{h_y} \frac{\partial (nT_i)}{\partial y}, \tag{2.71}$$

$$\tilde{V}_{y}^{(\mathrm{dia})} = \left(\frac{1}{B^2} - \frac{1}{\langle B^2 \rangle}\right) \frac{B_z}{Ze} \frac{1}{h_x} \frac{\partial (nT_i)}{\partial x}. \tag{2.72}$$

The bracketed terms correspond to the flux surface average in the usual way. Both sets of equations have the same divergence.[70]

Insertion of the effective drifts transforms Eq. (2.68) into

$$\frac{\partial n}{\partial t} + \frac{1}{\sqrt{g}} \frac{\partial}{\partial x} \left(\frac{\sqrt{g}}{h_x} n b_x V_{\parallel} \right) + \frac{1}{\sqrt{g}} \frac{\partial}{\partial x} \left(\frac{\sqrt{g}}{h_x} n b_z \tilde{V}_{\wedge} \right) + \frac{1}{\sqrt{g}} \frac{\partial}{\partial y} \left(\frac{\sqrt{g}}{h_y} n \tilde{V}_y \right) = S_n, \tag{2.73}$$

where the $\tilde{V}$ terms have the diamagnetic flows replaced with their respective effective counterparts. The orbit loss density source terms shown in Chapter 5 are implemented on the RHS of Eq. (2.73).

2.4.1.2 Parallel ion momentum equation

SOLPS solves the parallel ion momentum equation for the ions. As in the previous section, the parallel projection of Eq. (2.35) is taken,

$$m_i \left[\frac{\partial n V_{\parallel}}{\partial t} + \boldsymbol{b} \cdot \nabla \cdot (n \boldsymbol{V} \boldsymbol{V}) \right] = -\frac{Z e n b_x}{h_x} \frac{\partial \Phi}{\partial x} - \frac{b_x}{h_x} \frac{\partial p_i}{\partial x} - \boldsymbol{b} \cdot \nabla \cdot \boldsymbol{\pi_i} + \boldsymbol{R}_{i,\parallel} + \boldsymbol{S}^m_{i,\parallel}, \tag{2.74}$$

taking the following form in the code:

$$
\begin{aligned}
m_i \left[\frac{\partial n V_\parallel}{\partial t} + \frac{1}{h_z\sqrt{g}} \frac{\partial}{\partial x} \left(\frac{h_z\sqrt{g}}{h_x} n (b_z V_\wedge + b_x V_\parallel) V_\parallel \right) + \frac{1}{h_z\sqrt{g}} \frac{\partial}{\partial y} \left(\frac{h_z\sqrt{g}}{h_y} n V_y V_\parallel \right) \right] & \\
= -\frac{Zenb_x}{h_x} \frac{\partial \Phi}{\partial x} - \frac{b_x}{h_x} \frac{\partial p_i}{\partial x} + F_k & \\
+ \frac{4}{3} b_x B^{3/2} \frac{1}{h_x} \frac{\partial}{\partial x} \left[\frac{\eta_0 b_x}{B^2} \frac{1}{h_x} \frac{\partial}{\partial x} \left(\sqrt{B} (V_\parallel + b_x (V_\wedge^{(\mathrm{dia})} + V_\wedge^{(E)})) \right) \right] & \\
+ B^{3/2} b_x \frac{1}{h_x} \frac{\partial}{\partial x} \left(\alpha^{\mathrm{NEO}} \tau_{ii} \frac{b_x}{B^2} \frac{1}{h_x} \frac{\partial \left(\sqrt{B} q_i^{(0)} \right)}{\partial x} \right) + \frac{1}{h_z\sqrt{g}} \frac{\partial}{\partial y} \left(\frac{h_z\sqrt{g}}{h_y^2} \eta_2 \frac{\partial V_\parallel}{\partial y} \right) & \\
+ \frac{1}{h_z\sqrt{g}} \frac{\partial}{\partial x} \left(\frac{h_z\sqrt{g}}{h_x^2} \eta_2 \frac{\partial V_\parallel}{\partial x} \right) + S_{i\parallel}^m + R_{ie\parallel} + b_x n_a m_i V_{i\parallel}^2 \frac{1}{h_x h_z} \frac{\partial h_z}{\partial x}. &
\end{aligned}
\tag{2.75}
$$

In both Eqs. (2.74) and (2.75), the velocities correspond to the ion flows. There are several notable changes in from between Eqs. (2.74) and (2.75). The inertial and gyroviscous terms have been combined, completely canceling the divergence-free diamagnetic velocities.[70,84,91,92] Here, F_k is the Coriolis force associated with the diamagnetic drift velocity and the parallel rotation,[70,84]

$$
F_k = -m_i \left[\frac{1}{h_z\sqrt{g}} \frac{\partial}{\partial x} \left(\frac{h_z\sqrt{g}}{h_x} n b_z V_\parallel \tilde{V}_\wedge^{(\mathrm{dia})} \right) + \frac{1}{h_z\sqrt{g}} \frac{\partial}{\partial y} \left(\frac{h_z\sqrt{g}}{h_y} n V_\parallel \tilde{V}_y^{(\mathrm{dia})} \right) \right], \tag{2.76}
$$

η_0 is the Balescu parallel viscosity coefficient[93] which differs slightly from the Braginskii classical parallel viscosity coefficient,[89] $\eta_2 = n m_i D_{AN}^n$ is the perpendicular viscosity coefficient where the diffusion coefficient has been replaced by an anomalous value,[91,94] and $R_{ie\parallel}$ is the parallel component of the total Braginskii friction force,

$$
R_{ie\parallel} = -en \frac{j_\parallel}{\sigma_\parallel} + 0.71 b_x n \frac{1}{h_x} \frac{\partial T_e}{\partial x}. \tag{2.77}
$$

The fifth term on the RHS corresponds to the parallel viscosity driven by the parallel heat flux,

$$\begin{aligned} q_i^{(0)} &= q_{i\parallel}^{(0)} + q_{i\wedge}^{(\mathrm{dia})} \\ &= -\kappa_{i\parallel} b_x \frac{1}{h_x}\frac{\partial T_i}{\partial x} - \frac{5}{2}\frac{B_z B}{B_x \langle B^2 \rangle}\frac{n_a T_i}{e}\frac{1}{h_y}\frac{\partial T_i}{\partial y}, \end{aligned} \tag{2.78}$$

which is not included in the standard Braginskii equations and is on the same order as the parallel viscosity in a tokamak.[70,84] The $\alpha^{(\mathrm{NEO})}$ is related to the coefficient seen in Eq. (2.54) and roughly equals one in the collisional regime. Here, $\kappa_{i\parallel}$ is the classical ion thermal diffusivity and n_a specifies the ion density.

The source terms for the parallel ion orbit momentum loss discussed in Chapter 5 are implemented via the $S_{i\parallel}^m$ in Eq. (2.75).

2.4.1.3 Parallel electron momentum equation

The parallel electron momentum equation takes a much simpler form, the so-called parallel Ohm's law, as one is justified in omitting both the inertial and viscosity terms due to the small electron mass,

$$j_\parallel = \sigma_\parallel \left[\frac{b_x}{e}\frac{1}{h_x}\left(\frac{1}{n}\frac{\partial p_e}{\partial x} + 0.71\frac{\partial T_e}{\partial x} \right) - b_x \frac{1}{h_x}\frac{\partial \Phi}{\partial x} \right]. \tag{2.79}$$

It is well known that the physics of Eq. (2.79) largely determines the potential in the scrape off layer.[68,84]

2.4.1.4 Current continuity equation

The current continuity equation satisfies the quasineutrality condition,

$$\nabla \cdot \boldsymbol{j} = 0, \tag{2.80}$$

and when written in the SOLPS geometry, has the form

$$\frac{1}{\sqrt{g}}\frac{\partial}{\partial x}\left(\frac{\sqrt{g}}{h_x}\tilde{j}_x\right)+\frac{1}{\sqrt{g}}\frac{\partial}{\partial y}\left(\frac{\sqrt{g}}{h_y}\tilde{j}_y\right)=0, \tag{2.81}$$

where

$$\tilde{j}_x = b_x j_\parallel + b_z \tilde{j}_\wedge. \tag{2.82}$$

Again, tildes are used to represent the use of effective terms that are equivalent in divergence. The model does not explicitly involve a continuity equation for the electrons. Electron flows are implied via the coupled ion continuity and current continuity equations. Current flows without corresponding terms in the ion continuity equation are in effect movements of the electrons.

To be clear, throughout the text, discussions of current balance are always concerning the balance of the divergenceful currents, in other words, the balance of the depositions of charge. Insofar as current continuity is concerned, self-contained divergenceless current loops do not change the story. What is necessary is one or many divergenceless current loop(s) in the absence of sources. For any divergent plasma current, there must exist opposing currents to close the loop. The physics here is driven by the plasma quasineutrality and the ambipolar nature of equilibrium plasma flows.

The SOLPS literature shows that the toroidal rotation profile, and thus the radial electric field profile, very near the separatrix is increasingly governed by the anomalous transport, and the neoclassical assumption that $\langle \boldsymbol{B}\cdot\nabla\cdot\boldsymbol{\pi}_i\rangle = 0$ breaks down.[84,95] The parallel momentum and current balances predict a radially thin annulus, about 1–2 cm within the separatrix at the outer midplane, described as a 'viscous layer.'[95] Here, the effects of the parallel viscosity and the anomalous perpendicular viscosity tend to deepen the electric field well below the neoclassically predicted values. It will be shown that this annulus similarly describes the approximate domain of the thermal orbit losses leading up to the L-H transition, and the

interplay of the orbit loss and the viscous layer will be explored in Chapter 6.

2.4.2 The currents in the B2.5 model

The current continuity equation, the quasineutrality condition, is an essential balance between the flows of charged particles. The gridding of space into cells paints a clear picture: whatever flows in through the cell faces must be matched by an equal flow out, else, there would be an accumulation of charges. An implication, across the closed flux surfaces the radial current flows must sum to zero.

The B2.5 model accounts for several currents in the plasma: the diamagnetic current, the viscosity currents, the inertio-gyroviscous current, the ion-neutral friction current, the parallel current, etc. An anomalous electron current is also introduced into the system for numerical stability and should not contribute to any final solution.[84,96] One must ensure that the divergence of this current is subordinate to the other terms in Eq. (2.81). In the context of the orbit loss studies, the effective diamagnetic current and the perpendicular viscosity current are most important for the current balance in the edge, with the parallel and heat viscosity currents dominating the second order contributions. Expressions for the perpendicular currents are obtained by taking the cross product of the magnetic field with the sum of the ion and electron momentum equations,[84]

$$\boldsymbol{j}_\perp = \frac{\boldsymbol{B} \times m_i \frac{d(n\boldsymbol{V}_i)}{dt}}{B^2} + \frac{\boldsymbol{B} \times \nabla P}{B^2} + \frac{\boldsymbol{B} \times \nabla \cdot \boldsymbol{\pi}}{B^2} + \frac{\boldsymbol{B} \times \boldsymbol{R}_{iN}}{B^2} + \frac{\boldsymbol{B} \times \boldsymbol{S}_m}{B^2}. \tag{2.83}$$

The work of this thesis establishes the introduction of an additional current into the balance, the radially outward flow of orbit lost ions near the separatrix. The implemented forms of the currents in the SOLPS model are shown below for the relevant case of a single ion species.

2.4.2.1 The diamagnetic current

The diamagnetic current has the standard form

$$\boldsymbol{j}^{(\mathrm{dia})} = \frac{\boldsymbol{B} \times \nabla P}{B^2}, \tag{2.84}$$

where only the divergent part need enter into Eq. (2.81),[84,89,90,97]

$$\tilde{\boldsymbol{j}}^{(\mathrm{dia})} = P\left(\frac{\boldsymbol{B} \times \nabla B}{B^3} + \frac{\boldsymbol{B} \times (\boldsymbol{B}\nabla)\boldsymbol{b}}{B^3}\right), \tag{2.85}$$

which takes the following form in tokamak field geometry:[84,97]

$$\tilde{j}_x^{(\mathrm{dia})} = \frac{n(T_e + T_i)B_z}{h_y}\frac{\partial}{\partial y}\left(\frac{1}{B^2}\right), \tag{2.86}$$

$$\tilde{j}_y^{(\mathrm{dia})} = -\frac{n(T_e + T_i)B_z}{h_x}\frac{\partial}{\partial x}\left(\frac{1}{B^2}\right). \tag{2.87}$$

The effective diamagnetic current, Eq. (2.85), corresponds to the averaged single particle motions due to the spatial inhomogeneity of the magnetic field. The two terms can be respectively identified as the species-summed velocity-space averages of Eqs. (2.3) and (2.4) over assumed equilibrium Maxwellian distributions.

The divergence of this current, although comparatively small to the flow itself, is typically the largest in the SOLPS system, with the others typically acting to balance it.[84] The value of the net radial current through a flux surface due to the effective diamagnetic current is determined by quite subtle details in the pressure distribution along the flux surface. For this reason, the $E \times B$ flow can affect the magnitude of this net current flow by redistributing the pressure on closed flux surfaces.[84] Furthermore, the ion temperature is more free, in comparison to the electron temperature, to vary poloidally around a given flux surface. Consequently, rearrangements of the density about a flux surface disproportional affect the effective ion diamagnetic flows. It will be seen that the interplay between the orbit loss

current and the effective diamagnetic current is of principle importance in the plasma edge.

2.4.2.2 The viscosity currents

The viscosity current in Eq. (2.81) has the form

$$\boldsymbol{j}^{(\mathrm{vis})} = \frac{\boldsymbol{B} \times \nabla \cdot \boldsymbol{\pi}}{B^2}. \tag{2.88}$$

It is instructive to consider the classical viscosity tensor as the linear combination of tensors associated with distinct physical processes,

$$\begin{aligned} \pi_{\alpha\beta} &= -\eta_0 W_{0\alpha\beta} - \eta_1 W_{1\alpha\beta} - \eta_2 W_{2\alpha\beta} - \eta_3 W_{3\alpha\beta} - \eta_4 W_{4\alpha\beta} \\ &\approx -\eta_0 W_{0\alpha\beta} - \eta_1 \left(W_{1\alpha\beta} + 4W_{2\alpha\beta} \right) - \eta_3 \left(W_{3\alpha\beta} + 2W_{4\alpha\beta} \right), \end{aligned} \tag{2.89}$$

where

$$\eta_0 \sim n_i T_i \tau_i, \qquad \eta_1 \sim \frac{n_i T_i}{\Omega_i^2 \tau_i}, \qquad \eta_3 \sim \frac{n_i T_i}{\Omega_i}. \tag{2.90}$$

The viscosity coefficients in Eq. (2.90) respectively correspond to the parallel viscosity, perpendicular viscosity, and the gyroviscosity. The above and the tensor components, the $W_{i\alpha\beta}$, in Eq. (2.89) can be found in the seminal work of Braginskii.[89] The insensitivity of the gyroviscosity to the collisionality, τ_i^{-1}, allows for the combination of the inertial and gyroviscous terms as seen in Eq. (2.75). In a strongly magnetized plasma, the gyrofrequency sets one of the fastest timescales in the plasma, and

$$\Omega_i \tau_i \gg 1. \tag{2.91}$$

Consequently, $\eta_0 \gg \eta_1$.

The viscosity current in the SOLPS model is composed of three parts: the parallel vis-

cosity, the perpendicular viscosity, and the parallel heat viscosity,

$$\boldsymbol{j}^{(\mathrm{vis})} = \boldsymbol{j}^{(\mathrm{vis}\parallel)} + \boldsymbol{j}^{(\mathrm{vis}\perp)} + \boldsymbol{j}^{(\mathrm{visq})}. \tag{2.92}$$

The heat viscosity is an additional term not included in the standard Braginskii model.[84] The combined gyroviscous and inertia terms are represented in the current balance by the inertio-gyroviscous current, see Section 2.4.2.3. Similar to the diamagnetic current, the parallel and heat viscosity currents are conveniently replaced with expressions with equivalent divergences, thereby still satisfying the continuity equation.[70,84]

Parallel viscosity current

The parallel viscosity current is expressed as an effective current with the same divergence:

$$\tilde{j}_x^{(\mathrm{vis}\parallel)} = -b_z \frac{B_x \eta_0}{3\sqrt{B}} \frac{1}{h_x} \frac{\partial}{\partial x} \left(\sqrt{B} \left(V_\parallel + b_x \left(V_\wedge^{(\mathrm{dia})} + V_\wedge^{(\mathrm{E})} \right) \right) \right) \frac{1}{h_y} \frac{\partial}{\partial y} \left(\frac{1}{B^2} \right), \tag{2.93}$$

$$\tilde{j}_y^{(\mathrm{vis}\parallel)} = b_z \frac{B_x \eta_0}{3\sqrt{B}} \frac{1}{h_x} \frac{\partial}{\partial x} \left(\sqrt{B} \left(V_\parallel + b_x \left(V_\wedge^{(\mathrm{dia})} + V_\wedge^{(\mathrm{E})} \right) \right) \right) \frac{1}{h_x} \frac{\partial}{\partial x} \left(\frac{1}{B^2} \right). \tag{2.94}$$

In the model equations, only the dominant parallel velocity terms are maintained,

$$\tilde{j}_x^{(\mathrm{vis}\parallel)} \approx -b_z \frac{B_x \eta_0}{3\sqrt{B}} \frac{1}{h_x} \frac{\partial}{\partial x} \left(\sqrt{B} V_\parallel \right) \frac{1}{h_y} \frac{\partial}{\partial y} \left(\frac{1}{B^2} \right), \tag{2.95}$$

$$\tilde{j}_y^{(\mathrm{vis}\parallel)} \approx b_z \frac{B_x \eta_0}{3\sqrt{B}} \frac{1}{h_x} \frac{\partial}{\partial x} \left(\sqrt{B} V_\parallel \right) \frac{1}{h_x} \frac{\partial}{\partial x} \left(\frac{1}{B^2} \right). \tag{2.96}$$

The parallel viscosity current, along with the heat viscosity current, appears to play a significant role in balancing the effective diamagnetic current;[84] however, very near the separatrix, near the location of the E_r well, the perpendicular viscosity current plays a pivotal role.

Perpendicular viscosity current

The implemented form for the perpendicular viscosity current follows from the complete clas-

sical viscosity where only the largest term is maintained,[84] that involving radial derivatives of $V_\wedge$, the perpendicular flows within flux surfaces,

$$j_x^{(\mathrm{vis}\perp)} \approx 0, \tag{2.97}$$

$$j_y^{(\mathrm{vis}\perp)} \approx -\frac{1}{B}\frac{1}{\sqrt{g}}\frac{\partial}{\partial y}\left(\frac{\eta_{\mathrm{AN}}}{4}\frac{\sqrt{g}}{h_y^2}\frac{\partial V_\wedge}{\partial y}\right). \tag{2.98}$$

The classical perpendicular viscosity coefficient, η_2, has been replaced with an anomalous value, $\eta_{\mathrm{AN}} = nm_i D_{\mathrm{AN}}^n$. The enhanced perpendicular viscosity coefficient functions as a model for the anomalous transport, maintaining the structure of the classical equations[91] The fast parallel transport is sufficiently described by the classical physics and only the perpendicular coefficients are enhanced. The electric potential has been shown to be relatively insensitive to the magnitude of η_{AN}.[91,94]

Very near the separatrix in the SOLPS model, the perpendicular viscosity current is the dominant term that balances the effective diamagnetic current, primarily responsible for the compensating inward flow of cold ions from the SOL.[84] The dependence of this current on radial derivatives of the perpendicular flows within flux surfaces closely ties this current to the equilibrium E_r behavior. The eventual balance between the newly implemented ion orbit loss current, the effective diamagnetic current, and the perpendicular viscosity current will be explored in Chapter 6.

Heat viscosity current

The final viscosity current is associated with the heat fluxes,

$$\tilde{j}_x^{(\mathrm{visq})} = -b_z\alpha^{\mathrm{NEO}}\frac{0.24B_x}{\sqrt{B}\nu_{ii}}\frac{1}{h_x}\frac{\partial}{\partial x}\left(q_i^{(0)}\sqrt{B}\right)\frac{1}{h_y}\frac{\partial}{\partial y}\left(\frac{1}{B^2}\right), \tag{2.99}$$

$$\tilde{j}_y^{(\mathrm{visq})} = b_z\alpha^{\mathrm{NEO}}\frac{0.24B_x}{\sqrt{B}\nu_{ii}}\frac{1}{h_x}\frac{\partial}{\partial x}\left(q_i^{(0)}\sqrt{B}\right)\frac{1}{h_x}\frac{\partial}{\partial x}\left(\frac{1}{B^2}\right), \tag{2.100}$$

where

$$q_i^{(0)} = q_{i\|}^{(0)} + q_{i\wedge}^{(\mathrm{dia})}, \tag{2.101}$$

as defined by Eq. (2.78), considers the largest heat fluxes within the separatrix and is taken as zero beyond the LCFS.

The heat viscosity current often plays a role similar to the parallel viscosity current, as can been seen by the similar forms of Eqs. (2.95) and (2.96) and Eqs. (2.99) and (2.100). The currents often act in concert due to the similar nature of the parallel velocity and heat flux.

2.4.2.3 The inertio-gyroviscous current

The inertio-gyroviscous current, simply referred to as the inertial current in the SOLPS literature, combines the inertial and gyroviscous terms:

$$\begin{aligned} j_x^{(\mathrm{in})} = -m_i \frac{b_z}{B}\Bigg[\frac{\partial(nV_y)}{\partial t} + \frac{1}{h_z\sqrt{g}}\frac{\partial}{\partial x}\left(\frac{h_z\sqrt{g}}{h_x} n(b_z V_\perp^{(0)} + b_x V_\|)V_y\right) \\ + \frac{1}{h_z\sqrt{g}}\frac{\partial}{\partial y}\left(\frac{h_z\sqrt{g}}{h_y} n V_y^{(0)} V_y\right)\Bigg] - 2\frac{b_x b_z}{B}\frac{1}{h_x}\frac{\partial}{\partial x}\left(\eta_3 \frac{1}{h_x}\frac{\partial V_\|}{\partial x}\right) + m_i \frac{b_z}{B} n V_\|^2 \frac{1}{h_y h_z}\frac{\partial h_z}{\partial y}, \end{aligned} \tag{2.102}$$

$$\begin{aligned} j_y^{(\mathrm{in})} = m_i \frac{1}{B}\Bigg[\frac{\partial(nV_\wedge)}{\partial t} + \frac{1}{h_z\sqrt{g}}\frac{\partial}{\partial x}\left(\frac{h_z\sqrt{g}}{h_x} n(b_z V_\perp^{(0)} + b_x V_\|)V_\wedge\right) \\ + \frac{1}{h_z\sqrt{g}}\frac{\partial}{\partial y}\left(\frac{h_z\sqrt{g}}{h_y} n V_y^{(0)} V_\wedge\right)\Bigg] - 2\frac{b_x}{B}\frac{1}{h_x}\frac{\partial}{\partial x}\left(\eta_3 \frac{1}{h_x}\frac{\partial V_\|}{\partial x}\right) - m_i \frac{1}{B} n V_\|^2 \frac{1}{h_x h_z}\frac{\partial h_z}{\partial x}. \end{aligned} \tag{2.103}$$

The final terms are deemed to be the most significant and the others are ordered out.[84] Thus, the inertio-gyroviscous current is approximated by the following:

$$j_x^{(\mathrm{in})} = \frac{m_i}{B} n V_\|^2 \frac{1}{h_y h_z}\frac{\partial h_z}{\partial y}, \tag{2.104}$$

$$j_y^{(\mathrm{in})} = -\frac{m_i}{B} n V_\|^2 \frac{1}{h_x h_z}\frac{\partial h_z}{\partial x}. \tag{2.105}$$

Derivatives of the scale factor h_z are proportional to those of the magnetic field, and the inertial currents are implemented by the following:

$$j_x^{(\mathrm{in})} = \frac{B_z}{2} m_i n V_\parallel^2 \frac{1}{h_y} \frac{\partial}{\partial y} \left(\frac{1}{B^2} \right), \tag{2.106}$$

$$j_y^{(\mathrm{in})} = -\frac{B_z}{2} m_i n V_\parallel^2 \frac{1}{h_x} \frac{\partial}{\partial x} \left(\frac{1}{B^2} \right). \tag{2.107}$$

Physically, these currents represent the vertical drifts associated with centrifugal forces.[70,84]

2.4.2.4 The ion neutral friction current

The ion neutral friction current is treated by accounting for the associated momentum sinks,

$$j_x^{(\mathrm{s})} = b_z \frac{S_{iy}^m}{B} = -b_z \frac{n \mu_{iN} \nu_{iN} (V_\wedge - V_{\wedge N})}{B}, \tag{2.108}$$

$$j_y^{(\mathrm{s})} = -\frac{S_{i\wedge}^m}{B} = \frac{n \mu_{iN} \nu_{iN} (V_y - V_{yN})}{B}. \tag{2.109}$$

where μ_{iN} is the effective mass, ν_{iN} is the ion-neutral collision frequency, n_N is the neutral density, and the V_N terms are the neutral particle mean velocities. Combining Eq. (2.108) and (2.109) with the forms given by Eqs. (2.63)–(2.66) results in the following forms for the ion neutral friction current,

$$\tilde{j}_x^{(\mathrm{s})} = -\sigma_{iN} b_z^2 \frac{1}{h_x} \frac{\partial \Phi}{\partial x} - \sigma_{iN} b_z^2 \frac{1}{Zen} \frac{1}{h_x} \frac{\partial (nT_i)}{\partial x} + \sigma_{iN} B_z V_{yN}, \tag{2.110}$$

$$\tilde{j}_y^{(\mathrm{s})} = -\sigma_{iN} \frac{1}{h_y} \frac{\partial \Phi}{\partial y} - \sigma_{iN} \frac{1}{Zen} \frac{1}{h_y} \frac{\partial (nT_i)}{\partial y} - \sigma_{iN} B V_{\wedge N}, \tag{2.111}$$

where the ion-neutral collision frequency has been replaced by the ion-neutral perpendicular conductivity,

$$\sigma_{IN} = \frac{n m_i \nu_{iN}}{2B^2}. \tag{2.112}$$

The ion-neutral collision frequency is taken to be[84]

$$\nu_{iN} = n_N(3.2 \cdot 10^{-15}\ \mathrm{m}^3/\mathrm{s})\sqrt{\frac{T_i}{0.026\ \mathrm{eV}}}. \tag{2.113}$$

2.4.2.5 The anomalous current

An anomalous current carried by the electrons is included in the code to provide convergence of the numerical scheme, replacing the polarization current in the evolution of the electrostatic potential,[96]

$$j_x^{(\mathrm{AN})} = -\frac{1}{h_x}\sigma^{(\mathrm{AN})}\frac{\partial\Phi}{\partial x}, \tag{2.114}$$

$$j_y^{(\mathrm{AN})} = -\frac{1}{h_y}\sigma^{(\mathrm{AN})}\frac{\partial\Phi}{\partial y}, \tag{2.115}$$

with Eq. (2.115) contributing more greatly to the current balance due to the smaller radial length scale. It is possible that such a current exists within the edge region;[84,98] however, within the SOLPS model the term is artificial. For sufficiently small values of the anomalous conductivity, $\sigma^{(\mathrm{AN})}$, it has been shown that this anomalous current does not affect the steady-state solution while providing the necessary stability to the regime.[84,96] It is suggested that for AUG,

$$\sigma^{(\mathrm{AN})} = \tilde{\sigma}^{(\mathrm{AN})} e n_e \leq (1\text{–}5) \cdot 10^{-5}\,\mathrm{Sm}^2/\mathrm{C} \cdot e n_e, \tag{2.116}$$

is necessary for physically meaningful solutions to the potential equation.[96] We find that the potential retains a perceptible sensitivity to $\sigma^{(\mathrm{AN})}$ for the values prescribed by Eq. (2.116). Since the work of this thesis explicitly concerns the solution to the current continuity equation, $\tilde{\sigma}^{(\mathrm{AN})}$ is chosen to be $10^{-6}\ \mathrm{Sm}^2/\mathrm{C}$ across the parameter space, ensuring that the anomalous current does not alter the solution.

The reported value for $\sigma^{(\mathrm{AN})}$ such that the anomalous current does not influence the equilibrium solution is linear in the electron density, requiring lesser anomalous conductivities for lower density plasmas. The SOLPS model exhibits a numerical instability[96] that requires

timesteps proportional to $\sigma^{(\mathrm{AN})}$ and inversely proportional to the plasma pressure,

$$\delta t_{\max} \approx \frac{\sigma^{(\mathrm{AN})} B^2 R^2}{n(T_e + T_i)}. \tag{2.117}$$

Over a constant input power and thermal diffusivity, one expects the plasma temperature to be inversely proportional to the electron density to ensure energy conservation via the radial heat flux. Assuming that there is a linear increase in the plasma temperatures with heating power, and one sees that

$$\delta t_{\max} \sim \frac{n}{P}, \tag{2.118}$$

where the recommended $\sigma^{(\mathrm{AN})}$ was inserted into Eq. (2.117) and P, here, refers to the input heating power.

We find with the desirably small $\sigma^{(\mathrm{AN})}$, for a given input power there is some lower density threshold where the numerical instability prevents convergence in realistic times. Comparisons over increasing input power are therefore restricted by the density threshold at the maximum input power of interest. For the work in this thesis, the SOLPS runs are typically along the high density branch of the L-H transition power threshold.

The speed up scheme '*Method of partial flux surface averaging*', discussed in the work of Kaveeva *et al*,[96] designed specifically for the SOLPS code package has been implemented into the runs with results presented in Chapter 6, widening the explorable region of parameter space; however, the severity of the numerical instability seems somewhat greater than stated in the literature,[96] so it is likely that it is being exacerbated for the low density plasmas for some other unknown reason. The residuals associated with the neutral particle continuity and momentum equations are typically the highest, trailed by the potential equation, perhaps indicating an issue with the fluid neutral model. Future work will be done to allow for investigations of the orbit loss current's interactions with the low density plasmas within the SOLPS framework.

2.4.2.6 The ion orbit loss current

The main goal of this thesis is to develop a new method for estimating the local steady-state thermal ion orbit loss current in the edge of a diverted tokamak plasma valid for the collisional L-mode plasmas nearing the L-H transition and to present an analysis of its primary role in establishing the radial electric field. We study the impact of adding a new term, $j_y^{(\mathrm{iol})}$, to the radial current balance, such that

$$\frac{1}{\sqrt{g}}\frac{\partial}{\partial y}\left(\frac{\sqrt{g}}{h_y}(\tilde{j}_y^{(\mathrm{dia})}+\tilde{j}_y^{(\mathrm{vis})}+j_y^{(\mathrm{in})}+\tilde{j}_y^{(\mathrm{s})}+j_y^{(\mathrm{iol})}+j_y^{(\mathrm{AN})})\right)=0. \tag{2.119}$$

The term is included by way of kinetic source terms, corresponding to the divergence of the orbit loss current. Secondary orbit loss source terms associated with the particle, momentum, and energy loss will also be included in the continuity, ion parallel momentum, ion energy equations, although they have a comparatively muted effect.

2.4.3 Some notes on the use of SOLPS in this work

The orbit loss model detailed in Chapters 3–5 has been implemented into the SOLPS code suite, creating a back and forth between the source terms determined by the orbit loss model and updated plasma profiles determined by the transport equations of SOLPS. The entire SOLPS model has not been reworked to account for the obit loss on a first principles basis, and such an effort is probably best handled by kinetic models. The first order effects of the orbit loss current and other source terms are investigated though the coupling.

The geometry of ASDEX Upgrade discharge 16151, a test case available to SOLPS users, is used as the backdrop for all the presented plasma simulations. The simulations are modified forms of this baseline case achieved through manipulation of the core boundary conditions. The simulations treat a single ion species, deuterium, the electrons, and fluid neutral particles. Refer to Appendix A for further details concerning the field geometry, plasma profiles, and the boundary conditions.

As discussed in Section 2.4.2.5, simulation convergence is often in direct relation to the value of $\sigma^{(\mathrm{AN})}$, a parameter governing the fictitious radial anomalous current that provides numerical stability. Since the content of this thesis is directed interested in the radial current balance and equilibrium E_r, $\tilde{\sigma}^{(\mathrm{AN})} = 10^{-6}$ Sm^2/C was chosen to ensure physically meaningful solutions to the current continuity equation. Simulations of denser plasmas converge more quickly than less dense counterparts for such small anomalous conductivities, with there being some minimum threshold density that converges with a reasonable timestep or even converges at all. The simulations in this thesis are generally restricted to the high density branch of the L-H transition power threshold for this reason. For the orbit loss studies, convergence is determined when the parameters determining the orbit loss are no longer meaningfully changing over periods of time longer than the dynamics of the problem. For the lowest density simulations, especially at the higher levels of input power, the convergence is more tenuous, with some seemingly persistent dynamics that do not meaningfully alter the solution both with and without the additional orbit loss terms. Here, convergence can be easily achieved by increasing the anomalous conductivity, resulting in similar equilibrium solutions. The leading order difference is that the E_r well is generally shallower with a larger $\sigma^{(\mathrm{AN})}$,[84] since a non-negligible anomalous current softens the imbalance between the in- and out-flowing ions in the viscous layer. The orbit loss is sensitive to the electric field strength, and a self-consistent E_r response to the orbit losses demands that the anomalous current be driven down. Thus, the quasi-steady-state solutions are preferred for the orbit loss study to necessarily more stable simulations with non-negligible $j^{(\mathrm{AN})}$.

Chapter 3

Ion orbit loss cone characterization

Following the discovery of the high confinement regime, the H-mode, on the ASDEX tokamak, there have been many attempts to theoretically describe the L-H transition. To date, there is no first principles theoretical model which explains the seemingly spontaneous transition to a regime of suppressed turbulence and improved confinement. Prevailing consensus is that the some physics drives an increase in the edge rotational shear tied to the larger magnitude radial electric fields present in the H-mode edge. The current body of evidence suggests that some combination of turbulent effects and the neoclassical loss of thermal ions is responsible for driving the increased shear.[32]

Ion orbit loss has long been considered a potential catalyzing factor for the L-H transition. In 1989, Shaing and Crume presented a model for the transition which considered the poloidal rotation driven by ion orbit losses in the edge,[64,99] showing a possible bifurcation in the poloidal rotation at low

$$\nu_{*i} = \frac{\nu_{ii,T}\bar{R}q}{v_T\epsilon^{3/2}}. \tag{3.1}$$

Here, $\nu_{ii,T}$ is the ion-ion collisionality evaluated at the thermal velocity, v_T, $\bar{R}$ is the major radius, q is the safety factor, and ϵ is the inverse aspect ratio. Eq. (3.1) can be thought of as the product of the collisionality and a typical orbit period for a thermal ion, suggesting that an increase in low collisionality ions could trigger the transition. Improved upon by Shaing

in 1992, the model is perhaps the most complete analytic approximation for the collisionally driven steady-state orbit loss.[100] The model relies on several assumptions and simplifications, focusing on the gross scaling and the order of magnitude of the losses. Some examples include the use of a simple loss cone boundary, the use of a cylindrical field geometry,[101] simplifying the collisionless condition, omitting some important effects of the electric potential, not radially[102] or poloidally resolving the orbit loss, and averaging some important energetic scalings. At any rate, the model includes some features that appear lacking from more recent works in the literature, namely the importance of the ion-ion collisionality in terms of both loss cone repopulation and depopulation.

Contemporary studies often focus on studying the static structure of the loss cone both numerically[33,34,45,47] and analytically.[41–44,104] The loss cone is well understood for both analytic and experimental geometries, under the influence of a radial electric field, and under different plasma shaping conditions, where it is seen that an accurate representation of each is necessary to ascertain the loss trajectories. The static problem in relation to the ion-ion collisionality has not been sufficiently studied, a gap in the literature rectified within this thesis. Furthermore, insufficient progress has been made to model a steady-state description of the orbit loss beyond the Shaing model. Development of a comprehensive steady-state orbit loss model is necessary to investigate the interaction between the losses and the confined plasma.

Steady-state solutions are determined by the processes responsible for resupplying the loss cone, driving the orbit losses. Some recent steady-state solutions do not consider the scattering of ions on loss orbits into those confined, lacking a fundamental feature of the problem. Additionally, these solutions also employ some set of understandable but far reaching assumptions similar to the Shaing model, including the use of a liberal definition of loss, the under-resolution of the problem, and the averaging out of some important energy dependencies, leaving further room for improvement. Chapters 3–5 of this thesis develop a loss cone model that seeks to improve upon those existing, presenting a steady-state orbit loss

model that accounts for experimental tokamak geometry, effects of the radial electric field, and pitch angle scattering both into and out of the loss cone, while retaining sensitivity to the energetics of individually lost ions with regard to their pitch angle scattering and loss orbit period.

It is noted that kinetic models of tokamak plasmas are also able to resolve ion orbit losses depending on their set of assumptions. The first-principles-based electrostatic gyrokinetic simulations of the XGC1 code are reported to both include and be highly sensitive to the orbit losses in the plasma edge, indicating a coupled role of the losses and turbulent effects in the generation of the edge $E \times B$ shear.[32] The fully kinetic Monte Carlo orbit following simulations of the ASCOT code have also been used to calculate the orbit loss current and have found that it contributes to the $E \times B$ shear.[101,103] The expense of kinetic simulations provokes the study of the orbit losses in a reduced computationally light setting, like that of a fluid code. The assumptions made in the presented orbit loss model are typically made to ensure the levity of simulations when coupled to a fluid model. The final Chapter of this thesis presents the leading order effects of the steady-state collisionally driven orbit loss current coupled to the SOLPS transport code.

3.1 Ion orbit loss basics

The content of this chapter serves to develop an understanding of the phase-space loss cone that envelops all ions instantaneously on loss orbits with trajectories that intersect either the wall or the divertor, largely following the work of Brzozowski *et al.*[44] The guiding center orbits of particles in a toroidally symmetric field geometry are trivially known, being determined by their constants of motion. Therefore, the phase-space loss cone is immediately known for a given field geometry. It is often useful to project the phase-space loss cone to some observation point in configuration-space, resulting in a velocity-space loss cone. In the text, the velocity-space loss cones are also referred to as local loss cones, projected loss

cones, or even just as loss cones. A given velocity-space loss cone accurately describes orbits local to the given observation point, with these trajectories connecting disparate points in configuration space. For any given observation point the distribution of ions about the cone in velocity-space must be locally determined. The phase-space loss-cone is understood in the following by studying the projected velocity-space loss cones as a function of their projected location, in terms of its local energy and pitch angle dependencies and in response to the radial electric field.

Aside from edifying the basic physics of the orbit loss, the novel takeaways from this chapter include the focus on the study of the projected loss cones over the poloidal plane and the method used to determine the energy-dependent trapped-passing boundary in the presence of a non-trivial radial electric field. The former becomes important in treating the steady-state problem, where ions are fed into the loss cone upstream at arbitrary location. The timescale of the loss orbit is sensitive to this initial position, as is the structure of the local loss cone of which ions on lost orbits can diffuse out. The simplification in determining the trapped-passing boundary maintains computational levity while retaining the most important features of the radial electric field. An assumption made in Section 3.4 concerning the particle trajectories under an E_r further simplifies the collisionality considerations in the following chapter.

3.1.1 Guiding center constants of motion

Collisionless orbits in the axisymmetric toroidal tokamak geometry are classified using the familiar guiding center constants of motion:[41–43,45,104–106]

$$E = \frac{1}{2}mv^2 + Ze\Phi = \frac{1}{2}mv_0^2 + Ze\Phi_0, \tag{3.2}$$

$$\mu = \frac{mv_\perp^2}{2B} = \frac{mv_{\perp 0}^2}{2B_0} \\ = \frac{mv^2}{2B}(1-\zeta^2) = \frac{mv_0^2}{2B_0}(1-\zeta_0^2), \tag{3.3}$$

$$p_\phi = mRv_\parallel f_\phi + Ze\psi = mR_0 v_{\parallel 0} f_{\phi 0} + Ze\psi_0 \\ = mR\zeta v f_\phi + Ze\psi = mR_0\zeta_0 v_0 f_{\phi 0} + Ze\psi_0. \tag{3.4}$$

Here, m and Ze are an ion's mass and charge, R is the coordinate major radius, B is the magnitude of the magnetic field, Φ is the electric potential, ψ is the poloidal flux in (Wb/2π), v is an ion's velocity with components $v_\parallel = \boldsymbol{v}\cdot\boldsymbol{B}/B$ and $v_\perp$ representing parallel and perpendicular directions with respect to the local magnetic field vector, $\zeta = v_\parallel/v$ is the cosine of the pitch angle, and $f_\phi = B_\phi/B$. All quantities are in SI units unless otherwise noted. Spatial quantities are evaluated at the guiding center location, introducing possible errors first order in the gyroradius.[107,108] As discussed in Section 3.2, ions are considered lost when entering the divertor region after crossing the X-point plane typically in the vicinity of the X-point. In this region, the flux expansion mitigates the impact of the finite Larmor radius effects on the orbit loss. The subscript '0' represents the arbitrary initial conditions for the orbit under consideration. Note that the second line in Eq. (3.4) enforces that v is a positive quantity. It is noted that the conservation properties of each guiding center constant of motion are not equivalent.

The energy, E, shown in Eq. (3.2) is a perfectly conserved quantity, as for any other isolated system. An ion's total energy is conserved throughout a collisionless orbit and is allowed to exchange between the particle velocities and the electrostatic potential. The form of Eq. (3.2) suggests that the electrostatic potential can act as a barrier, trapping particles within a potential well, as is typically the case for the ions in the tokamak edge. Although particle collisions allow for the energy exchange between particles, the dominant collisional process for thermal ions only deflects the trajectories by some small angle, typically

conserving the energy.[109]

The magnetic moment, μ, of Eq. (3.3) is the well known first adiabatic invariant associated with the fast gyromotion about magnetic field lines. Its invariance relates to the 'slowness' of changes experienced by a gyrating orbit in an inhomogenous field structure. The magnetic moment is approximately conserved in the fields typical of a tokamak,[107,108,110] and it is common to treat μ as a true invariant in the tokamak environment. The ion velocity components are closely linked to the tokamak field structure by the conservation of the magnetic moment. In a larger magnitude magnetic field, a larger component of the ion velocity must be directed orthogonal to the magnetic field, reducing the component along the field line. The magnetic moment sets some threshold magnetic field magnitude that would require a perpendicular velocity greater than the ion's energy allows. Orbiting charged particles are prevented from entering into regions with such strong magnetic fields, and the particles bounce at this barrier, reversing their parallel velocities. The near vertical symmetry of the tokamak's magnetic field results in two vertically opposed bounce locations occurring at nearly the same major radii, largely determined by an ion's pitch. Such particle orbits pass through the outer midplane on the LFS moving between the bounce locations, being commonly referred to as 'trapped' or 'banana' orbits due to the shape of their trajectories. Particles that transit the poloidal plane without experiencing a parallel bounce, their μ never demands that $v_{\|} = 0$, are referred to as 'passing' particles.

The toroidal canonical momentum, p_ϕ, seen in Eq. (3.4) is an invariant that corresponds to the Lagrangian's invariance in the toroidal coordinate, ϕ, as prescribed by Noether's theorem. It is an exactly conserved quantity in axisymmetric magnetic fields. The canonical momentum relates the instantaneous toroidal angular momentum measured from the central axis to the local poloidal magnetic flux. Recall that the equilibrium poloidal flux is often used as a radial coordinate, so p_ϕ explicitly details the radial orbital motions. Here, the poloidal flux plays a similar role to the electrostatic potential in Eq. (3.2); for an initial toroidal angular momentum, conservation of p_ϕ determines which values of ψ are not strictly

forbidden for the particle. Contrary to the kinetic energy, the toroidal angular momentum is not inherently lower bounded, complicating the consideration of the poloidal flux as a trapping scalar field. Nonetheless, the poloidal flux acts like a trapping surface with deviations allowed through the changes in the toroidal angular momentum dictated by the other conserved quantities. It can be clearly seen that the trapped particle population experiences larger radial variations throughout their motions since their parallel velocities change sign over their orbits.

It should be noted that the discrete nature of the toroidal field coils creates a cyclic toroidal variation in the field strength, a field magnitude diminished by about one part in one hundred.[6] This toroidal field variation, referred to as the toroidal field ripple, allows for the asymmetrization of the parallel bounce locations of ripple trapped orbits, resulting in a drift out of the plasma. The direct ripple trapping occurs for orbits with banana tips within the so called 'ripple well region,' typically found along the LFS and across the midplane to the HFS.[6] The deeply trapped particles on the LFS that are potentialily ripple trapped are not candidates for the X-point mediated thermal orbit loss and only a small portion of the orbit losses from the HFS midplane are directly affected. However, a ripple well region can exist in the vicinity of the X-point in a diverted geometry,[111] likely enhancing the so-called X-losses attributed to the vertical drifts of trapped particles.[33] Tokamaks are generally designed to minimize the ripple effects and axisymmetry is assumed.

The work of this thesis proceeds under the assumption that these quantities are appropriately conserved for the thermal ion population. The three constants over their domains label all possible orbits. Since all thermal collisionless orbits in a tokamak pass through the outer midplane at the low field side, it is commonplace to label the trajectories along this line. As mentioned, we aim to eventually consider the effects of collisions on the orbiting ions, differentiating the properties of ions at differing locations along the same trajectories, and the orbits will be instead considered across the confined region. Any particular observation location sets an initial (R_0, z_0), or alternatively (ρ_0, θ_0). For a given species of ion,

all that remains to specify a particular trajectory, and thus its constants of motion, are the quantities (v_0, ζ_0).

The constants of motion are rearranged, solving for the parallel velocity as a function of the initial conditions and the location of the guiding center,

$$v_\parallel(R, z; R_0, z_0, v_0, \zeta_0) = \pm v_0 \sqrt{R_b^* + \frac{2Ze}{mv_0^2}(\Phi_0 - \Phi)}, \tag{3.5}$$

where

$$R_b^* = 1 - \frac{B}{B_0}(1 - \zeta_0^2). \tag{3.6}$$

The '$\pm$' in Eq. (3.5) signifies that for an ion described by initial conditions (E, μ, p_ϕ) the parallel velocity is double-valued for a spatial position (R, z). Orbits for which the radicand in Eq. (3.5) is always positive are the so-called passing particles and continuously circulate the tokamak with a consistently signed parallel velocity. The other class of orbits trapped in the magnetic mirror centered along the outer midplane bounce where the radicand is zero, reversing the sign of their parallel velocities in the process. At these bounce locations, the poloidal motions of the orbit are no longer primarily driven by the parallel motion along the poloidal component of the magnetic field lines, and the perpendicular guiding center drift velocities play a pivotal role. A similar effect naturally comes into play for orbits passing near the X-point. The null poloidal magnetic field at this location and its reduced value in the vicinity inhibit the parallel velocity's ability to contribute to the poloidal motion, again allowing for the prominence of the drift motions.

Inserting Eq. (3.5) into Eq. (3.4) gives an expression for the poloidal flux as a function of the initial conditions and the instantaneous guiding center position,

$$\Psi_\pm(R, z; R_0, z_0, v_0, \zeta_0) = \frac{1}{Ze}\left(p_\phi \pm mRv_0 f_\phi \sqrt{R_b^* + \frac{2Ze}{mv_0^2}(\Phi_0 - \Phi)}\right). \tag{3.7}$$

Eq. (3.7) can be thought of as either a double-valued surface, $\Psi_{\pm}$, or as two single-valued surfaces, Ψ_+ and Ψ_-, in (R, z, ψ)-space. Such surfaces will hereby be referred to as the constraint surfaces, defining the allowable values of the poloidal flux for the orbiting ion to conserve its constants of motion. Passing particles spend their entire orbits on either the Ψ_+ or Ψ_- surface, and the trapped orbits bounce at locations where the two surfaces touch, with the poloidal flux necessarily taking the value $\Psi_+ = \Psi_- = p_\phi/Ze$.

In (R, z, ψ)-space, Eq. (3.7) is a general structure that preserves a particle's initial constants of motion and is practically independent from the particular equilibrium field structure, taking a similar form for any axisymmetric toroidal field geometry with a dominant toroidal component. The few sensitivities are found within the constant p_ϕ and in the f_ϕ and R_b^* terms. A change in p_ϕ does not meaningfully change the structure of $\Psi_{\pm}$, there is only an overall shift in the surface. The quantity f_ϕ essentially is the sign of the toroidal field, due to its dominance in the field structure, $|f_\phi| \approx 1$, and for the same reason, we can approximate

$$R_b^* \approx 1 - \frac{R_0}{R}(1 - \zeta_0^2), \tag{3.8}$$

since the field ratio is essentially a spatial dependence. Note, that for a trapped orbit in the absence of an electric field, a parallel bounce occurs when $R_b^* = 0$,

$$R_{b,\text{no } E} \approx R_0(1 - \zeta_0^2). \tag{3.9}$$

The motion of a charged particle in a magnetic field clearly should be sensitive to the detailed structure of said field. The information missing within the constraint surfaces is supplemented by the true values of the poloidal flux determined by the equilibrium magnetic field. The intersection between the constraint surfaces and the surface representing the equilibrium poloidal flux corresponds to the poloidal projection of the guiding center orbit. A typical intersection of a confined trapped orbit is illustrated in Fig. 3.1. Recall that the

equilibrium poloidal flux is determined by the Grad-Shafranov equation, Eq. (2.8) in Chapter 2.

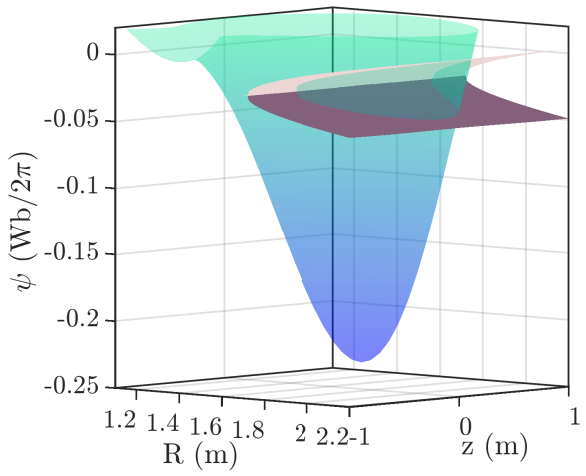

Figure 3.1: A sample intersection between the constraint surfaces, colored mauve and nude, and the equilibrium poloidal flux in the case of a negligible electric potential.

For an ion with a given initial location and pitch direction, the constraint surfaces allow for the determination of the initial velocity magnitude, thus the kinetic energy, required for some part of those surfaces to intersect the poloidal flux surface determined by the Grad-Shafranov equation at some given location,

$$E_{\pm} = \frac{(Ze)^2}{2m\xi^2}\left[\frac{R_0}{R^2}\frac{f_{\phi 0}}{f_\phi^2}\zeta_0(\psi-\psi_0) \mp \sqrt{R_b^*\frac{(\psi-\psi_0)^2}{f_\phi^2 R^2} + \frac{2m}{Ze}\xi(\Phi_0-\Phi)}\right]^2\Bigg|_{\mathcal{P}}, \tag{3.10}$$

where

$$\xi = \frac{R_0^2}{R^2}\frac{f_{\phi 0}^2}{f_\phi^2}\zeta_0^2 - R_b^*, \tag{3.11}$$

and all variable spatial quantities are evaluated at $\mathcal{P}$, the intersection location of interest. In the context of ion orbit loss, the determination of this loss point, or a family of loss points, is critical in diagnosing the magnitude of the effect and will be discussed in Section 3.2.

Eq. (3.10) corresponds to two equations: one for the energy of an intersection of Ψ_+,

$$E_+ = \frac{(Ze)^2}{2m}\left[\frac{1}{\xi}\left(\frac{R_0}{R^2}\frac{f_{\phi 0}}{f_\phi^2}\zeta_0(\psi-\psi_0) - \sqrt{R_b^*\frac{(\psi-\psi_0)^2}{f_\phi^2 R^2} + \frac{2m}{Ze}\xi(\Phi_0-\Phi)}\right)\right]^2\Bigg|_{\mathcal{P}}, \tag{3.12}$$

and the other for Ψ_-,

$$E_- = \frac{(Ze)^2}{2m}\left[\frac{1}{\xi}\left(\frac{R_0}{R^2}\frac{f_{\phi 0}}{f_\phi^2}\zeta_0(\psi-\psi_0) + \sqrt{R_b^*\frac{(\psi-\psi_0)^2}{f_\phi^2 R^2} + \frac{2m}{Ze}\xi(\Phi_0-\Phi)}\right)\right]^2\Bigg|_{\mathcal{P}}. \tag{3.13}$$

A cursory investigation suggests something problematic with the equations; they are equivalent under reversals in the initial pitch direction. In other words, the equations state that two identical ions only mirrored in motion about the local magnetic field vector will intersect the location $\mathcal{P}$ at the same minimum energy, given by Eq. (3.12) for $\zeta_0 < 0$ and Eq. (3.13) for $\zeta_0 > 0$, assuming $f_\phi < 0$,$\Psi - \psi_0 > 0$, and $\xi > 0$. Under the same assumptions $\Psi_- > \Psi_+$ for all locations, by construction. Considering the possible intersections of orbits starting from within the separatrix, while maintaining that $\psi_{\text{sep}} > \psi_{\text{core}}$, it must always be energetically favorable to be lost on Ψ_-. The caveat here is that the bracketed expressions in the equations are proportional to v_0, and per the definition of p_ϕ in Eq. (3.4), they must be non-negative to correspond to a physical orbit.

Under the conditions stipulated in the previous paragraph, the energy required for Ψ_- to intersect the equilibrium poloidal flux at some loss point $\mathcal{P}$ must be less than the energy for Ψ_+ to do the same. One might expect that the minimum loss energy is then always given by Eq. (3.13). This is only the case if the intersection of Ψ_- is actually part of the guiding center orbit, if there is a continuously connected intersection between $\Psi_\pm$ and the equilibrium flux beginning at ψ_0 and ending at the loss location. In the case of a passing orbit starting on Ψ_+, no transfer between the constraint surfaces takes place and the loss can only occur upon first intersection of Ψ_+ with the loss location. If an orbit starting on Ψ_+ is trapped, there is a bounce mediated at $\Psi_\pm = p_\phi/Ze$, and the loss becomes possible. In the absence of an electric potential, the determination of the trapped-passing boundary

in velocity-space is trivial. In the presence of an electric potential, the validity to applying Eq. (3.13) becomes more nuanced.

Another subtlety within Eqs. (3.12) and (3.13) again comes from the double-valued nature of the constraint surface. For a case again with $f_\phi < 0$ and $\Psi - \psi_0 > 0$, an ion with $\zeta_0 < 0$ is initially on Ψ_+. This can be seen by a quick calculation;

$$\begin{aligned}\Psi_\pm(R_0, z_0) &= \frac{1}{Ze}\left(p_\phi \pm mR_0 v_0 f_{\phi 0}\sqrt{\zeta_0^2}\right) \\ &= \frac{1}{Ze}\left(mR_0\zeta_0 v_0 f_{\phi 0} + Ze\psi_0 \pm mR_0 v_0 f_{\phi 0}\sqrt{\zeta_0^2}\right) \\ &= \psi_0.\end{aligned} \tag{3.14}$$

The above is only true if the '+' corresponds to $\zeta_0 \leq 0$ and the '-' to $\zeta_0 > 0$.

3.1.2 Mass and charge dependence

Inspection of Eq. (3.7) highlights why one studies the 'ion orbit loss' rather than the 'electron orbit loss'. For simplicity, consider the case of a constant electric potential,

$$\Delta\psi = \frac{m}{Ze} R f_\phi v_\parallel, \tag{3.15}$$

where the parallel velocity suffers no species dependent spatial behavior. The orbital widths of ions and electrons with the same parallel velocity are proportional to the ratio of their mass to charge ratios. Here, the basic logic of the plasma confinement is followed; the Lorentz force is linear in the charge and the affected inertia is linear in the mass. Comparing ionized deuterium to the electrons shows that the ion width is three orders of magnitude larger. If the species are considered to be in thermal equilibrium with each other, the electron thermal velocity is larger by the square root of the ion-electron mass ratio and the width ratio is nearly 10^2. The electron orbit losses are negligible by comparison.

Clearly the orbit loss is sensitive to the inherent properties of the ion. Unless otherwise

specified, referenced ions concern a thermal population of deuterium ions. The mass dependence of the collisionless orbit loss trajectories is completely contained within the preceding paragraph; heavier ions and those of lesser charge are more prone to orbit loss via their wider orbits. Accounting for the effects of particle collisions introduces another layer of ion mass dependence, discussed in Chapter 4.

3.2 Loss definition

The previous section established a method for determining the necessary energy for the constraint surfaces of an ion at a given observation point (R_0, z_0) with some initial pitch direction, ζ_0, to intersect the equilibrium poloidal flux at some location $\mathcal{P}$. In principle, this location is entirely arbitrary; for the classification of lost ion orbits, a choice of $\mathcal{P}$ is equivalent to defining what is meant by a lost orbit.

Ideally, $\mathcal{P}$ would be a family of points along the divertor and vessel wall, describing all orbits that lead to removal from the plasma. Such a choice mitigates the advantages of working with Eqs. (3.12) and (3.13), as the wall geometry requires a sufficiently dense number of points to resolve the general orbit loss problem. Furthermore, the poloidal structure of the plasma becomes increasing important in the SOL, both removing some symmetry properties of the core plasma and necessitating highly accurate two dimensional experimental data. Orbit following codes serve as a supplement when capturing the exact particle orbits up to the loss surfaces is desireable.[112]

The thermal orbit loss problem is easily reduced in scope since the diverted X-point geometry motivates the significant losses of the thermal population about that location.[33,34,41,45] Some authors choose $\mathcal{P}$ to be the horizontal plane running through the X-point,[34,42] capturing the topologically open orbits due to its influence. Another choice present in the literature defines $\mathcal{P}$ as the series of points along the separatrix.[43] Such a choice captures the relative scalings of the orbit loss but vastly overcounts the magnitude of the losses and discounts the

importance of the diverted geometry.

It has been shown using a fourth order Runge-Kutta algorithm for simulating guiding center orbits in a tokamak geometry that the energetic minima for loss orbits originating at some observation point as a function of the pitch angle is well-approximated by the class of orbits that directly intersect the X-point.[34] Orbits with energies above this threshold are unlikely to intersect the X-point but have paths open to the divertor passing through the X-point plane. This definition nearly captures all the losses found with the X-point plane loss condition. A class of, as far as the loss cone is concerned, relatively deeply-trapped high-energy loss orbits are missed by this definition.[34] This subset of the losses is relatively small and occupies less densely populated regions of velocity-space. However, such losses become important in the presence of a radial electric field, where the electrostatic potential more deeply traps ions at the outer midplane, preventing a sizeable fraction from reaching the X-point. If these ions are able to overcome their local $E \times B$ drift motions, they are able to cross the X-point plane on the low field side of the X-point. Therefore, $\mathcal{P}$ is defined to include the X-point and positions along the X-point plane at a greater major radius.[113]

As always, for a given observation point, an orbit with some initial pitch direction can possibly intersect the points in $\mathcal{P}$ on either constraint surface. In the event that both intersections are possible, the intersection of lower energy will define the lower bound of the loss region. In other words, for ions starting on the unfavorably lost constraint surface, the ions presently moving antiparallel to the induced plasma current, it must be determined if the constants of motion correspond to a trapped or passing particle. The trapped-passing boundary in velocity-space must be determined for particles local to any position in configuration-space. The existence of a non-trivial electric potential complicates this boundary by making it non-trivially energy dependent.

3.3 The case of a constant electric potential

First, consider the illustrative case of a constant electric potential. The constraint surfaces simplify to

$$\Psi_{\pm,\text{no } E} = \frac{1}{Ze}\left(p_\phi \pm mRv_0 f_\phi \sqrt{1 - \frac{R_0}{R}(1-\zeta_0^2)}\right). \tag{3.16}$$

To assess the orbit loss, the trapped-passing boundary in velocity-space must be determined to clarify for a given observation point if either Eq. (3.12) or Eq. (3.13) determines the minimum loss energy for a given ζ_0 or if there even is a minimum energy corresponding to an intersection with a point in $\mathcal{P}$. Of course, arbitrarily high energy orbits will intersect the first wall at some arbitrary poloidal position but are exceedingly rare for the thermal population. It can be seen that the energy for intersection, Eq. (3.10), goes like $(\Delta\psi)^2$; the energy required to traverse the radial extent of the SOL is far greater than to reach saddle point in the poloidal flux along the separatrix.

A particle bounces when its parallel velocity changes sign due to the conservation of the magnetic moment along a path of increasing field strength. Eq. (3.16) indicates that this occurs when $\Psi_+ = \Psi_- = p_\phi/Ze$. Since the poloidal projection of the guiding center orbit corresponds to the intersection of the constraint surfaces and the equilibrium flux, if the latter's contour corresponding to $\psi = p_\phi/Ze$ intersects with the vertical line defined by Eq. (3.9), then the orbit is trapped,

$$R_{\min}(\psi = p_\phi/Ze) \leq R_b \leq R_{\max}(\psi = p_\phi/Ze) \longrightarrow \text{trapped}. \tag{3.17}$$

Since the threshold loss orbit is generally taken as the orbit of X-point intersection, the lowest energy trapped losses have $R_b \lesssim R_X$. Loss orbits that bounce with $R_b \geq R_X$ are lost along the LFS X-point plane and require comparatively larger energies to traverse the greater $\Delta\psi$ deeper in the SOL. Although in the absence of a radial electric field R_b is energy independent,

the evaluation condition for the other terms in Eq. (3.17) have a weak dependence on the initial parallel velocity, given an initial observation point.

Consider a deuterium ion localized to the outer midplane, $R_0 \approx 2.0$, with $\zeta_0 f_{\phi 0} = 1.0$,

$$\frac{p_\phi}{Ze} \approx (4 \cdot 10^{-8} \text{ Wb s}/(2\pi \text{ m}))v_0 + \psi_0. \tag{3.18}$$

Consider the changes in p_ϕ/Ze when increasing the initial kinetic energy from 100 eV to 1 keV,

$$\Delta\frac{p_\phi}{Ze} \approx 0.009 \text{ Wb}/(2\pi). \tag{3.19}$$

For the equilibrium geometry for the baseline SOLPS case, see Appendix A, the change corresponds to a $\Delta R_{\min} \approx 0.015$ m, a minor effect. Regardless, counter-current ions of an increased energy have an unchanged R_b and a smaller contour that sustains bounces, slightly reducing the trapping of higher energy particles.

One might be tempted to write down something of the following form

$$|\zeta_{0,\text{t-p,no } E}| = \sqrt{1 - \frac{R_{\min}\big|_{\psi=\frac{p_\phi}{Ze}}}{R_0}}, \tag{3.20}$$

to establish the trapped-passing boundary. As previously discussed, the evaluation condition for $R_{\min}$ explicitly depends on the initial pitch angle, and Eq. (3.20) is in effect transcendental. If one were using an analytic formulation for the equilibrium, it is possible that Eq. (3.20) could be further solved. For any local observation point and initial pitch angle, the satisfaction of Eq. (3.17) is checked over a range of energies to determine if Eq. (3.12) or Eq. (3.13) provides the threshold orbit loss energy for the counter-current ions. The co-current threshold energies simply correspond to loss on their initial constraint surface. Over the velocity-space, these threshold energies form a boundary that is a commonly referred to as the velocity-space loss cone, a projection of the phase-space loss cone to a given obser-

vation point. Local ions with instantaneous velocities within the loss cone have trajectories open to the divertor via the X-point's influence. For a given pitch angle, all energies greater than the boundary are within the cone. At arbitrarily large ion energies, it is likely that these orbits do not all reach the divertor but are lost to the first wall at some location. The presented loss cones do not encapsulate the high energy orbits with pitch direction that intersect the first wall but are not lost via the diverted geometry at lower energies.

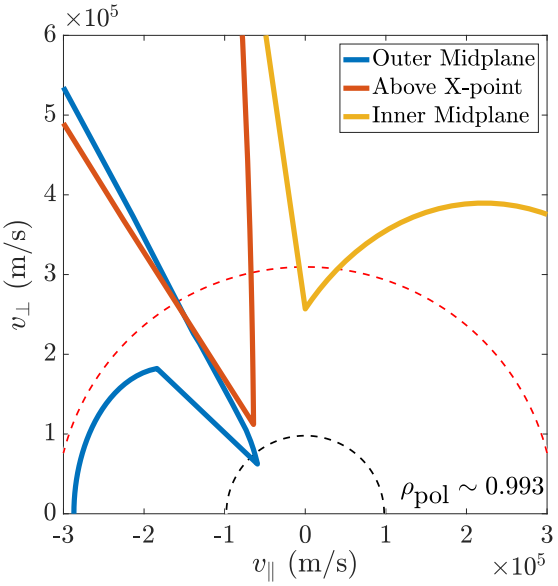

Figure 3.2: Typical velocity-space loss cones in the absence of a radial electric field projected to three observation points in configuration-space. The dashed black and red lines respectively correspond to energies of 10^2 and 10^3 eV.

Fig. 3.2 simultaneously plots velocity-space loss cones for three different locations in configuration-space along the same flux surface ($\rho_{\text{pol}} \approx 0.993$): along the outer and inner midplanes and directly above the X-point. The qualitative deformation from one to the other as a function of the poloidal angle is easily imagined. For any pitch direction, a single energy defines the loss cone boundary, a feature lost in the presence of a radial electric field. Collisionless orbits with greater energies will be lost on their first orbit. A few general truths can be discerned from the figure. The lowest energy losses from a given flux surface pass through that surface at the outer midplane, with the average threshold energy increasing as a function of the poloidal coordinate. The lowest energy losses for all locations correspond to

trapped orbits, generally those locally flowing antiparallel to the plasma current; for locations nearer the inner midplane, locally co-current trapped orbits can also lie in the local loss cone.

The shapes of the local loss cones reflect both the trapped fraction for the local observation point, all trapped orbits pass through the outer midplane and therefore the fraction is greatest at that location, and the ability of trapped or passing orbits with either orientation, co- or counter-current, to be lost via the X-point. For instance, co-current passing orbits in the confined region at the outer midplane will drift radially inward and will not be lost; however, such orbits found at the inner midplane drift outward from this position and are candidates for loss.

The large jump in the threshold loss energy for the local loss cone at the outer midplane lies upon the trapped-passing boundary and represents the energetic discrepancy between loss on Ψ_+ or Ψ_-. Moving poloidally toward the X-point does not wash this feature out but exacerbates the discontinuity; in Fig. 3.2, the jump is obfuscated for the local loss cone at R_X since the passing losses occur only at extremely large energies. Nearer the outer midplane, there is no discontinuity in the structure for the losses on the co-current half of velocity-space. Here, there is a smooth transition between the counter-current trapped, co-current trapped, and co-current passing losses, since all instances of loss do so on the same constraint surface.

Figure 3.3 plots several sample loss orbits while marking the poloidal locations corresponding to the mapped loss cones seen in Fig. 3.2. Subplot (a) shows a superthermal trapped loss orbit with a large width, allowing for an easier inspection of the trajectory. Subplots (b), (c), and (d) respectively show a counter-passing loss (within the confined region on the LFS), a trapped loss, and a co-passing loss (within the confined region on the HFS), each of which is more representative of trajectories contributing to the steady-state orbit loss on approach to the L-H transition. Each lost orbit is topologically open, being lost via the saddle point due to having sufficient energy for its pitch direction along any point on the trajectory such that the X-point deforms the orbit, leaving it open to the divertor.

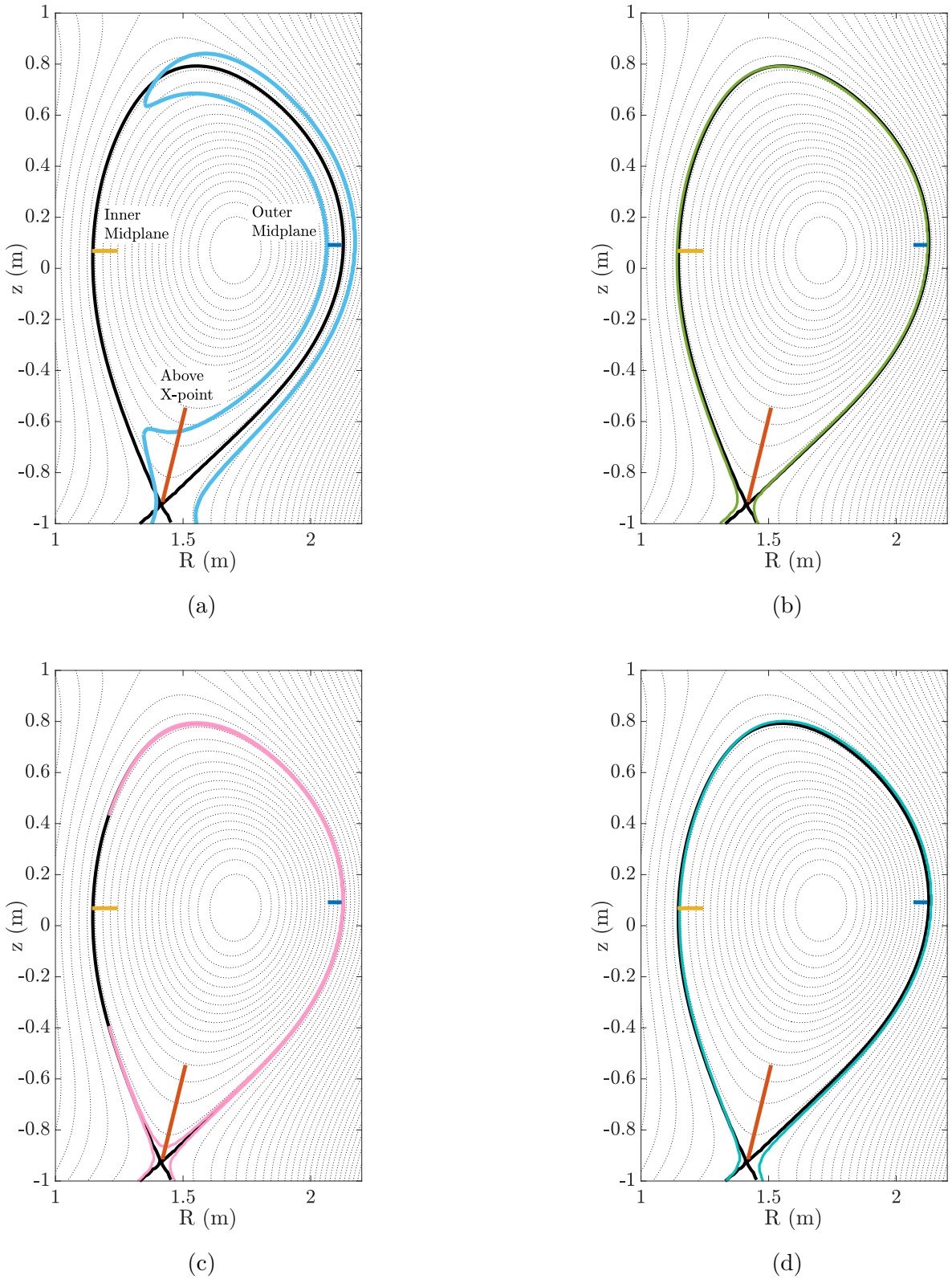

Figure 3.3: Example loss orbits in the geometry seen in Fig. 2.1. The line segments labeled in (a) correspond to the loss cones seen in Fig. 3.2.

Comparing the orbits in Figure 3.3 to the local loss cones in Fig. 3.2 deepens one's understanding of the orbit loss; the types of orbits passing through each location naturally determines the structure. The only thermal losses that pass through the loss cone mapped an appreciable distance directly above the X-point are trapped orbits. Any counter-current trapped ions within this velocity-space loss cone must each be connected to some more inward radial position along the outer midplane. The mapping between different velocity-space loss cones containing loss orbits passing through some location is quite complex. The trajectory of any loss orbit allows one to find the mapping of the velocity-space loss cone about the ion as it is lost.

Since the orbit loss is studied as a potential driver of larger magnitude radial electric fields, a self-consistent solution must consider the effects of E_r on the particle orbits and thus the loss. Recovering a non-trivial electric potential significantly affects the loss cone, most prominently shifting the trapped-passing boundary and allowing for the electrostatic trapping of low energy ions within the separatrix. The leading order effects of the radial electric field on the orbit losses are studied and maintained within the model throughout the thesis unless otherwise specified.

3.4 The case of a monotonically-increasing poloidally-constant electric potential

Restoring a non-trivial electric potential introduces a few complications into the loss cone calculation. With regard to the guiding center constants of motion, the potential only explicitly enters into the energy conservation with the obvious consequence of electrostatic trapping. Naturally, the parallel velocity is sensitive to the potential, complicating the boundary between trapped and passing orbits. An additional effect of the radial electric field is best understood by explicitly considering the $E \times B$ drift, which acts to decouple to parallel mirror bounce from the apparent bounce seen in the poloidal plane.

The electic potential is taken to be a flux function, $\Phi(\rho,\theta) \approx \Phi(\rho)$, simplifying the determination of the trapped-passing boundary. Furthermore, the potential is assumed to monotonically increase with the radial coordinate, $\Phi(\rho_2) > \Phi(\rho_1)$ where $\rho_2 > \rho_1$. The former is a standard assumption and the latter is a hallmark of the negative radial electric field well typical in the plasma edge. The standard choice of reducing the potential's degrees of freedom is well founded but becomes increasingly fraught on approach to the separatrix. There can be local extrema in the electric potential near the X-point,[114–116] encouraging the future relaxation of the flux function assumption. A first correction retains the poloidal variance of Φ in checking that no electrostatically trapped orbit is lost.

A parallel bounce still satisfies $v_\parallel = 0$ where $\Psi_+ = \Psi_- = p_\phi/Ze$ and therefore occurs when

$$\begin{aligned} 0 &= 1 - \frac{B_\mathrm{b}}{B_0}(1-\zeta_0^2) + \frac{2Ze}{mv_0^2}(\Phi_0 - \Phi_\mathrm{b}) \\ &\approx 1 - \frac{R_0}{R_\mathrm{b}}(1-\zeta_0^2) + \frac{2Ze}{mv_0^2}(\Phi_0 - \Phi_\mathrm{b}), \end{aligned} \tag{3.21}$$

resulting in

$$R_\mathrm{b} \approx \frac{R_0(1-\zeta_0^2)}{1 + \frac{2q}{mv_0^2}(\Phi_0 - \Phi_\mathrm{b}\big|_{\psi=\frac{p_\phi}{Ze}})}. \tag{3.22}$$

Again, consideration of the parallel bounce location is only necessary for the counter-current ions, those whose application of Eq. (3.12) or (3.13) to determine the threshold loss energy depends on their access to the preferred loss surface. For these ions, $\rho_0 < \rho(\psi = p_\phi/Ze)$ and the denominator of Eq. (3.22) is necessarily less than one, ensuring that

$$R_b \geq R_{b,\text{no E}}. \tag{3.23}$$

Note that the case of electrostatic trapping within the separatrix occurs before the problematic instance of the denominator in Eq. (3.22) reaching zero.

The electric potential pushes this bounce location to a greater major radius. Barely passing orbits can become trapped, and the most deeply trapped orbits that were lost via the X-point in the previous section are now more tightly trapped on the LFS and do not necessarily correspond to loss. For negligible ratios of the change in potential to the initial kinetic energy, Eq. (3.9) is recovered. It should be noted that the electric potential tends only to strictly increase into the near SOL. Particles with bounces beyond the separatrix can have $R_b < R_{b,\text{no E}}$; however, the concern is mitigated as the higher energy ions that are more apt to bounce at $\rho > 1$ are less sensitive to the electric field.

A poloidal bounce is now given by

$$0 = V_\theta \approx \frac{B_{x,\text{bp}}}{B_{\text{bp}}} v_\parallel - \frac{B_{z,\text{bp}}}{B_{\text{bp}}^2} E_{r,\text{bp}}, \tag{3.24}$$

where the magnetic drifts in the poloidal direction are taken to be negligible compared to the $E \times B$ drift. For the moment, consider the case with $B_x < 0$ and $B_z > 0$. Ions with $v_\parallel < 0$, the counter-current ions, at the outer midplane will drift outwards and are thus interesting to consider for losses. A negative radial electric field, the only possibility under the assumed electric potential, shifts the poloidal bounce location to a more negative parallel velocity, occurring earlier in the loss orbit than the parallel bounce. Rearranging Eq. (3.24) for the major radius gives

$$R_{\text{bp}} \approx \frac{R_0(1-\zeta_0^2)}{1 + \frac{2Ze}{mv_0^2}(\Phi_0 - \Phi_{\text{bp}}) - \left(\frac{E_{r,\text{bp}}}{B_{x,\text{bp}} v_0}\right)^2}, \tag{3.25}$$

which also clearly corresponds to Eq. (3.9) in the absence of an electric field. Note that the usual small decoupling of the parallel and poloidal bounce by the poloidal projection of the curvature and ∇B drift motions has been ignored. It is further noted that for the counter-current ions of interest, is is possible that $\rho_0 > \rho_{\text{bp}}$, and the considered ion has already poloidally bounced.

To better understand the relationship between the bounce locations, consider their ratio,

$$\frac{R_{\mathrm{b}}}{R_{\mathrm{bp}}} = \frac{1 - \frac{2Ze}{mv_0^2}\Delta\Phi_{\mathrm{bp}}}{1 - \frac{2Ze}{mv_0^2}\Delta\Phi_{\mathrm{b}}} - \frac{\left(\frac{E_{r,\mathrm{bp}}}{B_{x,\mathrm{bp}}v_0}\right)^2}{1 - \frac{2Ze}{mv_0^2}\Delta\Phi_{\mathrm{b}}}, \tag{3.26}$$

where the $\Delta\Phi_j = \Phi_j - \Phi_0$. As expected, Eq. (3.26) is independent of $R_{\mathrm{b,no}\,E}$ and purely depends on the relative size of the ion's kinetic energy and the radial electric field. The parallel bounce location is only sensitive to the changes in the electrostatic potential through the energy lost by climbing out of the well. The poloidal bounce location exhibits a similar sensitivity but also directly feels the $E \times B$ drift perpendicular to the magnetic field. For a modest strength E_r, both the decoupling of these positions and resultant changes in the orbital dynamics are expected to be small.[113]

The quantity $2Ze\Delta\Phi_b/mv_0^2$ is positive but less than unity for the counter-current non-electrostatically trapped ions whose trapping is of interest for the thermal orbit loss, provoking a Taylor expansion keeping only the leading order terms,

$$\frac{R_{\mathrm{b}}}{R_{\mathrm{bp}}} \approx 1 + \frac{2Ze}{mv_0^2}(\Phi_{\mathrm{bp}} - \Phi_{\mathrm{b}}) - \left(\frac{E_{r,\mathrm{bp}}}{B_{x,\mathrm{bp}}v_0}\right)^2. \tag{3.27}$$

The hastened reduction in the parallel energy acts to push both bounce locations to greater major radii, with a more pronounced effect on the parallel bounce location since $\rho_{\mathrm{b}} > \rho_{\mathrm{bp}}$, whereas the $E \times B$ drift acts similarly but only for the poloidal bounce position. The side of unity that Eq. (3.27) falls on depends on the relative strength of the second and third terms corresponding to the two described effects. For potential profiles typical of the tokamak edge, it seems that $R_{\mathrm{b}}/R_{\mathrm{bp}} > 1$, describing loss orbits that suffer an early poloidal bounce while continuing to drift outwards. The necessity of the continuation of the outward drift for the counter-current ions can be understood by considering the constants of motions just before and during the poloidal bounce. As the ion moves toward its poloidal bounce location, toward smaller major radii, the magnitude of the parallel velocity decreases via the increase in the

perpendicular energy demanded by the magnetic moment conservation. The parallel energy loss is exacerbated by the radial movement through the electric potential. After reversing direction at the poloidal bounce, the growth in the parallel velocity due to approaching the low field side cannot match the parallel velocities experienced before the poloidal bounce at the same major radius due to the net energy lost to the electric potential. Thus, after the poloidal bounce for the same R the lesser $|v_\parallel|$ must correspond to a further radial position. More simply put, the vertical magnetic drifts are unaltered and determine the projected particle motion at the poloidal bounce; in the upper and lower halves of the plasma, these drifts move the ion either radially inward or outward depending on the orientation of toroidal field component.

The primary effect of the electric field is determined by the parallel energy exchange between the ions and the electrostatic potential. For L-mode conditions in particular, the the separation between the bounce locations plays a minor role and is no greater than 10% for 100 eV ions in a 15 kV/m E_r well. On the basis of collisionality, lower energy ions are typically excluded from the collisionless portion of the loss cone, as will be seen in Chapter 4, and are not the focal point of the orbit loss problem.

We continue by assuming that $R_{\mathrm{bp}} \approx R_{\mathrm{b}}$, allowing for simpler estimations of the orbital paths in Chapter 4. It is important to point out that in this case $R_{\mathrm{bp}} \approx R_{\mathrm{b}} \neq R_{\mathrm{b,\ no\ }E}$, and the most significant effects of the electric field on the orbit loss are maintained: there is a shift in the trapped-passing boundary and low energy ions can be electrostatically trapped.[34,45,47,113] For H-mode conditions, where the electric field wells are more pronounced, the radial and horizontal distances between the two bounce locations are greater. Higher energy ions are strongly affected by the electric field and a significant portion of the ions cannot overcome the large $E \times B$ flows manifesting as a more pronounced $v_\parallel$ loss barrier. The barrier exists for ions on the low field side with local $E \times B$ drifts larger than the poloidal projections of

their parallel velocities,

$$V_{E\times B} > \frac{B_x}{B} v_{\parallel}, \tag{3.28}$$

introducing an E_r^2 scaling for the minimum energy describing the boundary.[34,45,47]

This thesis opts to focus on L-mode plasmas with a particular interest on those near the L-H transition criteria, in order to assess the possible role played by the ion orbit loss in the transition. The full effects of the radial electric field are included under the conditions necessary for the assumptions that the bounce locations are not strongly separated and that the potential is approximately a flux function. The results presented in the upcoming section well reproduce the effects of the radial electric field on the loss cone structure seen in the literature,[34,45,47,113] even for H-mode like field strengths. At any rate, the approximate methods for determining the orbital shapes and periods that will be discussed in Chapter 4 make use of the $R_{\rm bp} \approx R_{\rm b}$ assumption, and further care is required for quickly constructing the orbit characteristics under the influence of an H-mode like radial electric field.

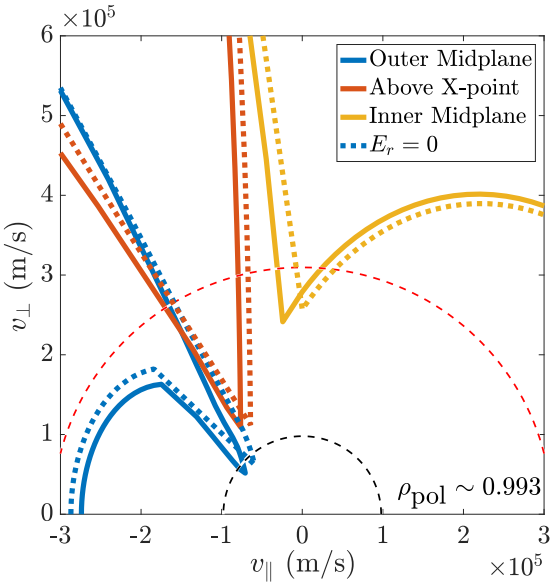

Figure 3.4: The effects of a modest L-mode magnitude radial electric field on the standard velocity-space loss cones. The lines of constant energy are the same seen in Fig. 3.2.

3.4.0.1 The loss cone in the presence of a radial electric field

For a given ion's orbit, all of the terms in Eq. (3.22) are precisely known. The major radius that sustains a parallel bounce exhibits a twofold energy dependence: in the kinetic energy term and also within the appropriate radial position to evaluate the electric potential. The former dependence dominates the relationship and the electrostatic potential has a marked influence on the local loss cone structure. A similar procedure to the one discussed in the previous section is performed to assess the possibility of a counter-current ion with a given pitch direction at a given observation point to have a mediated transfer between the constraint surfaces, allowing for a loss on the preferred surface.

Contrary to the previous section, the electrostatic potential can allow for a finite energy range that corresponds to trapped losses for a given pitch direction and observation point. Local loss cones with the upwardly bounded energy regions have three energies describing the loss cone boundary as a function of ζ_0: E_T describes the threshold energy such that any more energetic ions of similar pitch are lost, and E_U and E_L respectively describe the upper and lower boundaries of the finite loss regions. Again, the discussion is only relevant for the counter-current ions as those co-current are initially found on the preferred loss surface.

Fig. 3.4 shows the typical changes in the projected loss cone structures under the influence of an electric field typical of an L-mode. The electric field shifts the distribution function to favor the trapping of counter-current directed orbits, corresponding to a $v_\parallel$ shift in the loss region by E_r/B_x.[47,117] The shifted finger-like regions corresponding to the trapped losses narrow, most noticeably at the outer midplane, with the threshold energy for these losses being minimally changed. Sizable changes only occur when the orbits first become electrostatically trapped.[45] The counter-current passing losses from the LFS and the co-current passing losses from the HFS approach the X-point in the opposite directions, respectively against and with the local $E \times B$ rotation. Consequently, in the presence of the negative E_r well, the former require lesser loss energies and the latter greater. The increase (decrease) of the poloidal velocity due to the $E \times B$ drift decreases (increases) the ions' orbital widths.[45]

The progressive changes are studied over a scan in the electric field strength, presented in Fig. 3.5 subplots (a) (c) and (d), with subplot (b) showing the potential profiles scaled from the baseline SOLPS simulation. The radial electric field's impact on the local loss cone structure can be understood in terms of the ratio of the electric potential increase to the loss condition to the minimum loss energy for a particular velocity-space loss cone.[45] The qualitative behaviors match those seen in the literature[34,45,47,113] with quantitative differences being primarily attributed to differences in the equilibria, notably the horizontal location of the X-point, a dependence expounded upon in Chapter 5. Even for H-mode strength E_r profiles, the cones are effectively reproduced.

The trends first seen in Fig. 3.4 embolden in response to strengthening E_r. Notably, the finger-like projections thin and bend toward more counter-current orbits, and the multivalued nature of the loss cone for a given ζ_0 can be clearly seen. The deformation of the trapped loss region continues until such losses are made impossible. For a given flux surface, orbits originating at the outer midplane achieve this threshold first because the lowest energy losses are associated with this location. In the presence of strong electric fields, where Eq. (3.28) is satisfied for a growing subset of the ions, those on the low field side are unable to overcome their poloidal $E \times B$ drifts. This effect manifests as the eventual vertical boundary seen in Figure 3.5 subplot (a), delineating a cutoff $v_{\|}$ required to overcome the local $E \times B$ drift.

Projected loss cones nearer the inner midplane have perhaps the most nuanced response to a growing E_r. Although the losses in these regions typically require larger energies for the standard positive triangularity tokamak, the minimum loss energy decreases with increasing E_r until around when the electrostatic trapping condition is met. This decrease corresponds to the possibility of relatively low energy trapped losses that were confined barely passing orbits in the presence of a weaker E_r profile. Here, the overall shift in the loss region steadily increases the angular width of the high energy portions of the local loss cone. This effect coupled with the rising loss energies for the co-current passing losses creates a structure that deviates from the $E_r = 0$ baseline by having a lower loss energy nose region while the rest of

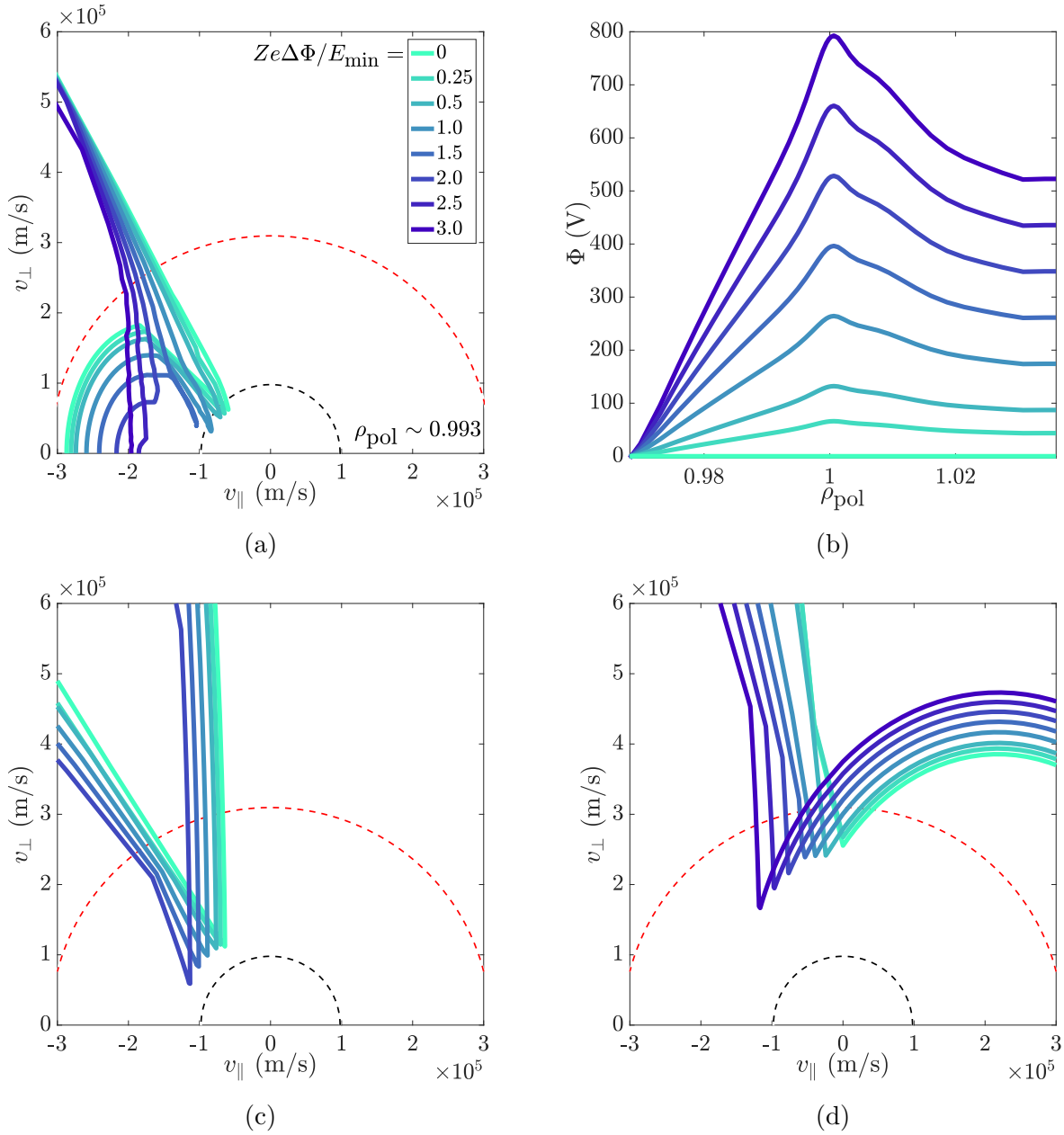

Figure 3.5: A closer look at the E_r sensitivity of the velocity-space loss cones over a scan of potential profiles of increasing steepness. Subplots (a), (c), and (d) respectively consider the outer midplane, above the X-point, and the inner midplane. Subplot (b) illustrates the potential profiles. Again, the lines of constant energy are the same seen in Fig. 3.2.

the local loss cone is at slightly higher energies but with an increased angular width.

This section developed the method by which one applies the loss energy Eqs. (3.12) and (3.13) in the case of a poloidally-constant monotonically-increasing electric potential in the

edge of a typical tokamak plasma. The generic effects of the radial electric field in pushing the poloidal and parallel bounce locations toward greater major radii and the electrostatic trapping of ions are the most significant consequences of E_r, whereas the decoupling of the poloidal and parallel bounce only plays a minor role. Changes in the local loss cones in relation to the poloidal positions of their projection have also been explored. Naturally, the projections exhibit a radial dependence suggesting the domain of flux surfaces supportive of thermal orbit losses.

3.5 The scope of orbit losses

The poloidal sensitivity of the projected loss cones has already been discussed, specifically at the inboard and outboard midplanes along with directly above the X-point. There is a smooth transition between the boundaries as a function of the poloidal coordinate over a given flux surface. It is worth pointing out the the orbits contained within any of the local loss cones over a flux surface are necessarily different, except in the case of an up-down symmetric tokamak where vertically mirrored local loss cones contain identical trajectories. At any rate, there exits an obviously fundamental and predictable radial dependence for the ion orbit loss: orbits nearer the separatrix tend to require less energy to be lost.

The previous statement is exactly true in the case of a constant electric potential, as seen in Eq. (3.10), $E_{\pm} \sim (\Delta\psi)^2$. The radial electric field can inhibit losses in a such way where more radially inward starting losses are preferred. For instance, in Fig. 3.5.a, the minimum energy jumps dramatically between $1.5 \lesssim Ze\Delta\Phi/E_{\min} \lesssim 2.0$. A slightly more radially inward position with $Ze\Delta\Phi/E_{\min} \lesssim 1.5$ could be described by a lower threshold loss kinetic energy. This phenomenon is the exception to the rule, and for a poloidal position, the threshold energy typically decreases on approach to the separatrix. The general $E_{\pm} \sim (\Delta\psi)^2$ scaling persists until the point of potential trapping, where the radial scaling of the electric potential sets the loss minima.

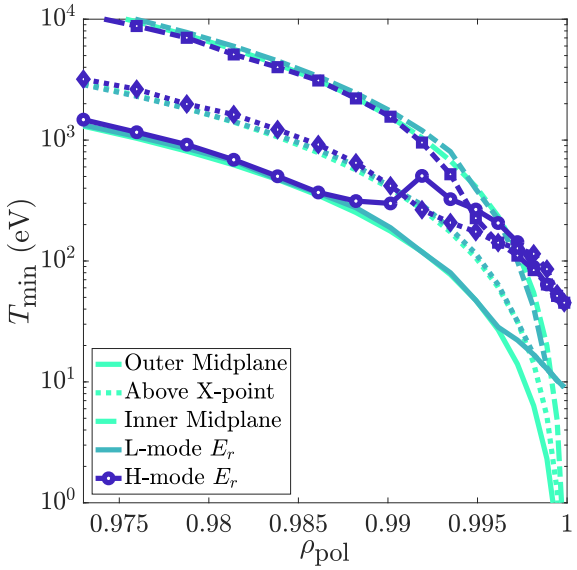

Figure 3.6: The radial dependence for the minimum kinetic energy achieving ion orbit loss for various observation points under different electric field conditions, corresponding to potential profiles of similar color in Fig. 3.5.b.

The radial dependencies for the minimum loss energies for the three previously discussed observation points in configuration-space are shown in Fig. 3.6. Very near the separatrix, the loss energies approach sub-thermal values. Here, the orbits are highly collisional, unlikely to complete a loss orbit before colliding out of the loss cone. For relatively weak electric fields, the projected loss cone shape is largely unchanged as a function of the radial position, and the poloidal hierarchy with respect to minimum loss energy remains unchanged. The significance of the potential trapping can be seen when comparing the L-mode E_r case to the case of no-E_r in Fig. 3.6. A deviation is seen very near the separatrix, where the energetic minima are given by the energy required to overcome the electrostatic potential barrier. Although the poloidal dependence for the potential is neglected in the model, when available, for instance in SOLPS simulations, the electrostatic trapping condition is checked using the maximum of the 2-d potential, often found near the X-point. When considering a stronger electric field, the lowest energy losses are not necessarily attributed to orbits localized to the outer midplane.[34] Here, a $v_{\|}$ barrier in the local loss regions correspond to the increased poloidal trapping of ions on the LFS.

At this point, the projected loss cone structure has been studied over the confined region in the poloidal plane and under the influence of a realistic radial electric field. The phase-space loss cone envelops all trajectories that are lost to the wall or the divertor in the absence of collisions. Here, the phase-space loss cone omits the large energy losses that intersect the first wall but do not correspond to divertor losses for identical ions of lower energy. The magnitude of the orbit loss effect depends on the population of phase-space near the loss cone. For any given local loss cone, this dependence becomes one of the population of particles local to the configuration-space observation point near the loss structure in velocity-space.

3.5.1 The equilibrium Maxwellian overlap

The distribution function describing the confined plasma determines if the thermal ions populate regions of velocity-space with energies relevant for the orbit loss. If the loss regions occur at energies far above the local ion temperatures, only the vanishingly small high energy tail of the distribution can contribute to the orbit loss. The existence of the loss cones at subthermal energies would predicate strongly non-Maxwellian local distribution functions, that is if the loss cone is appreciably empty due to the loss mechanism. The increasing collisionality of ions of decreasing energy suggests that the lowest energies of any loss cone are most likely to be collisionally in equilibrium with the local distribution and not empty at all.

The exact form for the equilibrium distribution function is not known, and a simple Maxwellian distribution function,

$$f(\rho_0, \theta_0, v) = n(\rho_0, \theta_0) \left(\frac{m}{2\pi T_i} \right)^{3/2} e^{-mv^2/2T_i}, \tag{3.29}$$

is often chosen when modeling a plasma, both for its relative ease of implementation and since it naturally satisfies the equilibrium kinetic equation. The existence of a velocity-space loss cone in the edge region of a tokamak plasma necessarily precludes such a distribution function

from serving as a complete description, unless the loss region only exists at superthermal energies ($\sim 10T_i$) or the loss cone is considered full. As shown in the previous sections, the former is not generally the case in the edge; the latter will be discussed in the upcoming chapter.

The general scope of the thermal ion orbit loss seen in Fig. 3.6 can be specified with local Maxwellian distributions described by some temperature T_i and density n by calculating the overlap of the assumed distribution function and local velocity-space loss cone. The local plasma density is defined by

$$\begin{aligned} n(\rho_0, \theta_0) &= \int f dv^3 \\ &= 4\pi \int_0^\infty f v^2 dv. \end{aligned} \tag{3.30}$$

Since the orbits deviate from flux surfaces, connecting radial positions at arbitrary poloidal angle, the local Maxwellian overlap, $F(\rho_0, \theta_0)$, is considered, being defined as the ratio of the density captured by the local loss region,

$$\begin{aligned} n_{\mathrm{LR}}(\rho_0, \theta_0) &= \int_\Sigma f dv^3 \\ &= 2\pi \int_{-1}^1 d\zeta \left(\int_{v_{\mathrm{T}}}^\infty f v^2 dv + \int_{v_{\mathrm{L}}}^{v_{\mathrm{U}}} f v^2 dv \right), \end{aligned} \tag{3.31}$$

to the local plasma density $n(\rho_0, \theta_0)$, such that

$$\begin{aligned} F(\rho_0, \theta_0) &= \frac{1}{\sqrt{\pi}} \int_{-1}^1 d\zeta \left(\int_{\epsilon_{\mathrm{T}}}^\infty \sqrt{\epsilon} e^{-\epsilon} d\epsilon + \int_{\epsilon_{\mathrm{L}}}^{\epsilon_{\mathrm{U}}} \sqrt{\epsilon} e^{-\epsilon} d\epsilon \right) \\ &= \frac{1}{\sqrt{\pi}} \int_{-1}^1 \left(\Gamma(3/2, \epsilon_{\mathrm{T}}) - \Gamma(3/2, \epsilon_{\mathrm{U}}) + \Gamma(3/2, \epsilon_{\mathrm{L}}) \right) d\zeta. \end{aligned} \tag{3.32}$$

The Maxwellian overlap for a flux surface is simply the flux surface average of the local

calculation,

$$F(\rho) = \frac{\int_0^{2\pi}\int_0^{2\pi} F(\rho_0,\theta_0)\sqrt{g}d\phi d\theta}{\int_0^{2\pi}\int_0^{2\pi}\sqrt{g}d\phi d\theta} = \frac{\oint F(\rho_0,\theta_0)\frac{dl}{B}}{\oint \frac{dl}{B}}. \tag{3.33}$$

The subscript 'T' in Eqs. (3.31) and (3.32) refers to energy of the upwardly unbounded portions of a local loss cone, while the subscript 'U' and 'L' respectively refer to the upper and lower bounding energies for the finite loss regions. The Γ functions seen in Eq. (3.32) are the well-known upper incomplete gamma functions.

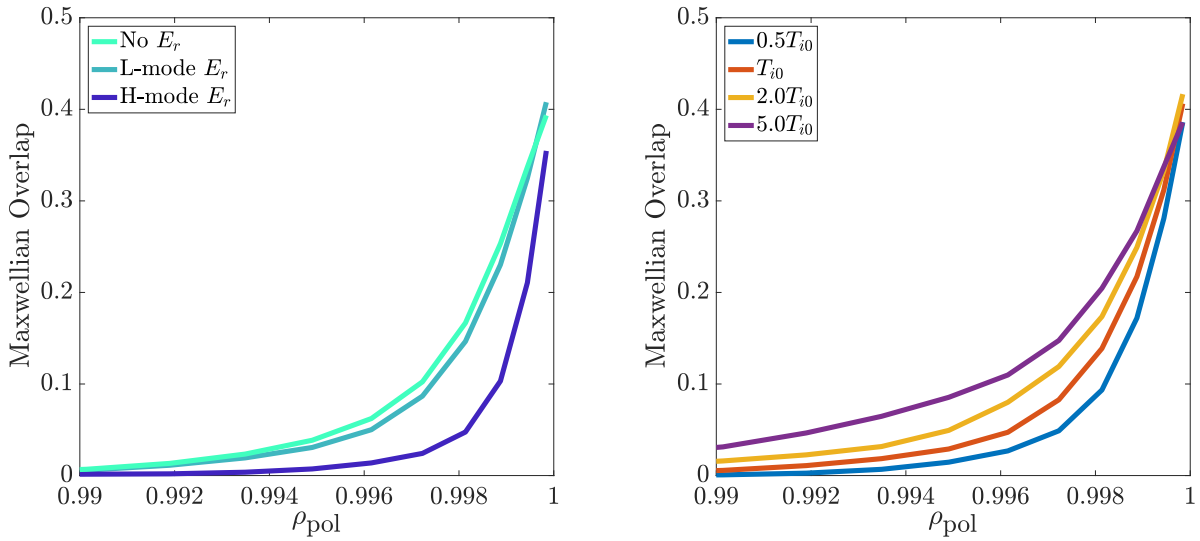

(a) (b)

Figure 3.7: Subplot (a) plots the Maxwellian overlap with the baseline temperature profile, see Appendix A, over an E_r scan, see Figure 3.5.b. Subplot (b) presents a coupled scan about the baseline temperature and potential profiles.

The Maxwellian overlap signifies the magnitude of the ion orbit losses as a function of the radial coordinate and has been referred to as the loss fraction in the literature.[43] Furthermore, this overlap can be used as a litmus test of sorts to determine the impact of errors introduced when modeling the plasma edge using simplistic Maxwellian functions. In fact, Eq. (3.33) could be generalized for any distribution function, providing a sanity check

for a particular choice of f used in edge modeling; however, without first making a meaningful statement about the true distribution function within the loss cone, any discussions of the overlap will overestimate the influence of the orbit loss.

Within the Maxwellian overlap, a few notable features are worth mentioning. Fig. 3.7.a shows the generic radial dependence of ion orbit loss in terms of the overlap for the baseline SOLPS test case AUG 16151 with electric potential profiles corresponding to those of matching color in Fig. 3.5.c and the baseline temperature profile seen in Appendix A. The gradient of the temperature profile is less steep than the orbit loss energy dependence seen in Fig. 3.6, and the overlap grows on approach to the separatrix, generally peaking somewhere around 40%. The electric field typically reduces the losses, but as discussed in Section 3.4.0.1 it can enhance losses from a particular locale. For large enough electric fields, the losses are significantly reduced for the same temperature profile.

Subplot (b) investigates the overlap's dependence on the ion temperature profile. Here, the electric field is scaled with the ion temperature, as will be discussed in the forthcoming Section 5.5. As expected, the overlap increases for increasing temperatures, with the mitigating E_r insufficient to generally suppress F at the higher temperatures. Notably, very near the separatrix the overlap decreases for sufficiently large electric field and temperature profiles. For temperatures far above the energy scale of the loss cone, increasing the average ion temperature inefficiently grows the overlap of the assumed Maxwellian. Here, the electric field growth eventually wins out, reducing F.

3.5.2 The intrinsic rotation

Another static feature of the loss cone that has been studied in the literature[113] is the intrinsic rotation associated with an empty loss cone structure. Under this tenuous assumption that the loss cone is strictly empty, one can easily find the rotational speed associated with the Maxwellian distribution over the loss region and posit that a Maxwellian with a hole rotates at the opposite speed.

A similar calculation to the Maxwellian overlap is performed to calculate the intrinsic parallel rotation under the assumption that the loss region is indeed empty,

$$
\begin{aligned}
V_{\parallel,\mathrm{iol}}(\rho_0,\theta_0) &= -\frac{1}{n}\int_{\Sigma} v_{\parallel} f dv^3 \\
&= -\frac{2\pi}{n}\int_{-1}^{1}\zeta d\zeta\left(\int_{v_\mathrm{T}}^{\infty} f v^3 dv + \int_{v_\mathrm{L}}^{v_\mathrm{U}} f v^3 dv\right) \\
&= -\sqrt{\frac{2T_i}{\pi m}}\int_{-1}^{1}\zeta d\zeta\left(\int_{\epsilon_\mathrm{T}}^{\infty} \epsilon e^{-\epsilon} d\epsilon + \int_{\epsilon_\mathrm{L}}^{\epsilon_\mathrm{U}} \epsilon e^{-\epsilon} d\epsilon\right) \\
&= -\sqrt{\frac{2T_i}{\pi m}}\int_{-1}^{1}\zeta\left(\Gamma(2,\epsilon_\mathrm{T}) - \Gamma(2,\epsilon_\mathrm{U}) + \Gamma(2,\epsilon_\mathrm{L})\right) d\zeta.
\end{aligned}
\tag{3.34}
$$

Again, the calculation is performed considering a poloidally localized Maxwellian since the velocity-space loss cone boundary is only applicable to ions at the location of projection. The flux surface average of Eq. (3.34) can also be taken, corresponding to the average intrinsic rotation about a flux surface.

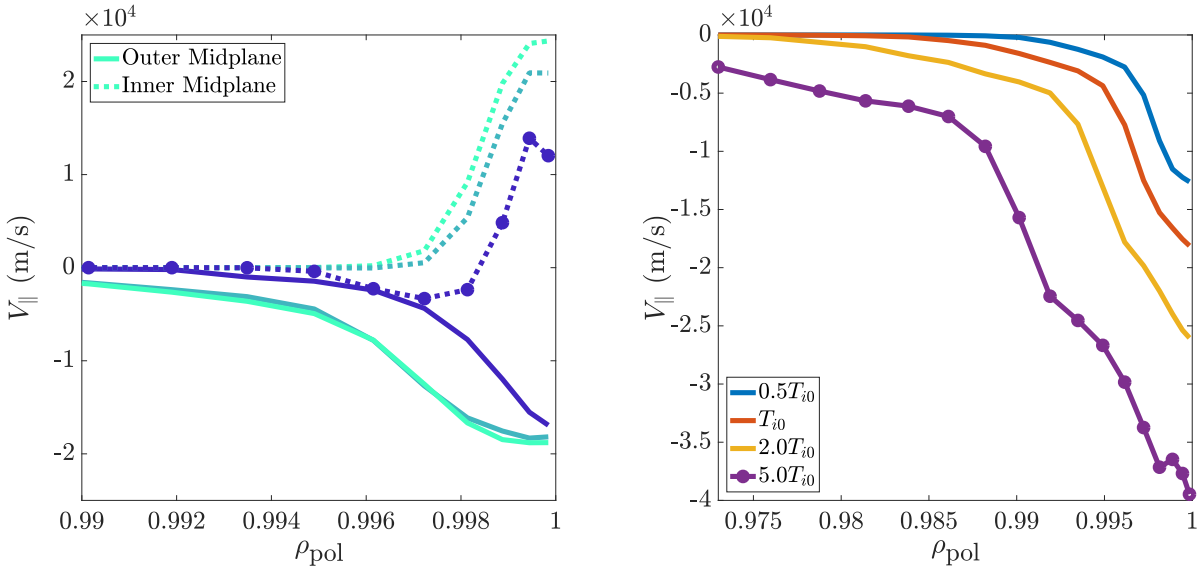

(a) (b)

Figure 3.8: The intrinsic rotation, (a), with the baseline temperature profile, see Appendix A, over an E_r scan, see Figure 3.5.b. Subplot (b) presents a coupled scan about the baseline temperature and potential profiles.

A significant difference between Eqs. (3.32) and (3.34) is that the integrand of the former

is strictly positive while the latter's changes sign with the velocity's orientation with respect to the local direction of the magnetic field. While the Maxwellian overlap measures the scope of the ion orbit loss, the intrinsic rotation measures the asymmetry in the co- and counter-current losses, a property influenced by the field geometry. Any loss cone symmetric about the $v_\perp$-axis will not contribute to the intrinsic rotation, no matter how large the Maxwellian overlap, granted that the distribution function is also symmetric about reflection across $v_\perp$.

The intrinsic rotation calculations are performed for the same cases shown in Figure 3.7, with the results displayed in Figure 3.8. Subplot (a) illustrates computations of Eq. (3.34) for both the inner and outer midplanes for the three potential profiles. Here, the rotation along the outer midplane has a larger radial width due to the positive triangularity of the equilibrium, see Section 5.8. The flows are larger at the HFS and LFS for small and large E_r magnitudes respectively. The intrinsic rotation at the inner midplane is more sensitive to the radial electric field. As can be seen in Fig. 3.5.d, the electric field both raises the energies of the co-current particle losses while allowing for more coverage of the loss cone in the counter-current half of velocity-space.

There is a strong poloidal variation in the local value for $V_{\parallel,\mathrm{iol}}$ which can be expected after inspection of Fig. 3.2, with the rotation being co-current directed near the outer midplane and counter-current directed nearer the inner midplane. Such strongly antisymmetric flows have been demonstrated in the edge of H-mode discharges in ASDEX Upgrade[119,120] for the impurity species. However, the impurity polodial asymmetry has been modeled without invoking the orbit loss physics.[121] Such rotations are also seen for the main ions in the standard SOLPS simulations, although the rotations seen in subplot (a) are several times larger than those seen in the corresponding SOLPS simulation, see Appendix A. It will be seen in the next chapter that correcting for the collisionality reduces the predicted rotation to values closer to the SOLPS results.

Subplot (b) shows the outer midplane parallel intrinsic rotation for the same scaled temperature and electric field profiles as in Fig. 3.7.b. The local intrinsic rotation typically

follows the behavior of the Maxwellian overlap since any local loss cone is typically dominated by co- or counter-current losses. The plotted results agree with those in the literature[113] in terms of both shape and magnitude, with differences being attributed to the present use of non-constant temperature and electric field profiles. The flux surface average of the intrinsic rotation is lesser in magnitude than either of the midplane flows due to their cancelation. The magnitudes of such flux surface averaged profiles are of the order of those seen in the literature.[118]

Chapter 4

Demarcating the loss cone on the basis of collisionality

In the previous chapter, the orbit loss basics were introduced and a method was presented to determine the region in velocity-space that contains orbits with paths to the divertor for a particular observation point in configuration-space. The construction of the local loss cones relies on the conserved quantities defining a collisionless ion orbit. In approaching a solution to the steady-state problem, the phenomena that resupply the loss cone must be studied. Before one is prepared to estimate the rate of the steady-state losses, the probability of any ion within the loss cone to be lost on a first orbit must be considered. If an ion is transported into the loss region but is also practically guaranteed to scatter out of the loss cone before it is lost, the original refueling event would not contribute to the orbit loss. In order to determine the rate of orbit loss, the behaviors of orbits within the cone must be assessed.

All ion orbits that cross the separatrix must do so at two locations, with the inflowing and outflowing locations determined by the ∇B drift direction. The summed difference between the particle flux for all such pairs must exactly equal the net flux of ions across the separatrix. For any one pair, this difference must equal the net transport and sourcing onto the orbit throughout the portion of its trajectory through the confined region of the

tokamak.[35]

The problem is reduced by considering the net transport and sourcing into the loss cone within the confined region rather than the net movement onto particular trajectories. An ion transferring from one loss orbit to another within the orbit loss time scale is largely inconsequential; both trajectories lead directly to the divertor. Ions fed into the loss cone and then scattered out before being lost do not contribute to a prompt orbit loss current and must be handled appropriately. It becomes clear that the loss cone needs to be demarcated about this qualitative difference in the orbit loss, creating a 'collisional' region corresponding to ions that are not expected to be lost before they scatter out of the loss cone and a 'collisionless' region where the opposite holds true. To be clear, the term 'collisionless' here does not truly mean 'without collision' but indicates that the collisions over the loss orbit are sufficiently small, allowing for loss.

Neither portion of the loss cone is truly empty. Any ion scattered into the collisional portion of the cone is scattered into a confined orbit before a loss occurs. It is possible that the particular ion can later scatter back into the loss region and be promptly lost. The collisional portions of the local loss cones are effectively in equilibrium with the local Maxwellians, and over timescales much longer than any individual collisions, a roughly constant number of particles are housed within this portion of the loss cone.[33] Any loss trajectory would at some location interior to the LCFS fulfill the collisionless loss condition. The magnitude of the orbit loss along any one trajectory is essentially determined by how deep into the plasma this condition is met. The collisionless part of the loss cone is comparatively empty. Ions within this region have a statistically non-negligible chance of completing a loss orbit before removal via Coulomb scattering. Here, ions were either just recently driven into the loss region or did so upstream, with a non-negligible fraction destined for the divertor. These orbits support the prompt losses, with a rate driven by resupply into the region.

In demarcating a local velocity-space loss cone, there are several details that are necessary to consider: the rates of the local collisional processes, the sheer size of the loss cone

projection (particularly the angular width), and the loss orbital periods. Each of these details will be considered in the following sections. Pitch angle scattering of ensembles of ions flowing through a Maxwellian background of their own species is considered for scattering out of the loss cone, and will also be considered for the collisional resupply of the collisionless loss cone in Chapter 5. Analytic results for guiding center orbital frequencies in a circular geometry serve as the starting point in determining the loss timescale. Two corrections to these periods will be discussed to adapt them to orbit loss calculations in experimental diverted tokamak equilibria. The magnitude of the ion orbit loss is in direct relation to these considerations, so care must be taken in demarcating the collisional-collisionless boundary.

4.1 Collisionality rates

Consider the collisional velocity-space relaxation of an ensemble of test ions of species α streaming with some velocity $\boldsymbol{v}_\alpha$ through a background Maxwellian of ion species β of the form

$$f_\beta(v) = n_\beta \left(\frac{m_\beta}{2\pi T_\beta}\right)^{3/2} e^{-m_\beta v^2/2T_\beta}, \tag{4.1}$$

a well-known result of the Fokker-Planck theory.[8,51,109,122,123] Here, large angle scattering by Coulomb collisions is treated as the sum of many small angle deflections due to the long-range interactions between charged particles within a Debye sphere. For thermal ions, the self-collisions between the main ions drive their relaxation in the presence of only trace impurities.[122,123] Therefore, $\alpha = \beta$ and the subscripts are dropped altogether. Such motions are typically regarded as the diffusive, momentum exchange (slowing-down), and energy exchange processes, respectively defined by

$$\frac{d}{dt}(\boldsymbol{v} - \bar{\boldsymbol{v}})^2_\perp = \nu_\perp v^2, \tag{4.2}$$

$$\frac{d}{dt}(\boldsymbol{v}-\bar{\boldsymbol{v}})_{\parallel}^{2}=\nu_{\parallel}v^{2}, \tag{4.3}$$

$$\frac{d\boldsymbol{v}}{dt}=-\nu_{s}\boldsymbol{v}, \tag{4.4}$$

$$\frac{dv^{2}}{dt}=-\nu_{\epsilon}v^{2}. \tag{4.5}$$

Eq. (4.2) describes the perpendicular velocity-space diffusion process, while Eq. (4.3) describes the related parallel process, with the $\bar{\boldsymbol{v}}_0$ terms representing the average velocity of the ensemble as it spreads out across velocity-space. For an ensemble of test particles initially localized in velocity-space, a competition develops between velocity-space diffusion, which seeks to achieve the thermal spread of the background, and the dynamical friction, which drives the average ensemble velocity to that of the background, driving equilibration.[51,123] Note that here the '$_\perp$' and '$\parallel$' directions are defined with respect to the initial velocity vector of the ensemble, not with respect to any magnetic field vector.

The collisionality rates are given by

$$\nu_{\perp}=2\nu_{0}\left(1+\frac{\gamma'(3/2,x)}{\gamma(3/2,x)}-\frac{1}{2x}\right)\gamma(3/2,x), \tag{4.6}$$

$$\nu_{\parallel}=\nu_{0}\frac{\gamma(3/2,x)}{x}, \tag{4.7}$$

$$\nu_{s}=2\nu_{0}\gamma(3/2,x), \tag{4.8}$$

$$\nu_{\epsilon}=2\nu_{0}\left(\gamma(3/2,x)-\gamma'(3/2,x)\right), \tag{4.9}$$

$$\nu_{0}=\frac{4\pi Z^{4}e^{4}\lambda n}{m^{2}v^{3}}, \tag{4.10}$$

where

$$x=\frac{mv^{2}}{2T}, \tag{4.11}$$

and

$$\gamma(3/2,x)=\frac{2}{\sqrt{\pi}}\int_{0}^{x}t^{1/2}e^{-t}dt. \tag{4.12}$$

Here, λ is the Coulomb logarithm evaluated for ion-ion collisions and all quantities are in CGS units. The primed quantities correspond to single derivatives in x. The processes are not independent from each other, and the rates are connected through the following relationship for the thermal ions

$$\nu_\epsilon = 2\nu_s - \nu_\perp - \nu_\parallel. \tag{4.13}$$

As expected, a net loss of energy translates to a loss of momentum. The interplay between the diffusive processes and the others are clear but more subtle. For instance, the completely perpendicularly diffused ensembles illustrated in Fig. 4.1 no longer have any net momentum due to the spherical symmetry of the delocalized ensemble; as the ensemble spread over the sphere, the total momentum decreased as the components held by each ion start to cancel those held by the others. One only need consider any three of the processes listed in Eqs. (4.2)–(4.5) to understand the relaxation.

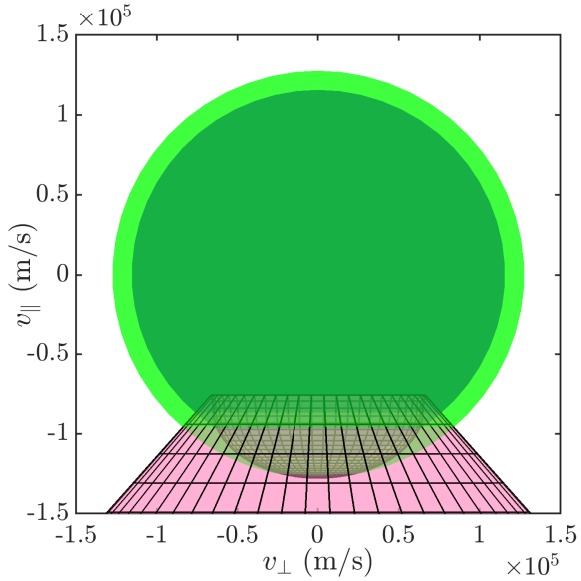

Figure 4.1: An illustration of a three dimensional loss cone (in pink) and two spheres representing the perpendicular velocity-space diffusion of two ensembles after a long period of time, $t \gg 1/\nu_0$. The inner sphere has two lines of intersection with the loss cone while the outer sphere is at the minimum energy to only sustain one.

Ions within the loss cone are statistically treated as ensembles, whose velocity-space motions are estimated by considering pitch angle scattering over a constant energy with rates determined by the local Maxwellian distribution. The momentum exchange is implied via Eq. (4.13) by considering the diffusive and energy exchange processes. As can be seen in Fig. 4.2, the parallel diffusion process occurs on a longer timescale than the other processes across nearly the entire energy spectrum and can be ordered out as a first approximation. The dominant process is the perpendicular diffusion, often described as pitch angle scattering in the presence of a strong magnetic field. The fast gyro-motion of the ion about the magnetic field quickly smooths out the distribution function over the now ignorable gyro-angle, and the diffusion only meaningfully occurs over the pitch angle. In any case, the perpendicular diffusion has a tendency not to alter the average energy of the ensemble as it acts symmetrically about the initial $\boldsymbol{v}_0$ vector, allowing for the process to be effectively decoupled from the energy exchange. As seen in Fig. 4.2, $\nu_\perp > |\nu_\epsilon|$ over the approximate range $0.25 < x < 3.45$. Within this range, corresponding to a majority of the relevant ions for the prompt orbit loss, see Section 4.4, the perpendicular diffusion occurs on a faster timescale than the average energy changes, and one can comfortably assume that the RHS of Eq. (4.2) does not exhibit a strong temporal dependence over the pitch angle scattering. Beyond this range, the two processes occur on essentially the same timescale. For the lower energies, the plasma is typically too collisional for any ions to be lost before scattering out of the loss cone. At the energetic tail of the Maxwellian, one must ensure that the energy loss does not remove orbits from the loss cone. The sharp decrease of a projected loss cone's energetic minimum on approach to the separatrix paired with the inherent $E^{-3/2}$ dependence of the ion-ion collisions and the decaying distribution function reduces the import of such considerations. Thus, the likelihood of some fraction of an ensemble to scatter out of the loss cone is determined by the one-dimensional pitch angle scattering diffusion process within a projected loss cone taken over a constant energy.

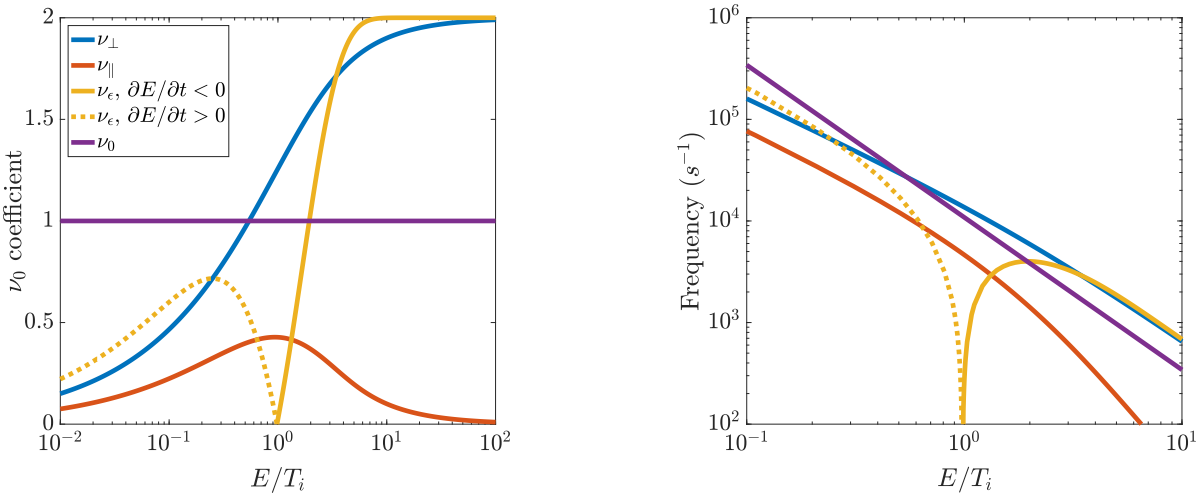

(a) (b)

Figure 4.2: Typical behaviors for the collisional relaxation rates for the diffusive and energy exchange relaxation processes. A dashed line indicates a negative frequency. Subplot (a) illustrates the general behaviors of the ν_0 coefficients. Subplot (b) shows physical values under typical L-mode edge conditions: $n_e = 10^{19}$ m^{-3} and $T_i = 100$ eV.

4.2 Scattering out of the loss cone

As discussed, the primary collisional process responsible for removing ions from the loss cone is pitch angle scattering.[33] Ideally, a comparison would be made between an exactly known loss time, T_{loss}, and a similarly known rate of scattering out of the loss cone, ν_{scatter}. Since the Coulomb collisions occur via proximate neighbors within a Debye sphere, the scattering rate is determined by the local Maxwellian. This rate is given by $\nu_{\Delta\theta}$, the rate of diffusion in pitch by the local loss cone width $\Delta\theta$, measured from the approximate location of null diffusive flux determined by symmetry. It will be shown in Section 4.2.1 that the angular width of the local loss cones housing a particle over its loss orbit typically grows, so $\Delta\theta$ is taken to be the average angular width over the trajectory. Here, an expression for $\nu_{\perp\Delta\theta}$ will be determined.

Continuing from Eq. (4.2) under the assumption that the diffusion approximately oper-

ates under a constant v and T_i,

$$\frac{du_\perp^2}{dt} = \nu_\perp v^2 \tag{4.14}$$
$$\sigma \approx \frac{u_\perp}{v} = \sqrt{\nu_\perp t},$$

where $\boldsymbol{u} = \boldsymbol{v} - \bar{\boldsymbol{v}}$ and σ describes the velocity-space angular width of a one-dimensional Gaussian distribution diffusing in the pitch angle.[123] It can be seen that the time required to diffuse some angle is quadratic in the angle, and small angles are therefore diffused disproportionately faster compared to large angles.[33,34,123] For this reason, the angular width of the projected loss cone plays a vital role in determining the collisional cutoff for the prompt orbit losses.

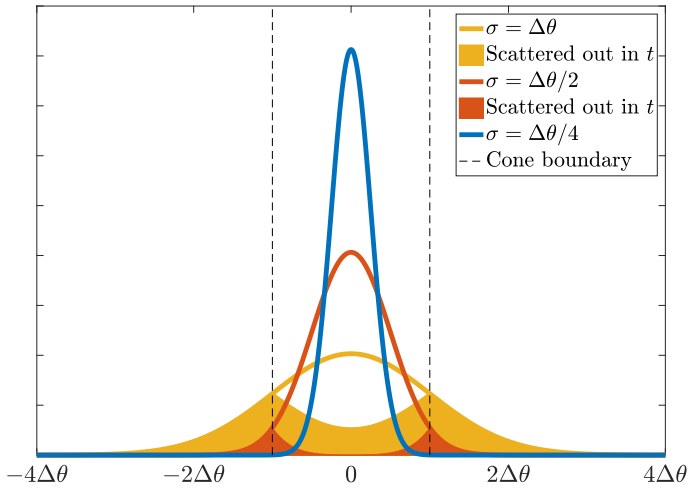

Figure 4.3: The distribution of an ensemble of particles pitch angle scattering within the velocity-space loss cone. The shaded portions approximate the fraction that has scattered out of the loss cone at least once during the diffusion.

For some angular width local loss cone, $\Delta\theta$, the fraction of the ensemble within the loss cone as a function of time is given by a well-known result concerning Gaussian distributions:

$$F_{\text{in loss cone}}(t) = \operatorname{erf}\left(\frac{\Delta\theta}{\sqrt{2}\sigma}\right), \tag{4.15}$$

where 'erf' is the well-known error function. Note that for the portions of the local loss cone twice bounded in pitch angle, the finger-like regions corresponding to trapped losses, the diffusive flux is null roughly at the center of the cone, and the width is measured from this location.

However, the concern lies not with the fraction of the ensemble within the cone following the loss timescale but with the fraction of the ensemble that has been within the loss cone throughout the entire diffusive process. It can be easily shown using one-dimensional random walks that the fraction outside the loss cone at some t is roughly proportional to the fraction within the loss cone that was outside the loss cone for some $t' < t = \sigma^2/\nu_\perp$. Therefore, the fraction within the loss cone for all $t' < t$ is nearly identified with

$$F_{\text{in } \forall t' < t}(t) \approx 2\text{erf}\left(\frac{\Delta\theta}{\sqrt{2}\sigma}\right) - 1, \tag{4.16}$$

where Eq. (4.16) is taken as zero when negative, being interpreted as a negligible portion of the ensemble remaining within the cone over the entire diffusion. Eq. (4.16) is referred to as the unscattered fraction. Figure 4.3 illustrates the evolution of the Gaussian distribution as the pitch angle scattering progresses. The shaded regions represent the fraction of the ensemble that was scattered out of the loss cone at least once and the unshaded region represents the unscattered fraction. When the spread of the Gaussian is of the same order as $\Delta\theta$, Eq. (4.16) describes a minority of the ensemble.

Figure 4.4 plots both Eqs. (4.15) and (4.16) as a function of the Gaussian width to local loss cone width ratio, essentially as a function of time. For widths smaller than the characteristic $\Delta\theta$, nearly all of the ensemble is within the cone throughout the process. Following this period, the unscattered fraction decays far more quickly than the total fraction of the ensemble within the loss cone, becoming negligible around $\sigma \sim 1.5\Delta\theta$. Also plotted are the results of one-dimensional random walks where the unscattered fraction was tracked. It can be seen that the analytic estimate gives a near perfect match over much of the process

and slightly underpredicts the fraction over longer timescales. The work continues using the analytic function in an attempt to more conservatively estimate the losses, providing an approximate hard boundary to a statistical estimate.

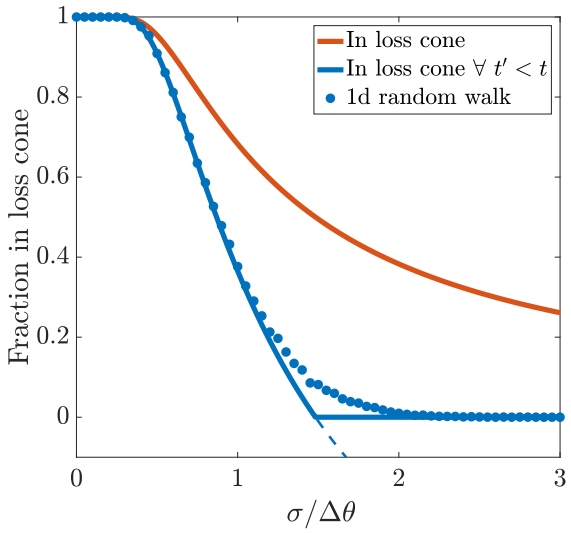

Figure 4.4: The fraction of an ensemble of ions that are not scattered out of the loss cone over the diffusive process. The dots correspond to 1d random walk simulations and the orange line to the fraction of the ensemble instantaneously within the loss cone.

The non-linear relationship between the time required to diffuse some angle and the angle itself makes the angular width of the loss cone an interesting parameter for the ion orbit loss. Before continuing, it would be prudent to familiarize oneself with the typical angular widths of different local velocity-space loss cone structures mapped to various observation points in configuration-space.

4.2.1 The angular width of the velocity-space loss cone: $\Delta\theta$

The angular width of a local loss cone exhibits a strong poloidal sensitivity. For all mapped loss cones, the lowest energy reaches corresponding to trapped losses are also the most narrow. At some increased energy, passing losses are possible, greatly increasing the angular width of the loss region, with the passing losses being favored for orbits locally at either

midplane. Conversely, the loss cones mapped directly above the X-point only experience substantial $\Delta\theta$ growth over energetic changes inaccessible to the thermal population.

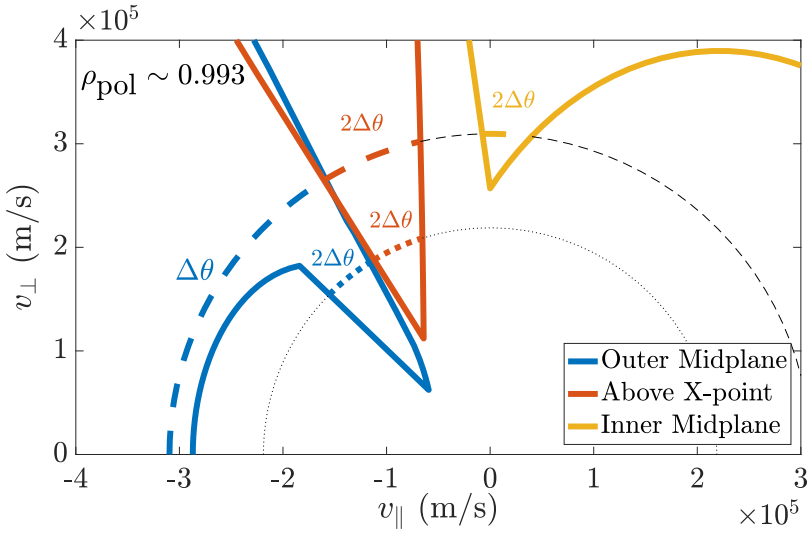

Figure 4.5: The angular width of the projected velocity-space loss cone exhibits poloidal and energetic dependencies and is measured from the approximate location of null diffusive flux. The lines of constant energy serve as a visual aid.

Fig. 4.5 shows the apparent $\Delta\theta$ growth for the local loss cone mapped to the standard three positions along a flux surface. The angular width is measured from the cone boundary to the approximate location where the diffusive flux is zero by symmetry. For the narrower regions of a local loss cone twice bounded in pitch angle for a given energy, this is estimated to be in the center of the region, whereas the angular width is measured from the symmetry axis for regions that are singly bound in the pitch angle. For the local loss cone at the outer midplane, the jump in $\Delta\theta$ when the passing losses are energetically accessible is more severe than the gradual growth characteristic of the velocity-space loss cone at the inner midplane, highlighting the similarity in the trapped and passing orbital losses that pass through the high field side. It should be noted that the maximum angular width of a loss cone mapped to the inner midplane is typically the largest for energies achievable by the thermal population.

As discussed in Section 3.5, the local loss cone shape is relatively insensitive to its radial location of projection, whereby all points along the projected loss cones experience the same

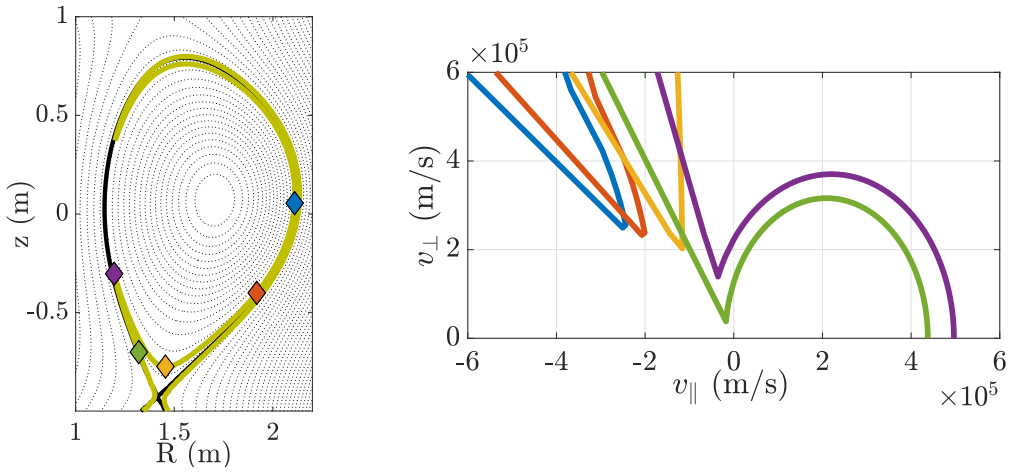

(a)

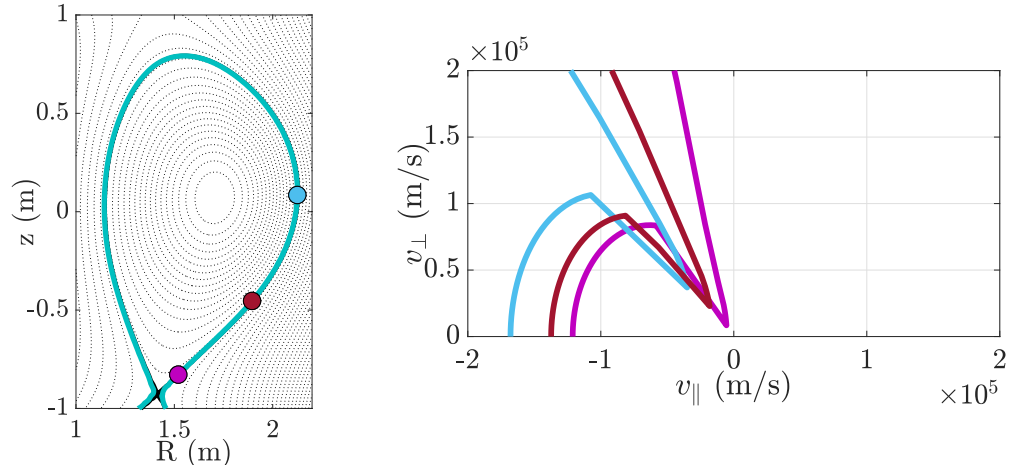

(b)

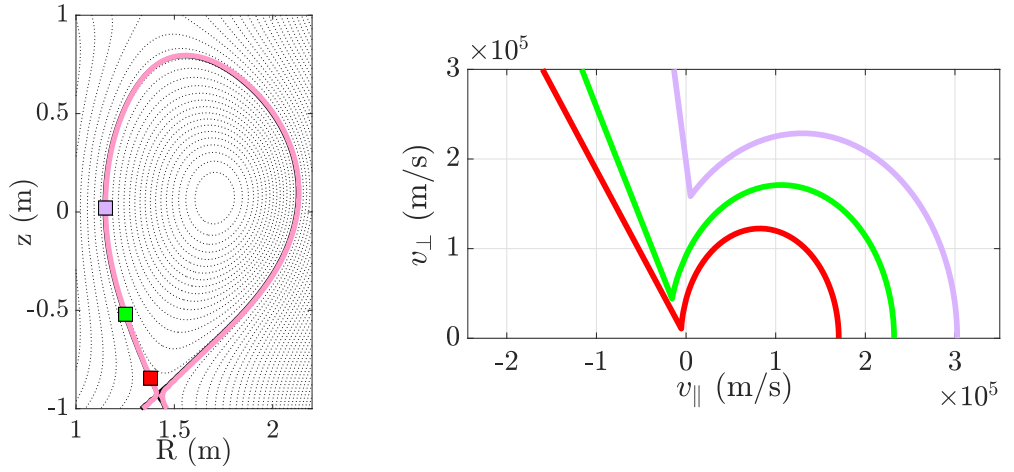

(c)

Figure 4.6: Approximate mapping of the velocity-space loss cone over three sample loss orbits: (a) a trapped orbit, (b) a passing-like orbit from the outer midplane, and (c) a passing orbit from the inner midplane. Marker colors align with the loss cone colors.

generic radial $(\Delta\psi)^2$ scaling. The exception to this rule can be seen in Fig. 3.6 due to the effect of the electric potential, enforcing a new energetic minimum for a given radial position. Up to the threshold for electrostatic trapping, these regions of increased $\Delta\theta$ are sustained at lowering energies with increasing radial position in the same fashion.

Although the projected loss cone seems to narrow upon poloidal approach of the X-point, this is only true when restricted to a given flux surface. The ions are candidates for loss explicitly because they are able to appreciably drift off of their initial flux surfaces. Typically, a prompt loss orbit does not approach the X-point from directly above but rather at an angle from either the low or high field side; on the last leg of these journeys the orbital path does not pass through the region characterized as being above the X-point.

Figure 4.6 characterizes the typical mapping of the velocity-space lone cone about an ion over a loss trajectory. As each ion completes its orbit, the local loss cone it occupies generally grow in angular width. When determining if an ensemble is likely to scatter out of the loss cone, the angular width is taken as the average over the loss orbit. This is possible since orbits of the same energy within a local loss cone are typically either mostly trapped or passing-like in nature and exhibit similar characteristics. For ions above the local minimum loss energy for their given pitch direction, the minimum energy of the projected loss cones they inhabit later in their orbit will decrease, as shown in Figure 4.6. Ions with the minimum energy for their given pitch angle typically have orbits that intersect the X-point while orbits above this energy will intersect the X-point plane at a poloidal flux value determined by their energy relative to the minimum and the remaining local change in poloidal flux to the separatrix, roughly following the $E \sim (\Delta\psi)^2$ scaling.

4.3 Loss orbit period

Eq. (4.16) approximates the fraction of an ensemble of ions initially localized within the loss cone that remains within the loss cone in variable time t. Evaluating this function at the

characteristic time for the orbits to be lost leads to the fraction of the ensemble that will be lost before scattering out of the loss cone. It is of course possible that an ion that scatters out will rescatter into the loss region and should be counted as a loss at the local position in configuration-space where this occurs. To that end, it is necessary to determine the time periods associated with ion orbit loss.

Analytic formulae are readily available for the orbital frequencies in ciruclar flux geometries.[124,125] In the following, modifications to these periods are discussed, which make them appropriate for application to ion orbit loss in experimental diverted tokamak flux geometry. First, a method for determining the lost orbit period rather than a confined orbit period is presented. Second, a correction is made for the discrepency between the experimental poloidal magnetic field and the one included in the circular model. This section of the thesis introduces the strong dependence of the ion orbit loss on the drift direction and its eventual influence on the radial electric field through significant loss period discrepencies dependent on the drift orientation. We find that the results of our calculations match theoretical expectations[38] as well as orbit following simulations to a high degree.[34,39]

4.3.1 Orbit periods in a circular geometry

In a finite inverse aspect ratio circular tokamak geometry the orbital frequencies for trapped particles,

$$\omega_t \approx \frac{\pi\omega_0}{2K(\kappa)}, \tag{4.17}$$

and for passing particles,

$$\omega_p \approx \frac{\pi\omega_0\kappa}{K(\kappa^{-1})}, \tag{4.18}$$

are known.[124] Here, a small inverse aspect ratio, $\epsilon = r/\bar{R}$, approximation has been made, r is the minor radius, $\bar{R}$ is the major radius at the magnetic axis, κ is a trapping parameter

which describes trapped orbits when below unity and passing while above, K is the complete elliptic integral of the first kind,

$$K(\kappa) = \int_0^{\pi/2} \frac{d\phi}{\sqrt{1 - \kappa^2 \sin^2(\phi)}}, \tag{4.19}$$

ω_0 is the characteristic frequency,

$$\omega_0 \approx \frac{\sqrt{E/m}\sqrt{\epsilon}}{l_0}, \tag{4.20}$$

l_0 is the characteristic length,

$$l_0 \approx \bar{q}\bar{R}, \tag{4.21}$$

$\bar{q}$ is a modification of the true safety factor q,

$$q(r) = \frac{1}{2\pi} \int_0^{2\pi} d\theta \frac{\boldsymbol{B} \cdot \nabla\phi}{\boldsymbol{B} \cdot \nabla\theta} = \frac{\bar{q}(r)}{\sqrt{1 - \epsilon^2}}, \tag{4.22}$$

and θ and ϕ respectively refer to the poloidal and azimuthal angles.

The trapping parameter κ is defined by the following:[124]

$$\frac{\mu}{E}\bar{B}\sqrt{1 + \frac{\epsilon^2}{\bar{q}^2}} = 1 + \epsilon - 2\epsilon\kappa^2, \tag{4.23}$$

with bounds

$$0 \leq \kappa_t \leq 1 \leq \kappa_p \leq \frac{1 + \epsilon}{2\epsilon}, \tag{4.24}$$

where the subscript 't' referring to 'trapped' and 'p' to 'passing'. The barely trapped and barely passing orbits have comparatively long periods compared to those further from the trapped-passing boundary as these orbits have vanishing parallel velocities at the high field

side. Additionally, the barely trapped orbits traverse larger poloidal angles than the deeply trapped ions localized to the LFS.

The calculations for the above periods do not take into account the effects of the radial electric field. Primarily, this means that κ does not take into account the shift in the trapped-passing boundary earlier discussed. Secondarily, the $E \times B$ rotation is omitted, which averages to zero for trapped orbits considered tied to a flux surface and imbalances the orbital periods of the co- and counter-passing orbits. It is noted that the $E \times B$ rotation can play an interesting role for orbits that cross the separatrix, where the direction of the flow is typically poloidally reversed, although such an effect is beyond the scope of this thesis.

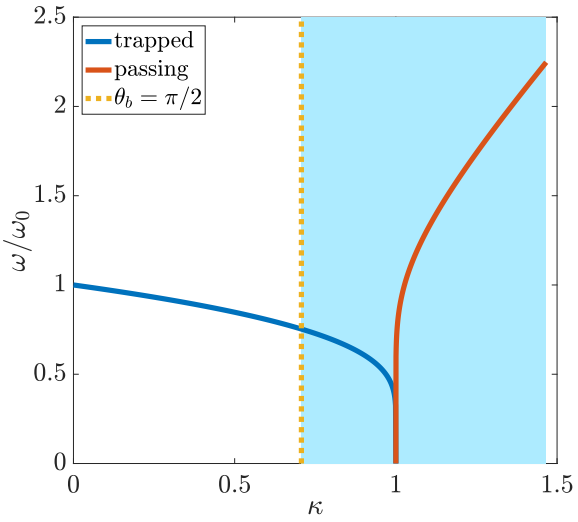

Figure 4.7: Normalized orbital frequencies for trapped and passing orbits in a circular geometry as a function of the trapping parameter, κ. Only particles within the blue field are candidates for X-point mediated orbit loss.

We are not interested solely in the periods of lost orbits in general, but in families of lost orbits that span a local loss cone at the same energy; these are roughly the orbits that can be sampled by an ensemble of some initial energy undergoing perpendicular diffusion over a loss orbit. The known properties of the orbits on the local loss cone boundary and the behaviors of those in between allow for the estimation of a statistical loss time for such

families. The primary relevant features of κ on the orbital periods seen in Figure 4.7 are maintained. Trapped orbits within the loss cone are consistently the least trapped, with the cutoff dependent on the X-point position. Approximately only those with $\kappa \geq 0.707$, corresponding to bounce locations at the plasma's top and bottom, are able to reach the X-point. The baseline trapped orbital period for orbits relevant for loss is taken as the average over the range $0.707 \leq \kappa < 1.0$,

$$T_t \approx 0.633 \cdot \frac{2\pi}{\omega_0} \approx 0.633 \cdot \sqrt{\frac{2}{\epsilon}} \frac{2\pi \bar{q} \bar{R}}{\sqrt{2E/m}}. \tag{4.25}$$

For any local loss cone, either the co- or counter-current passing orbits contribute to the ion orbit loss with the entire domain of corresponding pitch angle having an energy threshold corresponding to loss. Since all values of the trapping parameter greater than unity can correspond to orbit losses, and the periods of passing orbits are more sensitive to κ than trapped orbits, the baseline passing orbital period is determined by linearly mapping κ, $\kappa^2 \sim \zeta^2$ in Eq. (4.23), to the angular width in velocity-space corresponding to the passing orbits, such that

$$\tilde{\kappa}_p \approx \frac{1+\epsilon}{2\epsilon} - \frac{1-\epsilon}{2\epsilon} \left(\frac{1-\zeta}{1-\zeta_{\text{tp}}} \right), \tag{4.26}$$

where ζ_{tp} corresponds to the pitch direction of the trapped-passing boundary. The baseline passing period is then taken to be

$$T_p \approx \frac{2K(\tilde{\kappa}_p^{-1})}{\omega_0 \tilde{\kappa}_p}. \tag{4.27}$$

The statistical loss time is defined as the average loss time for orbits spanned by a local loss cone for a given energy, discussed further in Section 4.3.4.[34] The baseline orbital periods need to first be transformed into lost orbit periods and then corrected for an outstanding disparity between a circular and X-point geometry, the poloidal stagnation.

4.3.2 From confined orbit period to lost orbit period

The thermal velocity-space loss cone results from the topologically changed ion orbits in the vicinity of an X-point, a null in the poloidal magnetic field and thus a saddle point in the poloidal flux. Ions with sufficiently large energies sustain orbits that intersect with the first wall at arbitrary location; however, the thermal population of interest typically escapes via the X-point geometry. In a circular geometry defining the orbit periods found in the previous section, orbits that intersect the separatrix near where the X-point would be located in a diverted geometry continue their uninterrupted confined orbits, only the most energetic of which will be lost to the first wall. The confined orbit periods are transformed into loss orbit periods by considering the remaining fraction of the circular orbital path to reach the horizontal plane containing the X-point.

The orbital shapes of both trapped and passing orbits are robust, necessitating little information to estimate an orbit's shape in the poloidal plane. The fraction of the projected orbital path between the initial position and the loss location estimates the ratio of the loss period to the orbital period,

$$T_l = F_l T = \frac{\text{remaining poloidal path}}{\text{total poloidal path}} \cdot T. \tag{4.28}$$

Below, methods for determining F_l are presented. For now, only the favorable ∇B drift direction will be considered, with a lower active X-point. The impact of reversing the drift direction will be discussed in Section 4.3.5.

First, consider the passing losses. In order to estimate a passing loss period, the relevant points along its orbit are its initial location and the X-point, taken to be very near the loss location. The points are projected radially outward to the separatrix of the experimental geometry, introducing little error since the orbits of interest are thermal near-edge orbits and the taken ratios wash out the first order path length differences. For counter-current passing ions, the remaining poloidal orbital distance is taken as the clockwise distance, as seen from

above the poloidal plane, along the separatrix from the initial location to the X-point. For co-current passing ions, the counter-clockwise direction is taken. The remaining fraction is simply the ratio of these distances to the approximate total orbital path of the confined orbit present in the circular geometry, taken as the length of the separatrix enclosing the core region. The loss period is simply

$$T_{lp} = F_{lp} T_p. \tag{4.29}$$

The trapped losses require a different approach. The banana-like paths of the trapped particles are the result of strong variations in the parallel velocity characterized by high field parallel bounce locations. To first order, the angular motion of such orbits is sinusoidal,[124]

$$\theta(t) \approx \theta_b \sin\left(2\pi \frac{t}{T_b}\right), \tag{4.30}$$

with θ_b corresponding to the poloidal bounce angle. Eq. (4.30) implies that the guiding center spends an inordinate period of time near the bounce locations, where the parallel velocity vanishes and the drift motions dictate the particle motions. For a typical trapped orbit in a circular flux geometry, roughly 20% of the orbital period is contained in the final $\sim 5\%$ of the angular domain surrounding the bounce angle.[124]

The remaining portion of a trapped orbit is calculated in a similar way to that of the passing-like lost ions, only with the slow bounces artificially added. Third and fourth locations are necessary to approximate the orbital path, those being the bounce locations. For the classically trapped losses, a bit of mundane bookkeeping is introduced to classify which of three sections of the banana orbit the initial position is on: being segmented by the bounce locations and approximately by the X-point. Co-current ions instantaneously moving away from the X-point experience two parallel bounces before loss, counter-current ions one, and co-current ions moving toward the X-point none. For the passing-like trapped losses, sufficiently high energy counter-current trapped ions on the LFS that are lost on their

initial flux surfaces, no bounce occurs on the loss trajectory.

Again, the points are projected to the separatrix. The total poloidal orbital length for a trapped particle is estimated as twice the distance passing through the low field side from one bounce location to the other. For co-current bounce orbits presently moving away from the X-point, the remaining poloidal path length is taken as the shorter distance along the separatrix from the initial location to the upper bounce location, then the clockwise distance to the lower bounce location, followed finally by the counterclockwise distance to the X-point. The ratio of the projected remaining path to the projected total path is applied to the $\sim 0.8T$ of the orbital path that is well approximated as being spread evenly over the poloidally projected orbit. For the present case, both bounces must occur before the loss, so $0.2T$ must be added. The cases where fewer parallel bounces occur before loss follow in a straightforward manner, omitting the already traveled poloidal distances and the already bounced bounce(s). For initial positions within the last 5% of the angular domain near the bounce locations, the remaining portion of the bounce is linearly estimated as a function of this angle. The trapped loss period takes the following form:

$$T_{lb} = (0.8F_{lb} + 0.1N_b)T_b, \tag{4.31}$$

where N_b corresponds to the, perhaps fractional, number of remaining bounces.

Considering only the remaining poloidal distance of the orbit leads to the logical conclusion that orbits in the vicinity of the X-point will be lost extremely quickly. This is only partially true. Ions near the X-point on loss orbits have generally traversed a greater fraction of their poloidal path, but the stagnation of motion in the poloidal plane due to the vanishingly small poloidal component of the magnetic field near the X-point enhances the time required to complete the final stretch of the loss orbit.

4.3.3 Poloidal field stagnation

The X-point behaves as a saddle point in the scalar function ψ exactly because the poloidal component of the magnetic field vanishes on approach to this location, as illustrated in Fig. 4.8. An orbital path projected onto the poloidal plane advances typically via the poloidal component of the parallel velocity,

$$v_{\parallel,x} = \frac{B_x}{B} v_{\parallel}, \tag{4.32}$$

with the exception being very near the parallel bounce locations for trapped orbits, where the perpendicular drifts dominate. Near the X-point, apparent motion in the poloidal plane is increasingly governed by the slow local ∇B, curvature, and $E \times B$ drifts, regardless of the magnitude of the parallel velocity, poloidally stagnating the motion. The stagnation significantly enhances the parallel orbit length and thus the orbital period.

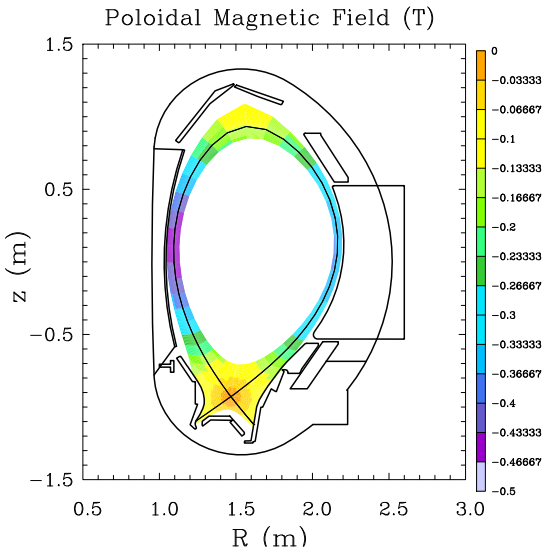

Figure 4.8: The typical structure of the poloidal magnetic field in an X-point geometry, shown in particular for AUG discharge 16151. The vanishingly small poloidal field in the vicinity of the X-point reduces the poloidal projection of the parallel ion velocity.

This effect is not included in the circular geometry orbits calculated with the following

magnetic field:

$$\boldsymbol{B} = \frac{\bar{B}\bar{R}}{R}\left(\hat{\phi} + \frac{\epsilon}{\bar{q}}\hat{\theta}\right), \tag{4.33}$$

where the poloidal field component only exhibits a poloidal variation due to the inverse dependence on R. Neglecting the poloidal stagnation both misrepresents the periods of orbits in an X-point geometry, having significant consequences directly relevant for the ion orbit loss. Orbits with sizable fractions of their poloidal projections near the X-point will be lost more slowly and are thus more likely to scatter out of the loss cone.

Assuming a shared form for the dominant toroidal field component, the poloidal component of the parallel velocity in the X-point geometry is lesser than in the circular geometry by the ratio of the respective poloidal magnetic fields,

$$v_{\parallel,x}^{X} \approx \frac{B_x^X}{B_x^C} v_{\parallel,x}^{C}, \tag{4.34}$$

where the superscripts refer to the circular expectation and the X-point reality in the obvious way. The orbit period in the X-point geometry is estimated by effectively stretching the poloidal distance by the ratio that the poloidal component of the parallel velocity is diminished,

$$\begin{aligned} T_{\mathrm{X}} &= \frac{T}{S}\oint \frac{v_{\parallel,x}^{\mathrm{C}}}{v_{\parallel,x}^{\mathrm{X}}} ds \\ &\approx \frac{T}{S}\oint \frac{B_x^{\mathrm{C}}}{B_x^{\mathrm{X}}} ds. \end{aligned} \tag{4.35}$$

Here, S refers to the orbital path in the poloidal plane. Shifting the effect from the poloidal ion velocity to a static effect on the configuration-space allows for the stagnation to be estimated as soon as the orbit's path is approximately known, a process outlined for the loss orbits in Section 4.3.2. In the context of a discretized spatial grid, like that used in SOLPS, the poloidal dimensions of the computational cells are stretched based on the average field

values over the cell. The drift motions are ever present, and a maximum threshold for the effective stretching can be implemented to ensure that stagnation only occurs up to the drift motions.

It is noted that projecting the orbital paths to the flux surface corresponding to the separatrix overestimates the stagnation because the poloidal field exactly vanishes at the X-point. For this reason, the orbital shapes are projected on the mean flux surface between the point of origin and the separatrix surface, and the lost orbit period calculated in the previous section is scaled by the ratio of the stretched remaining path to the physical remaining path,

$$T_{\mathrm{lX}} = \frac{T_l}{S_l} \oint \frac{B_x^{\mathrm{C}}}{B_x^{\mathrm{X}}} ds, \tag{4.36}$$

where S_l is the remaining poloidal path projection determined using the methods of the previous section, and the field quantities are evaluated along this path. A sensitivity is lost here, in that higher energy loss orbits cross the X-point plane further from the X-point itself. The structure of the poloidal magnetic field seen in Figure 4.8 indicates that the stagnation effect decays with distance from the X-point. Orbits above the threshold loss energies should feel the stagnation effect to a lesser degree.

4.3.4 Statistical loss times

Let us take a moment to regain the big picture here. For any location in configuration-space, we are able to generate a boundary in velocity-space that separates the confined orbits from those that will reach the divertor as a result of the X-point's influence on the orbit topology. Orbit loss is driven by the net transport and sourcing into the loss cone within the confined region of the tokamak. Flux into the loss cone contributes to the orbit loss only if it is not removed from the loss cone before it is lost from the plasma. Section 4.2 establishes the rate of scattering out of any local loss cone and finds that it is essentially

a monotonically decreasing function of the ion energy for a given plasma background: the rate of pitch angle scattering reduces with energy while the width of the velocity-space cone tends to grow, both acting to reduce the rate of removal from the loss cone. Methods for approximating the periods of loss for ions in an X-point geometry have also been discussed in Sections 4.3.1–4.3.3. To facilitate comparison with the rates of scattering out of the loss cone, statistical loss times, τ_l, are calculated for loss cone projections mapped to various locations in configuration-space. These loss times are taken as the average loss period across a local loss cone for a given energy,

$$\tau_l(\rho, \theta, E) = \frac{1}{\Delta\zeta} \int T_{lX}(\rho, \theta, E, \zeta) d\zeta. \tag{4.37}$$

Throughout this section, we again take the ∇B drift to point down, toward the active X-point.

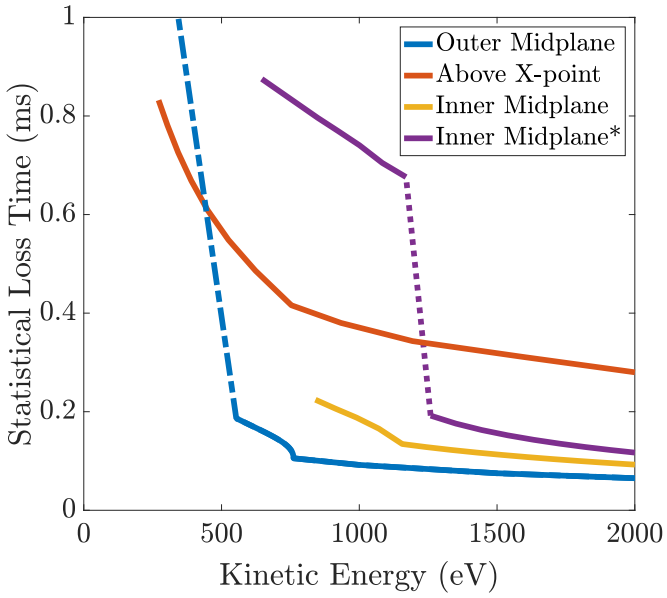

Figure 4.9: Statistical periods of orbit loss from local observation points as a function of the ion energy.

Figure 4.9.a shows the statistical loss times under favorable drift conditions for lost orbits contained within the local loss cones structures as a function of the kinetic energy for the

usual observation points along the $\rho = 0.993$ flux surface: at the outer midplane, above the X-point, and at the inner midplane. For comparison to Ku *et al*,[34] the chosen flux surface passes above the X-point at a distance of about ten centimeters. As expected, for each location, the loss time decreases for increasingly energetic particles. Beyond this, the trends are perhaps less than obvious and will be thoroughly discussed.

First consider the blue line corresponding to the local loss cone for ions passing through the given flux surface at the outer midplane, see Figure 3.2 for reference. The lower energy finger-like portion of the local loss cone, $E < 500$ eV in Fig. 4.9.a, corresponds to trapped orbits. The segment of this portion's boundary that can be identified with the trapped-passing boundary describes orbits that bounce at the inner midplane. These orbits typically experience a greater poloidal stagnation as they have greater portions of their orbit in the vicinity of the X-point. The opposite side of this boundary corresponds to orbits that bounce near the angular position of the X-point. The loss orbits of the finger region generally have comparatively long loss times due to their low energies, moderately long paths to the divertor, enhanced poloidal stagnation, and the fact that the baseline trapped orbital periods are long. This combined with the narrow angular width of the finger region often results in highly collisional loss trajectories.

The loss orbit periods for higher energy portions of the local loss cone describing orbits at the outer midplane are substantially smaller. As discussed in Chapter 3, a parallel bounce is the mediated transfer from one constraint surface to the other by the equilibrium poloidal flux surface. In the trapped portion of this velocity-space loss cone, there is a threshold energy such that the orbit reaches the loss condition on its initial constraint surface before undergoing the parallel bounce. The threshold can be seen by a continuation of the curve corresponding to the passing losses into the trapped region of the cone.[33,34] Thus, the loss orbits for the higher energy ions found at the LFS are passing-like in nature across the entire angular width of the local loss cone. Such orbits exhibit the shortest loss periods since they have higher energies, short paths to the divertor, a reduced poloidal stagnation, and do not

suffer any parallel bounces before loss.

Next, consider the local loss cone for orbits passing just above the X-point, drawn in orange in Figure 4.9. For all energies thermally accessible, the lost orbits are trapped, and thus there is no reasonable threshold for which the trapped orbits can escape on the initial constraint surface. Consequently, the statistical loss times have a smoother energy dependence. The lowest energies here correspond to faster losses than loss orbits at the outer midplane since they have already undergone some portion of their poloidal stagnation, have shorter remaining paths to the divertor, and simply are more energetic. The structure of this loss region is relatively static as the energy increases; the width only grows slightly with the energy. As expected, the behavior in the statistical loss period goes nearly like $E^{-\frac{1}{2}}$ when the shape of a local loss cone minimally changes with the energy, requiring substantial growth in ion energy for appreciably faster losses.

Finally, consider the local loss cone for orbits at the inner midplane. Per usual, the loss orbits with the lowest energies are the trapped orbits. In Fig. 4.9 two lines are plotted which correspond to this location: in purple just below the midplane and in yellow just above. Bounce locations at the former close downward while those at the latter close upward. Trapped orbits near their lower bounce locations have far shorter paths to the divertor, and have similar loss times to the passing orbits, having already completed most of the trapped trajectory. The higher energy portions of the inner midplane projected loss cone contain trapped orbits that have yet to bounce, trapped orbits that have already bounced, and co-passing orbits. The proportions described by these three classes changes with the energy until the angular width reaches its maximum value. The trapped orbits here are unable to be lost on their initial constraint surface, omitting the narrow range of low energy orbits dominated by the $E \times B$ drift, so there is no effective change in the loss behavior for the trapped portion as a function of the energy, like the passing-like losses originating from the LFS. Thus, the average loss period is slightly higher for the upper energies of the high field side losses compared to the low field side. The passing losses for the position just above the

inner midplane occur on practically the same time scale as those slightly below; however, the average of the high energy portion of this cone is greater due to the far longer trapped loss periods.

4.3.5 The up-down ∇B drift direction asymmetry

The expected strong asymmetry of the ion orbit loss with the ∇B drift direction was briefly mentioned as motivation in Chapter 1 and will be discussed here in more detail. Although the loss trajectories remain identical under both drift directions, there are significant path length differences to the divertor for the loss orbits.[34,38,39,45] For the favorable configuration, with the ∇B drift pointing toward the active X-point, the orbits cross the separatrix in the proximity of the X-point, already near the divertor. In the unfavorable configuration, the orbits leave the separatrix at the vertically opposite side of the active X-point, necessarily traversing the SOL on their paths to the divertor. Many of the ion trajectories in the near SOL are closed and the likelihood that the ions in the latter case scatter out of the loss cone while in the scrape off layer must be considered. This difference manifests in the model as an on-average increase of the τ_l in the unfavorable drift configuration, which can be considered as an increase in the effective collisionality.[39] Without loss of generality, the favorable configuration is taken as the case where the ∇B drift points downward.

As noted in the literature,[38,39,45] for orbits originating at the outer midplane, there is a typical increase in the projected poloidal loss orbit distance by a factor between 5/3 and 3 for trapped orbits and 3 for passing orbits, when comparing loss orbits in the unfavorable drift configuration to those in the favorable configuration. For orbits originating elsewhere, these factors can be even larger, as can be easily seen from analysis of poloidal projections of orbits. One should not expect a one-to-one correspondence between the remaining poloidal orbital distance and the orbital period; the poloidal velocity is non-constant over the orbit. As discussed in Section 4.3.3, the poloidal stagnation due to the vanishingly small poloidal field near the X-point exacerbates the inherent asymmetry of the poloidal velocity over an

ion's orbit. The stagnation effect is typically greater in the favorable drift case where the lost ions are brought nearer the X-point on average, a feature present in orbit following simulations in the literature.[34] The up-down drift asymmetry of the statistical loss periods is determined by a competition between the increased poloidal paths for loss orbits in the unfavorable drift and the increased poloidal orbit stagnation for losses in the favorable drift.

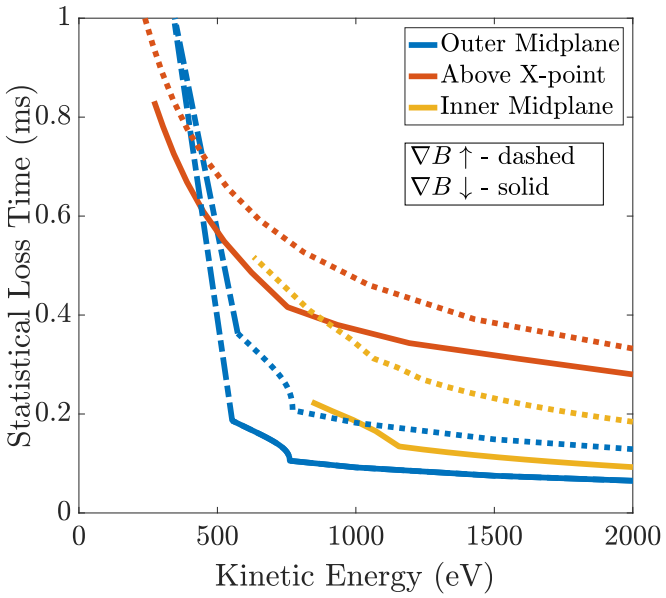

Figure 4.10: The drift orientation asymmetry of the periods of orbit loss for vertically opposing observation points.

Figure 4.10 compares the average loss times for the velocity-space loss cones mapped to the three usual locations in configuration-space and their vertically opposite positions under reversal of the ∇B drift direction, corresponding to losses from the same flux surface as in Fig. 4.9. Since the ions cross the separatrix at vertically opposite positions in the different configurations, it is more telling to compare the statistical loss times at these vertically mirrored positions for opposing ∇B drift directions.[34] Although the inner midplane does not have a vertically opposite position, this location is studied at some ϵ above and below, capturing the effects of the orbits closing respectively upward and downward, similarly to

Figure 4.9.

For the outer midplane, in the region of the local loss cone corresponding to passing-like losses, these orbits with minimal up-down poloidal stagnation asymmetry experience a rough doubling of the loss periods in the unfavorable drift.[39] These orbits reach the X-point plane on the same side as their initial approach, only significantly stagnating in the final stretches of their trajectories. A similar orbit stagnation is felt in the unfavorable configuration, in the sense that the trajectories only pass nearby the X-point once. Therefore, the asymmetry is dominated by the disparity in the poloidal path-length. For the passing-like trapped losses, the difference in the poloidal distance is even greater, between a factor of 3 and 5, since the particle still reaches the bounce location in the unfavorable drift. Since the increases in the poloidal distance do not affect the disproportionate time spent in the stagnated final leg, the overall increase is somewhat less than the ratio of the poloidal distances. The drift asymmetry for the passing losses is similar for the two midplanes.

The up-down drift asymmetry is more nuanced for the trapped losses that necessarily bounce on the HFS before being lost. Such thermal ions originating at the outer midplane, as discussed in the previous section, pass near the X-point twice in the favorable drift: on their initial constraint surface moving toward the HFS and again on the loss constraint surface. Similar ions in the opposite orientation only feel the X-point stagnation near the ends of their trajectories, like a passing-like loss. The stagnation up-down drift asymmetry roughly cancels the poloidal path up-down asymmetry, and the statistical loss periods are similar.[34] This rough balance is not exactly maintained for different poloidal positions. Although an interesting feature, this has little influence on the steady-state orbit losses in the presented model, since the long statistical loss times coupled with the narrowness of these regions of the local loss cones results in highly collisional trajectories in both cases.

The orange lines in Figure 4.10 compare the statistical loss times for the local loss cones above the X-point in the favorable configuration and at the top of the plasma in the unfavorable configuration. In the former case, the ions have already progressed through some portion

of their initial stagnation, reducing its ability to compensate for the increased length of the poloidal trajectories in the unfavorable drift. Here, the discrepancy is moderate, and the unfavorable configuration typically corresponds to losses that are longer by about a factor of 1.25. The stagnation asymmetry is further mitigated for ions on the HFS, and the statistical trapped loss periods at the inner midplane experience a similar up-down drift asymmetry to the passing-like losses. For vertically opposite positions in both drift configurations, the losses are only stagnated on final approach to the X-point, and the asymmetry is dominated by the poloidal path length difference.

The analytic formuale for the circular orbit periods and the subsequent approximations transforming them into loss orbit periods in a diverted experimental geometry with sensitivity to the ∇B direction well reproduce the orbital loss times, in both magnitude and behavior, seen in orbit following simulations presented in the literature for similar geometries.[34,39] The narrow regions of any velocity-space loss cone have typically longer average loss times while the angularly wide regions correspond to faster losses, instigating a nonlinear dependence of the unscattered fraction, Eq. (4.16), on the ion energy.

4.4 The demarcated loss cone

The unscattered fraction, Eq. (4.16), can now be evaluated along the boundary of a local loss cone at the rate of pitch angle scattering, loss cone angular width, and statistical loss period determined as functions of the ion energy for the given velocity-space loss cone. This function monotonically increases with the ion energy, describing ions that are less collisional, lost faster, and are more likely to collide onto other loss trajectories, exactly related to the monotonic increase of the angular width coupled with the monotonic decrease in both the scattering rate and the loss period with the ion energy. There is typically a large jump in the unscattered fraction at energies where the passing losses are made possible.

Portions of a local loss cone where the unscattered fraction is zero over the statistical

loss period are considered 'collisional'. Ions scatter into and out of the region at a sufficient rate that over a period of time longer than individual collisions, there is a roughly constant number of particles in these regions,

$$n(\rho_0, \theta_0)_{\text{collisional}} \approx \int_{\Sigma_{\text{coll}}} f d^3v, \tag{4.38}$$

each contributing to some small segment of a lost orbit before scattering out again.[33] Eq. (4.38) is only valid over the location in configuration-space accurately described by the loss cone projection. Note that 'collisional' here is in a sense an effective collisionality since the measure is of the rate of scattering out of the loss cone compared to the rate of loss. Two loss regions with the same true particle collisionality can return different unscattered fractions dependent on the rate of loss and the local loss cone angular width.

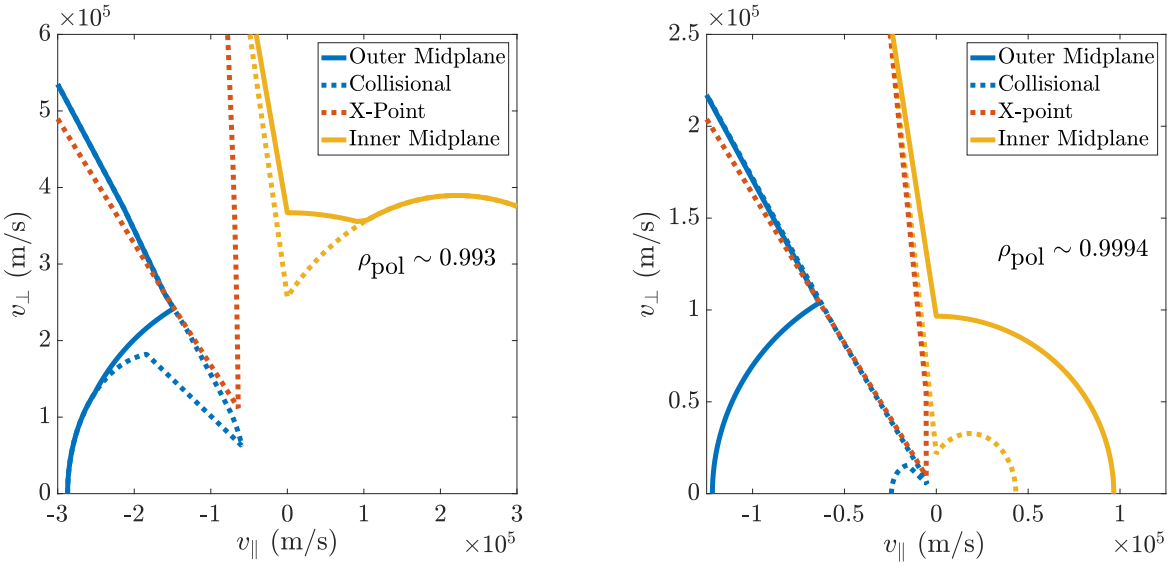

Figure 4.11: The collisionless (solid) and collisional (dashed) local loss cones for two different radial positions. The collisionless energy scale is set by the passing losses in the former and the collisionality in the latter. Here, $E_r = 0$ for simplicity.

The remainder of the loss cone, where the unscattered fraction is greater than zero, contributes to the prompt losses of ions fed into the loss regions and is considered 'collisionless'.

Upstream, ions supply the loss cone and the fraction determined by Eq. (4.16) are lost on a first orbit. By continuity, in the steady-state the rate of resupply is equal to the rate of the loss; the refueling mechanisms drive the rate of loss, only requiring modification by the fraction expected to survive the transit.

Demarcating the loss cone along the collisional-collisionless cutoff introduces two radial regions with differing energy scaling for the projected collisionless loss cone, similar to the effect of the electric potential seen in Chapter 3. Figure 4.11 illustrates the typical collisional-collisionless cutoffs characteristic of these two regions: one more core-like and the other roughly occupying the so-called viscous layer, approximately within a centimeter of the separatrix measured at the outer midplane. In the former, the energy scale of the local collisionless loss cone is typically that of the passing losses. The narrow regions of a loss cone comprising the slow trapped losses do not typically satisfy the presented collisionless condition. Nearing the separatrix, the general $\sim (\Delta\psi)^2$ decrease in the threshold energies for the passing losses eventually reaches energies where the pitch angle scattering is too great for the lengthening loss periods, and the large $\Delta\theta$ regions of the velocity-space loss cones cannot support prompt losses at their lowest energies. Here, the threshold energy is primarily set by the collisionality of the plasma and $\Delta\theta$. It can be seen that the inner midplane supports lower energy losses very near the separatrix, resulting from the larger angular width of the local loss cone.

Figure 4.12 compares the radial dependence for the minimum energy of the collisional and collisionless velocity-space loss cones mapped to the inner and outer midplanes. The threshold energies of the collisional local loss cones correspond to those of the undemarcated projected loss cone, and the energy scale is still determined by the lower energy trapped losses. It can be easily seen that the collisionless energy scale is set by the passing losses and more directly by the collisionality very near the separatrix. The energetic minima of the collisionless velocity-space loss cones are typically above the threshold for electrostatic trapping for the L-mode like radial electric field profiles and are only sensitive to the shift in

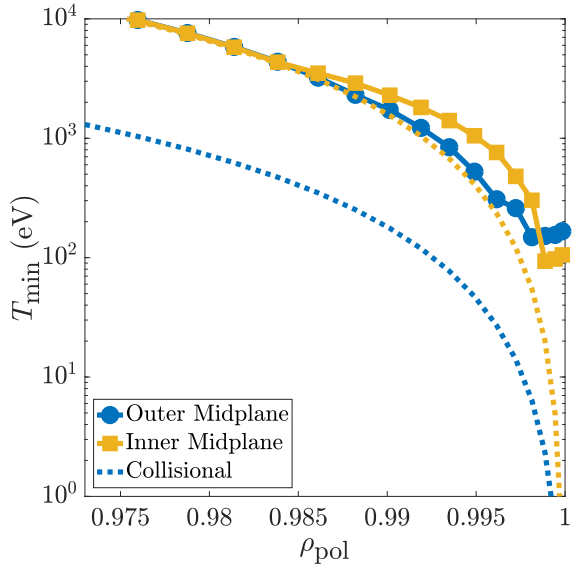

Figure 4.12: The radial energy scale for minimum energy loss for the collisionless and collisional portions of the loss cone about the outer and inner midplanes with a constant electric potential.

the trapped-passing boundary, as can be seen in Fig. 3.6. For more substantial E_r-wells, like those found in the H-mode, the local collisionless loss cones can begin to feel the influence of the electrostatic trapping, and as discussed in Chapter 2, for large E_r magnitudes such that the poloidal Mach number for the $E \times B$ rotation, $V_{E\times B}/(v_{\|}B_x/B)$, is greater than one at the outer midplane, the $E \times B$ drift can trap otherwise lost ions and dominate the low field side energy scales.[34,47]

4.5 The equilibrium Maxwellian overlap and intrinsic rotation collisionality corrections

As discussed in Section 3.5, the Maxwellian overlap has been referred to as the loss fraction in the literature,[43,44] and has previously overestimated the effects of the ion orbit loss by including the collisional portion of the loss cone which should be considered full. In the following, both the overlap and the intrinsic rotation are reconsidered, now only assuming that the collisionless portion of the loss cone is empty. Again, both measures will overestimate

the orbit loss since the sparsely filled collisionless loss cone is refueled upstream in the steady-state; however, the error is expected to be far less than that of Section 3.5.

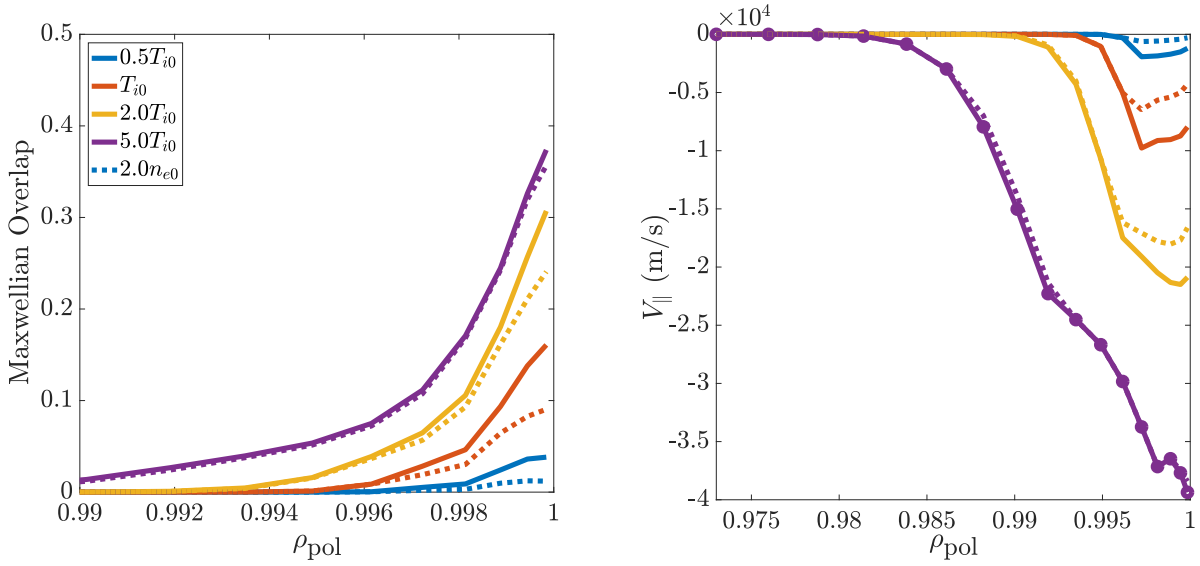

(a) (b)

Figure 4.13: The collisionality corrected Maxwellian overlap and intrinsic rotation. The baseline temperature and potential profiles are scanned at both the baseline density profile and a case twice as dense.

The Maxwellian overlap is corrected to only include the collisionless loss cone,

$$F(\rho_0, \theta_0) = \frac{1}{\sqrt{\pi}} \int_{-1}^{1} \Gamma(3/2, \epsilon_{\mathrm{T}}^*) d\zeta. \tag{4.39}$$

where ϵ_{T}^* is the energy threshold for the local collisionless loss cone for a given pitch direction. Figure 4.13.a shows the corrected Maxwellian overlap for the same temperature profiles corresponding to the lines in Fig. 3.7.b. The overlap profiles are presented at both the baseline density and a case that is twice as dense and therefore twice and collisional.

The collisionality reduces the overlap in two distinct ways. The narrow loss regions comprising the trapped orbits rarely contribute to collisionless losses and the overlap suffers a global reduction that appears more or less binary in accounting for reasonable collisionalities. Very near the separatrix, where the energy thresholds are determined by the collisionality, as

shown in Fig. 4.12, the effect of the scattering is more finely sensitive to the edge collisionality. The higher density plasma directly raises the energy thresholds of the local collisionless loss cones near the edge, proportionately reducing the maximum overlap by an amount inversely dependent on T_i.

Additionally, the intrinsic rotation is corrected to only account for the rotation of the collisionless loss cone,

$$V_{\parallel,\mathrm{iol}}(\rho_0,\theta_0) = -\sqrt{\frac{2T_i}{\pi m}}\int_{-1}^{1}\zeta\Gamma(2,\epsilon_{\mathrm{T}}^{*})d\zeta. \tag{4.40}$$

Subplot (b) illustrates the reduction in the outer midplane rotation associated with the omission of the highly collisional orbit trajectories for the same profiles used in subplot (a). Like the overlap, the collisionality reduces the radial extent of the rotation and reduces the magnitude near the separatrix by an amount inversely proportional to the ion temperature. Recall that the average loss times discussed in Sections 4.3.4 and 4.3.5 are about a factor of two longer for collisionless ions in the unfavorable drift, equivalent to a similar increase in the collisionality of the ions within the loss cone. The collisionality correction introduces an up-down drift asymmetry that has been experimentally observed; the intrinsic rotation along the outer midplane is more co-current in the favorable configuration. The difference in the rotation due to the orbit losses in the opposing configurations appears less than that experimentally measured; however the measured difference is greatest in the SOL and the orbit loss calculations here only approach the separatrix.[39] The calculated difference within the separatrix appears to be on the same order as seen in the experiment. Furthermore, the corrected intrinsic rotation calculation predicts the parallel rotation profiles in the matching baseline SOLPS simulation to a high degree, see Appendix A.

Chapter 5

Steady-state ion orbit loss

It is now appropriate to extend the orbit loss model to estimate the steady-state losses. Chapter 3 established a framework for the construction of the ion orbit loss cone for thermal orbits lost via the influence of the X-point, classifying the ion trajectories open to the divertor. Chapter 4 considered the effects of collisions on ions with these instantaneous trajectories, determining their likelihood for a first orbit loss. Velocity-space loss cones describing ions localized to a spatial observation point have unique separations demarcated about the qualitative change in the probability that a non-negligible fraction of ions in the local cone will be lost on first orbits. The two regions, discussed in Chapter 4, are referred to as the collisional and collisionless loss cones.

The collisional portions of the local loss cones describe a roughly constant number of particles in thermal equilibrium with the local Maxwellian that each undergo a small segment of a lost orbit before scattering out, being replaced by a different ion.[33] Any loss trajectory within the collisional loss cone will satisfy the collisionless criterion at some point sufficiently near the loss condition. For the collisionless velocity-space loss cone mapped to some observation point, any ensemble of ions within the cone launched from that location will perpendicularly diffuse in velocity-space such that an appreciable fraction remains in the loss cone throughout the loss orbit, by construction. It follows that this very fraction of

ions resupplying the loss cone are lost to the divertor on their first orbit. Continuity informs that in the steady-state, the rate of refueling the loss cone, modified by the fraction that are lost on a first orbit, is equivalent to the rate of loss. Any mechanism that refills the collisionless loss cone contributes to the prompt orbit loss current. Naturally, pitch angle scattering should also be considered as a refueling mechanism. Such a collisional process is largely unaware of the downstream field structure and simply acts to spread initially directed ensembles of ions across the pitch angle space. Simply put, the physics driving the scattering into and out of the loss cone is the same. In the presence of the loss mechanism, the collisionless loss cone is expected to be more sparsely filled, corresponding to a diffusive particle flux into the cone.

The collisional refueling of the loss cone does not capture the complete picture. The anomalous radial particle flux associated with the ambipolar turbulent transport contributes to the net transport of ions from confined trajectories to those lost. The typical dominance of the anomalous transport compared to the neoclassical transport suggests that this contribution could be significant. In Section 5.10.1, an estimate for the orbit loss current associated with the radial particle flux into orbits within the loss cone is adapated from the literature[49] for the presented orbit loss model, where it appears that the anomalous contribution is of the same order as the current resulting from the collisional processes. Furthermore, the ionization of neutral particles contributes to the sourcing of the collisionless loss cone and is briefly discussed in Section 5.10.2. The remainder of the thesis maintains a focus on the interplay of pitch angle scattering into and out of the loss cone structure over the timescales of orbit loss.

The appearance of the upcoming section title as an oxymoron deserves a brief reprisal of a discussion found in the previous chapter. The definition of the collisionless loss cone does not exclude orbits that experience collisions. Orbits on loss trajectories scattering to other loss trajectories will still correspond to a loss and are thus maintained. The interplay between the local ion collisionality and the local loss cone structure is influential in demarcating the

collisional and collisionless portions. The collisionless loss cone can be appreciably refilled by collisions exactly because the orbits within this portion experience a non-negligible amount of collisions on their paths to loss. The lack of collisional drive into the truly collisionless parts of the loss cone will be found to be of crucial importance for the temperature and density dependencies of the orbit loss.

5.1 Collisionally refilling the collisionless loss cone

A Maxwellian distribution with a hole caused by the magnetic field structure can never relax this feature away. Even for local ion temperatures far below the loss cone boundary, some portion of the energetic tail will interact with the loss structure. In the steady-state, the collisions continue to redistribute the constituents of the distribution function, with no clearly defined beginning nor end to the process. All locations in the velocity-space experience such motions.

This steady-state is captured by averaging the perpendicular diffusion, Eq. (4.2), over a period of time longer than its characteristic scale,

$$\begin{aligned} \left\langle \frac{du_\perp}{dt} \right\rangle &= \frac{1}{T} \int_0^T \frac{du_\perp}{dt} dt \\ &= v \sqrt{\frac{\nu_\perp}{T}}, \end{aligned} \tag{5.1}$$

where $\boldsymbol{u} = \boldsymbol{v} - \bar{\boldsymbol{v}}$. The forms of the slowing down and energy exchange processes and their connection to the diffusion processes via Eq. (4.13) suggest that T should be taken to be some number of time constants $\tau_\perp = 1/\nu_\perp$,

$$\left\langle \frac{du_\perp}{dt} \right\rangle = \frac{\nu_\perp v}{\sqrt{n}}, \tag{5.2}$$

where n is the chosen number of time constants, acting as a tunable model parameter. The model is, perhaps surprisingly, relatively insensitive to reasonable changes in n due to the

slow growth of the inverse root dependence. For the duration, this parameter is chosen to be $n = 3$, mirroring a standard choice for decaying processes. The motions described by Eq. (5.2) are immaterial for Maxwellian distributions without loss regions; fungible ions are replaced by each other; the diffusive and dynamical friction processes are balanced.[51,123] In the presence of a loss cone, Eq. (5.2) finds utility. A symmetry of the system is lost. Ions diffusing towards the loss cone are not necessarily replaced by those diffusing out of that region, since the latter is depopulated by the loss orbits open to the divertor.

Accounting for the probability of rescattering out of the local loss cone and the alignment of the loss cone's surface in regard to the direction of pitch angle scattering modifies the characteristic steady-state width per unit time, seen in Eq. (5.2), to only include the ions that contribute to the fruitful refueling of the loss cone,

$$\left\langle \frac{dw_\perp}{dt} \right\rangle = F(E)\frac{\nu_\perp v}{\sqrt{3}} \left|\cos(\alpha)\right| . \tag{5.3}$$

Here, α is taken as the angle between the normal of a velocity-space loss cone surface and the direction of the scattering in velocity-space, and $F(E)$ is the unscattered fraction seen in Eq. (4.16), which is evaluated at the statistical loss periods of Eq. (4.37). The change from u to w is meant to highlight that Eq. (5.3) no longer considers the velocity-space flows but rather those across the local collisionless loss cone boundary that result in first orbit losses. Eq. (5.3) represents the effective velocity-space width per unit time that contributes to the refueling of the loss cone and will simply be referred to as the effective width. In the steady-state, the number of ions that flow into the loss cone over a given time is directly proportional to this time frame.

Figure 5.1.a investigates the effective width as a function of energy over a simple velocity-space loss cone boundary that is assumed to lie upon a line of constant pitch angle, $\alpha = 0$. Each line corresponds to a velocity-space loss cone of a different and constant angular width, in effect each similar to a standard local collisionless loss cone comprising the passing-like

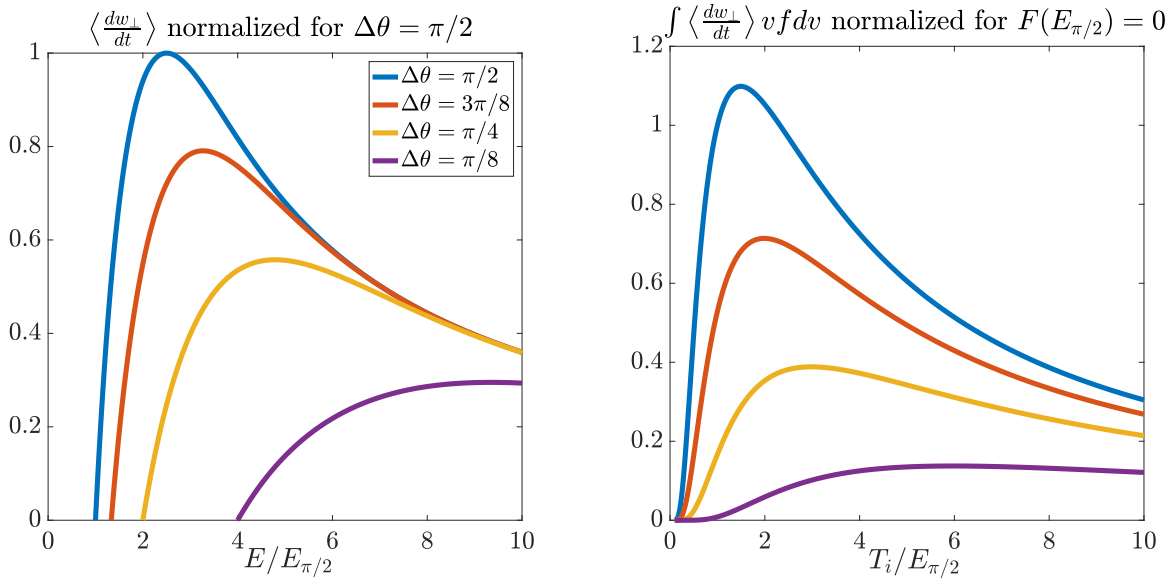

(a) (b)

Figure 5.1: The effective width for a variety of constant angular width simple loss regions, subplot (a). The steady-state collisionless orbit loss's temperature dependence is estimated in (b) via integration over the simple loss cone boundary with the effective width.

orbit losses. The effective width is normalized such that the maximum for the $\Delta\theta = \pi/2$ case is unity, and the energy scale is normalized to the cutoff energy for this case. It is also chosen that the normalization energy is equal to the local ion temperature. A different choice for the ion temperature would explore the sensitivity of Eq. (5.3) to the discrepancy between the ion-ion collisional frequency, Eq. (4.10), and the perpendicular diffusion frequency, Eq. (4.6). The collisionless cutoff energy, where $F(E) = 0$, scales with the inverse of the angular width of the local loss cone, and consequently, the wider cones are more supportive of steady-state orbit loss. For each case, the contributing width peaks about some energy, typically slightly above twice the cutoff energy, with the lower energy branch being suppressed by the increased rate of scattering out of the loss cone and the higher energy branch by the decreased rate of scattering into the region. The crucial implication here is that the collisionality and local loss cone structure set an energy that is most efficient at driving the prompt orbit losses. If the distribution function places local ions at these energies, the losses will be great.

Figure 5.1.b considers the effect of the velocity-space particle distribution by integrating

local Maxwellian distribution functions of differing temperature over the effective width. The same constant angular width cases shown in subplot (a) are presented, with the ion temperature again being normalized to the same cutoff energy. The integrated orbit loss was normalized to unity at the normalized ion temperature for the $\Delta\theta = \pi/2$ case. For temperatures beneath the cutoff energies, there is a strong growth in the rate of orbit loss with increasing temperature. The orbit loss reaches a maximum when the distribution function optimally concentrates particles at energies that effectively refill the loss cone with ions on orbits that can be lost sufficiently quickly. This temperature is called the saturation temperature as the orbit losses decrease for higher temperatures at the same density, albeit at a slower rate than the low temperature growth. Although higher energies of the local loss cone are thermally accessible at the higher temperatures, the conservation of particles dictates that the lower energy regions of velocity-space become more dilute. Beyond the saturation temperature, the peaked contributing width seen in subplot (a) spans a decreasing number of ions. Compared to estimates in the literature,[50,64] the effective width features two notable improvements: the scattering of ions out of the loss cone is considered by comparing the energy dependent collisionality to the loss orbit timescales and the energy dependence of the collisional refueling is maintained.

We briefly expand on a subtlety that is only mentioned in the above. The contributing widths illustrated in subplot (a) are sensitive to the ion temperature, with a weak sensitivity in the Coulomb logarithm evaluated in ν_0 and a stronger sensitivity in the perpendicular diffusion rates found in the time-averaged pitch angle scattering and the unscattered fraction. For a position along the velocity-space loss cone boundary corresponding to some fixed energy, increasing the temperature decreases the rate of pitch angle scattering at this position, as seen in Figure 4.2.a, shifting the cutoff and peak to lower energies and increasing the rate of the high energy falloff. Increasing the temperature by an order of magnitude maximally results in a reduction of $\nu_\perp$ by about a factor of three, simultaneously reducing the effective width by the same factor and lowering the cutoff energy by its root. These lower energies

now supportive of the orbit losses are prone to depopulation in the distributions of greater temperature.

5.2 The collisionless ion orbit loss current

The number of ions lost due to the fruitful scattering of ions into the collisionless loss regions in the steady-state is calculated by integrating the distribution function over the loss cone with a width given by $\Delta t \left\langle \frac{dw}{dt} \right\rangle$, see Eq. (5.3). Here, Δt is simply a reference change in the time over which the losses are counted, analogous to a timestep in a numerical scheme. For simplicity, the distribution function is taken to be constant over this width. Thus, the local charge density loss rate takes the form

$$\begin{aligned} \nabla \cdot \boldsymbol{j}_{\text{c-less}} &= Ze \int_S \left\langle \frac{dw}{dt} \right\rangle f dS \\ &= \frac{Ze}{\sqrt{3}} \int_S \nu_\perp v \left(2\text{erf}\left(\frac{\Delta\theta}{\sqrt{2\nu_\perp \tau_l}} \right) - 1 \right) |\cos(\alpha)| \, f dS. \end{aligned} \tag{5.4}$$

S refers to the surface of the collisionless loss cone in velocity-space. Eq. (5.4) can easily be reduced to a line integral due to the symmetry about the $v_\parallel$ axis. Additional loss terms beyond the current can be similarly constructed and will be discussed in Section 5.9. Since the projected velocity-space loss cones only accurately describe the lost orbits for a given observation location, the distribution function in Eq. (5.4) is local. To be consistent with the chosen particle distributions to estimate the collisionality rates, local Maxwellian distributions determined by the local temperature and density are chosen. The distribution in Eq. (5.4) can easily be changed, but more care is necessary to determine the collisional behaviors in different backgrounds. It is assumed that the anomalous radial transport of energy and particles maintains these profiles in the steady-state, as is seen in the SOLPS code.

The analysis is continued by investigating the results of calculating Eq. (5.4) within the

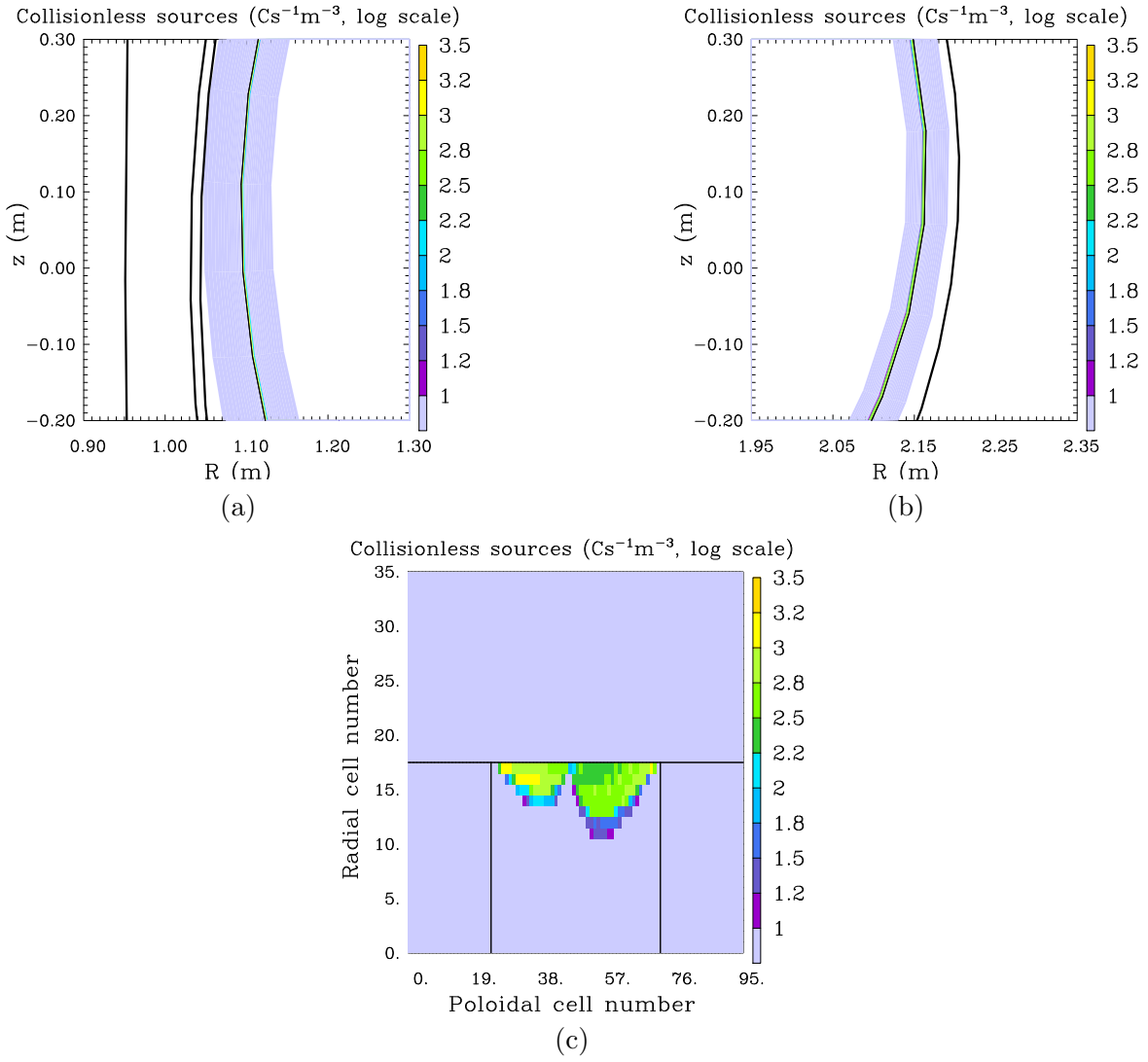

Figure 5.2: The log-scaled distribution of collisionless ion orbit losses in the physical plane, (a) and (b), and the computational plane, (c).

SOLPS framework under the assumption of Maxwellian distributions described by the local plasma conditions. Configuration-space is represented by cells, gridding the poloidal plane along a radial and poloidal component. The orbit loss calculations are performed at the cell centers and applied over the cell. Cells at the same radial position correspond to the same flux surface, therefore the configuration-space radial resolution is finest near the separatrix along the midplanes and coarsest near the X-point. Poloidally, the resolution is chosen to be greatest near the X-point. The results shown are for the baseline L-mode case nearing the L-H transition, seen in Appendix A.

The loss distribution corresponding to the baseline case is presented in Figure 5.2. As expected, the losses are significant in the edge region where the collisionless loss cone is thermally accessible. The radial domain for non-negligible losses is quite narrow, about half a centimeter at the outer midplane, making it difficult to analyze when plotted in the physical domain, subplots (a) and (b). For this reason, the computational domain is preferred for analysis. Refer to Appendix A or the SOLPS user manual for a visualization of the mapping between the computational and physical domains in SOLPS. The collisionless ion orbit loss current consists of a similar order of particles flowing from the low field and high field sides, with the losses centered about the X-point; however, the qualitative behavior of the collisionless losses flowing from either side are different.

The radial domain of the collisionless loss orbits originating from the low field side is greater than those from the high field side. Toward the core, the energy scale of the collisionless portions of the local loss cones is determined by the minimum energies associated with passing losses. For a standard positive triangularity tokamak, the energy threshold for the HFS co-passing losses is naturally higher, being only accessible over a narrower radial annulus than the LFS counter-passing losses, see Section 5.8 for a discussion on the plasma shaping and the orbit loss current. Very near the separatrix where the collisionality determines the energy scale of the collisionless losses, the large angular widths of the HFS local loss cones sustain collisionless losses at lower energies, enhancing the HFS losses near the LCFS. The uniformly slightly diminished losses very near the LCFS are a consequence of the localized radial electric field well and the slower baseline orbit periods associated with an increased safety factor.

5.3 The collisional ion orbit loss current

Any loss orbit contained within a collisional portion of a local velocity-space loss cone will satisfy the collisionless condition at some more advanced position along the loss trajectory.

The collisionless loss cone model estimates the collisional transport onto these segments where a non-negligible fraction of the loss cone refueling is lost on a first orbit. Within the considered framework, there are two classes of orbit losses that are missed by the collisionless current calculated in the previous section. The first is simply related to an under resolution in configuration-space; trajectories within collisional portions of projected loss cones very near the separatrix are not resolved to a position near enough the loss condition where they inhabit a local collisionless loss cone. The second is the so-called X-loss, a particular subset of the general orbit loss where the trapped particles bounce in the vicinity of the X-point.[33] As seen in Fig. 4.11, the local loss cone mapped very near and directly above the X-point does not contribute to the losses calculated in the previous section.

This current is modeled following the work of Chang *et al*,[33]

$$\boldsymbol{j}_{\nabla B,\mathrm{coll}}(\rho,\theta) = Ze \int\limits_{\Sigma_{\mathrm{coll}}} \left(\boldsymbol{v}_{\boldsymbol{\nabla B}} + \boldsymbol{v}_C\right) f d^3v, \tag{5.5}$$

where Σ_{coll} is the local collisional loss cone, housing particles that are taken to be in thermal equilibrium with the local Maxwellian. The flow described by Eq. (5.5) is vertically directed and models the vertical drift motions of the roughly constant number of particles within the local collisional cone. In form, the so-called collisional loss current behaves similarly to the effective diamagnetic current employed in SOLPS; however, the collisional ion orbit loss current only includes the effects of orbits satisfying the loss condition, and only a subset of the ions contribute. Therefore, it is assumed that the length scale is given by the vertical distance above the X-point, the point defining the loss plane,

$$\begin{aligned} \nabla \cdot \boldsymbol{j}_{\mathrm{coll}} &\approx \frac{Ze}{z - z_X} \int\limits_{\Sigma_{\mathrm{coll}}} \left(v_{\nabla B} + v_C\right) f d^3V \\ &\approx \frac{m}{2RB(z - z_X)} \int\limits_{\Sigma_{\mathrm{coll}}} v^2 \left(1 + \zeta^2\right) f d^3v, \end{aligned} \tag{5.6}$$

where it has been assumed that the ∇B and curvature drifts can be combined,[126]

$$\boldsymbol{v}_{\nabla \boldsymbol{B}} + \boldsymbol{v}_C = \frac{m}{2Ze}(v_\perp^2 + 2v_\parallel^2)\frac{\boldsymbol{B} \times \nabla B}{B^3}. \tag{5.7}$$

In implementation, the length scale is extended by about an order more than a typical Larmor radius, ~ 1 cm for a 100 eV ion, to ensure the ions are destined for the divertor.

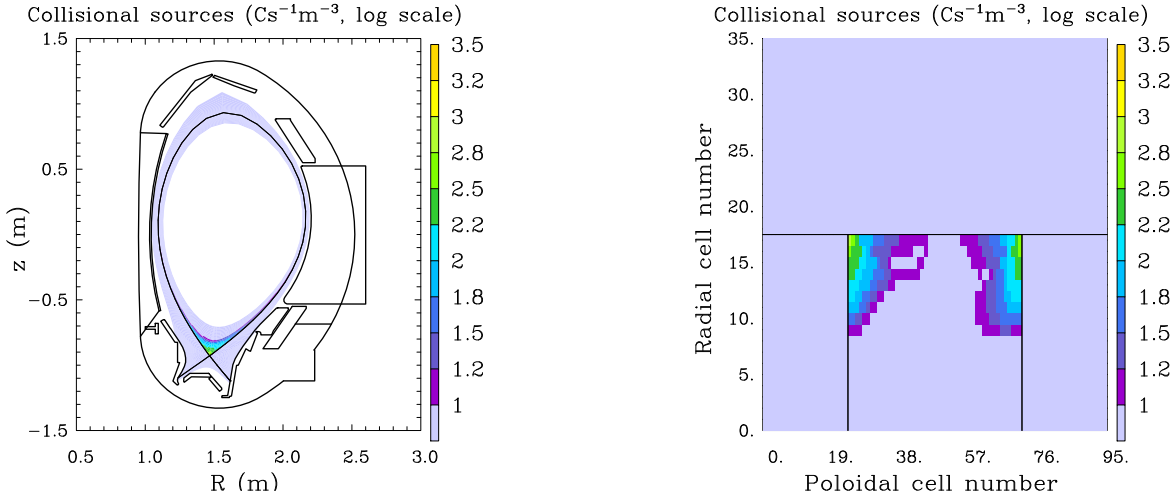

(a) (b)

Figure 5.3: The log-scaled distribution of collisional current source terms in the physical plane (a) and the computational plane (b).

The collisional losses for the same L-mode parameters behind Fig. 5.2 can be seen in Fig. 5.3, taking on a much simpler distribution. For these parameters, the collisional losses are lesser in magnitude compared to the collisionless losses, although they are non-negligible. The losses are also centered around the X-point. This is partially by construction, as the length scale was knowingly selected, but this choice is rooted in the fact that the loss cones for orbits vertically above the X-point are narrow up to typically superthermal energies due to the rarity of passing losses at these positions. The energy scale for the collisional losses is the favored loss energy scale of the trapped orbits, allowing the collisional losses to contribute from deeper inside the plasma.

Figure 5.3 reflects a notable feature of the equilibrium that will be further discussed in

Section 5.6. The collisional losses are far easier to perceive in the physical domain due to the flux surface expansion near the X-point. The same source terms mapped to the top of the plasma would correspond to fewer losses because the plasma density is roughly the same over the radially thinner cells bounded by identical flux surfaces.[34]

5.4 The total ion orbit loss current

The distributive nature of the divergence operation allows for the representation of the total ion orbit loss current in the current continuity equation to simply be the sum of Eqs. (5.4) and (5.6),

$$\nabla \cdot \boldsymbol{j}_{\text{iol}} = \nabla \cdot \boldsymbol{j}_{\text{c-less}} + \nabla \cdot \boldsymbol{j}_{\text{coll}}. \tag{5.8}$$

Figure 5.4 illustrates the full distribution of the ion orbit loss current for this particular L-mode. The constituent parts of the total current can be recognized following the discussions in Sections 5.2 and 5.3. Here, the dominant part of the current results from perpendicular velocity-space diffusion into upstream local collisionless loss cones, with a smaller component coming from the collisional loss estimate. This relationship will be studied over parameter space in Section 5.5.

Subfigures (a) and (b) in Fig. 5.4 illustrate the same current distribution in terms of the absolute contributions to the radial current per cell, with units Amperes, and as the source terms found in the continuity equation, with units Amperes per cubic meter. When plotted in absolute terms, the collisional contributions above the X-point appear more significant due to the larger cell volumes via the flux expansion. Similarly, the HFS losses appear less dominant since the poloidal plane sweeps out a smaller volume at smaller major radii when rotated about the toroidal coordinate. The edge-most cells at the outer midplane appear to contribute less due to the flux squeezing.

The last closed flux surface satisfies a simple steady-state quasineutrality condition: there

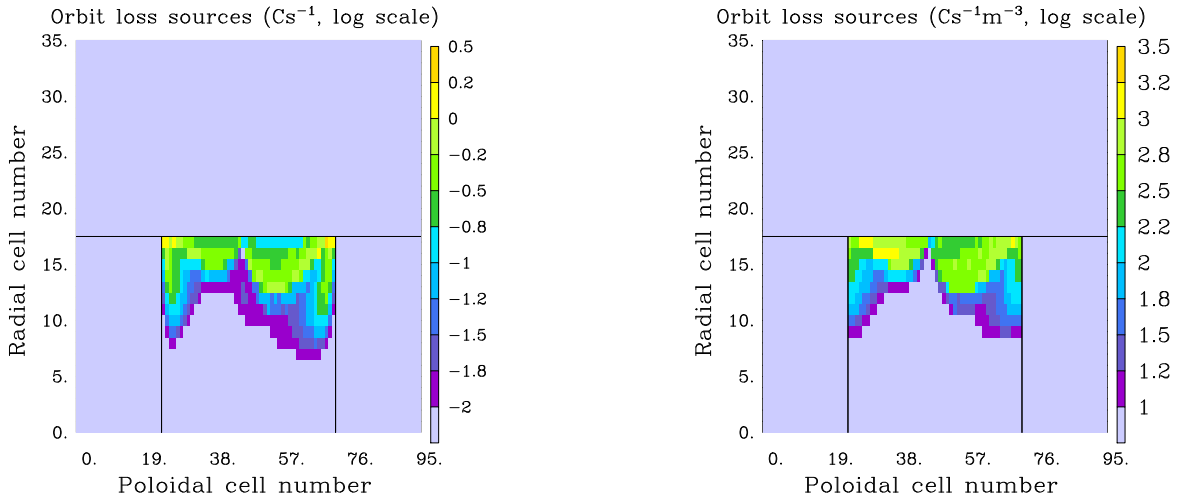

Figure 5.4: The log-scaled distribution of the total ion orbit loss in the computational plane. Subplot (a) is presented in terms of the absolute contribution while (b) presents the source terms as current per volume.

must be no net charge flowing across the separatrix, or else there would be a build-up of charge and quasineutrality would be destroyed. From this perspective, the two-dimensional structure of the ion orbit losses is less important. The cumulative radial sum, starting from the core boundary, of the poloidal sum of the losses seen in Fig. 5.4.a results in the radial current profile for the orbit loss. The radial current profiles corresponding to the earlier plots in this chapter are shown in Figure 5.5. The radial domain of influence nearly matches that of the collisionless Maxwellian overlap, with a qualitatively similar profile. The dominance of the collisional current nearer the core and of the collisionless losses very near the separatrix can be clearly seen. We note that the order of magnitude of the orbit loss current reproduces that seen in the literature.[100,101,127]

To maintain quasineutrality, there must be some composition of currents with the equal and opposite divergence. This topic is discussed in the upcoming chapter in the environment of the tokamak edge as modeled by SOLPS. As seen in Chapter 2, the equilibrium solution for this radial current balance simultaneously sets the toroidal rotation and the radial electric field, within the context of the force balance. Before that discussion begins in earnest, we

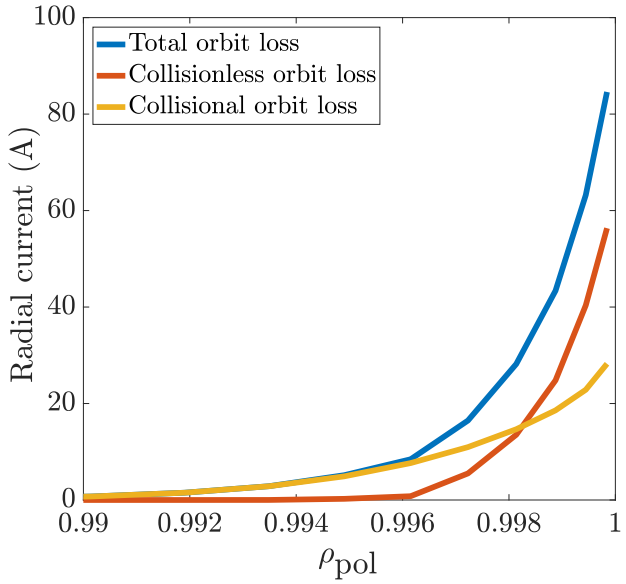

Figure 5.5: Radial current profiles for the distributions seen in Figures 5.2–5.4

will investigate the orbit loss current as a function of both the ion temperature and density, the ∇B drift direction, ions of different mass, and the horizontal position of the X-point. The chapter will conclude with brief descriptions of the secondary ion orbit loss source terms and additional mechanisms that resupply the loss cone.

5.5 Analytic parameter scans: Ion temperature and electron density

Here, we will investigate the dependency of the orbit loss current on both the ion temperature and the electron density. The corresponding baseline profiles are taken from an L-mode SOLPS simulation with an input heating power of 1.2 MW split evenly between the ions and electrons and a core density level held at $2.4 \cdot 10^{19}$ m^{-3}, see Appendix A. The electric potential profile is obtained in a similar way. Here, and for the remainder of the thesis, the core boundary specifically refers to the $\rho_{\mathrm{pol}} = 0.973$ flux surface, the inner boundary chosen for the simulations. The analytic scans are performed with profiles related to the baselines by

multiplicative factors, essentially under the assumption that the profiles maintain a constant shape and the length scales do not considerably change. In Chapter 6, similar parameter scans will be investigated over a necessarily more narrow parameter space with the plasma background being self-consistently modeled within the SOLPS framework.

Let us first gather our expectations and intuitions about these parameters. The ion temperature primarily determines the access of the thermal ions to the loss region, as can be seen in Figures 3.6 and 4.12, with the lowest energy access occurring nearest the separatrix. The radial coordinate energy dependence for the local collisionless loss cones is locally far steeper than the collisional portions of the loss cone; shape preserving increases of the temperature profile will favor growth in the collisional current. Beyond simply providing access to the local loss cone structures, the ion temperature determines the specific distribution of ions in velocity-space along the loss cone boundary, where the effectiveness of ions contributing to the orbit loss is maximized about an energy dependent on the local loss cone structure and plasma parameters, see Fig. 5.1. To ideally maximize the orbit losses, the temperature profile would need to become steeper rather than increase as a whole, allowing for losses originating deeper from the core without reducing the losses nearer the separatrix.

The radial electric field is neoclassically expected to grow with the ion temperature under constant length scales. Consider the pressure gradient term,

$$E_r \sim \frac{\nabla p}{n} \sim \left(T\frac{\nabla n}{n} + \nabla T \right) \sim \frac{T}{h_y} \sim T. \tag{5.9}$$

Scanning over the ion temperature should naturally be coupled with a similar scan over the electric field strength. For L-mode strength E_r wells, the local collisionless loss cones are typically only shifted in velocity-space whereas the lower energy collisional portion can be appreciably affected by the electrostatic trapping.

Scanning over the ion temperature can be thought of as scanning over the input power. For reference, the ion temperature at the baseline density increases linearly with the input

power by about 45 eV over an increased heating of 1 MW, again evenly distributed to the ions and electrons. In the SOLPS scans in the upcoming Chapter 6, the ion temperature is scanned via a scan in the energy flux through the inner core boundary at a constant plasma heat conductivity χ_i associated with the anomalous transport.

The electron density plays a fundamental role in the ion orbit loss. First and foremost, a larger density makes available more ions to be orbit lost, $f \sim n$, while the matching increase in the number of electrons still correspond to orbits more closely tied to a flux surface. Furthermore, the ion collisionality is directly proportional to the density, a first consequence being that the boundary between the collisional and collisionless loss cone for a given field geometry $\sim \sqrt{n}$, see Fig. 5.1. The increased pitch angle scattering out of the loss cone is matched by an increased pitch angle scattering into the cone, and the receded local collisionless loss cones are refueled at a greater rate. These properties suggest that a high density plasma corresponds to a greater orbit loss, which can be true if the ion temperature is held constant, a condition that clearly requires an increased input power for the greater particle densities.

Over the parameter scan, one expects energy to be conserved such that the heat flux through each closed flux surface remains constant,

$$q_i = n\chi_i \nabla T_i. \tag{5.10}$$

For a constant heat conductivity and spatial scale, one expects that $T \sim 1/n$. However, it is seen in SOLPS simulations that the effective heat conductivity including the effects of the neutrals is sensitive to the electron density. For low density plasmas, the neutrals can penetrate more deeply into the core from the SOL and are able to more effectively cool the edge. For a given input power, the relation between the temperature and density more

closely resembles

$$T \sim 1/\sqrt{n}. \tag{5.11}$$

Subplots (a) and (b) in Figure 5.6 illustrate the temperature scan with the baseline density profile: (a) maintains the baseline electric field profile while (b) also scans over the radial electric field strength as indicated by Eq. (5.9). The two collisionless currents are relatively similar, both experiencing a steep initial growth at the low plasma temperatures. In both cases, the collisionless current peaks for some scaled temperature profile, generalizing the notion of the saturation temperature. There is an enhanced reduction in the collisionless losses at the high temperatures when coupled with scaled electric fields; the discrepancy grows with increasing E_r. Here, the $E \times B$ rotation is able to trap ions on the low field side. The radial electric field further plays the significant role of suppressing the lower energy collisional loss current, which exhibits a moderate linear growth with the ion temperature when the field is held constant. In the coupled scan, the collisionless losses dominate until the two components contribute roughly equally at high temperatures atypical of an L-mode, resulting in the plateaued total orbit loss current at high temperature.

The dashed lines in subplots (a) and (b) correspond to an artificial 50% increase in the baseline potential profile, since the orbit loss current is expected to positively contribute to the magnitude of the edge electric field. An enhancement of the radial electric field profile has little effect on the initial period of strong growth and influences the magnitude of the current plateau.

Subplots (c) and (d) illustrate the density scans. The former, again, presents a naïve viewpoint where the other parameters are held constant. The latter figure alters the temperature and electric field profiles as specified by Eqs. (5.9) and (5.11), approximating a density scan over a constant input power. When comparing the two cases, the change in the losses inflects about the point of normalization; the simpler case has enhanced losses for $n_e/n_{e0} < 1$

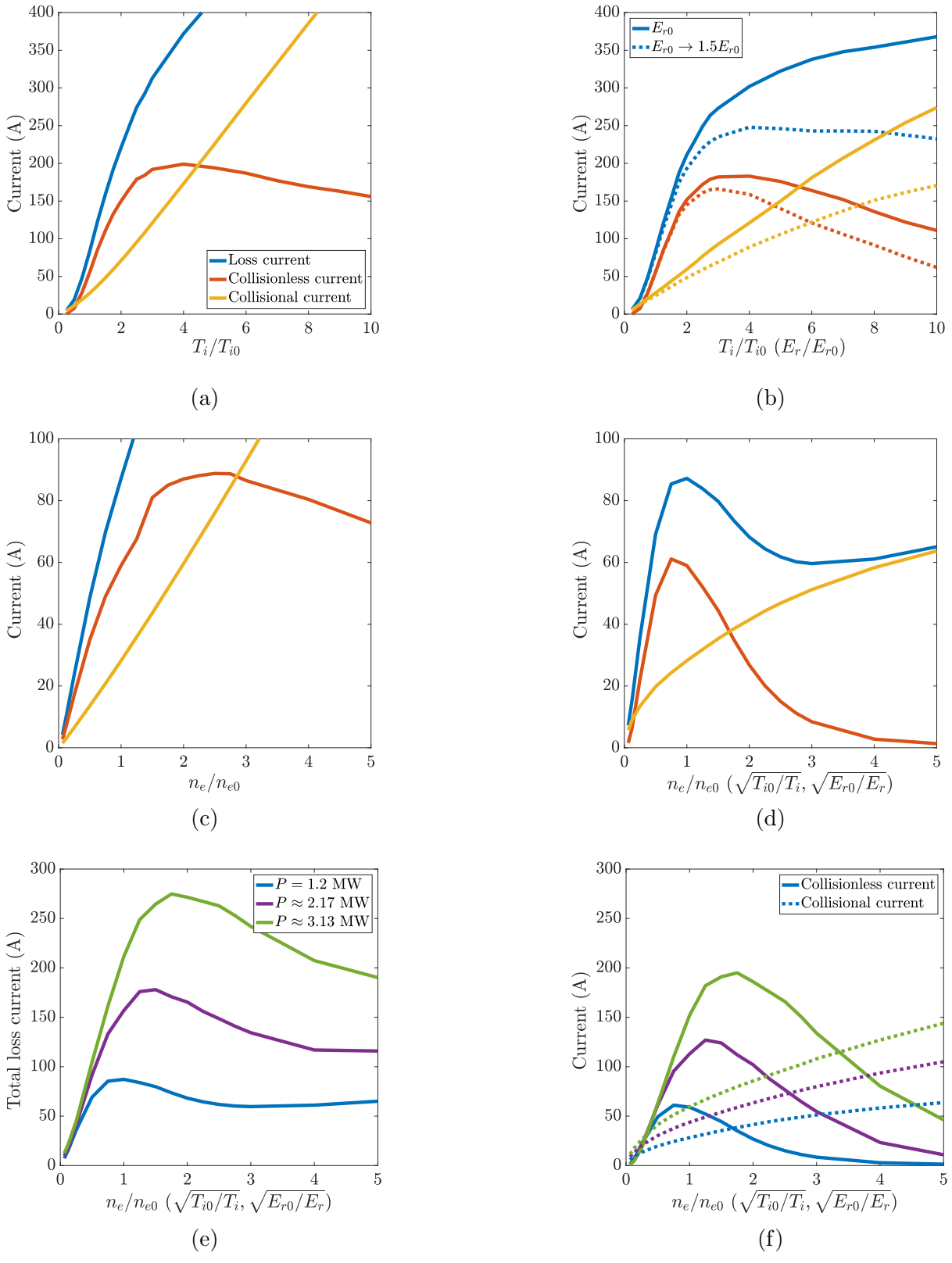

Figure 5.6: Analytic scans of the loss current flowing across the separatrix in temperature, density, and E_r strength. The x-axes indicate which quantities participate in each scan.

and reduced losses for $n_e/n_{e0} > 1$ compared to the more complete scan. In the first range, the ion temperature is underpredicted, with the opposite occurring in the second. The collisionless loss at the lowest densities are notably greater with the underpredicted temperature due to the collisionless oversaturation.

A well-defined high and low density branch can be seen in Figure 5.6.d. Along the low density branch, there is a rapid increase in the orbit loss with increasing density. In the context of Fig. 5.1, the edge local collisionless loss cones here have lower threshold energies but experience both a reduction in number of ions available for scattering into the loss cone and the rate at which they do so. The collisionless velocity-space loss cones achieve their maximum loss at a lower temperature, and, in a sense, saturate at some level of loss related to the density. The low density branch corresponds to the oversaturation of an increasing number of thermally accessible local collisionless loss cones. The total loss's peak occurs near the peak of the collisionless losses, slightly shifted toward higher density by the collisional loss current. The high density branch is characterized by a reduction in the collisionless losses that is replaced, typically at a reduced rate, by the collisional current. The collisionless loss reduction follows the classical principles of the ion orbit loss: the thermal ions at low temperatures are not able to access the collisionless loss cone, which here is receding toward higher energy due to the $\sqrt{n}$ dependence for the collisionless cutoff. The collisional current grows with the density for two reasons: the number of particles uniformly increases and the collisional region increases in size. The growth is mitigated by reduced accessibility to the loss cone with decreasing temperature.

Subplots (e) and (f) illustrate the density scans over a constant input power at three different levels, introducing scans corresponding to a 50% and 100% increase in the ion temperatures. Subplot (e) shows the total current while (f) shows the breakdown by component. As the input power is increased, both the maximum orbit loss current and the density that it occurs at increase, signifying a dynamic change in the density branches. As the local collisionless loss cones for a given density profile approach saturation, the loss growth stagnates.

An increase in the input power naturally increases the range of densities corresponding to this behavior, thus increasing the range of the low density branch where increases in the ion temperature have diminishing returns. Along the high density branch, the majority of thermally accessible local collisionless loss cones are still in the initial period of strong growth with increasing temperature as seen in Fig. 5.6.b, and the losses strongly respond to increasing temperatures until they join the low density branch. The high density branch for the collisionless losses inherently decays more slowly than the growth in the low density branch. This rate of decay is mitigated in the total loss current by the growing collisional current found at higher densities.

Both the collisionless orbit loss current and the total orbit loss current exhibit high and low density branches at a constant input power. This feature of the orbit loss is newly reported and helps cement the role played by the orbit losses in the L-H transition, which shares the behavior in its power threshold. For both, the low density branch is steeper than the high density branch, and the maximum orbit loss occurs at similar densities to the minimum power threshold.[22,23] The branching behavior is thought to emphasize the importance of the ion channel as the low density branch at AUG is typically characterized by $T_e > T_i$;[19,23] however, the behavior is also exhibited on JET where $T_e = T_i$ along the low density branch,[19,22] suggesting that the phenomenon persists for well-heated ions. The results suggest that a more detailed survey of the orbit loss current should be performed using experimental equilibria and profiles for different density plasmas near the L-H transition power thresholds to determine to what degree the suppressed low density branch orbit loss current is responsible for the behavior. In a similar vein, Sections 5.6–5.8 explore other well-known behaviors in the empirically known L-H transition power threshold: the ∇B drift direction, the main ion mass, and the horizontal position of the X-point.

5.6 ∇B drift direction

The lost orbit periods calculated in Section 4.3.5 are sensitive to the ∇B drift direction, see Figure 4.10. In the unfavorable drift, the minimum energy losses cross the separatrix at the top of the plasma, about the position vertically opposite the X-point. In the SOL, these ions have long trajectories around the core plasma toward the lower divertor and are able to rescatter onto confined orbits before being lost. In other words, the loss orbit paths in the poloidal plane are generally far greater in the unfavorable drift; however, this discrepancy overestimates the increase in the orbital period due the poloidal orbit stagnation effect near the X-point. In the unfavorable drift, the unscattered fraction, see Eq. (4.16), is evaluated at statistical loss periods that are roughly a factor of two greater for the important regions with large $\Delta\theta$, a similar effect to a reduction of the local loss cone angular width by a factor of $\sqrt{2}$, see Figure 5.1. The on-average increase of the loss orbit periods under the unfavorable drift can alternatively be thought of as an effective increase in the particle collisionality in terms of scattering out of the loss cone: orbits are more likely to be removed from the loss cone before achieving loss but are not more likely to scatter in.[38,39] Consequently, the average local loss cone supports fewer collisionless losses due to the greater cutoff energies.

The increased energetic threshold for collisionless losses with the ion drifts pointing away from the active X-point naturally increases the proportion of the loss cone deemed collisional. In spite of this, the collisional orbit loss current is not substantially greater in this regime. The centralization of the losses about the top of the plasma consequently describes locations with more moderate flux expansion compared to the region near the X-point. The steady-state collisional current covers larger areas of velocity-space that correspond to radially thinner areas of configuration-space.[34] The loss condition for orbits considered in the collisional loss current is also weaker in the unfavorable drift, and the assumed length scale is extended by a few centimeters to ensure loss.

Figure 5.7.a illustrates the loss distribution in the unfavorable configuration, while subplot (b) reproduces the downwards drift case from Section 5.4 with a matching scale for

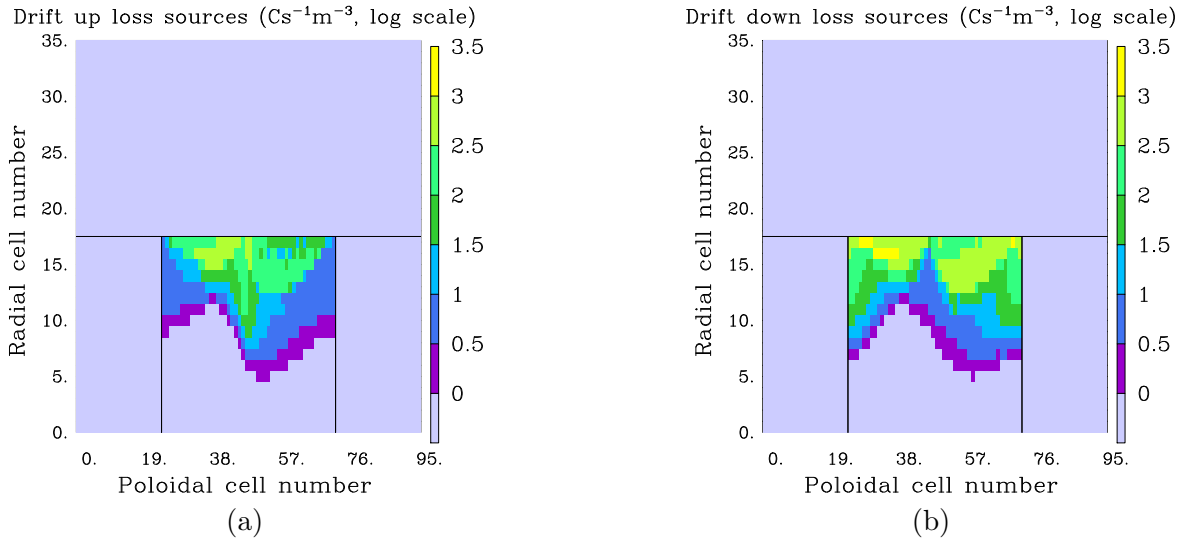

Figure 5.7: The log-scaled distribution of the total ion orbit loss in the computational plane for the unfavorable, subplot (a), and favorable, subplot (b), configurations.

comparison. Both cases have identical plasma profiles, taken from the baseline favorable drift configuration case. The basic features are easily seen: a shift in the losses, now centering about the top of the plasma, along with a total reduction in the loss.

Figure 5.8 is analogous to Figure 5.6.e, presenting the total orbit loss current in the unfavorable drift direction as a function of the electron density over a constant input power. The comparison is again made for identical profiles taken from the baseline favorable drift simulation, with the same input powers shown in the earlier figures. The loss current still exhibits low and high density branch behaviors in the same way as in the favorable configuration. The local collisionless loss cones in the unfavorable configuration recede toward higher energy, requiring an increased temperature to reach saturation. A rough doubling of the input power in the unfavorable drift corresponds to a similar total loss current in the favorable configuration. The high density current plateau is slightly elevated for the unfavorable drift, due to the slight increase in the collisional current.

Again, the total orbit loss current displays another known feature of the L-H transition power threshold. Although such a behavior has been suspected of the orbit loss current,[38,39] it is newly reported here for the steady-state orbit loss current. A next step would be to

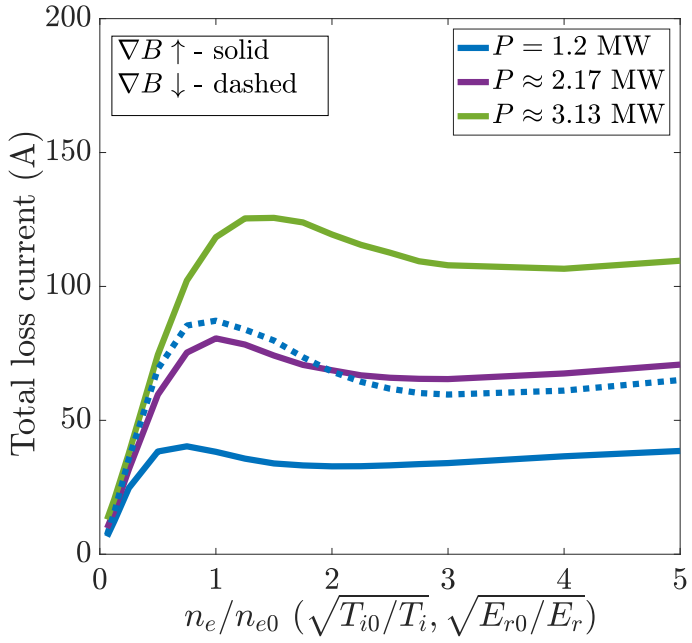

Figure 5.8: The total orbit loss current as a function of the edge density at a constant input power for the unfavorable drift configuration. The dashed line corresponds to the favorable configuration.

compare the orbit loss current in the opposite drift orientation using profiles determined under these conditions.

5.7 Main ion mass

Section 3.1.2 briefly introduced the dependence of the ion orbit loss, through the orbital width, on the mass of the orbiting particle. The conclusions reached were that the electron loss is negligible compared to the ions, since $m_e \ll m_i$, and that heavier ions with the same electric charge have loss trajectories at lesser energies. This qualitative relationship between the orbit loss and the ion mass is another common factor with the L-H transition power threshold, which exhibits an m_i^{-1} dependence,[25] and should be explored in greater detail.

The orbital width mass sensitivity manifests a similar mass dependence in the threshold orbit loss energies, Eq. (3.10). Since the X-point mediated orbit loss trajectories approach

arbitrarily low energies near the separatrix, see Fig. 3.6, the ion mass dependence essentially expands or contracts the radial domain where the loss cone is thermally accessible and, as seen in Fig. 4.12, the radial domain where the collisionality sets the threshold for the collisionless losses.

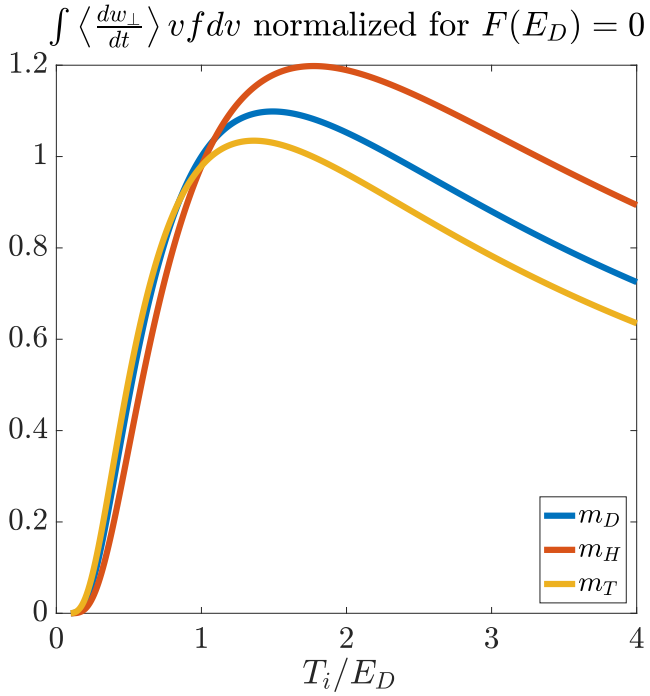

Figure 5.9: The temperature dependence born from the effective width for different hydrogen isotopes.

Although the more massive ions have thermally accessible local loss cones that penetrate deeper into the core for similar temperatures,[40] the rates of the collisional refueling of the cones are decreased, complicating the steady-state orbit loss dependence on the ion mass. The ion-ion collisionality, Eq. (4.10), exhibits an $m^{-1/2}$ dependence when considering ions of the same kinetic energy. This behavior propagates into the effective width, Eq. (5.3), in the collision frequency and in the unscattered fraction, Eq. (4.16), which shifts toward a larger cutoff energy, $F(E) = 0$.

The influence of the ion mass on the orbit loss via the collisionality can be seen in Figure 5.9, which is similar in nature to Fig. 5.1.b. Again, the orbit loss is estimated by integrating

the flux into a simple loss region that lies upon a line of constant pitch direction. The energy and ion temperature are normalized to the cutoff energy for the deuterium case shown in blue. Also plotted are cases where the ion mass corresponds to that of hydrogen or tritium. The shift in the cutoff energy materializes as a shift in the saturation temperature for the loss and follows an $m^{-1/4}$ trend. Below the saturating temperatures, the losses are roughly equivalently driven into the loss cone, with a slight preference for the higher masses due to the shift in the cutoff energy. For the higher temperatures nearing and above the peaking temperatures, the less massive species are more effectively driven into the loss cone due to the increased collisionality. For increasing temperatures, the scaling approaches the $m^{-1/2}$ dependence of the collisionality. Comparatively, the asymmetry is significantly reduced for lower energies where a significant fraction of the distribution functions lie along $F(E) < 1$.

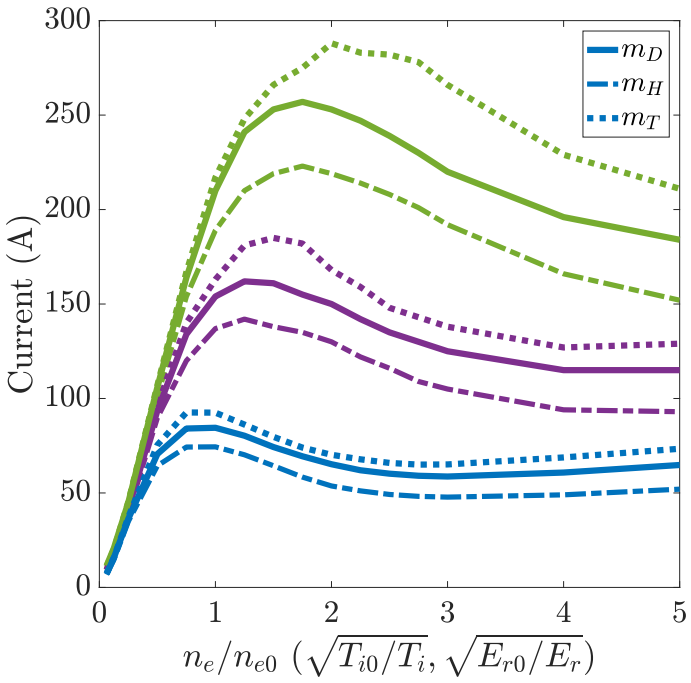

Figure 5.10: The total orbit loss current flowing across the separatrix as a function of the edge density at constant input powers for the different hydrogen isotopes: hydrogen, deuterium, and tritium. The temperature profiles correspond to those in Fig. 5.6.e for matching colors.

The interplay between the increase in the orbital width and the decease in the ion-ion collisionality with mass can be seen in Figure 5.10. The total orbit loss currents are

plotted for the three ion species seen in Fig. 5.9 over the same density, temperature, and E_r profiles matching the lines of corresponding color seen in Fig. 5.6.e and Fig. 5.6.f and Fig. 5.8. It is assumed that the relationship between these parameters is the same for the three species, neglecting changes in the ion-neutral interactions with the ion mass. Also, note that the stated input powers for the referenced figures only directly apply to the deuterium case. There is experimental evidence that the edge (here $\rho_{\mathrm{pol}} \sim 0.98$) ion temperatures and gradients are similar between the different isotopes just before the L-H transition, implying that the heat diffusivities at the transition $\sim m_i^{-1}$.[25,26] Under the strong assumption that the similarity continues to the separatrix, the ion temperature profiles would be similar for the respective required input powers. To that end, it is fruitful to compare the different species under the same profiles, with the understanding that the exact conditions corresponding to these profiles are murky.

It can be generally seen under these conditions that the orbit losses scale with the ion mass. For a given edge density, the losses scale directly with the ion temperature, again displaying low and high density branches where the temperatures scaling is reduced in the former. Along the low density branch, the losses are virtually identical for each species. Here, the increased collisional loss cone refilling of the light species is approximately canceled out by the increased radial ranges of the heavier species. For the constant yet not precisely known input powers that correspond to the same temperature profiles, the peaked orbit loss current is lesser and occurs at a lower density for smaller mass isotopes. The peaking location here shifts due to the shift in the collisionless cutoffs due to the increased collisionality for decreasing ion mass. For the high density branch, the losses are greater for the higher mass isotopes. The absolute difference between the species grows with the ion temperature for a given density. Here, the isotope dependence is dominated by the increase of the radial range enjoyed by the heavier ions, as the rates of collisional refueling are similar between the isotopes at temperatures below the saturation temperatures, see again Fig. 5.9.

The similarity between the forms seen in Figures 5.9 and 5.10 is a bit deceptive. The

x-axes in the two plots are essentially reversed; the ion temperature decreases with increasing density at a given input power in Fig. 5.10. The high temperature behavior seen in Fig. 5.9 mirrors the high density behavior seen in Fig. 5.10, where the relative magnitudes of the lines for each ion mass are inverted. The near cancellation of the orbit width and collisional effects for the low density orbit loss branch can be understood here. The ratios of the orbit loss for the different species along the high density branch, where the mass dependency is governed by the orbit width, is nearly the inverse of those for the simple loss cone orbit loss estimate at temperatures above saturation. Since the orbit loss width effect is insensitive to the collisionality, it is maintained for the low density branch, and the two effects nearly cancel in the region.

A more rigorous study on the relationship between the plasma profiles and the input power for the different isotopes is necessary to make more concrete connections between the orbit loss and L-H transition power threshold's ion mass dependencies. Nonetheless, a few of the salient features can be listed. For similar ion temperatures, the orbit loss currents are of a similar magnitude. Even so, the lighter mass ions require greater temperatures to exactly match the orbit loss currents associated with heavier ions. The peaking position of the orbit loss current is both dependent on the ion mass and the input power. A more precise relationship between the input power and the ion temperature for a given mass is necessary to determine if the orbit loss calculations predict the shift, with ion mass, in the density that minimizes the power threshold seen on AUG.[25] Furthermore, the decreased mass dependence seen on the low-density branch insinuates that the power thresholds for the different isotopes, if stongly and linearly dependent on the orbit loss current, should at least approach one another along the low density branch, a feature which appears to be the case for AUG[25] but not for JET.[26] At any rate, the above has not considered inherent changes to the plasma resulting from changing the ion species. It is possible that significant changes to the return current that closes the orbit loss current result from the isotope change, and an analysis of the orbit loss current in isolation is not sufficient. Future work should be

done to understand the complete role played by the lost ions as a function of their mass. A natural start would be to investigate SOLPS runs with hydrogen as the main ion species. The remainder of this thesis continues with the assumption that the bulk ions are deuterium ions.

5.8 Plasma shaping: Triangularity and the horizontal position of the X-point

So far, we have largely discussed the loss cone structure and the associated orbit loss current within the context of a standard positive trangularity tokamak, specifically within the context of the geometry of ASDEX Upgrade shot 16151. As discussed in Chapter 3, the lowest energy thermal orbit losses are a product of the X-point field geometry. Clearly, the static loss cone structure will be sensitive to the position of the X-point.[47,48] Furthermore, the steady-state orbit loss model highlights the importance of the angular widths of the local loss cone provoking further study of $\Delta\theta$ manipulation.

Consider the velocity-space loss cones presented in Fig. 3.2. Loss cones projected to locations with $R \geq R_X$ have finger-like projections describing the minimum energy trapped particle losses. These regions of the cones are bounded in pitch angle by the trapped-passing boundary and the minimum $|\zeta_0|$ such that the saddle point remains accessible for ions at this locale. Manipulating the radial position of the X-point directly affects the angular width, $\Delta\theta$, of the local loss cone while also affecting which fraction of the plasma is on either side of the X-point. To clarify, the manipulation of R_X manifests this behavior only if the rest of the plasma shape remains more or less constant, akin to a triangularity sweep in the half of the plasma with the active X-point. For a greater R_X, the angular width of the LFS local loss cones are greater while a greater portion of the plasma is on the HFS of the X-point. The opposite holds when decreasing R_X.

An additional effect of changing the radial position of the X-point is felt in the passing

orbit loss energy thresholds. Consider passing orbits on the same closed flux surface localized to the inner and outer midplanes. At the inner midplane, the co-passing orbits are able to be lost, while the counter-passing trajectories are possibilities at the outer midplane. For the positive triangularity tokamak, it was shown that the passing trajectories from the outer midplane were lost at far lower energies than those from the inner midplane, see Fig. 3.2. The reason for this is purely geometric; the inner midplane was horizontally closer to the X-point than the outer midplane. The orbit width is essentially a comparison of the perpendicular drifts to the poloidal projection of the parallel velocity. The typically lesser in magnitude magnetic drifts grow directly with the ion's energy while the parallel velocity grows like $\sqrt{E}$, resulting in larger orbital widths with increasing energy. The longer the orbital path to the X-point, the longer the ∇B drift has to widen the orbit. Manipulating R_X to greater values decreases the threshold energies for the HFS passing losses while increasing the threshold energies for the LFS passing losses.

The trapped losses experience a more minor version of this effect. Those nearest the trapped-passing boundary already have long orbital paths that are made longer by the additional distance they now need to travel back to the X-point. The most deeply trapped orbits will have slightly shorter paths since they still bounce near the X-point, which has been pushed closer to their initial positions. Overall, for trapped orbits localized to $R > R_X$, the most deeply trapped losses correspond to slightly higher energies while the least trapped losses correspond to slightly lower energies. For trapped orbits localized to an $R < R_X$, the energies are typically lower since the most deeply trapped losses do not access these regions. The inverse relationship holds true when decreasing R_X. It is important to keep in mind that the processes that allow for the lower energy losses explicitly correspond to longer loss orbit periods, potentially disfavoring the orbit losses. It must be considered if particles on these trajectories are likely to contribute to loss following the procedures detailed in Chapter 4.

It has been seen that very near the separatrix, the collisionless boundary is determined

by the collisionality and the angular width of the local loss cones, see Figure 4.12. The width of this region is set by the threshold energies of the passing losses. Increasing R_X increases the radial width of this region near the inner midplane and decreases this width near the outer midplane, while increasing the proportion of the plasma that exhibits the HFS behavior. Furthermore, the radially narrower outer midplane region supports collisionless loss at lower energies due to the increased angular width of the local loss cones. The changes in the orbital periods associated with the increased (decreased) poloidal path from the HFS (LFS) to an X-point with a greater R_X is expected to be minimal for the more important passing-like losses due to the hardly changing disproportionate portion of the orbit spent near the X-point due to the poloidal stagnation.

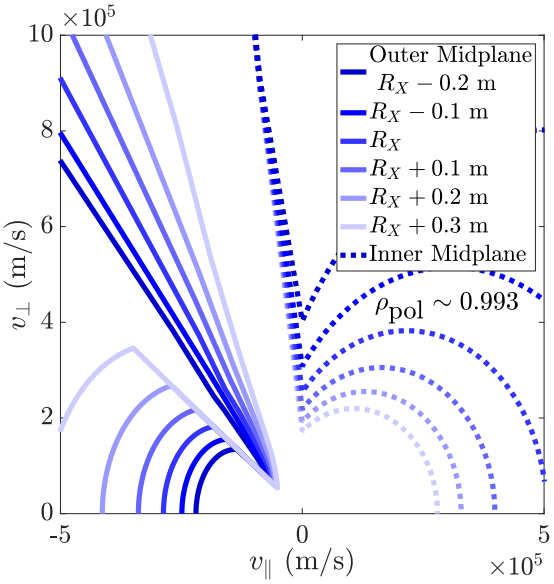

Figure 5.11: The velocity-space loss cone dependence on the horizontal position of the X-point.

Figure 5.11 illustrates the change in the velocity-space loss cone structure for the cones mapped to the outer and inner midplanes on the same flux surface with a changing horizontal position of the X-point. For simplicity, the analysis is performed for a constant electric potential. The cone shapes are still robust when considering different flux surfaces, with the loss energies scaling like $(\Delta\psi)^2$. The features discussed in the above paragraphs are

easily seen. Under increases in R_X, the LFS local loss cones grow in angular width, have an increasing passing loss energetic threshold, and have a decreasing trapped loss energetic threshold. The HFS local loss cones maintain their angular width, since all trapped orbits localized to an $R < R_X$ either interact with the X-point or would at some increased energy, and experience a wholesale decrease in their energetic thresholds.

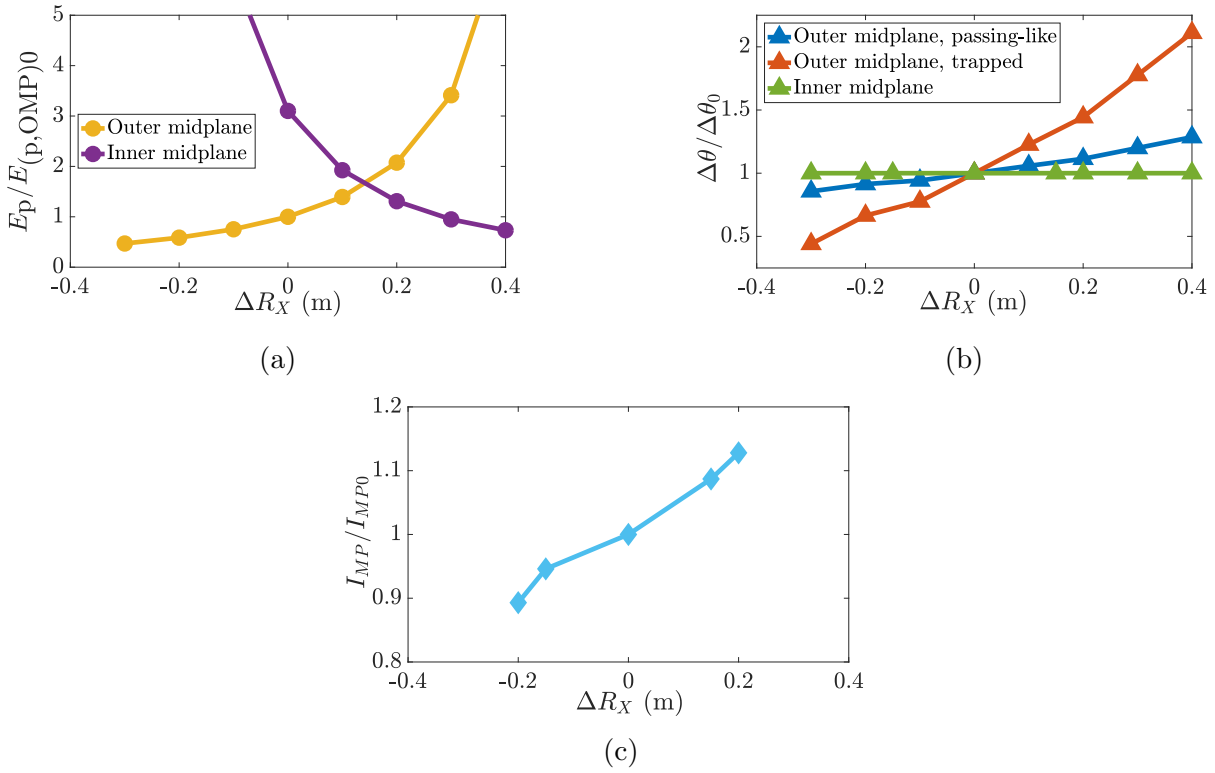

Figure 5.12: A deeper look at the orbit loss under changing R_X. Subplot (a) shows the passing loss energy threshold with changing X-point position, subplot (b) the growth of the angular width with decreasing triangularity, and subplot (c) an estimate for the orbit loss current dependence including contributions from the midplanes.

Figure 5.12 details the projected loss cone's sensitivities to the horizontal position of the X-point. Subfigure (a) plots the minimum energy for the passing losses for both the inner and outer midplane. Here, the energies are normalized to the threshold energy for counter-passing orbits at the outer midplane in the baseline positive triangularity case. The threshold energies are quadratic in R_X, with the counter-passing (co-passing) losses requiring increased (decreased) energies for a larger R_X. The energies are equal at an R_X nearly

equidistant in major radius to the inner and outer midplanes, slightly toward the HFS due to the increased parallel velocities on the LFS. Energetically, the counter-passing (co-passing) orbits are preferential for loss in the positive (negative) triangularity configuration, agreeing with the literature.[47]

Subfigure 5.12.b shows the change in the angular width of the local loss cones at the outer and inner midplanes. The velocity-space loss cones on the LFS have significantly larger $\Delta\theta$s for increasingly negative triangularity field configurations, with the proportional growth of the narrow region being significantly greater. The angular width of the high energy portion of the local loss cone is constant at the inner midplane. As seen in Figure 5.11, the disparity between the threshold energies of the smaller narrow region and the passing losses decreases with increasing R_X, increasing the fraction of the loss region described by this $\Delta\theta$.

The influence of R_X on the orbit loss current is assessed by considering the loss current source terms along the midplanes. As seen in Figure 5.2, the outer and inner midplanes capture the respective LFS and HFS loss behaviors. The losses are estimated by evaluating the orbit loss calculations with an artificially shifted R_X. The loss periods from the baseline geometry are maintained, thus the assumption is made that the loss periods from the midplanes are not strongly changed across the R_X scan. Here, changes to the orbital period are primarily caused by changes to the poloidal path lengths; however, such changes are expected to be far less than those seen under a ∇B reversal, see Section 4.3.5 and 5.6. As seen in Figure 5.12.c, the loss current shows a modest change over the horizontal position of the X-point, increasing with decreasing triangularity. Analysis with experimental equilibria covering the R_X scan is necessary to fully investigate this particular shaping parameter on the orbit loss current. In that vein, experiments have been proposed for the internal ASDEX Upgrade 2020 and 2021 campaigns[128] to investigate the radial electric field and plasma rotation in response to the triangularity of the active X-point. The experiments are performed under both ∇B directions to couple the drift reversal and shaping effects, creating maximum and minimum orbit loss scenarios. Scans over R_X have been performed on NSTX, showing

a decreased $P_{\text{L-H}}$ for greater R_X,[29] in line with the expectations of this section.

5.9 Secondary orbit loss terms

Similar integrals to those seen in Eqs. (5.4) and (5.6) can be evaluated to return source terms for the ion continuity, ion parallel momentum, and ion energy equations. Each scales with the magnitude of the orbit loss, but the effects of these terms are found to be minor compared to the current supplied by the ion losses, typically by an order of magnitude, but should be considered within a full treatment of the problem. The impact of the terms are discussed for the baseline SOLPS parameter set, where it will be seen in the upcoming chapter that the E_r well is deepened by $\sim 20\%$ in response to the orbit loss current. Beyond this section, the SOLPS simulations are performed only accounting for the loss current terms of primary importance.

5.9.1 Density source

The ion orbit loss particle flux is exactly equal to the current density unscaled by the charge per ion, resulting in the same relationship between the source terms, such that

$$S_{n,\text{c-less}} = \int_S \left\langle \frac{dw}{dt} \right\rangle f dS, \tag{5.12}$$

$$S_{n,\text{coll}} = \frac{1}{z - z_X} \int_{\Sigma_{\text{coll}}} \left(v_{\nabla B} + v_C \right) f d^3 v. \tag{5.13}$$

Both the collisionless and collisional density source terms are accounted for.

The density source terms are the most significant of the secondary orbit loss sources, decreasing the separatrix density by a few parts in one hundred. Even slighter changes, yet of similar order, are seen in the temperature, electric field, and rotation profiles. The disparity is centered about edge region contributing to the orbit loss and decreases in either

radial direction. Although the trend favors the steepening of the density profile in the edge region, it does not appear that the orbit loss in isolation can produce such steep changes necessary to form an H-mode pedestal.

5.9.2 Parallel momentum source

Estimating the parallel momentum loss directly associated with the ion orbit losses is less clear than calculating either the density or energy sources. The parallel momentum is a dynamic quantity over an orbit. To estimate the order of the momentum source, the calculation is performed in two ways. First, the lost parallel momentum is taken at the boundary of the loss cone where a previously confined orbit is considered scattered in,

$$S_{m\parallel,\text{c-less}} = m_i \int_S \zeta v \left\langle \frac{dw}{dt} \right\rangle f dS. \tag{5.14}$$

The second calculation estimates the parallel momentum of the orbit as it crosses the separatrix and considers this the lost momentum,[129]

$$S_{m\parallel,\text{c-less}} = \int_S \frac{p_\phi}{R_X f_\phi} \left\langle \frac{dw}{dt} \right\rangle f dS, \tag{5.15}$$

where it is assumed that $\psi_{\text{sep}} = 0$ and that the orbit is lost near the X-point. Note that p_ϕ is not a constant in Eq. (5.15), as the integral is over orbits on the boundary of the loss cone surface. It is assumed that p_ϕ does not greatly change due to the possible collisions from one loss orbit to another. Since the higher energy ions carry more momentum, only the collisionless portion of the loss cone is considered for either case.

Both methods result in apparent changes of the plasma density and temperature at the separatrix of far less than 1% for the baseline case. The more relevant term to compare, the parallel velocity, changes on the order of 1% at the separatrix, in absolute terms, changing by tens of m/s. The order of these changes is roughly maintained farther into the core. The

direct influence of the ion orbit loss on the parallel momentum is subordinate to both the effects in the particle and current continuity equations, and does not appear to be driving new physics. The orbit loss plays a more indirect role in influencing the parallel rotation via the mere existence of the loss cone structure, as seen in Sections 3.6.2 and 4.6.

5.9.3 Energy source

The energy source term is determined by the following:

$$S_E = \frac{1}{2} m_i \int_S v^2 \left\langle \frac{dw}{dt} \right\rangle f dS. \tag{5.16}$$

Again, only the collisionless loss cone is considered due to the disproportionate energy carried by faster ions.

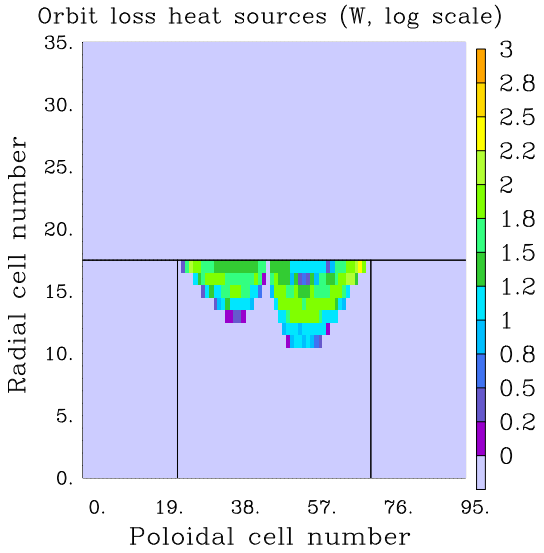

Figure 5.13: The log-scaled distribution of the orbit loss heat sources.

The distribution of the heat sources closely follows that of the collisionless losses, as seen in Figure 5.13. Although the loss cone contains trajectories up to arbitrarily large energies, the loss cone is refilled at a diminished rate at such high energies, tempering the heat loss. Similarly to the particle sink term, the energy sink slightly steepens the relevant profile,

here the ion temperature. Again the effect is small for the baseline case; the temperature is reduced at the separatrix by about one part in one hundred.

The density sink appears to largely wash out the energy sink term when simultaneously implemented. The natural inverse proportionality between the plasma temperature and density, Eqs. (5.10) and (5.11), coupled with the slightly larger magnitude density source term results in a slightly raised ion temperature at the separatrix, at about the difference in the magnitudes of the individual effects.

5.10 A brief look at further refueling mechanisms

In the preceding sections, pitch angle scattering was considered as the sole mechanism for refilling the collisionless loss cone. Any mechanism that contributes to the net transport of ions from confined to lost orbits contributes to the orbit loss and should be considered in a full treatment. Two neglected mechanisms are the anomalous radial transport resulting from turbulent plasma flows and the ionization of neutral particles within the loss cone. This chapter concludes with brief investigations of these two processes within the framework developed in Chapters 2–4.

5.10.1 Anomalous transport

The radial transport of particles in a tokamak plasma is typically dominated by the so-called anomalous transport, a namesake born from its unexpected observation in light of standard neoclassical calculations. Its origin is the plasma turbulence and the transport is fluctuation-driven. The significant role of the anomalous transport for the radial particle flux suggests importance for the radial orbit loss current. Particles driven radially outward enter regions with energetically accessible local collisionless loss cones, potentiating an annulus where the ions can be lost on a first orbit via the X-point and the electrons are fixed to the anomalous transport process. If the timescale for the anomalous radial transport across the separatrix

is slower than a typical loss orbit period, then the electrons lag the ions, necessitating a return current of cooler ions from the scrape off layer. If the radial transport outpaces the loss timescale, then the orbit loss effect is negligible. We precede under the assumption that the former is true and investigate a formulation for the orbit loss current rooted in the radial particle flux seen in the literature.[49]

It is assumed that the particle flux is evenly distributed in velocity-space over the local Maxwellian and flows radially outwards. Such an assumption is in no way guaranteed. Nonetheless, at some radial position, some fraction, F, of the particle flux, Γ, overlaps the local loss cone. The radial transport of ions already within the loss cone is immaterial for the orbit loss, and we only consider the first flux into the loss region,

$$\nabla \cdot j^{(\text{iol, AN})} \sim \frac{\Gamma}{h_y} \frac{\partial F}{\partial y}, \tag{5.17}$$

where F is the Maxwellian overlap, see Sections 3.6.1 and 4.4, of the collisionless loss cone, the fractional overlap of the local collisionless loss cone with the local Maxwellian. Here, we differ from the literature in that we only consider the anomalous flows into the loss cone that will be lost on a first orbit.

It is not immediately obvious how to directly implement Eq. (5.17) within the framework developed within the scope of this thesis. A local collisionless loss cone is demarcated by a hard boundary which represents the evaluation of the unscattered fraction, Eq. (4.16), as zero. For energies above this boundary, the unscattered fraction grows toward unity as a function of both the plasma and loss cone properties. To make a first order estimate of the orbit loss current driven by the anomalous radial particle flux, we redefine the collisionless loss cone to be demarcated by $F(E) = 1/2$ (Note: $F(E)$, the unscattered fraction, is a different quantity than F, the Maxwellian overlap) and take the unscattered half of the ions

refueling the loss cone to be lost,

$$\nabla \cdot j^{(\text{iol, AN})} = \frac{Ze}{2} \frac{\Gamma}{h_y} \frac{\partial F}{\partial y}, \tag{5.18}$$

where the radial particle fluxes are conveniently determined by SOLPS.

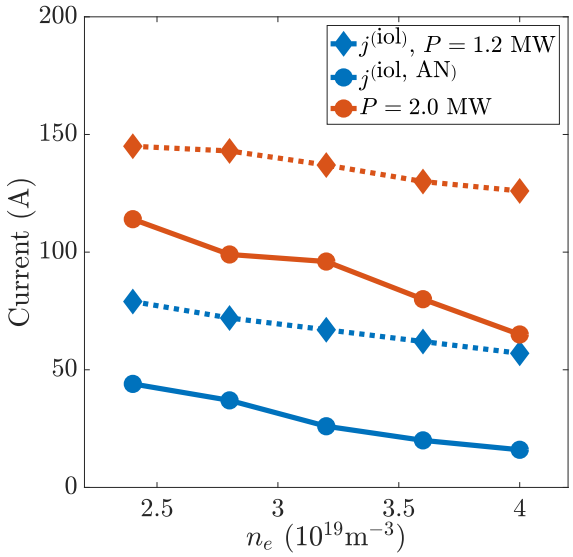

Figure 5.14: A comparison between the collisionally driven steady-state orbit losses and an estimate for the turbulence driven losses, each across the separatrix.

Figure 5.14 compares the total orbit loss current presented earlier in the chapter with the anomalous radial flux driven orbit loss current, Eq. (5.18), for two different input powers over the high density branch. Here, the density value represents the specified value for the core ($\rho_{\text{pol}} = 0.973$) ion continuity boundary condition, see Appendix A. The two currents are of the same order of magnitude and exhibit a similar behavior over the explored parameter space. The similar magnitudes can be understood by considering the radial particle flux into a numerical cell in SOLPS. The loss current sourced in the i^{th} cell considers only the ion flux into the local loss cone from radially inward confined orbits,

$$\left(\nabla \cdot \boldsymbol{j}^{(\text{iol, AN})}\right)_i = \frac{Ze}{2} \frac{\Gamma_{\text{i}}}{h_y} \left(F_i - F_{i-1}\right), \tag{5.19}$$

where i labels cells of increasing radius, Γ_i is the radial particle flux into the cell, and F_i is the Maxwellian overlap calculated at the cell center. It is seen that on the thermal collisional timescale, the radial particle flux into the cell is similar to the number of particles within the cell. Thus,

$$\nu_0^{-1}(T_i)\left(\nabla\cdot\boldsymbol{j}^{(\text{iol, AN})}\right)_i \approx \frac{Zen}{2}\left(F_i - F_{i-1}\right), \tag{5.20}$$

where $\nu_0^{-1}(T_i)$ is the ion-ion collisionality for thermal ions. Over the same timescale, the resupply of the local collisionless loss cone can be thought of as over the entire angular domain for the preferred thermal loss energies, see Figure 5.1.a, and the loss is on the order of the cone's overlap with the local Maxwellian over this band of energies, hence the similarities seen in Fig. 5.14.

A full treatment of the ion orbit loss should consider the net turbulent transport into the loss cone along with the net collisional transport into the loss cone. A more nuanced understanding of the velocity-space distribution of the radial particle transport is necessary to more accurately model the anomalously driven losses. Under the simple assumption that the distribution follows that of the local Maxwellian, it is seen that the contributions are of the same order. Furthermore, it is possible that turbulent fluctuations enhance the orbit losses,[34] and a systematic integration of turbulent effects into the loss cone model is a natural next step.

5.10.2 Neutral ionization

It should be noted that an additional source of ions refilling the loss cone is the ionization of neutrals.[35] Neutral particles flow through the plasma with first order disregard of the magnetic and electric fields. As they probe deeper into the plasma, entering regions of higher temperature, their interactions with the background are increasingly likely to leave them ionized. If the ionization occurs within the bounds of the collisionless loss cone, then

the ion will be lost on its first orbit, contributing to the steady-state ion orbit losses.

As it stands, the ionized neutrals are considered within the SOLPS framework and influence the equilibrium solution beyond the orbit loss calculations. Future work should be performed to investigate the velocity-space distribution of the ionized neutral particles in the edge, in order to determine their contributions to the ion orbit loss. Initial estimates indicate that the neutral ionization is not a main instigator of the orbit losses but plays a supplementary role. For the baseline SOLPS case presented throughout the chapter, the orbit loss current from the neutral ionization is on an equal footing with the total orbit loss current driven by pitch angle scattering if all ions born on flux surfaces with thermally accessible local collisionless loss cones are assumed lost. This assumption grossly overestimates the loss as it neglects the probability of scattering out of the loss cone and the more likely than not chance that the ionization occurs outside of the collisionless loss cone.

Throughout this thesis, SOLPS runs were performed using a fluid model for the neutral population. The SOLPS-ITER code package couples the fluid plasma code B2.5 with a Monte Carlo neutral transport code Eirene, which can assist in future investigation of the role played by the neutral ionization.

Chapter 6

The plasma response in SOLPS

The thermal ion orbit loss current in a diverted tokamak has been studied in isolation and has been shown to share several features with the empirically known L-H transition power threshold: branching density behavior, a strong ∇B drift direction dependence, and a dependence on the horizontal position of the X-point. It is naturally of interest to determine if the current that displays such behaviors interacts strongly enough with the plasma in order to play a role in catalyzing the transition. The non-ambipolar nature of the orbit losses necessitates closure via some other process. The tokamak edge environment modeled by the SOLPS fluid transport code is used to investigate the plasma response to the orbit loss current, largely focusing on the return current responsible for ambipolar closure and the resulting E_r response.

Naturally, the particulars of the plasma model in which the orbit loss calculations are embedded determines this physics and should be kept in mind. For instance, the SOLPS model, see Chapter 2, does not explicitly resolve the small spatial scale turbulent physics and models the phenomenon via the standard anomalous radial diffusion of energy and particles. The governing diffusivities are kept constant over the scans, thus the turbulent dynamics is not studied. Additionally, SOLPS is not built upon a framework which is sensitive to non-Maxwellian distribution functions in the plasma edge resulting from the loss cone structure,

and thus the model does not perfectly capture the orbit loss physics. In essence, the first order plasma response to the orbit loss current is presented. Significant developments would be necessary to study the higher order effects,[86–88] an effort beyond the scope of this thesis. Taken as a baseline, the SOLPS edge environment must shift in response to the radially outward ion orbit loss current to supply some combination of similarly flowing electrons or a return ion current, the expectation being an inward flow of cooler ions from the SOL.[64] The interplay between these currents and the physics driving them sets a new equilibrium condition near the separatrix, influencing the toroidal rotation and the radial electric field.

As seen in Chapter 2, there are a plethora of electric currents worthy of study within the edge of a tokamak plasma; refer to Section 2.4.2 for reference to the currents modeled in SOLPS. Although a research topic of great interest, we neglect the modeled current behaviors in the far scrape off layer and private flux regions, focusing on the core and SOL immediately beyond the separatrix. These currents in the far open field regions are effectively treated as boundary conditions for the ion orbit loss studies. With that in mind, we first take a look at the radial current balance in the absence of an orbit loss current, followed by a discourse on the impact of including the ion orbit loss current into the SOLPS framework. Again, the discussion is centered around the baseline ASDEX Upgrade discharge 16151 case, with scans occurring about this baseline, see Appendix A.

6.1 The radial current balance in the absence of ion orbit loss

The edge radial current balance as modeled by SOLPS under L-mode conditions can be separated into two qualitatively different regions: one nearer the core and the other within around one centimeter of the separatrix when measured along the outer midplane. The one-dimensional radial current balance is illustrated in Figure 6.1. Recall that many of the currents in the SOLPS model are effective currents with the same divergence as their physical

counterparts. Refer to Section 2.4.2 or the SOLPS user manual[71] for their exact forms.

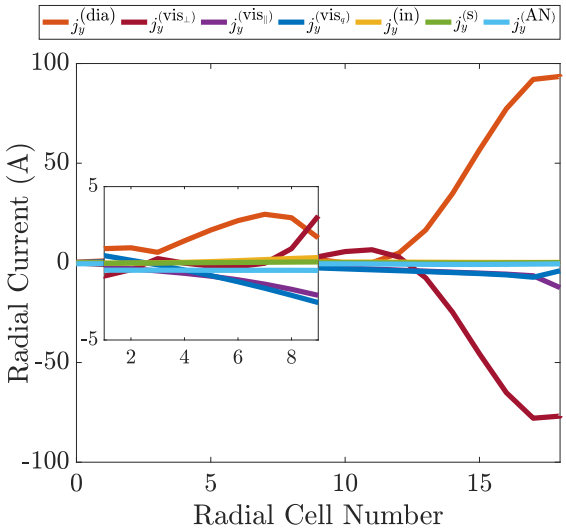

Figure 6.1: Divergenceful radial current flows within the separatrix in SOLPS obtained by integrating the contributions over the flux surfaces.

The more core-like region contains a current balance primarily involving a radially outward effective diamagnetic current that is closed by a combination of inward currents caused by the parallel and heat viscosities.[84,95] The effective diamagnetic current, Eq. (2.87), takes on a form which is sensitive to poloidal asymmetries in the plasma pressure, which result in divergent current flows in the plasma edge. Recall that this current is identified with the average guiding center motions of orbits in a spatially varying magnetic field,[70,84,89,90] and is thus inclined to disproportionately represent ion motions. The parallel and heat viscosity currents have similar forms, Eq. (2.96) and Eq. (2.100), and often appear to support the other, with possible dominance between the terms shifting due to subtle differences in the parallel ion particle and heat fluxes. Contributing less are the inertial current associated with centrifugal forces, Eq. (2.107), the perpendicular viscosity current, Eq. (2.98), and the current generated from the ion-neutral momentum sinks, Eq. (2.111). The first and third appear to be relatively divergenceless throughout the entire plasma edge, contributing relatively little to the current balance. The perpendicular viscosity current contains radial derivatives

of flux surface flows, which are expected to have limited importance toward the core. For nearly all radial positions, the anomalous current, Eq. (2.115), plays no significant role in the current balance, a consequence of setting the anomalous conductivity to a sufficiently small value.[84,96] Here, $\tilde{\sigma}^{(\mathrm{AN})} = 10^{-6}$ Sm^2/C. At the soft boundary between this region and the one nearer the separatrix, the role of the effective diamagnetic flow is replaced by a perpendicular viscous ion flow while the effective diamagnetic current has been suppressed. It would appear the the parallel and heat viscosity currents are reluctant to balance the outward flow of ions caused by the perpendicular viscosity current driven by the inner shear of the plasma rotations, requiring a dampening of the radial effective diamagnetic current flow.

Within about a centimenter of the separatrix measured at the outer midplane is the so-called viscous layer.[95] Here, the divergence of the effective diamagnetic current begins to grow on approach to the last closed flux surface, reaching values an order of magnitude greater than those involved in the balance toward the core boundary. The parallel and heat viscosity currents do not similarly become more divergent, a statement that the poloidal variation of the parallel ion and heat flows are not greatly changed from the inner region. However, the perpendicular viscosity current has a large divergence for these radial positions, providing closure for the effective diamagnetic current.[84,95] Such a current is associated with radial derivatives of flux surface flows, which can be extreme when crossing the separatrix. The other currents near the separatrix are at least an order of magnitude smaller than the discussed currents and do not appear to have a strong effect on the equilibrium solution.

Figure 6.2 shows the two-dimensional flow patterns for the two dominant currents in the near-separatrix balance, where the orbit loss current is significant. Subplot (a) shows the global current structure of the effective diamagnetic current in configuration-space, where the connection to the vertical drifts is more apparent. In the upper half of the confined plasma the flux surfaces are concave down and the ion (electron) flows are radially inward (outward) and vice versa for the lower half. More easily seen in subplot (b), the local core

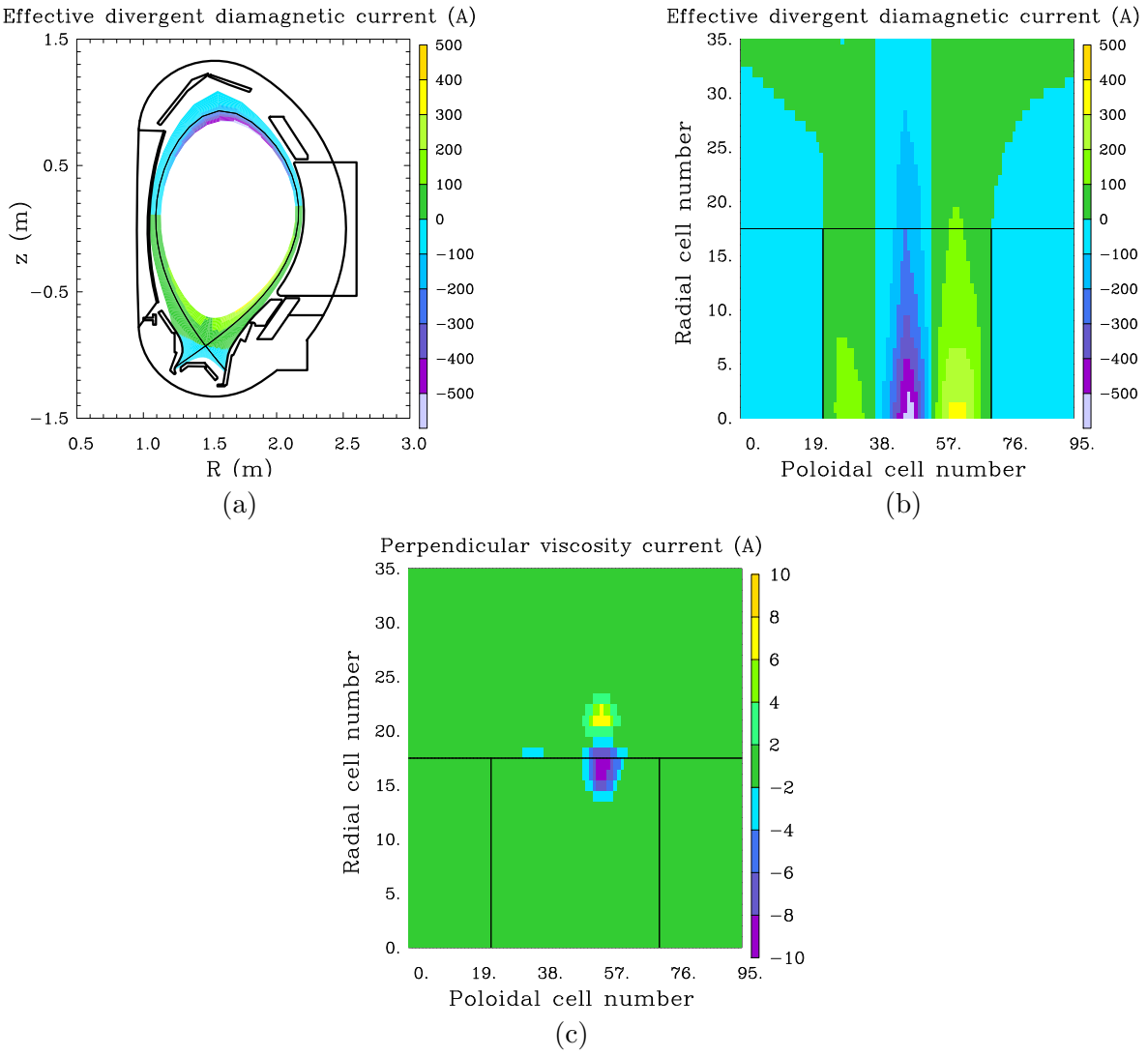

Figure 6.2: The effective diamagnetic and anomalous perpendicular viscosity currents in SOLPS.

divergent diamagnetic current flows are quite large and average to much smaller values over a closed flux surface. The poloidal pressure asymmetries which govern the magnitude of the net effective diamagnetic current flow across a flux surface are greatest very near the separatrix, see Fig. 6.1, and will be further discussed in the upcoming section. The relevant perpendicular viscosity flows involved in the edge current balance are centered about the separatrix near the outer midplane and, to a lesser extent, the inner midplane, as seen in subplot (c). Ions in the near SOL tend to flow either inward or outward depending on their relative positioning around the peak of the flux surface flows in the SOL. Those that

flow radially inward provide the bulk of the necessary closure for the effective diamagnetic current.

The thermal ion orbit losses are of primary importance within the annulus described by the viscous layer near the separatrix. The interplay between the ion orbit loss current and the effective diamagnetic and perpendicular viscosity currents will define the new radial current balance in this region. Before introducing the orbit loss current, the behavior of the driving effective diamagnetic current is studied over parameter space, and thus also the necessary perpendicular viscosity current for closure.

6.1.1 The current balance over parameter space

The behavior of the standard current balance in terms of the relevant parameters for the orbit loss, the ion temperature and the electron density at a constant input power, is briefly studied, providing context for the orbit loss studies. The radial current balance near the separatrix typically reflects the specific instance plotted in Figure 6.1, so the focus is turned to the balance between the effective outward diamagnetic current and the inward perpendicular viscosity current. Since the perpendicular viscosity current can be thought of as the response to the outward diamagnetic ion flow, it is natural to study the driving effective diamagnetic current.

The effective diamagnetic current takes the form of the distribution averaged vertical drifts resulting from single particle motion in an inhomogeneous magnetic field. The velocity-space average removes any sensitivity to the loss cone structure and describes the averaged drift motions for each species in terms of pressure disparities about a given flux surface. Orbits both inside and outside of any loss cone contribute equally to this current. For a circular flux surface with a constant pressure profile, vertical drifts in the upper half of the plasma move ions radially inward, exactly canceling the current associated with the outward motion of the same drifts in the lower half of the plasma, assuming that ∇B points down. The larger orbital widths for the ions allow for greater poloidal temperature asymmetries,

allowing for a greater poloidal deviation in the ion pressure away from the density variation. This and the strong shaping of the flux surfaces near the separatrix allow for a net divergent radial current flow. Larger average pressures over one half of a flux surface indicate either higher temperatures or larger densities, both increasing the vertical flux of ion in the inward (outward) direction for the top (bottom) half of the device and vice versa for the electrons, again, assuming that ∇B points down.

It would be remiss not to note an inconsistency born of simultaneously treating the effective diamagnetic current and the orbit loss current. The orbit loss current tracks an excess ion flow through the separatrix due to topologically open orbits lost to the divertor via the X-point while the effective diamagnetic current counts an imbalance of flux surface averaged vertical drifts linked to poloidal pressure asymmetries. The possibility for these currents to flow in opposing directions is noted. This particular form of the effective diamagnetic current is not directly sensitive to the features of a non-Maxwellian distribution function caused by the presence of the loss cone and neglects the sparse population of the collisionless loss cone. The effective diamagnetic current could be recalibrated to exclude orbits within the collisionless loss cone, instead averaging over a Maxwellian with a hole. Such a correction is left for future works, and in Section 6.2 the orbit loss current will be implemented into the standard SOLPS regime.

Figure 6.3.a illustrates the effective diamagnetic current flow across the separatrix over a scan in the input power for two different core density cases. Here and throughout the chapter, the density values represent the specified value for the core ($\rho_{\text{pol}} = 0.973$) ion continuity boundary condition, see Appendix A. The simulated densities are typically limited to the high density branch for the orbit loss current due to a numerical instability in SOLPS found below some threshold density for a given input power, see Section 2.4.2.5.[96] Also plotted for reference is the instantaneous orbit loss current for similar profiles. Both currents are of similar magnitude and scale directly with the input power, with the effective diamagnetic current responding more greatly. Interestingly, the gap between the two density cases lessens

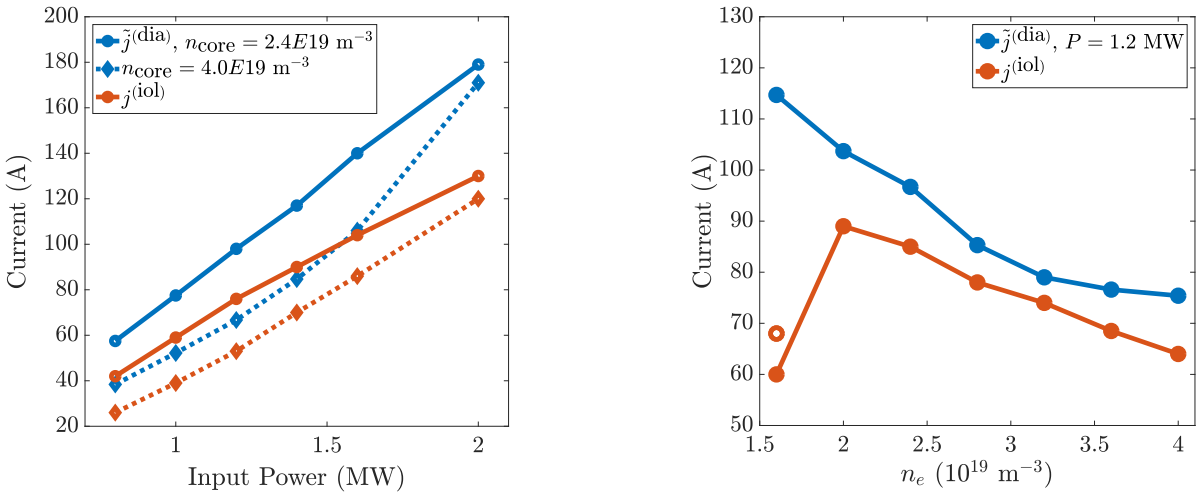

(a) (b)

Figure 6.3: The effective diamagnetic current flowing across the separatrix in SOLPS over parameter scans. The instantaneous orbit loss current is shown for comparison. The hollow point in (b) corresponds to artificially reducing the electric field to half strength.

for the largest input power. The reasoning for the two currents is different, as can be seen by the steepened slope of the effective diamagnetic current for the high density case and the tempered slope of the orbit loss current for the lower density case. The poloidal ion temperature variations are proportionally smaller for the former at increasing input power, bringing the electron and ion pressure asymmetries more into phase with each other via the growing dominance of the density asymmetry. The density variations do not change in relative size, but shift toward an up-down asymmetry, further increasing the net effective diamagnetic current. As discussed in Section 5.5, the low density orbit loss case suffers a decreased current due to surpassing the saturation temperatures of the average local collisionless loss cone.

Figure 6.3.b illustrates the effective diamagnetic current flowing through the separatrix over a core density scan with a constant input power of 1.2 MW. Over the high density branch of the orbit loss current, the two currents are similar in magnitude and unsurprisingly scale similarly since both effects are dependent on the orbital widths. Although, the diamagnetic current appears to experience accelerated growth with decreasing density, and unlike the orbit loss current, it does not exhibit a low density branch within the probed parameter

space. As will be seen in the Fig. 6.5, the electric field strength is about a factor of two larger for the lowest density case compared to the next least dense. The disconnected orange marker with a white center corresponds to the instantaneous orbit loss current calculated using an electric field profile at half strength. It serves to remind that the low density branch results largely from the decreases in the density and collisionality paired with the higher temperatures and is secondarily suppressed by the larger field strength.

Figure 6.4 illustrates the near separatrix poloidal asymmetries in the pressure, density, and temperatures for the minimum and maximum density cases seen in Fig. 6.3.b. Subfigures (a) and (b) plot the ion, electron, and plasma pressures about a flux surface very near ($\rho \sim 0.999$) the separatrix, respectively for the low and high density case. Subfigures (c) and (d) show the poloidal variations of the constituent parts of the pressures. The larger effective diamagnetic current flow through the separatrix is linked to larger pressure asymmetries about the near separatrix flux surfaces in the low density cases. Here, the density asymmetry is proportionally large and dominates the pressure asymmetry, affecting both the ions and electrons similarly. The density is largely up-down antisymmetric, forcing both species to experience the same up-down asymmetry in their pressures, resulting in a significant effective diamagnetic current flow. At the higher densities, the ion temperature asymmetry proportionally dominates the ion pressure variation and has nearly the inverse distribution of the density asymmetry, which for the high density cases shifts toward an in-out asymmetry. The smaller electron temperature variations leave the electron pressure asymmetry more closely tied to the density. Thus, the ions and electrons experience an opposite in-out pressure asymmetry, resulting in a lesser net diamagnetic current flow across the LCFS. The physics determining the poloidal symmetry differences is beyond the scope of this thesis and could be further explored using the SOLPS model. Likely candidates include differences between neoclassical collisional regimes or the poloidal distribution of ionizing neutrals.

The electric field well depths for the simulations corresponding to the points seen in Fig. 6.3 are shown in Figure 6.5. The linear growth of the electric field in response to increased

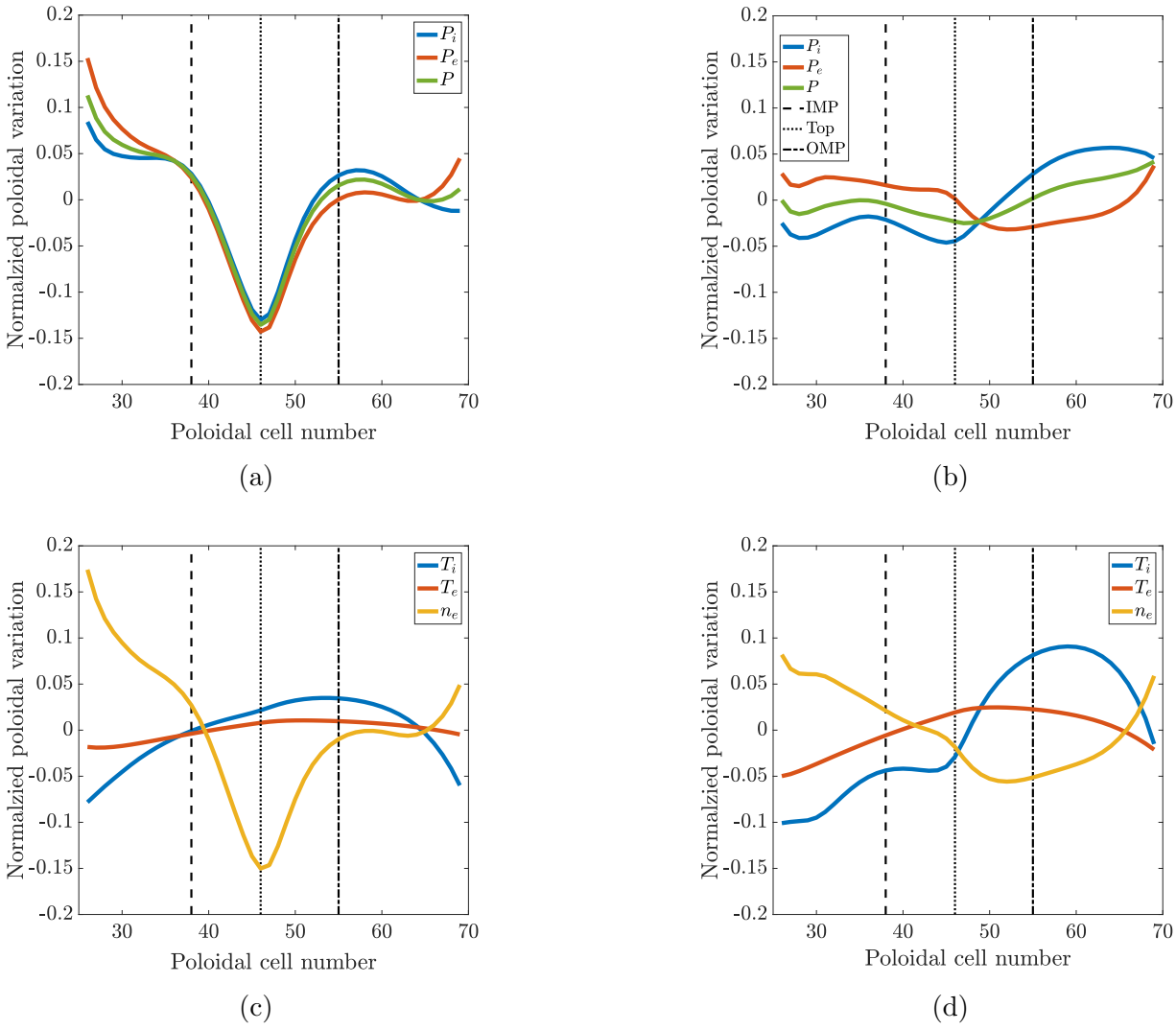

Figure 6.4: The poloidal pressure asymmetries driving the effective diamagnetic current at low, subplots (a) and (c), and high, subplots (b) and (d), density.

heating is seen in subplot (a), with the E_r wells in the lower density plasmas deepening at a faster rate. The E_r strength follows the basic scaling of the effective diamagnetic current; however, the high density case is, in a sense, less effective at converting the diamagnetic current into the E_r response. The two simulations corresponding to the highest input power have nearly identical radial current balances, with differences on the order of the subordinate parallel and heat viscosity currents. The higher density case is necessarily driven to a lesser radial electric field in order to support the necessary equal inward perpendicular viscosity

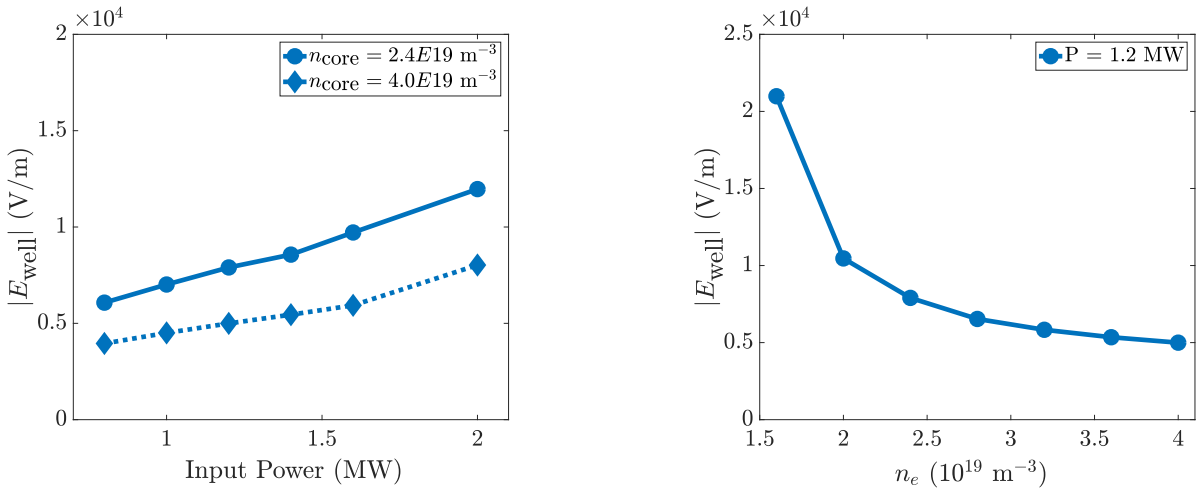

(a) (b)

Figure 6.5: The minimum E_r well depth in SOLPS without the orbit loss current.

current. The neoclassical poloidal rotation in the closed field line region is lesser for the higher density case with lower temperature, see Eqs. (2.48) and (2.54), but the poloidal rotation is of the same order in the near SOL for both cases. In the perpendicular viscosity current, the decreased shear across the separatrix of the poloidal rotation in the high density plasma is scaled by $\eta_{\text{AN}} \sim n$, allowing for a similar return current in a lesser shear system. It is noted that the classical perpendicular viscosity shows an identical scaling when the plasma pressure is held constant, but $\eta_2 \sim n^{3/2}$ when including the effective χ_i of the fluid neutrals, see Eq. (5.11).

Subplot (b) illustrates the E_r well magnitude as a function of the core density for 1.2 MW of input power, mirroring subplot (b) of Fig. 6.3. Again, the field strength follows the basic behavior of the diamagnetic current, which non-linearly grows with decreasing density as discussed above. The E_r response deviates from the effective diamagnetic current behavior again due to the ease of higher density plasmas supplying the necessary return current with lesser shear poloidal flows. This trend continues throughout the chapter, where the orbit loss current is less effective at generating a large E_r response at higher densities.

6.2 Implementation of the orbit loss model into SOLPS

The orbit loss model is implemented into the SOLPS source code as a subroutine that can be called any set number of timesteps. The static field geometry used by the simulation and the dynamically evolved plasma profiles are provided to the subroutine, the field quantities at cell vertices and the profiles at cell centers. Finer data is required to determine the electric field sensitive trapped-passing boundary and simple interpolations on this data are performed.

The orbit loss calculations are performed at the cell centers. The local loss cones for orbits passing through the center of each cell are calculated following the guidelines seen in Chapter 3. The cones are then demarcated into the local collisional and collisionless loss cones using the local plasma conditions, as described in Chapter 4. The orbit loss current source terms shown in Chapter 5 are determined again by assuming local Maxwellian distributions functions with the temperatures and densities provided by SOLPS. The source terms are applied evenly over each cell. The altered SOLPS equations contribute to the evolution of the profiles, and the cycle between the orbit loss subroutine and the SOLPS code is established. As seen in Section 5.9, the secondary orbit loss source terms effect minor changes to the plasma and are not included in the following simulations.

6.3 The radial current balance in the presence of orbit loss

We next introduce the steady-state total ion orbit loss current as discussed in Chapter 5. The orbit loss current contributes to the current balance on the same scale as the most significant contributors very near the separatrix, the effective diamagnetic current and the perpendicular viscosity current. Toward the core, the orbit losses are negligible and only affect the solution here by virtue of the core's response to changes near the LCFS. The orbit

loss current enters the current continuity equation through its divergence and the associated flows are not modeled, leaving the plasma response insensitive to these flows themselves. Corrections would modify terms that depend on the radial particle and heat flows, such as the poloidal ion neutral friction current, Eq. (2.108). The presented results represent the first order effects of the orbit loss current on the tokamak plasma.

The new radial current balance in the presence of the orbit losses can be seen in Figure 6.6. The core region's current balance remains relatively unchanged; the qualitative behaviors of each current here appear robust with magnitudes slightly shifting to ensure quasineutrality. The most flexible currents appear to be the parallel and heat viscosity currents, responding to the changed parallel flows at the separatrix.

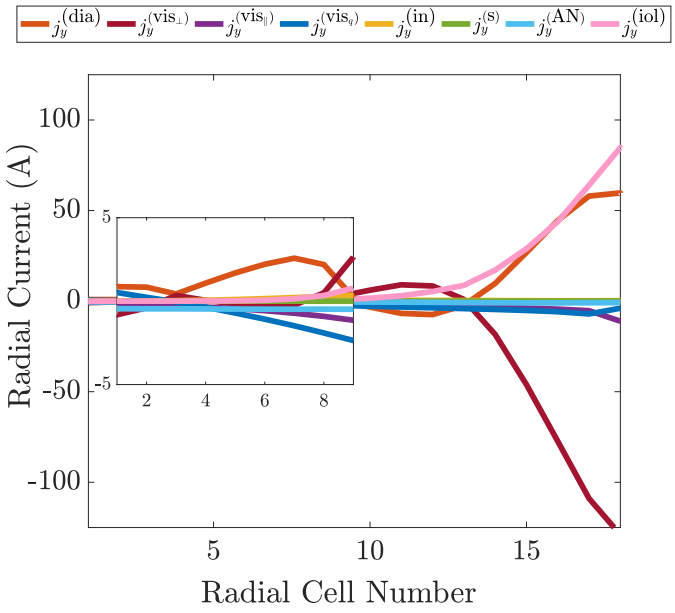

Figure 6.6: Divergenceful radial current flows within the separatrix in SOLPS including the ion orbit loss current.

Nearer the separatrix, there is an obviously more significant change in the current balance. The ion orbit loss contributes on an equal footing with the effective diamagnetic current. Nonetheless, the dynamics of the current balance are relatively unchanged; now, an outward flow of diamagnetic ions and orbit lost ions are compensated by an inward flow of ions due

to the perpendicular viscosity. The next order contributions again come from the heat and parallel viscosity currents, with the inertial and ion-neutral friction currents contributing to a lesser degree. The artificial anomalous current has been ordered down to the level of these latter two via the appropriate choice of $\tilde{\sigma}^{\mathrm{AN}} = 10^{-6}\ \mathrm{Sm}^2/\mathrm{C}$.

At the interface of the two regions described in the above, there is an interesting behavior briefly mentioned in Section 6.1, which grows in prominence in response to the orbit losses. The perpendicular viscosity current changes signs more or less at inflection points of the perpendicular flux surface flows. For typical core plasma rotations, see Appendix A, the required rotations at the separatrix that ensure quasineutral particle flows across the LCFS must be part of a radial profile that inflects further towards the core, thus requiring a change in the current flow associated with the perpendicular viscosity. The other viscous currents within the SOLPS framework appear inadequate at balancing the necessary, albeit small, outward flow, generally requiring a dampening of the effective diamagnetic current. The orbit loss exacerbates this effect as it tends to both increase the shear of the near separatrix flows and push the minima of well-like phenomena closer to the separatrix. A result being that the effective diamagnetic ion flows in this intermediate region can further dampen to the point that this radial current locally reverses orientation.

A poloidal redistribution of the plasma pressure, largely tied to a poloidal redistribution in the electron density, reduces the net effective diamagnetic current through the separatrix in the presence of the orbit loss. As seen in Figure 6.7, the electron and ion temperatures remain relatively fixed, and there is a displacement of particles from the lower half of the plasma on the HFS to the upper half of the plasma, maintaining a roughly constant number of particles about a flux surface. Quasineutrality ensures that the redistribution is ambipolar, and both species are shifted uniformly; however, the larger variation in the ion temperature results in a disproportionate change in the effective diamagnetic current carried by the ions. The change in the poloidal density profile near the separatix is an unsurprising display, considering the redistribution seen when switching on the $E \times B$ and diamagnetic drifts in

the SOLPS regime.[84]

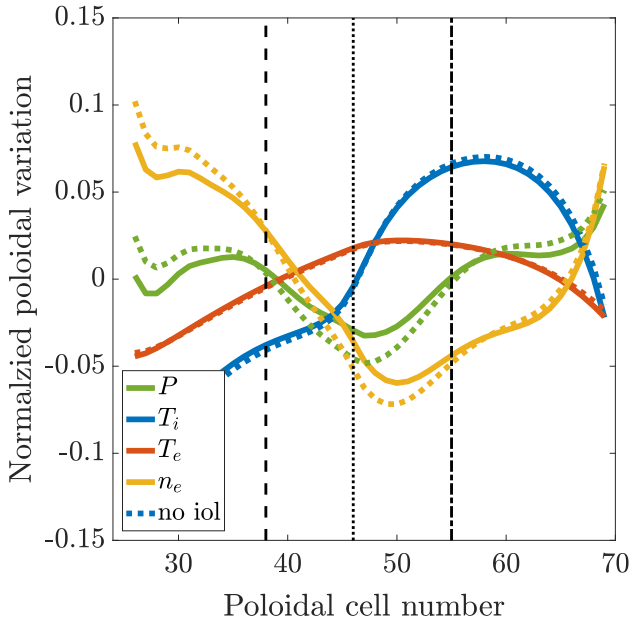

Figure 6.7: The poloidal pressure redistribution in the presence of the ion orbit loss current.

For the standard case omitting orbit losses, the equilibrium state is achieved through the balance of the effective diamagnetic flows and the return ion current largely supplied via the perpendicular viscous effects. The introduction of the orbit loss current instantaneously increases the outward current flow, instigating a matching return current. The current balance does not occur in a vacuum, necessitating a response in the plasma rotations driving the viscous current. The plasma equilibrium met in the absence of the orbit losses is broken and evolves into a new state where the effective diamagnetic current is suppressed. Although this effective current flow through the last closed flux surface is reduced for a given input power and density, its sum with the ion orbit loss current corresponds to a greater current carrying ion flow across the separatrix into the SOL. A roughly 50% increase is typically seen over the explored parameters. For instance, compare the currents of the baseline case seen in Figures 6.1 and 6.6. The net increase is the outflowing radial current is naturally matched by a stronger inward current carried by the perpendicular viscous flows. The implication is the presence of stronger sheared flux surface flows that are also perpendicular to the magnetic

field. Per the discussions of Chapter 2, the terms in the lowest order equilibrium radial force balance are further constrained by other typically higher order projections of the momentum balance. The toroidal force balance can be rewritten in terms of radial particle fluxes, finding equivalency with the quasineutrality condition. In the steady-state, this balance sets the toroidal rotation and thus the equilibrium radial electric field. The introduction of the orbit loss current generically increases the magnitude of the radial electric field well near the separatrix through its interaction with the other currents in the force balance.

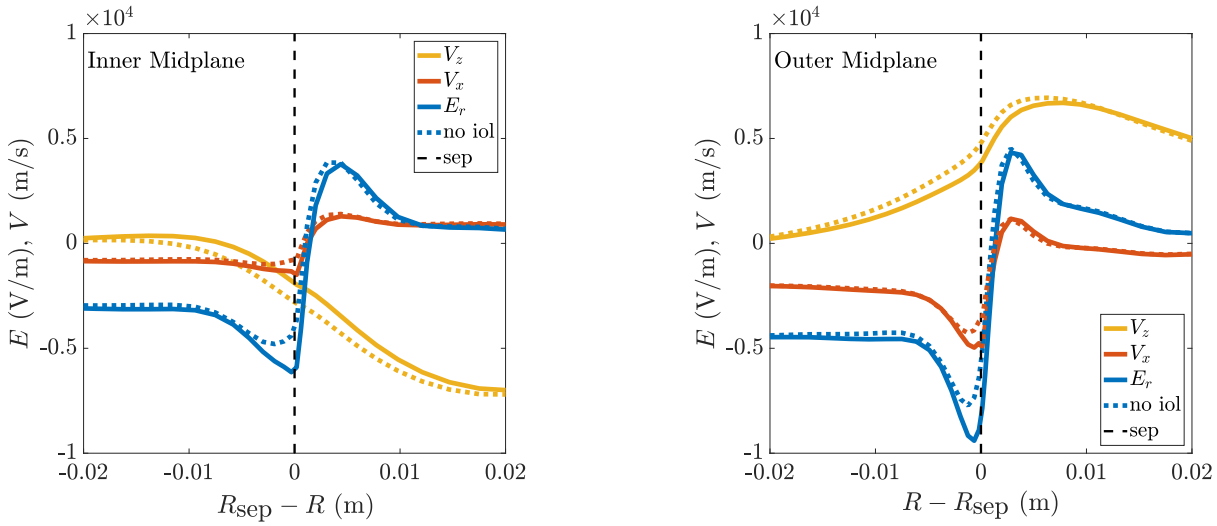

Figure 6.8: The plasma response to the ion orbit loss current: Rotations and E_r. Subplot (a) is along the inner midplane while subplot (b) is along the outer midplane.

The impact on the plasma rotations and the radial electric field of the orbit losses is illustrated for the baseline case in Figure 6.8, presented as radial profiles along the inner and outer midplanes. Approximately proportional changes occur over the poloidal coordinate. The responses scale with the net orbit loss and diamagnetic currents and will be explored over parameter space in the next section. The changes are mostly isolated to the domain of the orbit loss current. The far scrape off layer remains relatively unchanged by the orbit loss, a result of the assumption that the orbit lost ions are effectively removed from the system at the divertor, and the ion orbit loss current is divergenceless in the open field line region.

The fluid velocity profiles are steepened near the separatrix, with the changes in the toroidal velocity decaying over a longer distance, being felt in both the near SOL and deeper into the core. The changes in the plasma rotation are matched by a deepened E_r well. In this specific instance, the well has deepened by about one part in five, a magnitude still on the same order of the neoclassical electric field. The deeper E_r well following the inclusion of the orbit losses is reminiscent of the discrepency seen between SOLPS simulations and particle following ASCOT simulations that numerically determine the orbit loss current.[103,130]

There is an outward radial shift in both the well position within the separatrix and the peak position in the SOL by about half a millimeter at the outer midplane. The ion orbit losses increase both the inner and outer E_r shear. The effectiveness of the orbit losses in increasing the magnitude of the E_r gradient appears to be dependent on the neoclassical E_r values describing the more core region for the inner shear and the SOL E_r determined largely by the parallel electron dynamics for the outer shear, both of which are mostly insensitive to the modeled ion orbit loss. In any case, the ion orbit loss steepens the plasma rotation and radial electric field profiles in the plasma edge, emblematic features of the L-H transition.

6.4 SOLPS parameter scans with the orbit loss current

The radial current balance and leading order force balance responses are investigated over scans in the input power and the core electron density. This section focuses on the combined effects of the orbit loss current and the other currents modeled in SOLPS in establishing the tokamak edge environment. For a discussion on the dependence of the orbit loss current on the plasma parameters, refer to Section 5.5. As earlier mentioned, the density scan is limited by a lower bound set by a numerical instability seen below some threshold density for a given input power,[96] necessitating unfavorably small time steps for the desirably small σ^{AN}. Unfortunately, the low density branch of the orbit loss current lies in this omitted region, and only the high density branch is effectively studied over the parameter scan. Future work

will be done to investigate the lower densities.

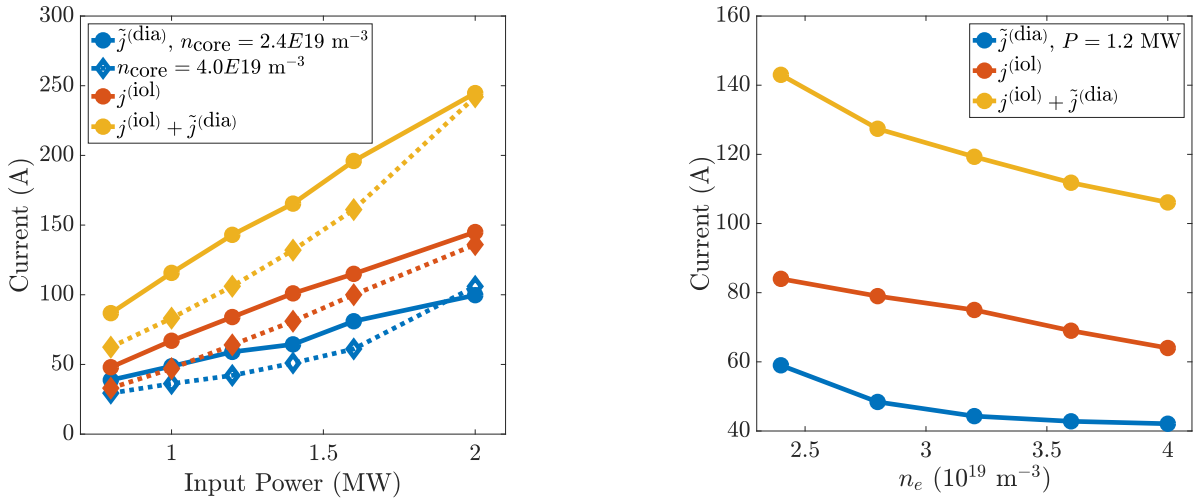

(a) (b)

Figure 6.9: The orbit loss and effective diamagnetic currents flowing across the separatrix.

Figure 6.9 illustrates the dominant outward radial current flows across the separatrix. Again the perpendicular viscosity current is largely responsible for the compensating inward flow of ions and can be thought of as nearly equal in magnitude to the sum of the outward orbit loss and effective diamagnetic flows, with leading order differences attributed to the parallel and heat viscosity currents. Subplot (a) scans over the input power, under the assumption that the power is delivered equally to the electrons and ions: an input power of 1.0 MW delivers 0.5 MW to each species. Similarly to Figure 6.3.a, two core density cases are presented. Recall that the density values represented in the SOLPS scans are for the specified value for the core ($\rho_{\mathrm{pol}} = 0.973$) ion continuity boundary condition, see Appendix A. As discussed in Section 6.3, see Figure 6.6 and ultimately Figure 6.7, the effective diamagnetic current is reduced in the presence of the orbit loss current and is of the same magnitude but subordinate to the orbit loss current over the parameter space. The suppression of the effective diamagnetic current is non-trivial as it depends on both the strength of the orbit loss current, the effective diamagnetic current in the absence of the orbit losses, and the plasma parameters. In general, the suppressed current grows with the

orbit loss current, although the proportional suppression appears to wane with increasing input power. The orbit loss current is less than that seen in Fig. 6.3.a due largely to the growth in the E_r magnitude in response to the orbit loss current.

The total outward current flow largely maintains a linear scaling over the range of input powers since the simulations occur over the high density branch of the orbit loss. Slight deviations in the linear behavior can be seen because the lower density case is transitioning to the low density branch at the largest input power, manifesting as a decreasing slope. Additionally, the high density case shows signs of non-linear growth for the largest input power, a consequence of the effective diamagnetic current discussed in the previous section. The total outward flowing current grows roughly 30% faster with increasing input power compared to the effective diamagnetic current in the absence of orbit losses and over the plotted range corresponds to an increase between a factor of 4/3 and 3/2.

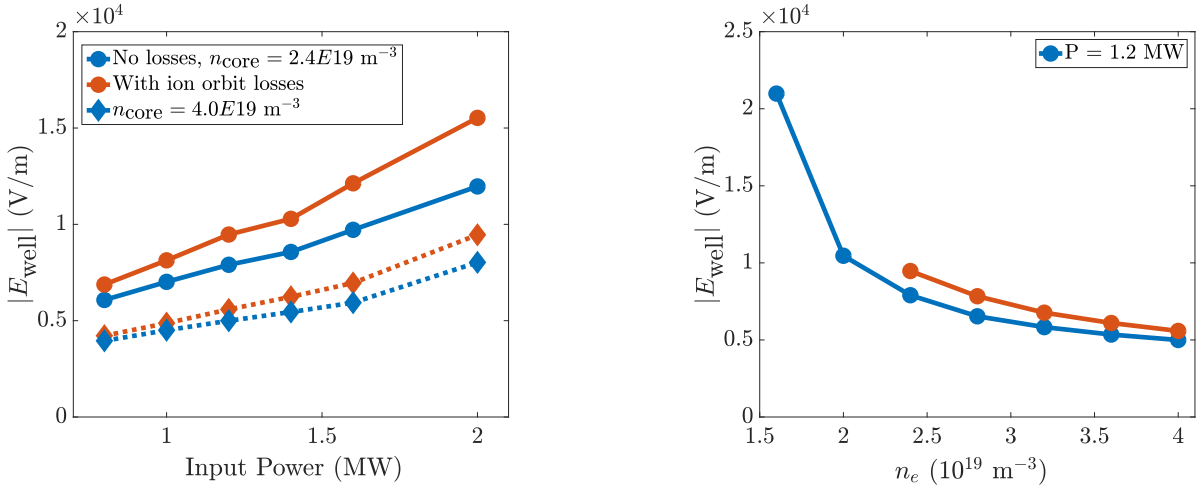

(a) (b)

Figure 6.10: The minimum E_r well depth in SOLPS with the orbit loss current. The lines determined in the absence of the orbit losses are reproduced from Fig. 6.5.

The magnitude of the electric field well at the outer midplane in the presence of the orbit loss is presented in Figure 6.10 with conditions matching simulations represented by the points in Fig. 6.5. The electric field responses in the absence of the orbit loss current are

reproduced for comparison. The low density instability is exacerbated by the orbit loss, and the parameter scan is firmly set over the high density branch of the loss current. The essential behavior of the electric field response remains: the field strengthens with increasing input power, favoring growth for the lower density plasmas. The electric field again roughly scales with the current flowing outward across the separatrix, and for similar reasons that cause the lower density plasmas to exhibit larger electric fields under similar current balances, the bolstered outward current flow results in a disproportionate growth in the electric field for the lower densities of the high density branch.

The L-H transition is often thought to occur when some critical E_r shear is sustained by the plasma.[21,31] Here, the more or less static length scales of the electric field structure directly ties the shear to the well depth, the critical E_r shear corresponding to some threshold depth. For instance, if the threshold well depth is 10^4 V/m, the simulations with the lowest electron density achieve this strength E_r around 1.28 MW with the orbit losses and 1.64 MW without. Similarly, extrapolating to larger input powers for the highest density simulations shifts the threshold input power from 2.35 MW to 2.09 MW, a similar order, yet smaller, reduction. The orbit losses affect the radial electric field on a scale of interest for the L-H transition. The high density branch of the L-H transition power threshold should be systematically studied with SOLPS coupled to the orbit loss model to probe if the enhanced radial electric field due to the orbit loss current reproduces the input powers experimentally required to access the H-mode.

It is an open question whether the damped orbit loss current along its low density branch will suppress the effective diamagnetic current such that the total current flow exhibits a branching behavior under a scan in the electron density. It is possible that the reduction of the diamagnetic current through correcting for the loss cone structure makes this possible. Furthermore, if the electric field could exhibit such a response also remains an open question, one more tenuous thanks to the density dependence of the anomalous viscosity coefficient. These questions necessitate pushing the SOLPS simulations to lesser densities. Once this

is feasible with the coupled orbit loss model, a similar study to the one mentioned above should be performed over the low density branch of the L-H transition power threshold.

The entire parameter scan is shown in Figure 6.11: scanning over input powers 0.8, 1.0, 1.2, 1.4, 1.6, and 2.0 MW and core boundary densities 2.4, 2.8, 3.2, 3.6, and $4.0 \cdot 10^{19}$ m^{-3}. Each vertex in subplots (a) and (c) represent a single SOLPS simulation coupled with the orbit loss calculation while those in subplot (b) correspond to a simulation omitting the orbit loss current. The vertices in subplots (c), (d), and (e) represent pairs of simulations with and without the orbit loss current implemented. An interpolation scheme is used to represent the parameter space interior to the vertices. The basic features of the orbit loss over the high density loss branch can be seen as well as the electric field response in the SOLPS environment.

Subplot (a) presents the maximum radial electric field well depth found near the outer midplane in each of the simulations with the orbit loss current added to the current balance while subplot (b) shows the same in the absence of the loss current. Subplot (c) plots the magnitude of the orbit loss current flowing across the separatrix in each of the simulations in (a). The absolute change in the electric field well depth, ΔE_r, following the introduction of the orbit loss current is shown in subplot (d). The well deepens in every case. Subplot (e) illustrates the fraction of the equilibrium radial electric field that is attributed to the orbit loss current, that is, the change in the electric field well scaled by its final magnitude.

The stagnated growth of the orbit loss current for increased input power can be seen for the lower densities along the high density branch, as discussed in the previous chapter. The absolute change in the electric field is decoupled from the orbit loss current behavior due to the weaker electric field response at higher densities for a similar current balance. The E_r magnitude seen in (a) roughly maintains the behavior seen in SOLPS before accounting for the orbit loss, see subplot (b), since the absolute change follows the same behavior, see subplot (d). The outward flowing current for the high density cases must exceed that seen for the less dense plasmas by some margin in order to exhibit a stronger radial electric

field. Although the high density plasmas exhibit a weaker response, the portion of the radial electric field attributed to the orbit losses is more evenly distributed across the parameter space, at the lower input powers taking a form similar to the orbit loss current. At the greatest input power, the nonlinear growth in the electric field is noted, favoring stronger growth at lower density, and this dependence overpowers the orbit loss current sensitivity. The orbit loss current like behavior in subplot (e) transitions to the generic SOLPS electric field behaviors seen in subplots (a), (b), and (c) at the highest input powers.

Over the high density branch of the orbit loss current, the response in the radial electric field to the steady-state orbit loss current is substantial. The strength of the response grows nearly linearly with increasing input power and decreasing density over the parameter space. The input power required to achieve some threshold E_r is reduced by $\sim$ 10–20% with the reduction increasing with decreasing edge density. The magnitude of the orbit loss effect paired with its qualitatively similar dependencies to the L-H transition power threshold serves as strong evidence for their connection.

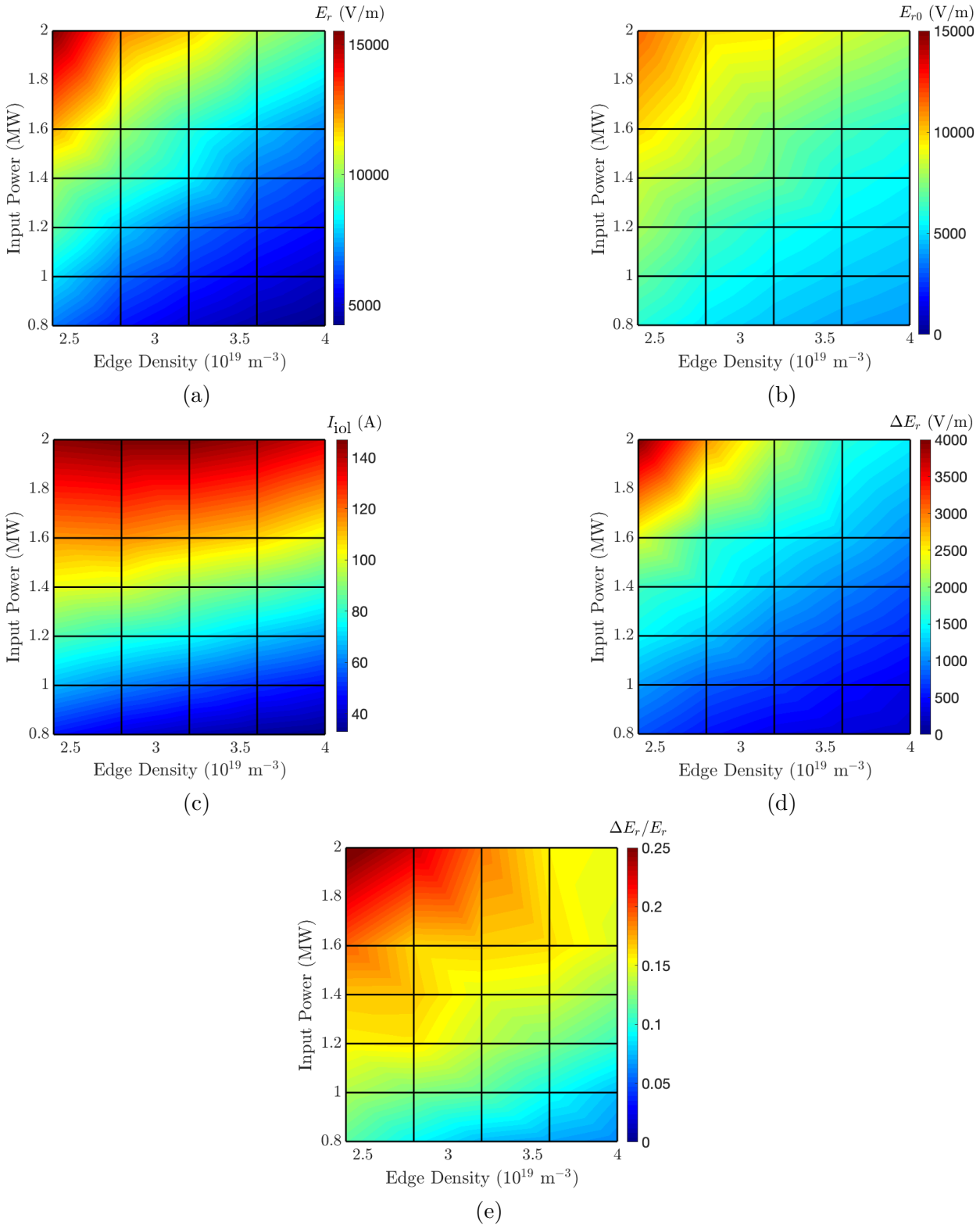

Figure 6.11: SOLPS parameter scans. Each vertex represents at least one simulation. In order, the minimum well depth following, (a), and preceding, (b), the orbit loss, the orbit loss current, (c), the response change in the well depth, (d), and the fraction of the field attributed to the orbit loss, (e), are shown.

Chapter 7

Summary and outlook

7.1 Summary of key developments

The body of this thesis developed an orbit loss model that for the first time includes a comprehensive consideration of the effects of pitch angle scattering on ions either interior or exterior to the loss cone, retaining sensitivities to a particular ion's energy, the background plasma characteristics, and the structure of the velocity-space loss cone. A focus is placed on the importance of the configuration-space location of loss cone refueling, impacting both the collisional properties and the periods of orbit loss. The scattering events are self-consistently allowed to both populate and depopulate the loss cone, giving rise to a division of the cone about a qualitative change in the loss behavior. The collisional portion of the loss cone describes ions that are in equilibrium with the local Maxwellian and is considered full. The collisionless loss cone is more sparsely populated as a non-negligible fraction of ions on these trajectories are lost from the plasma on a first orbit. In the steady-state, such losses are driven by the rate of transport onto these trajectories. Estimates for the loss currents and other associated kinetic source terms driven by the pitch angle scattering are detailed in the text, allowing for the coupling of the model with a fluid code package that does not resolve the orbit loss.

The orbit loss model is relatively fast since it does not require the resolution of entire particle orbits. A local loss cone specifies which trajectories are lost to the divertor when launched from a given observation point, and partial orbit reconstruction is typically sufficient to determine the likelihood of loss on a first orbit, thanks to the well-connected nature of any local loss cone and the similarities between proximate loss orbits in velocity-space. Compared to other loss cone models, cone construction is also simplified under reasonable assumptions of the electric potential profile, maintaining the most significant features of the radial electric field. Computational levity is further achieved through the approximate treatment of collisions through its timescales. The significance of scattering out of the loss cone is assessed by comparing the loss time scale, including both velocity-space sensitivities and the poloidal stagnation near the X-point, to the timescale of perpendicular diffusion by the relevant angular width of a velocity-space loss cone. The time-averaged asymmetric pitch angle scattering near the boundaries of the local collisionless loss cones determines the rate of loss cone refueling which is corrected for the probability of scattering out of the loss cone. The order of the ion orbit loss reproduces that seen in the literature; however, this model's loss current exhibits newly presented behaviors.

The orbit loss model discussed in this thesis is the first to present a low- and high-density branch for the loss current over a constant input power. The orbit losses are maximized for some edge density, decreasing with both global increases or decreases to the profile. The existence of such branches provides further evidence for the link between the L-H transition power threshold and the ion orbit loss. This behavior is rooted in the existence of a saturation temperature for any particular local collisionless loss cone. Immersion of such a loss region in a background plasma with an ion temperature above saturation results in a reduced collisionless orbit loss related to the increased particle concentration about the higher energies of the local loss cone boundary where the pitch angle scattering refills the cone at a reduced rate. Along the low density orbit loss branch, the average local collisionless loss cone is oversaturated. The supplemental collisional current is also small here largely due to the

direct reduction in the number of particles in these regions at lower density. Growth in the orbit loss current with increasing ion temperature is stagnated on this branch and the losses can even reduce. Over the high density orbit loss branch, a typical local collisionless loss cone is not oversaturated, and there is strong growth with the ion temperature. The density that maximizes the orbit loss is therefore dependent on the input power as densities transition to the low density branch at increased input powers. The collisional current supports the high density branch, reducing the orbit loss falloff with increasing density.

The steady-state orbit losses calculated by the model further cement the influential role played by the thermal ion orbit loss leading up to the L-H transition. As long expected, the steady-state orbit loss is about a factor of two larger for the favorable ∇B drift direction due to an effective increase in the collisionality along a loss trajectory. The orbit loss current profiles are similar for the two drift orientations when the input power is roughly a factor of two larger for the unfavorable case, again echoing a known feature of the L-H transition power threshold. The dependence of the loss current on the horizontal location of the X-point also qualitatively agrees with experimental results on NSTX, with new experiments on ASDEX Upgrade currently under analysis to provide a quantitative comparison. The dependence of the orbit loss on the ion mass has been explored by considering the coupled effects of larger orbital widths and lesser collisionalities with increased inertia.

The implementation of the new orbit loss model into the SOLPS code package allows for the determination of the leading order plasma response to the thermal orbit losses. It is shown that the orbit loss current instigates the largest effects, establishing itself as a leading force in the edge current balance. The combined outward flow of the orbit loss current and a suppressed effective diamagnetic current is largely balanced by a perpendicular viscosity current sensitive to the anomalous transport. The new equilibrium state exhibits a more strongly sheared radial electric field with a well deepening proportional to the orbit loss current as a function of the density. Higher density plasmas in the SOLPS environment can more easily supply the necessary return current, so the orbit loss effect appears most

significant at lower density. It is noted that the simulations were necessarily restricted to the high density orbit loss current branch due to a numerical instability found a low densities for sufficiently small anomalous conductivities. It is an open question as to how the plasma responds to the low density branch of the orbit loss current.

The simulations show that the electric field both grows and becomes increasingly attributed in origin to the orbit loss current with increasing input power. The well depths and associated shear appear to reach values thought necessary to trigger the L-H transition at input power levels within the ballpark of those experimentally known to do so. In the absence of the orbit loss current, the input powers corresponding to radial electric fields of similar magnitude are $\sim$ 10–20% greater. The evidence indicates that the loss of thermal ions due to the geometry of a poloidally diverted tokamak must be considered in any model of the L-H transition.

7.2 The continuing path forward

There are many obvious next steps to continue the work presented in this thesis: relaxing various assumptions and approximations in the orbit loss model, extending the parameter scans of the SOLPS simulations, introducing new physics into the model or the model into an environment with new physics, and bolstering comparisons made to experiment. Each of these will be briefly discussed in the concluding paragraphs of this chapter.

Here, the weaknesses, approximations, and assumptions most deserving of further efforts will be enumerated. The order here is by introduction in the text and not by any sense of criticality.

- The electric potential could be allowed to vary poloidally, as evidenced by simulation and experiment. The trapped-passing boundary, which is of importance for the loss cone structure, would gain an additional level of complexity with a new sensitivity to the poloidal coordinate.

- Furthermore, the assumption that the parallel and poloidal bounce positions remain close could be relaxed. A reliable method for determining the orbital shapes would be necessary, but the model could be more comfortably extended to include arbitrary strength radial electric fields following this improvement.

- In the present implementation, the collisionality rates and the particle distributions are both determined under the assumption of local Maxwellians. A next step would be to model local Maxwellians with a velocity-space hole or another appropriate distribution function.

- The collisionless condition could be more finely tuned to not require the supplementary collisional current.

- Further refueling mechanisms for the collisionless loss cone should be studied in greater detail, particularly the turbulent transport.

- The effective diamagnetic current in the SOLPS model equations could be corrected for the existence of the collisionless loss cone. The current would be most strongly damped at low densities, where the collisionality is lowest. This could perhaps help resolve the stability issues seen at the low densities that exhibit large magnitude radial electric fields.

Each of these would do well to improve the model fidelity, but none are expected to wholesale alter the presented results.

The SOLPS simulations along the high density loss current branch show promising signs for the significance of the orbit loss approaching the L-H transition. Analytic analysis of the orbit loss model additionally suggests shared dependencies with the L-H transition power threshold, namely the branching density behaviors, the ∇B drift direction asymmetry, the main ion mass, and the horizontal position of the X-point. The scope of the SOLPS simulations should be extended to study this wide parameter space. Aside from the aforementioned

low density numerical instability for a given input power, nothing within the B2.5 model precludes investigating these effects. Even the known instability can be resolved by allowing for slightly larger anomalous currents or accepting the necessarily small time steps. Furthermore, the model equations could be adapted to more rigorously account for the orbit losses.

A major next step for the orbit loss model would be to consider its relation to the plasma turbulence. Although there is evidence that the turbulence can enhance the orbit losses,[34,55] a first principles analytic model does not exist which couples the effects of turbulence and Coulomb collisions on the ion orbit loss. The suggested theory that some combination of the orbit loss and the turbulent dynamics is responsible for triggering the L-H transition[115] demands that both effects be studied in unison. There are two obvious ways of approaching this: one could develop a similar orbit loss model, accounting for the effects of turbulence from the ground up, or one could implement the present model into a larger framework that resolves turbulent effects. A promising candidate for the later is the fluid turbulence code GRILLIX.[131]

Finally, the strengthened connections between the ion orbit loss and the empirically known $P_{\text{L-H}}$ highlight the importance of the experiment-theory feedback loop. To ensure that the presented results are physically sound, experimental measurements must be more directly compared to the predictions made by the coupled orbit loss and SOLPS models. As discussed, analysis is underway for experiments that were designed to measure the influence of the thermal orbit loss on the radial electric field in ASDEX Upgrade under changes in both the ∇B drift direction and the horizontal position of the X-point. The insight gained from these measurements will help direct the path forward. Furthermore, analysis should be performed on existing discharges or new experiments should be proposed to investigate the other known dependencies of the orbit loss.

Appendix A

Baseline SOLPS parameter set: ASDEX Upgrade 16151

The results presented in this thesis are largely based on calculations and simulations about a standard example SOLPS simulation of ASDEX Upgrade discharge 16151. Unless otherwise mentioned, the figures within the text apply to this baseline case. This appendix details the geometry, profiles, boundary conditions, and other features of this foundational case. Analytic scans over the profiles are referenced in the text and are contextualized in the following. The array of simulations referenced in Chapter 6 can be first order inferred from these simpler scans.

The baseline simulation consists of a plasma composed of a single ion species (deuterium), the electrons, and fluid neutral particles. The field geometry is a lower single null (LSN), with a single active X-point at the lower end of the plasma, and is positive in its triangularity. The toroidal field strength at the major radius is $|B_z| \sim 2.9$ T. The anomalous particle and heat diffusivities are taken to be $D^n_{\mathrm{AN}} = 0.4$ m^2/s and $\chi_{i,e} = 1.6$ m^2/s. It is noted that the effective heat diffusivity is affected by the neutral physics. The full SOLPS drift terms are switched on as described in the literature,[70,71] and the vertical ∇B and curvature drifts are directed toward the active X-point. The anomalous conductivity, $\tilde{\sigma}^{\mathrm{AN}}$, has been lowered to

10^{-6} Sm^2/C, ensuring a physically meaningful solution to the potential equation.[96] Radial ion flows are kept in the ion channel, as opposed to the simpler modeling achieved by implying electron motions via the coupled ion and current continuity equations sometimes invoked in SOLPS simulations. Each simulation contributing to this thesis maintains these features.

A.1 Geometry

The magnetic field geometry used in the baseline simulation can be seen in Figure 1.1, where subplot (a) shows the toroidal field and (b) the scaled poloidal flux, and in Figure 4.8 which shows the poloidal component of the magnetic field. The basic R^{-1} field strength dependence as well as the dominance of the toroidal component can easily be seen. The toroidal field component is pointing out of the page, ensuring the correct drift direction. The direction of the poloidal field component insinuates that the counter-current directed particles are described by $v_{\|} < 0$. The shaping of the flux surfaces can be seen in Fig. 1.1.b, where the separatrix indicates the lower triangularity $\delta_{\text{lower}} = 0.3$.

A.2 Profiles

The plasma profiles for the baseline case along the outer midplane can be seen in Figure A.1. The density and temperature profiles are largely set by the anomalous diffusion coefficients, which are held constant across all the simulations, and the core (interior) boundary conditions, which will be briefly discussed in the upcoming section. Parameter scans are thus achieved by altering the core boundary density and power flux. For every scanned value of the power flux, the energy is even distributed between the electrons and the ions. The analytic scans seen in Chapter 5 simply scale the profiles of Fig. A.2, while the scans in Chapter 6 self consistently determine the profiles for each set of parameters within the SOLPS model.

The rotation and electric field profiles are determined by the model equations as described

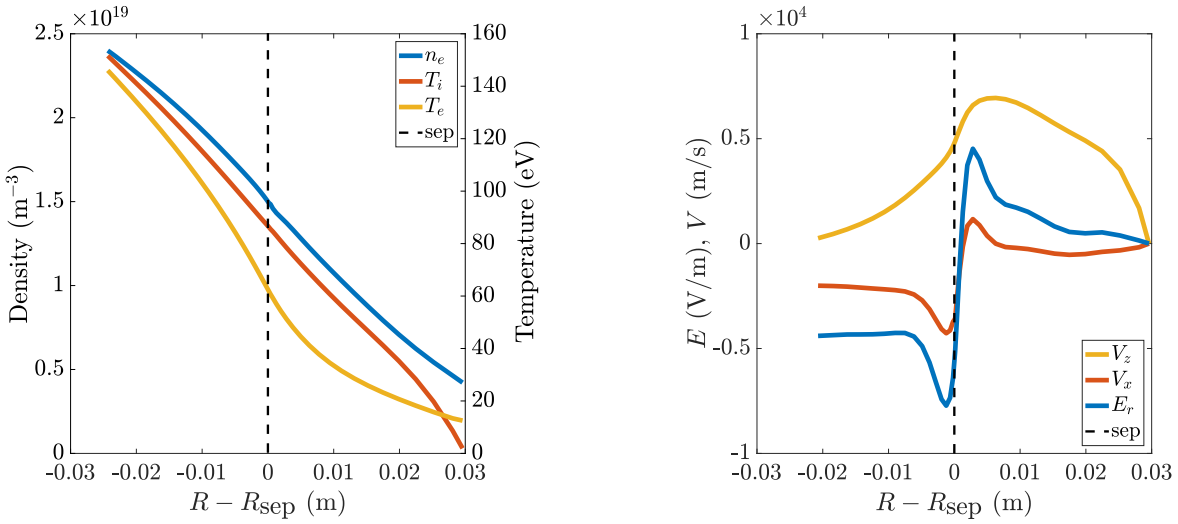

Figure A.1: The baseline density, temperature, E_r, and rotation profiles.

in Section 2.4. The neoclassical force balance generally provides an apt description for the poloidal rotation in the more core like region; however, there is a thin viscous boundary where the quasineutrality condition, sourceless current continuity, sets a more nuanced balance. This region is where the thermal orbit loss is of importance on approach to the L-H transition. The balance is highly dependent on the value of $\tilde{\sigma}^{\mathrm{AN}}$, so the value 10^{-6} Sm^2/C is chosen to ensure a physical solution.[96]

A.3 Boundary Conditions

There are six boundaries for SOLPS simulations of a single-null geometry that can easily be seen by considering the code's computational regions illustrated in Figure A.2. The four regions are the core (1), the SOL (2), the western divertor (3), and the eastern divertor (4). The boundaries are described in terms of their location in the computational plane using the compass directions: north, south, east, and west. In subplot (b), the separatrix is the horizontal black line while the vertical lines correspond to artificial cuts separating the private flux regions from the core. The southern boundary of the core corresponds to the

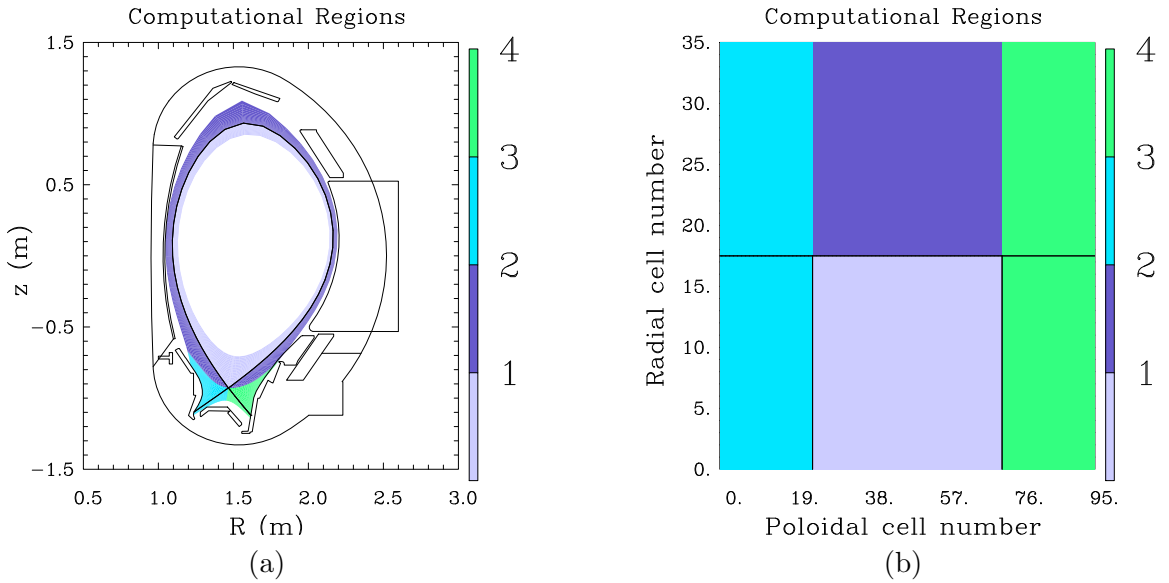

Figure A.2: The SOLPS computational regions for a single-null geometry.

interface of the confined plasma with the interior. Regions (1), (2), and (3) have a shared northern boundary that corresponds to the plasma approaching the first wall. The eastern and western boundaries respectively correspond to the conditions of the plasma's interaction with the east and west targets. The final boundaries are found on the south sides of regions (3) and (4), corresponding to the private flux region's interface with the divertor. These two boundaries are treated equivalently here.

There are a wide variety of boundary conditions available to SOLPS users, each of which is described in the user manual.[71] Each boundary requires conditions for the continuity, momentum, and energy equations for each species, as well as for the potential equation. Recall that there is no electron continuity equation, and therefore there are only continuity boundary conditions for the ions and neutrals. The following briefly describes the conditions used in the baseline and other simulations. For the orbit loss studies, the core boundary conditions are the most significant and are manipulated to scan over the parameter space of interest.

A.3.1 Core boundary

- The neutral particles maintain a constant null flux through the core boundary since the plasma in near complete ionization in the core. (BCCON = 8)
- The electron density is held at a constant value at the core boundary, $n_e = 2.4 \cdot 10^{19}$ m^{-3} for the baseline case. Quasineutrality demands that the ion density is equivalent. The boundary condition is manipulated in the density scans. (BCCON = 1)
- The parallel velocity for each species is held to zero at the core boundary. The condition is soft and is forced depending on a chosen variable strength, here $2 \cdot 10^5$. (BCMOM = 4)
- Both the electrons and ions have a specified power flux across the interior flux surface. The baseline case has 0.6 MW carried by each species, for a total of 1.2 MW. This boundary condition is manipulated for the ion temperature/input power scans, with the power evenly allotted to the ions and elections. (BCENE=16)
- The currents due to the drifts for the core boundary are imposed. (BCPOT = 12)

A.3.2 North boundary

- Both the neutrals and the ions are treated using a leakage boundary condition determined by $\Gamma_{\text{loss}} = \alpha C_{s,a} n_a$, where $C_{s,a}$ is the local sound speed and n_a is the species density. The coefficient α is null for the neutrals and $\alpha = -1 \cdot 10^{-3}$ for the ions. This condition is recommend for drift cases. (BCCON = 10)
- Again, the parallel velocity for each species is held to zero at the north boundary. The condition is soft and is forced depending on a chosen variable strength, here $2 \cdot 10^5$. (BCMOM = 4)
- The electrons and ions have a specified decay length for the temperature profiles. The baseline case has a decay length of 0.02 m for both species. (BCENE=16)

- The gradient of the potential, the electric field, is taken to be null at the northern boundary. (BCPOT = 2)

A.3.3 East and west boundaries

- The neutral particles have a prescribed null particle flux through these boundaries. (BCCON = 5)
- The ion continuity condition is set by a recommended sheath boundary condition for the sound speed velocity flux. (BCCON = 14)
- The parallel velocity for the neutrals is held to zero at the east and west boundaries. (BCMOM = 1)
- The sheath boundary conditions for the parallel momenta of the charged species is implemented. (BCMOM = 13)
- The sheath boundary conditions for the ion and electron energy equations are used. (BCENE=15)
- The sheath boundary conditions for the potential equation is used. (BCPOT = 11)

A.3.4 Private flux southern boundaries

- Both the neutrals and the ions are treated using a leakage boundary condition determined by $\Gamma_{\text{loss}} = \alpha C_{s,a} n_a$, where $C_{s,a}$ is the local sound speed and n_a is the species density. The coefficient $\alpha = -1 \cdot 10^{-2}$ for the neutrals and $\alpha = -1 \cdot 10^{-3}$ for the ions. This condition is recommend for drift cases. (BCCON = 10)
- The parallel velocity for all species is held to zero at the southern private flux boundaries. The condition is soft and is forced depending on a chosen variable strength, here $2 \cdot 10^5$. (BCMOM = 4)

- Here the electron and ions have a specified decay length for the temperature profiles. The baseline case has a decay length of 0.01 m for both species. (BCENE=16)

- The gradient of the potential, the electric field, is taken to be null at the boundaries. (BCPOT = 2)

Bibliography

[1] Syvitski *et al*, Communications Earth and Environment **1**, 32 (2020).

[2] U.S. Energy Information Administration, *Monthly Energy Review*, April 2020

[3] P. Hawken. *Drawdown*. Penguin Books, (2017).

[4] J. Tsao, N. Lewis, and G. Crabtree. *Solar FAQS*, U.S Department of Energy, Office of Basic Energy Science (2006).

[5] L.W. Shemilt and G. Sheng, Energy Exploration and Exploitation **2**, 41 (1983).

[6] J. Wesson *et al*. *Tokamaks*. Oxford, Oxford University Press, (1987).

[7] J.D. Lawson. *Some Criteria for a Useful Thermonuclear Reactor*. Atomic Energy Research Establishment, (1955).

[8] N.A. Krall and A.W. Trivelpiece. *Principles of Plasma Physics*. McGraw-Hill, (1973).

[9] Wagner *et al*, Physical Review Letters **49**, 19 (1982).

[10] A.H. Boozer. *Stellarators as a Fast Path to Fusion*. arXiv:2104.04621 [physics.plasm-ph], (2021).

[11] F.L. Hinton and R.D. Hazeltine, Reviews of Modern Physics **48**, 239 (1976).

[12] A.J. Woottoon *et al*, Physics of Fluids B: Plasma Physics **2**, 2879 (1990).

[13] J.W. Connor and H.R. Wilson, Plasma Physics and Controlled Fusion **36**, 719–795 (1994).

[14] F. Ryter *et al*, Plasma Physics and Controlled Fusion **40**, 725 (1998).

[15] ASDEX Team, Nuclear Fusion **29**, 1959 (1989).

[16] T.N. Carlstrom *et al*, Plasma Physics and Controlled Fusion **36**, A147 (1994).

[17] T.N. Carlstrom *et al*, Fusion Science and Technology **48:2**, 997–1010 (2005).

[18] S.M. Kaye *et al*, *LH Threshold Studies in NSTX* [Princeton Plasma Physics Laboratory Report] (2011).

[19] C. Bourdelle *et al*, Nuclear Fusion **55**, 073015 (2015).

[20] Y. Andrew *et al*, Plasma **2**, 328–338 (2019).

[21] M. Cavedon *et al*, Nuclear Fusion **60**, 066026 (2020).

[22] Y. Andrew *et al*, Plasma Physics and Controlled Fusion **48**, 479–488 (2006).

[23] P. Sauter *et al*, Nuclear Fusion **52**, 012001 (2012).

[24] V. Philipps *et al*, ECA **25A**, 1761–1764 (2001).

[25] F. Ryter *et al*, Plasma Physics and Controlled Fusion **58**, 014007 (2016).

[26] C.F. Maggi *et al*, Plasma Physics and Controlled Fusion **60**, 014045 (2018).

[27] C.F. Maggi *et al*, Nuclear Fusion **59**, 076028 (2019).

[28] U. Plank *et al*, Nuclear Fusion **60**, 074001 (2020).

[29] D.J. Battaglia *et al*, Nuclear Fusion **53**, 113032 (2013).

[30] Y.R. Martin *et al*, Journal of Physics: Conference Series **123**, 012033 (2008).

[31] H. Bilgari, P.H. Diamond, and P.W. Terry, Physics of Fluids B: Plasma Physics **2**, 1 (1990).

[32] C.S. Chang *et al*, Physical Review Letters **118**, 175001 (2017).

[33] C.S. Chang, S. Kue, and H. Weitzner, Physics of Plasmas **9**, 9 (2002).

[34] S. Ku, H. Baek, and C.S. Chang, Physics of Plasmas **11**, 12 (2004).

[35] T. Stoltzfus-Dueck, Nuclear Fusion **60**, 1 (2019).

[36] J.W. Connor and H.R. Wilson, Plasma Physics and Controlled Fusion **42**, R1 (2000)

[37] D. Kalupin *et al*, Plasma Physics and Controlled Fusion **48**, A309 (2006)

[38] K.C. Shaing, Physics of Plasmas **9**, 1 (2002).

[39] J.A. Boedo *et al*, Physics of Plasmas **23**, 092506 (2016).

[40] W.M. Stacey, Physics of Plasmas **25**, 122506 (2018).

[41] K. Miyamoto, Nuclear Fusion **36**, 927 (1996).

[42] J.S. deGrassie *et al*, Nuclear Fusion 49, 085020 (2009).

[43] W. Stacey, Physics of Plasmas **18**, 102504 (2011).

[44] R.W. Brzozowski III *et al*, Physics of Plasmas **26**, 042511 (2019).

[45] A.V. Chankin and G.M. McCracken, Nuclear Fusion **33**, 10 (1993).

[46] T.P. Kiviniemi, T. Kurki-Suonio, S.K. Sipilä, Czechoslovak Journal of Physics **51**, 10 (2001).

[47] Y. Nishimura, F.L. Waelbroeck, and L.J. Zheng, Physics of Plasmas **27**, 012505 (2020).

[48] J. Ou, G. Wu, and X. Li, Physics of Plasmas **21**, 072505 (2014).

[49] W.M. Stacey, Physics of Plasmas **21**, 014502 (2014).

[50] J.S. deGrassie, J.A. Boedo, and B.A. Grierson, Physics of Plasmas **22**, 080701 (2015).

[51] J.A. Bittencourt. *Fundamentals of Plasma Physics*. New York, Springer, (2004).

[52] E.A. Azizov *et al*, Atomnaya Energiya **52**, 2 p. 108–112 (1982).

[53] G. Grieger, Europhysics News, **16**, 5 p. 11–14 (1985).

[54] T. Kobayashi *et al*, Physical Review Letters **111**, 035002 (2013).

[55] S. Wang, Scientific Reports **10**, 6986 (2020).

[56] W.D. D'haeseleer *et al. Flux Coordinates and Magnetic Field Structure*. Springer (1991).

[57] V.D. Shafranov, Reviews of Plasma Physics **2**, p. 103 (1966).

[58] B. Scott (2001). *Low Frequency Fluid Drift Turbulence in Magnetized Plasmas* (IPP 5/92) [Habilitation thesis, Düsseldorf University and Max Planck Institute for Plasma Physics].

[59] F. Jenko *et al*, Physics of Plasmas **7**, 1904 (2000).

[60] Görler *et al*, Physics of Plasmas **23**, 072503 (2016).

[61] N. Tronko *et al*, Physics of Plasmas **24**, 056115 (2017).

[62] P. Crandall (2019). *Collisional and Electromagnetic Physics in Gyrokinetic Models*[Doctoral thesis, University of California, Los Angeles]

[63] S-I. Itoh and K. Itoh, Physical Review Letters **60**, 20 (1988).

[64] K.C. Shaing and E.C. Crume, Jr., Physical Review Letters **63**, 21 (1989).

[65] M. Tendler, Plasma Physics and Controlled Fusion **39**, B371 (1997).

[66] J. Schirmer *et al*, Nuclear Fusion **46**, 9 (2006).

[67] E. Viezzer *et al*, Nuclear Fusion **54**, 012003 (2014).

[68] M. Cavedon (2016). *The role of the radial electric field in the development of the edge transport barrier in the ASDEX Upgrade tokamak*[Doctoral thesis, Technical University Munich]

[69] U. Stroth, P. Manz, and M. Ramisch, Plasma Physics and Controlled Fusion **53**, 024006 (2011).

[70] V. Rozhansky *et al*, Nuclear Fusion **49**, 025007 (2009).

[71] D.P. Coster *et al*, *SOLPS-ITER User Manual*

[72] D.A. Clarke, *A Primer on Tensor Calculus* (2011).

[73] P. Helander. *Collisional Transport in Magnetized Plasmas*. Cambridge University Press, (2005).

[74] J.A. Holmes, Y-K.M. Peng, and K.E. Rothe, Journal of Fusion Energy **2**, 2 1982

[75] J.D. Callen, A.J. Cole, and C.C. Hegna, Physics of Plasmas **16**, 082504 (2009).

[76] E. Viezzer (2012). *Radial electric field studies in the plasma edge of ASDEX Upgrade* [Doctoral thesis, Ludwig-Maximilians-University Munich]

[77] P.J. Catto, R.J. Hastie, and I.H. Hutchinson, Physics of Plasmas **8**, 3334 (2001)

[78] P. Helander, Physics of Plasmas **8**, 10 (2001)

[79] B.J. Braams (1987). *A Multi-Fluid Code for Simulation of the Edge Plasma in Tokamaks* [NET Report].

[80] S. Wiesen *et al*, Journal of Nuclear Materials **463**, 480–484 (2015).

[81] X. Bonnin *et al*, Plasma and Fusion Research: Regular Articles **11**, 1403102 (2016).

[82] D. Reiter, M. Baelmans, and P. Börner, Fusion Science and Technology **47:2**, 172–186 (2005).

[83] E.T. Meier *et al*, Plasma Physics and Controlled Fusion **58**, 125012 (2016).

[84] V.A. Rozhansky *et al*, Nuclear Fusion **41**, 387 (2001).

[85] W.M. Stacey, Physics of Plasmas **16**, 042502 (2009).

[86] W.M. Stacey and T.M. Wilks, Physics of Plasmas **23**, 012508 (2016).

[87] T.M. Wilks, W.M. Stacey, and T.E. Evans, Physics of Plasmas **24**, 012505 (2017).

[88] W.M. Stacey, Nuclear Fusion **57**, 066034 (2017).

[89] S.I. Braginskii, Review of Plasma Physics **1**, p. 205 (1965).

[90] A.V. Chankin, Journal of Nuclear Materials **241–243**, 199–213 (1997).

[91] T.D. Rognlien and D.D. Ryutov, Contributions to Plasma Physics **38**, 152–157 (1998).

[92] F.L. Hinton and Y.-B Kim, Nuclear Fusion **34**, 899 (1994).

[93] R. Balescu, *Transport processes in plasmas I*, North Holland, New York, (1998).

[94] T.D Rognlien *et al*, Physics of Plasmas **6**, 1851 (1999).

[95] V. Rozhansky, Contributions to Plasma Physics **46**, 575–585 (2006).

[96] E. Kaveeva *et al*, Nuclear Fusion **58**, 126018 (2018).

[97] V. Rozhansky, Reviews of Plasma Physics **24**, p. 1 (2008).

[98] J. Loizu *et al*, Journal of Plasma Physics **83**, 575830601 (2017).

[99] K.C. Shaing, E.C. Crume, and W.A. Houlberg, Physics of Fluids B: Plasma Physics **2**, 1492 (1990).

[100] K.C. Shaing, Physics of Fluids B: Plasma Physics **4**, 3310 (1992).

[101] J.A. Heikkinen *et al* Plasma Physics and Controlled Fusion **40**, 693 (1998).

[102] H.J. de Blank, 46th EPS Conference on Plasma Physics **P2**, 1020 (2020).

[103] T.P. Kiviniemi *et al*, Physics of Plasmas **10**, 2604 (2003).

[104] C. Pan, S. Wang, and J. Ou, Nuclear Fusion **54**, 10 (2014).

[105] J.A. Rome and Y-K.M. Peng, Nuclear Fusion **19**, 1193 (1979).

[106] C.T. Hsu and D.J. Sigmar, Physics of Fluids B: Plasma Physics **4**, 1492 (1992).

[107] R.G. Littlejohn, J. Plasma Physics **29**, part 1 pp. 111–125 (1983).

[108] T. G. Northrop and J. A. Rome, The Physics of Fluids **21**, 384 (1978).

[109] B.A. Trubnikov, Reviews of Plasma Physics **1**, (1965).

[110] C.D. Stephens, R.W. Brzozowski III, and F. Jenko, Physics of Plasmas **24**, 102517 (2017).

[111] S. Putvinskii, Plasma Physics Control. Fusion **35**, 219 (1993).

[112] E. Hirvijoki *et al*, Computer Physics Communications **185**, 1310–1321 (2014).

[113] J.S. deGrassie, S. H. Müller, and J.A. Boedo, Nuclear Fusion **52**, 013010

[114] M.J. Schaffer *et al*, Physics of Plasmas **8**, 2118 (2001).

[115] C.S. Chang, S. Ku, and R.M. Churchill, Physics of Plasmas **26**, 014504 (2019).

[116] M. Wensing *et al*, Nuclear Fusion **60**, 054005 (2020).

[117] G. Kagan and P. Catto, Physics of Plasmas **16**, 056105 (2009).

[118] T. Stoltzfus-Dueck *et al*, Physical Review Letters **114**, 245001 (2015).

[119] T. Pütterich *et al*, Nuclear Fusion **52**, 083013 (2012).

[120] E. Viezzer *et al*, Plasma Physics and Controlled Nuclear Fusion **55**, 124037 (2013).

[121] V. Rozhansky *et al*, Nuclear Fusion **55**, 073017 (2015).

[122] J.D. Huba, 1950-. NRL Plasma Formulary. Washington, DC :Naval Research Laboratory, 1998.

[123] J.D. Callen. *Fundamental of Plasma Physics: DRAFT*. (2006).

[124] C.D. Stephens, X. Garbet, and F. Jenko, Physics of Plasmas **27**, 052504 (2020).

[125] A.J. Brizard, Physics of Plasmas **18**, 022508 (2011).

[126] H.J. de Blank, Fusion Science and Technology **49**, 2T (2006).

[127] J.R. King *et al*, *Testing model of ion orbit loss (IOL)*, APS-DPP 2019 (2019).

[128] P. Cano-Megias *et al*, *Role of thermmal ion orbit loss on* E_r[Experimental Proposal for ASDEX Upgrade campaign 2021](2020).

[129] A. Chankin, *How to correctly calculate the generation of toroidal momentum by ion orbit losses*[Private communication] (2019).

[130] J.A. Heikkinen *et al*, Journal of Computational Physics **173**, 527–548 (2001).

[131] A. Stegmeir *et al*, Plasma Physics and Controlled Fusion **60**, 035005 (2018).